A MESOSCOPIC FORMALISM FOR SIMULATING PARTICLE-LADEN FLOWS WITH APPLICATIONS IN ENERGY CONVERSION PROCESSES

A Dissertation

Presented to the Faculty of the Graduate School

of Cornell University

in Partial Fulfillment of the Requirements for the Degree of

Doctor of Philosophy

by

Jesse Samuel Capecelatro

August 2014

A MESOSCOPIC FORMALISM FOR SIMULATING PARTICLE-LADEN FLOWS WITH APPLICATIONS IN ENERGY CONVERSION PROCESSES

Jesse Samuel Capecelatro, Ph.D.

Cornell University 2014

The non-linear and multiscale nature of turbulent flows is further complicated in the presence of inertial particles. Intimate coupling between the phases may lead to a high degree of spatial segregation that reorganizes the structure of the underlying turbulence. The wide range of relevant length and timescales associated with fluid-particle systems poses significant challenges in understanding and predicting their behavior. In recent years, the advent of petascale computing has enabled the direct numerical simulation (DNS) of large-scale turbulent flows, though DNS of particle-laden flows remains severely limited.

This work presents methods to alleviate previous numerical constraints on the computational grid when considering finite-size particles. Volume filtered equations for the carrier phase are derived in detail for variable-density flows in the presence of particles and solved in a highly-scalable Eulerian-Lagrangian framework. The filter introduces a separation in length-scales during the interphase exchange process, where everything smaller than the support of the filtering kernel requires modeling (e.g., surface reactions and drag), and everything larger than the support of the filtering kernel is captured explicitly. To remain computationally tractable, the filtering procedure is solved in two steps, by first transferring the particle information to the nearest neighboring cells, and then making use of an implicit diffusion operation. In flows that exhibit strong spatial segregation in particle concentration, a separation of length scales must be established when

extracting Lagrangian statistics. To accomplish this, an adaptive spatial filter is employed on the particle data with an averaging volume that varies with the local particle-phase volume fraction.

The filtered Euler-Lagrange formalism is shown to yield highly accurate and physical results for large-scale particle-laden flows from the dilute to dense regime. An analysis of chemically reacting species in circulating fluidized bed risers reveals that the non-homogeneities caused by the formation of clusters significantly reduces the efficiency of the conversion process. To better understand the fundamental nature of particle clustering and its effects on the carrier-phase turbulence, a canonical flow is introduced, referred to as cluster-induced turbulence (CIT). Simulations of fully-developed, gravity-driven CIT are investigated, revealing for the first time the local instantaneous distribution of particle-phase dynamics in collisional gas-solid flows.

BIOGRAPHICAL SKETCH

Jesse Capecelatro was born in White Plains, New York, on November 29, 1986, and grew up in Brewster, a small suburb of New York City. After graduating from Brewster High School in 2005, he went on to pursue a Bachelor's degree in Mechanical Engineering at the State University of New York in Binghamton. During his time at Binghamton he became interested in thermal and fluid sciences and their applications to renewable energy systems. He spent the summer prior to his senior year working in the Chemical and Biological Engineering Department at the University of Maine, conducting research on the conversion of second-generation biomass into ethanol. This experience spawned an interest to further his education, and after graduating from Binghamton in 2009, he accepted an offer for admission to the Ph.D. program at the University of Colorado. Under the guidance of Prof. Olivier Desjardins, his research focused on developing numerical methods for large-scale computations of particle-laden flows in collaboration with the National Renewable Energy Laboratory. Two years later he left Colorado with a Master's degree in Mechanical Engineering and returned to New York, following Prof. Desjardins to Cornell University to complete his Ph.D in the interdisciplinary study of turbulence, multiphase flows, and high performance computing.

ACKNOWLEDGEMENTS

There are many people who deserve recognition for the achievements documented in this work. I am extremely grateful to have met and collaborated with so many of these talented and inspiring individuals in the last five years. I would like to begin by thanking my advisor Prof. Olivier Desjardins, whose ambition for pushing the frontiers of turbulence research has been inspirational. His constant support and standards for high quality work have been instrumental to my success. I would also like to thank the members of my Special Committee, Prof. Michel Louge and Prof. Donald Koch for their availability and interest in my work. Their curiosity and deep understanding of the fundamental nature of gas-solid flows have led to many useful insights and lively discussions. Prof. Perrine Pepiot, who first introduced me to Lagrangian particle tracking, is also owed significant acknowledgment. She has provided consistent guidance and direction throughout my doctoral studies, and for that I am very grateful. I also want to thank Prof. Rodney Fox for many fruitful discussions and sharing his expertise through our collaboration on cluster-induced turbulence.

There are a number of students I feel extremely fortunate to have met and worked along side of, some of which include Mark Owkes, Jeremy McCaslin, Bret Van Poppel, Peter Brady, Sunil Arolla, Mohomed Houssem Kasbaoui, and John Palmore. We have shared much joy and frustration in pursuit of advancing the current state of multiphase flow research. I will not forget the many late nights spent coding and debugging, sometimes encountering bugs that make us question the very nature of reality. I owe great thanks to my parents for their constant support and frequent reminders to enjoy life and not always work so hard. Finally, I would like to thank Sarah, Clyde, and Liam for their unfailing encouragement and constant reminders of why it is we pursue science in the first place.

This work has been supported in part by the Office of Biomass Program of the U.S. Department of Energy under contract XCO-0-40641-01 with the National Renewable Energy Laboratory. Computational resources provided by the Extreme Science and Engineering Discovery Environment (XSEDE), which is supported by National Science Foundation (NSF), as well as the computational resources purchased through the NSF Major Research Instrumentation (MRI) Program grant number CNS 1229081 and NSF Computer and Information Science and Engineering (CISE) Research Infrastructure grant number 1205413, are gratefully acknowledged.

TABLE OF CONTENTS

LIST OF TABLES

LIST OF FIGURES

CHAPTER 1

INTRODUCTION

1.1 The role of particle-laden turbulence

With rising environmental concerns and record-high oil prices, the need for cleaner and more efficient energy technologies is paramount. The fluid dynamics associated with such technologies are often complex and highly turbulent. In many systems, such as chemical transformation reactors, spray combustors, and slurry pipelines, the non-deterministic nature of the carrier-phase turbulence is further complicated by the presence of a disperse phase (i.e., solid particles, liquid droplets, or gaseous bubbles). A key challenge in understanding and predicting the multiphase dynamics is the fundamental importance of processes occurring on extremely small scales that ultimately influence the macroscopic behavior. As depicted in Fig. 1.1, the length scales associated with industrial-scale power generation plants may span several orders of magnitude. Key processes at the particle scale (e.g., surface reactions, wakes, and particle collisions), are responsible for organizing the flow into various regimes, such as particle clustering in risers of circulating fluidized bed reactors as shown in Fig. 1.1(b). Such phenomena may inhibit mixing between the phases and therefore impact reaction rates and heat transfer in energy conversion processes, potentially lowering operating efficiencies significantly. Accurate predictions of disperse multiphase flows (referred to throughout as particle-laden flows) are crucial to ensure optimal performance during the design process and enable large-scale industrialization of new technologies.

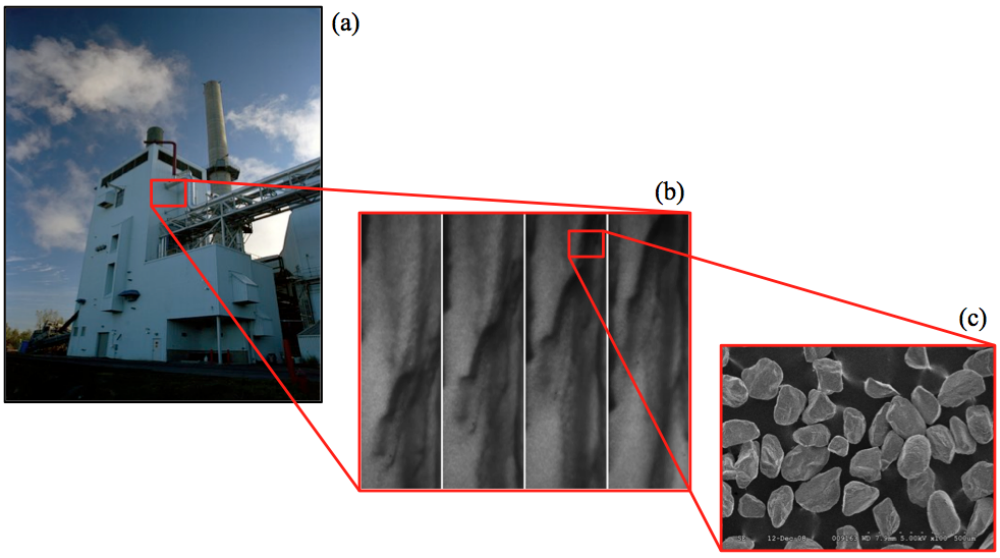

Figure 1.1: Example of the multiscale nature of particle-laden flows. (a) Biomass gasification plant (*http://www.windsohy.com*), (b) particle clustering in a lab-scale CFB riser [1], and (c) scanning electron microscopy image of sand particles [1].

One of the most intriguing (and challenging) aspects of particle-laden flows that distinguishes it from other branches of fluid mechanics is the inertia associated with the motion of individual particles. High inertia particles will retain information from previous collisions and interactions with distant turbulent eddies, causing them to deviate from fluid pathlines [2]. The velocities of neighboring particles may therefore be uncorrelated, while ensembles of particles collectively respond to large-scale motions of the flow. In finite Reynolds number flows, non-linearities caused by particle inertia contribute significantly to the overall dynamics of the system. Intimate coupling between the phases may result in a wide variety of interesting phenomena that amplify these non-linearities. Flows with particles of varying size (i.e., polydisperse flows) often exhibit strong segregation in particle size distribution, where small and large particles migrate to separate regions of the flow. In dense particulate flows, such as those found in fluidized bed reactors,

mean velocity differences between the phases will generate concentration waves in the direction of the flow in the form of bubbles [3]. Flow instabilities encountered in dilute particulate flows, such as those found in circulating fluidized bed risers, often lead to the spontaneous generation of dense clusters [3–7]. Meanwhile, a fundamental understanding of these mesoscale features and their effect on the carrier phase remains elusive.

1.2 Progress in experimental understanding of particle-laden flows

Due to the wide range of relevant length and timescales associated with particle-laden flows, and because the disperse phase limits optical access into the flow, obtaining detailed experimental measurements has proven to be an arduous task. Recently, novel techniques based on high-resolution particle image velocimetry (PIV) have emerged, which in limited granular regimes are capable of resolving the flow around individual particles [8]. Meanwhile, most experiential work to date aims at gathering global statistical quantities. Crowe [9] compiled numerous measurements of the turbulence intensity in disperse two-phase flows from experimental work found in the literature. The data included gas-solid, gas-liquid, and liquid-solid flows in axisymmetric jets and pipes at various orientations. Despite the enormous variations in particle concentrations and Reynolds numbers, a general trend was observed indicating that small particles attenuate fluid-phase turbulence intensity, while large particles augment turbulence. In general, the change in turbulence intensity is correlated with the particle loading and the ratio of the particle diameter to the Kolmogorov length scale. In some cases, the turbulence

intensity was observed to be four-times greater than its single-phase counterpart. Kulick *et al.* [10] made similar observations in a fully developed channel flow. The experiment was performed in a wind tunnel and data was measured using a forward-scatter laser Doppler anemometer (LDA). The lightest particles were 50 μm glass beads with a particle Stokes number of $\mathrm{St} = 0.18$. The heaviest particles were 70 μm with $\mathrm{St} = 0.93$. In each case, the particles had no effect on the mean gas velocity. The lighter particles were observed to have minimal effect on the turbulence while the heavier particles lead to a significant reduction. At a mass loading of 80% of the heavy particles the velocity fluctuations were almost reduced entirely.

A large body of experimental work exists on the topic of particle clustering in fluidized bed reactors. Noymer and Glicksman [11] reported cluster fall velocities from numerous experimental studies found in the literature, observing that although the flow conditions vary significantly, as well as the reactor geometries and particle parameters, the measured velocities were typically close to 1.0 m/s. Previous investigations on risers indicate that clusters tend to fall within 100 μm of the wall [12], placing them within the hydrodynamic boundary layer. Additionally, particles tend to reduce the gas-phase velocity gradients [13], implying that clusters falling near the walls are generally unaffected by the superficial gas velocity. Recent studies by Chew *et al.* [14–17] used a fiber optic probe and high-speed video camera to characterize clustering of monodisperse and polydisperse particles in a riser of a pilot-scale circulating fluidized bed reactor. It was found that the riser axial position greatly influences the radial profiles of cluster duration and frequency, but has negligible effect on cluster appearance probability. The particle size distribution and particle properties were shown to have comparatively minor effects on cluster characteristics. Two recent studies [1, 18] used high-speed

video and wavelet decomposition analysis of backscattered optical data to show that clusters were much more prevalent in the fully developed flow region of the riser. It was concluded that a better understanding of particle clustering and their interactions with the gas phase is clearly needed to improve existing models found in the literature.

1.3 Challenges in simulating particle-laden flows

With increasing computational resources and advancements in numerical methods, computational fluid dynamics (CFD) has emerged as a promising tool to investigate complex fluid-particle systems. To date, a relatively large number of modeling approaches have been developed (e.g., [19–24]). Yet, because of the prohibitively large number of particles associated with most practical flows, and limited understanding of the underlying non-linear physics, such models frequently rely on phenomenological approaches that require fine-tuning with the aid of experimental data. Model-free calculations of finite-size particles that fully-resolve all relevant length scales are currently limited to $\mathcal{O}(10^4)$ particles with current state-of-the-art computational resources [25].

In developing a numerical methodology that accounts for a large ensemble of particles, it is convenient to define a phase space containing all possible values of particle volume and velocity in space and time [26]. The stochastic nature of the particle phase is described by a Liouville equation for the multiparticle density function f. The Liouville equation represents the exact description for the complete phase space of each particle [27]. Due to the large number of independent variables associated with f in a three-dimensional flow, a direct solution is usually

intractable, and various mathematical approximations are made to arrive at models capable of simulating systems of interest.

Two common approaches for modeling disperse phase flows include Euler-Euler (EE) and Euler-Lagrange (EL) methods. EE representations reduce the Liouville equation to a one-particle density function represented by a kinetic equation [28–30]. In general, the kinetic description is unclosed and requires mesoscale models for the collision operator. EE methods approximate the kinetic equation by considering a set of moments of the particle density function, and solve both the fluid and particle phase on a common Eulerian grid. In the small Knudsen number (highly collisional) limit with an underlying assumption that the flow is nearly at equilibrium, the particle density function is close to Maxwellian and a Chapman-Enskog expansion can be used to derive a two-fluid model (TFM) using ensemble or volume averaging [31–34]. This approach leads to particle-phase transport equations that closely resemble the Navier-Stokes equations using moment closures obtained from kinetic theory. TFM greatly reduces the cost of simulating large-scale systems as it does not require interactions at the particle scale to be resolved. However, in the dilute limit, the constitutive models fail to correctly describe important features of the flow [35]. Several studies proposed solutions to overcome the limitations of standard TFM by considering higher-order moments of the kinetic equation and incorporating multivariate velocity distributions [35–39]. While EE methods have been widely successful, in particular due to their computational efficiency when solving systems containing a large number of particles, statistical and physical closures continue to pose a significant challenge.

EL strategies provide an alternative framework with the potential of simpler closures. In such methods, the disperse phase is represented in a Lagrangian

manner by discretizing the multiparticle density function into a number of individually tracked stochastic particles. As expected in Discrete Simulation Monte Carlo (DSMC) approaches, EL methods yield very accurate solutions, though they require a large number of stochastic particles to control statistical errors [40]. It is typical in EL simulations to consider as many particles as there are physical particles, or a smaller number of computational particles in order to reduce simulation cost. However, most existing EL coupling schemes require the Eulerian mesh to be an order of magnitude larger than the diameter of the largest particle, potentially preventing the capture of dynamically important mesoscale processes. In typical EL formulations, errors that arise during interphase exchange processes increase with grid refinement, resulting in non-convergent solutions [41, 42]. This can be problematic when dealing with non-uniform meshes or a disperse phase with a wide size distribution. In particular, it would be impossible to fully resolve the fluid-phase turbulence when the particle diameter is on the order of the Kolmogorov length scale, as this would require a mesh size to particle diameter ratio of unity.

Without improved numerical algorithms, the errors associated with transferring information between the phases will prevent tractable simulations of finite-size inertial particles in turbulent flows. Beyond the numerical restrictions, new physical models are necessary to account for velocity fluctuations and dissipation generated by the particles when the mesh size is capable of partially resolving these features [43]. In a recent review on EL methods [44], it was stated that any predictive multiphase tool must be based on

1. a mathematical representation that is capable of representing the physical phenomena of interest,

2. accurate and consistent models for the unclosed terms that need to be modeled, and

3. a numerically stable and convergent implementation.

The work presented in this dissertation aims at addressing these challenges in order to develop a predictive EL simulation methodology for turbulent particle-laden flows.

1.4 Objectives of this work

The overarching goal of this work is to advance the current state-of-the-art in numerical modeling of collisional particle-laden flows in order to investigate the effects of mesoscale structures (e.g., bubbles and clusters) on the carrier-phase turbulence in practical systems. Model-free calculations that fully-resolve all relevant length scales are currently limited to two regimes: computational grid cells much smaller than the particle diameter (particle-resolved DNS), and grid cells much larger than the particle diameter (point-particle methods). The present approach applies a mesoscopic formulation based on volume filtering to explore the intermediate regime. The new methods are implemented within a conservative finite difference scheme of arbitrary high-order accuracy tailored for turbulent flow computations. Note that although the focus of this dissertation concerns suspensions of solid particles, the formulation and tools developed in this work can be easily extended to sprays and bubbles. The specific objectives of this dissertation include:

1. Develop a predictive numerical framework that can simulate a large number of particles in arbitrary geometries. The method must be formulated

from first principles, have accurate and consistent models for the unclosed terms, converge under mesh refinement, and exhibit excellent scalability on massively parallel architectures.

2. Validate the numerical framework through the full spectrum of flow regimes (dilute to dense).
3. Develop a tool capable of accurately separating local instantaneous granular temperature from the total granular energy in an Eulerian frame of reference.
4. Apply the numerical framework to simulations of turbulent reacting gas-solid flows in order to characterize and quantify the effect of cluster formation on the catalytic conversion process.

1.5 Organization of the dissertation

This dissertation is divided into seven chapters. Chapters 2 - 6 represent pre-prints of manuscripts that have been published or are in preparation for submission to a journal.

In Chapter 2 [45], volume filtered equations for variable density, low Mach number flows in the presence of solid particles are derived and closure models for the unclosed terms are discussed. The volume filtered formalism is solved in an Eulerian-Lagrangian framework, and details on the implementation of the various algorithms are provided. The computational approach is then applied to several detailed studies of turbulent particle-laden flows.

First, the methodology is validated against various laboratory-scale fluidized bed reactors operated from minimum fluidization to highly turbulent configura-

tions. In Chapter 3 [46], large-eddy simulations (LES) of high Reynolds number liquid-solid slurries are conducted to investigate the multiphase dynamics associated with operating conditions above and below the critical deposition velocity. Model constants are extracted from the simulations and used to infer recently-developed Reynolds-average Navier-Stokes (RANS) closures [47].

A detailed study of wall-bounded circulating fluidized bed (CFB) risers is presented in Chapter 4 [7], demonstrating the capability of three-dimensional Eulerian-Lagrangian methods to reproduce particle clustering with physical characteristics. In Chapter 5 [48], an analysis of heterogeneously reacting species in CFB risers is performed. Results suggest that the non-trivial multiphase dynamics significantly reduce the efficiency of the chemical conversion process.

To better understand the fundamental nature of particle clustering and its effects on the carrier-phase turbulence, a canonical flow is introduced in Chapter 6 [49] referred to as cluster-induced turbulence (CIT). To isolate the effects of momentum coupling on the production of fluid-phase turbulent kinetic energy, a simulation of statistically homogeneous, gravity-driven CIT is performed. To measure the local distribution of granular temperature, an adaptive spatial filter is employed on the particle data with an averaging volume that varies with the local particle-phase volume fraction. To assess the validity of the adaptive filter, two-point statistics from both Eulerian and Lagrangian data are compared for a single realization of the flow.

Finally, Chapter 7 summarizes the major findings, contributions and conclusions from this work.

CHAPTER 2

AN EULER-LAGRANGE STRATEGY FOR SIMULATING PARTICLE-LADEN FLOWS

2.1 Abstract

In this work, a strategy capable of simulating polydisperse flows in complex geometries is employed where the fluid transport equations are solved in an Eulerian framework and the disperse phase is represented as Lagrangian particles. Volume filtered equations for the carrier phase are derived in detail for variable density flows, and all unclosed terms are discussed. Special care is given to the interphase coupling terms that arise, in order to ensure that they are implemented consistently and that they converge under mesh refinement. This provides the flexibility of using cell sizes that are smaller than the particle diameter if necessary. Particle collisions are handled using a soft-sphere model that has been modified for parallel efficiency. Simulations are carried out for a number of laboratory-scale configurations, showing excellent agreement with experiments.

2.2 Introduction

Suspensions of solid particles in a carrier fluid are common in many engineering applications, including sediment transport, gas and liquid fluidized bed reactors, and turbulent risers. Such flows are ubiquitous during biomass thermochemical conversion, and with recent interests in the production of renewable fuels, great effort has been put forward in understanding and predicting such processes. The presence of the disperse phase leads to a wide range of length and time scales that need to be

considered. Consequently, a relatively large number of modeling approaches have been developed (e.g. [19–24]). Whenever possible, such models should be based on well-defined physical parameters from the underlying microscale flow physics, and not derived from interpretations of a specific flow regime [19]. With the rapidly growing computational resources, new opportunities arise to develop more reliable and predictive computational fluid dynamics (CFD) models for exploring the complex behavior of disperse multiphase flows.

In this work, we consider a disperse phase that consists of smooth, spherical particles. A particle p is characterized by its position $\boldsymbol{x}_p(t)$, its volume $V_p(t)$, and its velocity $\boldsymbol{u}_p(t)$ at time t. Although the methods described in this paper assume solid particles, most of the formulation could be extended to droplets and bubbles as well. For an ensemble of N_p particles, it is convenient to define a phase space $\boldsymbol{X} = \left(\boldsymbol{x}_1, \boldsymbol{x}_2, \ldots, \boldsymbol{x}_{N_p}, \boldsymbol{u}_1, \boldsymbol{u}_2, \ldots, \boldsymbol{u}_{N_p}, V_1, V_2, \ldots, V_{N_p}\right)$. The phase space contains all possible values for each degree of freedom, and each particle is represented by a point in phase space [26]. The stochastic nature of the particle phase is described by a Liouville equation for the multiparticle density function, $f\left(t, \boldsymbol{x}, \boldsymbol{X}\right)$, given by

$$\frac{\partial f}{\partial t} + \boldsymbol{u}_p \cdot \frac{\partial f}{\partial \boldsymbol{x}_p} + \frac{\partial}{\partial \boldsymbol{u}_p}\left(f\frac{\boldsymbol{F}_p}{m_p}\right) = \mathbb{C}, \tag{2.1}$$

where $\boldsymbol{F}_p$ represents external forces acting on each particle (e.g., gravity, drag, added mass, etc.), m_p is the mass of each particle, and $\mathbb{C}$ is the collision operator. Note that Eq. 2.1 implies a summation over all particles. Due to the large number of independent variables associated with f in a three-dimensional flow, a direct solution is usually intractable, hence various mathematical approximations are made to arrive at models capable of simulating systems of interest. In a recent review paper, Fox [19] summarizes such modeling strategies, in addition to providing a systematic approach for developing large-eddy simulation (LES) tools starting from microscale physics. Another noteworthy review on that topic is due

to Balanchandar and Eaton [20], where the current state-of-the-art experimental and computational techniques for turbulent dilute disperse flows are discussed.

Two common approaches for modeling disperse phase flows include Euler-Euler (EE) and Euler-Lagrange (EL) methods. Note that Pai and Subramaniam [50] established consistency relationships between the two representations in the framework of a probability density function formalism, presented advantages and limitations of each approach, and identified unclosed terms that arise. EE representations reduce Eq. 2.1 to the one-particle density function appearing in the kinetic equation [28–30]. In general, the kinetic description is unclosed and requires mesoscale models for the collision operator. EE methods approximate the kinetic equation by considering a set of moments of f, and solve both the fluid and particle-phase on a common Eulerian grid. In the small Knudsen number (highly collisional) limit with an underlying assumption that the flow is nearly at equilibrium, the particle density function is close to Maxwellian and a Chapman-Enskog expansion can be used to derive a two-fluid model (TFM) using ensemble or volume averaging [31–34]. This approach leads to particle phase transport equations that closely resemble the Navier-Stokes equations using moment closures obtained from kinetic theory. TFM greatly reduces the cost of simulating large-scale systems as it does not require interactions at the particle scale to be resolved. As a result, TFM has been used in a large number of studies, for example in dense fluidized bed reactors [51, 52] and riser flows in vertical channels [53–57]. However, in the dilute limit, the constitutive models fail to correctly describe important features of the flow. Desjardins *et al.* [35] showed the challenges EE formulations face for finite Knudsen number and non-equilibrium flows, for which particle trajectory crossings play an important role and higher moments of the particle number density must be considered to yield an accurate result. Several studies proposed

solutions to overcome the limitations of standard TFM. Simonin [36] used a moment method based on the Grad [58] approach to study non-equilibrium dilute gas-particle flow behavior. Desjardins *et al.* [35] proposed to approximate the kinetic equation using a two-node quadrature approach based on the quadrature method of moments [59], leading to a method capable of handling highly non-equilibrium, finite-Stokes number flows, including impinging jets, jet crossing, and particle rebound off walls, which previously could not be treated accurately with EE formulations. Following this work, Passalacqua *et al.* [37] implemented a third-order quadrature-based moment method coupled with a fluid solver to deal with dense flows. They demonstrated the importance of considering the effect of the local particle Knudsen number, which they found to be large if solid packing is small or the particle Mach number is large, which is the case in many disperse two-phase flows. Yuan and Fox [38] developed a conditional quadrature method of moments (CQMOM) based on 1-D adaptive quadrature of conditional velocity moments to improve the accuracy of the quadrature-based moment method. They applied CQMOM to a range of problems involving particle trajectory crossing and collisions. While EE methods have been widely successful, in particular due to their computational efficiency when solving systems containing a large number of particles, statistical and physical closures continue to pose a challenge.

Euler-Lagrange (EL) strategies provide an alternative framework with the potential of simpler closures. EL methods represent the disperse phase in a Lagrangian manner by discretizing the multiparticle density function introduced earlier into a number of individually tracked stochastic particles. As expected in Discrete Simulation Monte Carlo (DSMC) approaches, EL methods can yield very accurate solutions, though they can require a large number of stochastic particles to control statistical errors [40]. A few examples of applications of EL methods

within the literature include simulations of impinging stream reactors [60], cluster formation of gas-solid flows in vertical channels [61, 62], and dense fluidized beds [62, 63]. It is typical in EL simulations to consider as may particles as there are physical particles, or a smaller number of computational particles in order to reduce simulation cost. Garg *et al.* [42] demonstrated that if the spatial distribution of particles becomes highly non-uniform, regions with fewer particles have higher statistical error, which might prevent numerical convergence of the interphase momentum transfer term. They proposed to dynamically ensure that the number of stochastic particles per cell remains nearly constant and showed much improved convergence. However, this strategy remains to be extended to colliding particles. Similarly, Salman and Soteriou [41] demonstrated limitations of the EL approach in their study of evaporating sprays. They reviewed typical interpolation schemes used to couple the two phases and showed that such procedures do not converge under mesh refinement. In fact, most existing EL coupling schemes require the Eulerian mesh to be an order of magnitude larger than the diameter of the largest particle, potentially preventing the capture of dynamically important mesoscale processes. This can be problematic when dealing with non-uniform meshes or a disperse phase with a wide size distribution.

Despite these limitations, a single realization of DSMC accounts discretely for all individual particle processes such as drag and collisions, and can therefore provide much needed insights in the physics of particle-laden flows, and even help guide the development of improved EE closures. This level of modeling is referred in the literature as discrete element models (DEM) [64]. The coupling of DEM with a finite volume description of the gas phase based on the Navier-Stokes equations was first reported by Tsuji *et al.* [65] and Hoomans [66] using a soft-sphere [64] and hard-sphere [67] collision models, respectively. Deen [22] provided a detailed

review on DEM for the study of gas-solid flows in fluidized bed reactors.

Coupling DEM with the spatially-filtered equations of motion for the gas phase is the strategy that we follow in this paper. In the next section, we start from the point wise variable density Navier-Stokes equations, coupled to Newton's second law for the particles, and derive volume filtered continuity, momentum, and scalar transport equations appropriate for the EL simulations. All unclosed terms and assumptions are given explicitly and discussed. Interphase coupling is discussed in detail in Sec. 2.4, and a dual filter approach is introduced to guarantee convergence under mesh refinement. Coupling with a conservative immersed boundary method [68] to account for realistic geometries is described in this section as well. A soft sphere model [64] accounts for particle collisions. This model has been modified compared to other versions in the literature in order to recover the correct close-packing limit, as well as to account for inter-particle friction and rotation in a scalable manner. The collision model and its parallel implementation are presented in Sec. 2.5. Section 2.6 summarizes the implementation of the numerical approach and presents parallel performance. In this work, all simulations are performed using NGA, an arbitrarily high order multi-physics CFD code [69]. It is shown that the overall strategy is capable of producing simulations of realistic, three-dimensional, polydisperse flows on massively parallel architectures.

2.3 Mathematical description

This section presents the equations employed to describe the flow of solid particles in a low Mach number, variable density carrier fluid. We begin by presenting the point wise equations of motion for each phase. These equations require re-

solving the flow around each individual particle, which is excessively expensive for engineering systems of interest. Consequently, we derive a set of volume filtered equations for a variable density fluid, which can be solved on a scale larger than the particle diameter. The particles are solved in a Lagrangian framework described by Newton's laws of motion. The two phases are fully coupled through momentum exchange terms. Unclosed terms that arise from the filtering approach are presented and discussed.

2.3.1 Point wise description

The carrier fluid is described by the Navier-Stokes equations for a low Mach number, variable density flow. Continuity is given by

$$\frac{\partial \rho_f}{\partial t} + \nabla \cdot (\rho_f \boldsymbol{u}_f) = 0, \tag{2.2}$$

where ρ_f and $\boldsymbol{u}_f$ are the point wise fluid density and velocity, respectively. Conservation of momentum is expressed as

$$\frac{\partial}{\partial t} (\rho_f \boldsymbol{u}_f) + \nabla \cdot (\rho_f \boldsymbol{u}_f \otimes \boldsymbol{u}_f) = \nabla \cdot \boldsymbol{\tau} + \rho_f \boldsymbol{g}, \tag{2.3}$$

where $\boldsymbol{g}$ is the acceleration due to gravity, and $\boldsymbol{\tau}$ is the point wise value of the fluid stress tensor, given by

$$\boldsymbol{\tau} = -p\boldsymbol{\mathcal{I}} + \mu \left[\nabla \boldsymbol{u}_f + \nabla \boldsymbol{u}_f^{\mathsf{T}} - \frac{2}{3} (\nabla \cdot \boldsymbol{u}_f) \boldsymbol{\mathcal{I}} \right]. \tag{2.4}$$

The hydrodynamic pressure and dynamic viscosity coefficient are given by p and μ, respectively. $\boldsymbol{\mathcal{I}}$ is the identity tensor. Interactions with the solid phase are incorporated by imposing no-slip and no-penetration boundary conditions at the surface of each particle.

The displacement of an individual particle p is calculated using Newton's second law of motion,

$$m_p \frac{d\boldsymbol{u}_p}{dt} = \boldsymbol{f}_p^{\text{inter}} + \boldsymbol{F}_p^{\text{col}} + m_p \boldsymbol{g}. \tag{2.5}$$

The particle mass is defined by $m_p = \pi \rho_p d_p^3/6$, where ρ_p and d_p are the particle density and diameter, respectively. $\boldsymbol{F}_p^{\text{col}}$ is the particle collision force, which will be described in detail in Section 2.5. The force $\boldsymbol{f}_p^{\text{inter}}$ exerted on a single particle p by the surrounding fluid is given by the integral of the stress tensor over the surface of the particle,

$$\boldsymbol{f}_p^{\text{inter}} = \int_{S_p} \boldsymbol{\tau} \cdot \boldsymbol{n} \; dS, \tag{2.6}$$

where $\boldsymbol{n}$ is the outward unit normal vector of the particle surface S_p. This term is discussed further in Section 2.3.5.

The angular momentum of the particle, $\boldsymbol{\omega}_p$, is computed by taking the cross product of the position vector outward from the particle with Eq. 2.5, giving

$$I_p \frac{d\boldsymbol{\omega}_p}{dt} = \int_{S_p} \frac{d_p}{2} \boldsymbol{n} \times (\boldsymbol{\tau} \cdot \boldsymbol{n}) \; d\boldsymbol{y} + \sum_j \frac{d_p}{2} \boldsymbol{n} \times \boldsymbol{f}_{t,j \to p}^{\text{col}}, \tag{2.7}$$

where $\boldsymbol{f}_{t,j \to p}^{\text{col}}$ is the tangential component of the collision force of particle j acting on particle p. This term will be made explicit later. I_p is the particle's moment of inertia, given for a sphere by

$$I_p = \frac{m_p d_p^2}{10}. \tag{2.8}$$

2.3.2 Volume filtering operators

In order to account for the effect of particles without requiring to resolve the fluid-phase equations on the scale of the particle surface, the point wise fluid equations can be split into microscale processes, i.e., processes that take place on the scale of a

particle and below, and meso/macro-scale processes, i.e., processes that take place on a scale much larger than the particle size. Anderson and Jackson [70] detail such an approach for particle-laden flows by applying a local volume filtering operator to the Navier-Stokes equations, thereby replacing the point variables (fluid velocity, pressure, etc.) by smoother, locally filtered fields. This local volume filtering strategy is employed in this work. Another strategy based on ensemble averaging is proposed by Zhang and Prosperetti [71], which leads to comparatively similar equations.

We begin by defining a filtering kernel G with a characteristic length δ_f, such that $G(r) > 0$ decreases monotonically with increasing r, and is normalized such that its integral over the entire physical space is unity. The local voidage at a point $\boldsymbol{x}$ and time t is defined as

$$\varepsilon_f(\boldsymbol{x}, t) = \int_{V_f} G(|\boldsymbol{x} - \boldsymbol{y}|) d\boldsymbol{y}, \tag{2.9}$$

where V_f indicates that the integral is taken over all points $\boldsymbol{y}$ occupied by the fluid. Although this quantity is a function of both space and time, we will simply use ε_f throughout to represent the local fluid volume fraction. Similarly, the particle volume fraction can be computed by taking the volume integral of the filtering kernel over all space occupied by the solid phase. Since G varies little within a single particle, it can be taken outside of the integral and the particle volume fraction can be expressed as

$$\varepsilon_p(\boldsymbol{x}, t) = 1 - \varepsilon_f \approx \sum_{i=1}^{N_p} G(|\boldsymbol{x} - \boldsymbol{x}_i|) V_i, \tag{2.10}$$

where V_i, as previously mentioned, is the volume of particle i, and N_p is the number of particles.

Let $\boldsymbol{a}(\boldsymbol{x}, t)$ be any point property of the fluid of arbitrary tensorial order, and

$\boldsymbol{a}'(\boldsymbol{x},t)$ denote its residual field, such that

$$\boldsymbol{a}\left(\boldsymbol{x},t\right)=\overline{\boldsymbol{a}}\left(\boldsymbol{x},t\right)+\boldsymbol{a}'(\boldsymbol{x},t)\,, \tag{2.11}$$

where the volume filtered field $\overline{\boldsymbol{a}}\left(\boldsymbol{x},t\right)$ is computed by taking the convolution product with the filtering kernel G, giving

$$\varepsilon_f\overline{\boldsymbol{a}}\left(\boldsymbol{x},t\right)=\int_{V_f}\boldsymbol{a}\left(\boldsymbol{y},t\right)G(|\boldsymbol{x}-\boldsymbol{y}|)d\boldsymbol{y}. \tag{2.12}$$

Due to surface contributions of the solid particles, there is no commutation between filtering and differentiation. Consequently, filtering derivatives of point variables will lead to additional terms in the form of integrals of the point wise quantity about the surface of the particle. Volume filtering the gradient, divergence, and time derivative of a point property of the fluid are respectively given as

$$\int_{V_f}\nabla\boldsymbol{a}\left(\boldsymbol{y},t\right)G(|\boldsymbol{x}-\boldsymbol{y}|)d\boldsymbol{y}= \nabla\left(\varepsilon_f\overline{\boldsymbol{a}}\left(\boldsymbol{x},t\right)\right)-\sum_{i=1}^{N_p}\int_{S_i}\boldsymbol{n}\otimes\boldsymbol{a}\left(\boldsymbol{y},t\right)G(|\boldsymbol{x}-\boldsymbol{y}|)\;d\boldsymbol{y}, \tag{2.13}$$

$$\int_{V_f}\nabla\cdot\boldsymbol{a}\left(\boldsymbol{y},t\right)G(|\boldsymbol{x}-\boldsymbol{y}|)d\boldsymbol{y}= \nabla\cdot\left(\varepsilon_f\overline{\boldsymbol{a}}\left(\boldsymbol{x},t\right)\right)-\sum_{i=1}^{N_p}\int_{S_i}\boldsymbol{n}\cdot\boldsymbol{a}\left(\boldsymbol{y},t\right)G(|\boldsymbol{x}-\boldsymbol{y}|)\;d\boldsymbol{y}, \tag{2.14}$$

and

$$\int_{V_f}\frac{\partial\boldsymbol{a}\left(\boldsymbol{y},t\right)}{\partial t}G(|\boldsymbol{x}-\boldsymbol{y}|)d\boldsymbol{y}= \frac{\partial}{\partial t}\left(\varepsilon_f\overline{\boldsymbol{a}}\left(\boldsymbol{x},t\right)\right)+\sum_{i=1}^{N_p}\int_{S_i}\boldsymbol{n}\cdot\boldsymbol{u}_i\boldsymbol{a}\left(\boldsymbol{y},t\right)G(|\boldsymbol{x}-\boldsymbol{y}|)\;d\boldsymbol{y}, \tag{2.15}$$

where S_i represents the surface of particle i. A detailed derivation can be found in the work of Anderson and Jackson [70]. In order to reach these expressions it is

assumed that the shortest distance from the location of the point property to the surface bounding the fluid is significantly larger than the radius of G. Treatment for solving filtered quantities near walls will be discussed in Sec 2.4.2. For simplicity, all fluid properties in the remainder of the paper will be assumed to be a function of space and time and the parentheses will be left out.

For flows with density changes, such as those found in chemically reacting systems, it is often convenient to introduce a Favre filtering operation (see for example [72]). The density-weighted volume filtered quantity $\widetilde{\boldsymbol{a}}$ is given by

$$\widetilde{\boldsymbol{a}} = \frac{\varepsilon_f \overline{\rho_f \boldsymbol{a}}}{\varepsilon_f \overline{\rho_f}}, \tag{2.16}$$

where $\overline{\rho_f}$ is the volume filtered fluid density. Any fluid property $\boldsymbol{a}$ may be split into its density-weighted and residual components $\boldsymbol{a} = \widetilde{\boldsymbol{a}} + \boldsymbol{a}''$.

The definitions above are most useful when constructing the equations of motion if the filtered variables are invariant with the chosen filtering kernel G and the filter length δ_f. Spatial variations in point properties manifest from scales on the order of the particle diameter and interparticle spacing (from boundary layer effects and collisions) to scales comparable to the dimensions of the complete system. Choosing δ_f such that the local filtered variables are unaffected by the filtering process is not trivial. Instead, we allow the filter length to be small enough for the mesoscale flow features to be unaffected, while maintaining a filter length large enough for microscale processes such as drag to be appropriately modeled by classical models. In the context of particle-laden flows, δ_f proportional to several particle diameters meets this criterion.

2.3.3 Volume filtered equations of motion

Filtering Eq. 2.2 by multiplying by $G(|\boldsymbol{x}-\boldsymbol{y}|)$ and integrating over all fluid points yields the continuity equation in terms of the volume filtered, density weighted velocity,

$$\frac{\partial}{\partial t}\left(\varepsilon_f \overline{\rho_f}\right) + \nabla \cdot \left(\varepsilon_f \overline{\rho_f} \widetilde{\boldsymbol{u}_f}\right) = -\mathcal{S}_\rho. \tag{2.17}$$

Using the fact that $\boldsymbol{u}_f\big|_{S_i} = \boldsymbol{u}_i + \frac{dr_i}{dt}\boldsymbol{n}$, where $\frac{dr_i}{dt}$ is the rate of change of the radius of particle i, $\mathcal{S}_\rho$ is given by

$$\mathcal{S}_\rho = \sum_{i=1}^{N_p} \dot{m}_i G(|\boldsymbol{x}-\boldsymbol{x}_i|)\,, \tag{2.18}$$

where

$$\dot{m}_i = -\rho_f\big|_{S_i} S_i \frac{dr_i}{dt}. \tag{2.19}$$

When considering phase change, a particle may change size due to evaporation or devolatilization processes. However, this term vanishes when considering inert particles.

With respect to the momentum balance, volume filtering the non-linear convective term requires special care. Applying Eq. 2.14, 2.15, and 2.16 to the left-hand-side of Eq. 2.3 gives

$$\int_{V_f} G(|\boldsymbol{x}-\boldsymbol{y}|)\left[\frac{\partial}{\partial t}\left(\rho_f \boldsymbol{u}_f\right) + \nabla \cdot \left(\rho_f \boldsymbol{u}_f \otimes \boldsymbol{u}_f\right)\right] d\boldsymbol{y} = \frac{\partial}{\partial t}\left(\varepsilon_f \overline{\rho_f} \widetilde{\boldsymbol{u}_f}\right) + \nabla \cdot \left(\varepsilon_f \overline{\rho_f} \widetilde{\boldsymbol{u}_f} \otimes \widetilde{\boldsymbol{u}_f}\right) + \nabla \cdot \boldsymbol{\mathcal{R}}_u - \boldsymbol{\mathcal{S}}_{\rho u}, \tag{2.20}$$

where

$$\boldsymbol{\mathcal{R}}_u = \varepsilon_f \overline{\rho_f} \widetilde{\boldsymbol{u}_f'' \otimes \boldsymbol{u}_f''} \tag{2.21}$$

is a residual stress akin to a Reynolds stress resulting from volume filtering. The momentum source term $\boldsymbol{S}_{\rho u}$ accounts for the momentum flow rate from the particle

surface due to mass transfer, which simplifies to

$$\boldsymbol{\mathcal{S}}_{\rho u} = \sum_{i=1}^{N_p} \dot{m}_i \boldsymbol{u}_i G(|\boldsymbol{x} - \boldsymbol{x}_i|)\,. \tag{2.22}$$

Substituting $\boldsymbol{a} = \boldsymbol{\tau}$ in Eq. 2.14 and decomposing the point wise stress tensor into its filtered and residual components gives

$$\int_{V_f} G(|\boldsymbol{x} - \boldsymbol{y}|)\, \nabla \cdot \boldsymbol{\tau}\; d\boldsymbol{y} = \nabla \cdot (\varepsilon_f \overline{\boldsymbol{\tau}}) - \sum_{i=1}^{N_p} \int_{S_i} G(|\boldsymbol{x} - \boldsymbol{y}|)\, \boldsymbol{n} \cdot \overline{\boldsymbol{\tau}}\; d\boldsymbol{y} - \sum_{i=1}^{N_p} \int_{S_i} G(|\boldsymbol{x} - \boldsymbol{y}|)\, \boldsymbol{n} \cdot \boldsymbol{\tau}'\; d\boldsymbol{y}. \tag{2.23}$$

Applying Gauss' theorem to the second term on the right-hand-side of Eq. 2.23 and assuming both the filtered stress tensor and its derivatives vary little over distances comparable with the radius of G, the surface integral of the volume filtered stress tensor becomes

$$\sum_{i=1}^{N_p} \int_{S_i} G(|\boldsymbol{x} - \boldsymbol{y}|)\, \boldsymbol{n} \cdot \overline{\boldsymbol{\tau}}\; d\boldsymbol{y} \approx \overline{\boldsymbol{\tau}} \cdot \nabla \varepsilon_f. \tag{2.24}$$

Now considering the last term in the right-hand-side of Eq. 2.23, the filtering kernel $G(|\boldsymbol{x} - \boldsymbol{y}|)$ may be replaced by $G(|\boldsymbol{x} - \boldsymbol{x}_i|)$ and taken outside of the integral since the filtered value of $\boldsymbol{\tau}'$ taken over S_i is small compared with variations about its filtered value, and these variations are smooth. Using this and putting Eq. 2.24 in Eq. 2.23 yields

$$\int_{V_f} G(|\boldsymbol{x} - \boldsymbol{y}|)\, \nabla \cdot \boldsymbol{\tau}\; d\boldsymbol{y} = \varepsilon_f \nabla \cdot \overline{\boldsymbol{\tau}} - \sum_{i=1}^{N_p} G(|\boldsymbol{x} - \boldsymbol{x}_i|) \int_{S_i} \boldsymbol{\tau}' \cdot \boldsymbol{n}\; d\boldsymbol{y}. \tag{2.25}$$

For simplicity, the filtered stress tensor $\overline{\boldsymbol{\tau}}$ can be written as

$$\overline{\boldsymbol{\tau}} = -\overline{p}\boldsymbol{\mathcal{I}} + \mu \left[\nabla \overline{\boldsymbol{u}_f} + \nabla \overline{\boldsymbol{u}_f}^{\mathsf{T}} - \frac{2}{3}\; (\nabla \cdot \overline{\boldsymbol{u}_f})\, \boldsymbol{\mathcal{I}} \right] + \boldsymbol{\mathcal{R}}_\mu, \tag{2.26}$$

where $\boldsymbol{\mathcal{R}}_\mu$ arises from filtering the velocity gradients in $\boldsymbol{\tau}$. Note that when dealing with reactive flows, μ may vary significantly and will contribute additional terms to $\boldsymbol{\mathcal{R}}_\mu$.

We now exploit the similarities between Eq. 2.6 and Eq. 2.25 to elucidate the nature of the surface integral term on the right-hand-side of Eq. 2.25. Using the divergence theorem and the fact that $\nabla \cdot \overline{\boldsymbol{\tau}}$ varies little over the scale of a particle, Eq. 2.6 can be expanded as

$$\begin{aligned} \boldsymbol{f}_p^{\text{inter}} = \int_{S_p} \boldsymbol{\tau} \cdot \boldsymbol{n} \; d\boldsymbol{y} &= \int_{S_p} (\overline{\boldsymbol{\tau}} + \boldsymbol{\tau}') \cdot \boldsymbol{n} \; d\boldsymbol{y} \\ &= \int_{V_p} \nabla \cdot \overline{\boldsymbol{\tau}} \;\; d\boldsymbol{y} + \int_{S_p} \boldsymbol{\tau}' \cdot \boldsymbol{n} \; d\boldsymbol{y} \approx V_p \nabla \cdot \overline{\boldsymbol{\tau}} + \int_{S_p} \boldsymbol{\tau}' \cdot \boldsymbol{n} \; d\boldsymbol{y}. \end{aligned} \tag{2.27}$$

We now multiply through by $G(|\boldsymbol{x} - \boldsymbol{x}_p|)$, and sum over all particles. The left-hand-side of Eq. 2.27 is used to define the interphase momentum exchange $\boldsymbol{F}^{\text{inter}}$,

$$\boldsymbol{F}^{\text{inter}} = \sum_{i=1}^{N_p} G(|\boldsymbol{x} - \boldsymbol{x}_i|) \, \boldsymbol{f}_i^{\text{inter}}. \tag{2.28}$$

Now considering the first term on the right-hand-side of Eq. 2.27, $\nabla \cdot \overline{\boldsymbol{\tau}}$ may be taken outside the summation, and using Eq. 4.4(b) this term reduces to

$$\sum_{i=1}^{N_p} G(|\boldsymbol{x} - \boldsymbol{x}_i|) \, V_i \nabla \cdot \overline{\boldsymbol{\tau}} = (1 - \varepsilon_f) \, \nabla \cdot \overline{\boldsymbol{\tau}}. \tag{2.29}$$

Finally, combining Eqs. 2.25, 2.27, 2.28, and 2.29 yields

$$\int_{V_f} G(|\boldsymbol{x} - \boldsymbol{y}|) \, \nabla \cdot \boldsymbol{\tau} \; d\boldsymbol{y} = \nabla \cdot \overline{\boldsymbol{\tau}} - \boldsymbol{F}^{\text{inter}}. \tag{2.30}$$

From the above formulation, the momentum equation is then given by

$$\frac{\partial}{\partial t} \left(\varepsilon_f \overline{\rho_f} \widetilde{\boldsymbol{u}_f} \right) + \nabla \cdot \left(\varepsilon_f \overline{\rho_f} \widetilde{\boldsymbol{u}_f} \otimes \widetilde{\boldsymbol{u}_f} \right) = \nabla \cdot \left(\overline{\boldsymbol{\tau}} - \boldsymbol{\mathcal{R}}_u \right) + \varepsilon_f \overline{\rho_f} \boldsymbol{g} - \boldsymbol{\mathcal{S}}_{\rho u} - \boldsymbol{F}^{\text{inter}}. \tag{2.31}$$

2.3.4 Filtered scalar transport equation

A similar approach can be used to describe a generalized conservative transport equation, which is relevant when dealing with reactive flows. Given a point wise scalar quantity, ϕ, its transport equation is given by

$$\frac{\partial \rho_f \phi}{\partial t} + \nabla \cdot \left(\rho_f \boldsymbol{u}_f \phi \right) = \nabla \cdot \left(D \nabla \phi \right), \tag{2.32}$$

where D is the diffusion coefficient. Multiplying through by G and integrating the left-hand-side of the above equation yields

$$\int_{V_f} g(\boldsymbol{x}-\boldsymbol{y})\left[\frac{\partial \rho_f \phi}{\partial t}+\nabla\cdot(\rho_f \boldsymbol{u}_f \phi)\right]d\boldsymbol{y} = \frac{\partial}{\partial t}\left(\varepsilon_f \overline{\rho_f}\widetilde{\phi}\right)+\nabla\cdot\left(\varepsilon_f \overline{\rho_f}\widetilde{\boldsymbol{u}_f}\widetilde{\phi}\right)+\nabla\cdot\boldsymbol{\mathcal{R}}_\phi+\mathcal{S}_{\rho\phi}, \quad (2.33)$$

where

$$\boldsymbol{\mathcal{R}}_\phi = \varepsilon_f \overline{\rho_f}\widetilde{\boldsymbol{u}_f'' \phi''}. \quad (2.34)$$

Assuming the scalar quantity at the surface of particle i, $\phi\big|_{S_i}$, is uniform, the source term is given by

$$\mathcal{S}_{\rho\phi} = \sum_{i=1}^{N_p} \dot{m}_i \phi\big|_{S_i} G(|\boldsymbol{x}-\boldsymbol{x}_i|)\,. \quad (2.35)$$

Filtering the right-hand-side of Eq. 2.32 gives

$$\int_{V_f} \nabla\cdot(D\nabla\phi)\, G(|\boldsymbol{x}-\boldsymbol{y}|)\;\, d\boldsymbol{y} = \nabla\cdot\left(\varepsilon_f \overline{D\nabla\phi}\right)-\mathcal{S}_{\nabla\phi}, \quad (2.36)$$

where

$$\mathcal{S}_{\nabla\phi} = \sum_{i=1}^{N_p}\int_{S_i} \boldsymbol{n}\cdot\nabla\phi D G(|\boldsymbol{x}-\boldsymbol{y}|)\;\, d\boldsymbol{y}. \quad (2.37)$$

Note that the source term $\mathcal{S}_{\nabla\phi}$ vanishes when considering a Neumann boundary condition at the surface of the particle, namely $\nabla\phi\cdot\boldsymbol{n}\big|_{S_i}=0$. Using the same arguments described when handling the fluid stress tensor to rewrite $\overline{D\nabla\phi}$, the filtered general scalar transport equation is given by

$$\frac{\partial}{\partial t}\left(\varepsilon_f \overline{\rho_f}\widetilde{\phi}\right)+\nabla\cdot\left(\varepsilon_f \overline{\rho_f}\widetilde{\boldsymbol{u}_f}\widetilde{\phi}\right)+\nabla\cdot\boldsymbol{\mathcal{R}}_\phi = \nabla\cdot\left(\varepsilon_f D\nabla\overline{\phi}+\boldsymbol{\mathcal{R}}_D\right)-\mathcal{S}_{\rho\phi}-\mathcal{S}_{\nabla\phi}, \quad (2.38)$$

where $\boldsymbol{\mathcal{R}}_D$ is an unclosed term defined by $\boldsymbol{\mathcal{R}}_D = \overline{D\nabla\phi}-D\nabla\overline{\phi}$.

2.3.5 Closures

As a result of filtering the equations of motion for the fluid phase, sub-grid terms (Eq. 2.21,2.26,2.27) arise and require closure. The general problem consists of formulating expressions for these terms based on filtered quantities, applicable for a wide range of particle Stokes and Reynolds numbers from the dilute to dense limit. First, $\boldsymbol{\mathcal{R}}_u$ and $\boldsymbol{\mathcal{R}}_\phi$ are similar to Reynolds stresses and involve velocity fluctuations about their filtered values. For classical turbulence the Reynolds stress is closed via a turbulent viscosity model, given by

$$\boldsymbol{\mathcal{R}}_u \approx \mu_t \left(\nabla \overline{\boldsymbol{u}_f} + \nabla \overline{\boldsymbol{u}_f}^{\mathsf{T}} \right), \tag{2.39}$$

where μ_t is the turbulent viscosity. In the context of particle-laden flows, the turbulent kinetic energy cascade is more complicated than with single-phase turbulence [9]. For varying particle-phase Stokes numbers and concentrations, the presence of the disperse phase can either augment or attenuate turbulence relative to single-phase turbulence [21]. Some studies have shown that a dilute concentration of particles located inside the fluid boundary layer suppresses the generation of turbulence, while larger particles contribute to Reynolds stresses [73]. For dense flows, fluidization can be generally associated with two kinds of turbulence; velocity fluctuations that arise from granular agitation at the particle scale (via interparticle collisions and wake instabilities), as well as from mesoscale features such as particle clustering and bubbles, and it is therefore incorrect to use standard turbulence models to close this term. For the majority of the work presented in this paper, we will assume that the carrier-phase velocity fluctuations do not contribute significantly to the flow dynamics, allowing us to neglect $\boldsymbol{\mathcal{R}}_u$. However, in certain cases, such as spouting fluidized beds where fluid-phase Reynolds numbers may be very large (above to 58,000 in some lab-scale experiments [74]), $\boldsymbol{\mathcal{R}}_u$ requires

proper closure. For these cases, a dynamic Smagorinsky model [75,76] based on Lagrangian averaging [77] is employed to estimate μ_t. Although this model does not account for turbulence modulation by the particles, it will be highlighted later that the cases considered exhibit high turbulent viscosity in regions free of particles.

Filtering the point wise velocity gradients in the viscous term leads to unclosed stresses, which can be handled in several ways, such as combining them with the stress tensor [70], accounting for them through the introduction of an effective viscosity [23, 71], or simply neglecting them [78]. To deal with the unclosed term $\boldsymbol{\mathcal{R}}_\mu$ in the filtered fluid stress tensor, an effective viscosity μ^* is introduced, giving

$$\boldsymbol{\mathcal{R}}_\mu \approx \mu^* \left[\nabla \overline{\boldsymbol{u}_f} + \nabla \overline{\boldsymbol{u}_f}^{\mathsf{T}} - \frac{2}{3} \left(\nabla \cdot \overline{\boldsymbol{u}_f} \right) \boldsymbol{\mathcal{I}} \right], \tag{2.40}$$

where μ^* was derived by Gibilaro [79] for fluidized beds, and is given by

$$\mu^* = \mu \left(\varepsilon_f^{-2.8} - 1 \right). \tag{2.41}$$

The force $\boldsymbol{f}_p^{\text{inter}}$ that couples the individual particles and the carrier fluid comes from the momentum exchange at the particle surface, which has been expanded in Eq. 2.27 to give

$$\boldsymbol{f}_p^{\text{inter}} \approx V_p \nabla \cdot \overline{\boldsymbol{\tau}} + \int_{S_p} \boldsymbol{\tau}' \cdot \boldsymbol{n} dS. \tag{2.42}$$

Equation 2.42 can be better understood by considering a flow past a single, isolated particle. In that case, $\boldsymbol{\tau}$ varies on the scale of the particle diameter, and therefore $\overline{\boldsymbol{\tau}}$ is approximately constant for $\delta_f \gg d_p$. Then $\nabla \cdot \overline{\boldsymbol{\tau}}$ vanishes, and it becomes clear that $\int_{S_p} \boldsymbol{\tau}' \cdot \boldsymbol{n} dS$ represents the drag force due to the uniform flow, which we will write

$$\int_{S_p} \boldsymbol{\tau}' \cdot \boldsymbol{n} dS \approx \boldsymbol{f}^{\text{drag}}, \tag{2.43}$$

where $\boldsymbol{f}^{\text{drag}}$ can be obtained though classical models. Other contributions to the surface integral might include added mass, the Basset history term, lift and Faxen

forces. For gas-solid flows, the added mass term becomes negligible and is therefore not included in the simulations presented herein. However, when the density difference between fluid and particles decreases, the volume of fluid the particle needs to displace as it moves through it will provide non-negligible acceleration (or deceleration). Zhang and Prosperetti [33] give an exact expression for the added mass term for an inviscid fluid at low particle concentrations. At higher values of concentration, they include a correction to account for the local volume fraction. They also derive an expression for the lift force for spherical particles in an inviscid fluid. A quite different expression is given by Saffman [80] for viscous flows at low Reynolds numbers.

The drag model of Tenneti *et al.* [81] is employed in this work, which was derived from particle-resolved direct numerical simulation. An ensemble-averaging approach was used to calculate the unclosed average interphase momentum transfer of flow past random fixed configurations of monodisperse spheres. In their approach, the drag correlation models the complete stress tensor, while our equations require only the fluctuating part. However, this drag was determined for a statistically homogeneous suspension at steady-state, and does not include the effect of the filtered pressure gradient. Assuming the contribution of the averaged stress tensor is negligible in their simulations, the correlated drag coefficient is appropriate for the equations presented in Section 2.3.3. The expression for the drag is given as

$$\frac{\boldsymbol{f}_i^{\text{drag}}}{m_p} = \frac{1}{\tau_p}(\widetilde{\boldsymbol{u}_f} - \boldsymbol{u}_p)F(\varepsilon_f, \text{Re}_p), \tag{2.44}$$

where the particle response time τ_p derived from Stokes flow is

$$\tau_p = \frac{\rho_p d_p^2}{18\mu\varepsilon_f}. \tag{2.45}$$

The dimensionless drag force coefficient is valid for a wide range of Reynolds num-

bers and solid packing, and is given by

$$F(\varepsilon_f, \mathrm{Re}_p) = \frac{1 + 0.15\mathrm{Re}_p^{0.687}}{\varepsilon_f^2} + \varepsilon_f F_1(\varepsilon_f) + \varepsilon_f F_2(\varepsilon_f, \mathrm{Re}_p), \tag{2.46}$$

where the particle Reynolds number is

$$\mathrm{Re}_p = \frac{\varepsilon_f \rho_f |\widetilde{\boldsymbol{u}_f} - \boldsymbol{u}_p| d_p}{\mu}. \tag{2.47}$$

The remaining two terms are given by

$$F_1(\varepsilon_f) = \frac{5.81\left(1-\varepsilon_f\right)}{\varepsilon_f^3} + \frac{0.48\left(1-\varepsilon_f\right)^{1/3}}{\varepsilon_f^4},$$
$$F_2(\varepsilon_f, \mathrm{Re}_p) = (1-\varepsilon_f)^3 \mathrm{Re}_p \left(0.95 + \frac{0.61\left(1-\varepsilon_f\right)^3}{\varepsilon_f^2}\right).$$

In the context of wall-bounded particle-laden flows, the accuracy of the drag coefficient and particle volume fraction diminishes at regions close to walls, where key assumptions that were used in the formulation of the models are often violated. For example, the definition of the volume filtered fluid quantity, Eq. 2.12, assumes that $\overline{\boldsymbol{a}}$ is evaluated far from the nearest fluid boundary, Γ. This allows for all surface integrals of the point property to be taken about the surface of the particle while neglecting contributions due to the fluid boundary, namely

$$\int_\Gamma \boldsymbol{n} \cdot \boldsymbol{a} G(|\boldsymbol{x} - \boldsymbol{y}|)\, d\boldsymbol{y} = 0. \tag{2.48}$$

For regions of the fluid close to a wall, this assumption is no longer valid. Note that when considering $\boldsymbol{a} = \boldsymbol{u}_f$, this term vanishes due to the no-penetration condition. However, when dealing with the fluid stress tensor for example, this term must be accounted for. A model for the fluctuating stress tensor is already given in the form of a drag force, so a drag model that accounts for wall interactions directly would be convenient. In addition, the effective viscosity model defined in Eq. 2.41 is dubious at walls. We assume that the particle volume fraction at the surface of

the wall vanishes, since only a single point of the particle surface can be in contact with the wall, and therefore we use the molecular viscosity for viscous fluxes at the walls. Details on the numerical implementation of the wall interactions will be provided in Sec. 2.4.2.

With regards to particle rotation, the first term on the right-hand side of Eq. 2.7 is neglected, and rotation is attributed only to the tangential component of the collision force, $\boldsymbol{f}^{\mathrm{col}}_{t,j\to p}$, between particle p and all other particles j. It should be noted that particle lift forces, such as Saffman lift and Magnus effect, are not accounted for and might play a significant role in dilute flows with wall interactions, such as clustering of particles in risers, but this assumption should be appropriate in dense systems as shown herein. Note that the choice of closures proposed in this section is clearly not unique, and could be improved significantly with a better understanding of the intricate microscale physics. With the advance of high performance computing, there is an opportunity for fully-resolved particle DNS to provide data necessary to guide the development of such improved models.

2.4 Interphase coupling

Coupling between the carrier fluid and disperse phase appears in the form of the volume fraction ε_f, defined by Eq. 2.9, and interphase exchange term $\boldsymbol{F}^{\mathrm{inter}}$, defined by Eq. 2.28, as well as the source terms that arise during particle evaporation and devolatilization, defined by Eqs. 2.18, 2.22, and 2.35. These terms are first computed at the location of each particle, using information from the fluid, and are then transferred to the Eulerian grid. To interpolate the fluid variables to the particle location, a second order trilinear interpolation scheme is used. To extrapolate

the particle data back to the Eulerian mesh, it is necessary to perform a volume filtering operation that is consistent with the mathematical formulation. Classically, this filtering operation takes the form of a linear extrapolation of the particle data to the nearest cells [23, 82]. Salman and Soteriou [41] and Garg *et al.* [83] reviewed typical interpolation schemes used to couple the two phases, and showed that such procedures lead to significant error that depends heavily on the ratio of the particle diameter to the grid spacing. With such approaches, the size of the Eulerian mesh sets the filtering length scale. As discussed in Section 2.3.2, the characteristic filter size should be larger than the particle, hence these approaches require for the mesh size to be much larger than the particle diameter. This requirement can become problematic under certain circumstances. For example, polydisperse particle systems where some particles are very large can require excessively coarse meshes, while boundary layer flows or flows in cylindrical geometries require locally finer meshes at the wall or at the pole, respectively, for which the Lagrangian approach seemingly breaks down. However, note that mathematically there should be no intrinsic limitation on how fine a mesh can be used for solving the fluid equations of motion (Eqs. 2.17 and 2.31).

Transferring Lagrangian data to the Eulerian frame has already been defined within the derivation of the equations of motion (see Eqs. 4.4(b), 2.18, 2.22, 2.28, and 2.35). Let $\boldsymbol{b}_i$ be any property associated with particle i, its volume filtered value $\widehat{\boldsymbol{b}}(\boldsymbol{x},t)$ can be defined following Eq. 2.12 by

$$\varepsilon_p \widehat{\boldsymbol{b}}(\boldsymbol{x},t) = \int_{\mathcal{V}_S} \boldsymbol{b}_i(\boldsymbol{y},t)\, G(|\boldsymbol{x}-\boldsymbol{y}|) d\boldsymbol{y}, \tag{2.49}$$

where $\mathcal{V}_S = \mathcal{V}_1 \cup \mathcal{V}_2 \cup \cdots \cup \mathcal{V}_{N_p}$. Assuming $\boldsymbol{b}_i$ to be constant for each particle, and since G varies little over the particle volume, we can approximate $\widehat{\boldsymbol{b}}(\boldsymbol{x},t)$ as

$$\varepsilon_p \widehat{\boldsymbol{b}}(\boldsymbol{x},t) \approx \sum_{i=1}^{N_p} \boldsymbol{b}_i G(|\boldsymbol{x}-\boldsymbol{x}_i|)\, V_i. \tag{2.50}$$

Note that this definition is compatible with our derivation so far, in that the particle volume fraction is obtained by filtering $\boldsymbol{b}_i = 1$ for each particle, and $\boldsymbol{F}^{\text{inter}}$ by filtering $\boldsymbol{b}_i = \boldsymbol{f}^{\text{inter}}/V_i$. Clearly, any mesh restriction arises from the discrete implementation of our volume filter G. If the volume filter is implemented explicitly according to Eq. 2.50, then we expect to retain full control of the particle diameter to mesh size ratio.

2.4.1 Filter discretization

Transferring the particle data to the Eulerian mesh requires discretizing the filtering kernel G, in order to solve Eq. 2.50. The support of the filtering kernel determines the number of Eulerian cells that are influenced by the presence of each particle. For example, consider a filter that spans $10d_p$ on a grid with cell spacing $\Delta x = 2d_p$. In three dimensions, the support of G spans approximately a $5 \times 5 \times 5$ cell volume, which would require looping over the 125 neighboring cells to compute the volume filtered particle data. This is clearly overly expensive for a system with a large number of particles. To alleviate this issue entirely, it is natural to introduce a two-step filtering process. First, the particle data is transferred on the Eulerian mesh through a conservative mollification operation. This filter has a characteristic length scale that corresponds to the mesh size, Δx. Then, the Eulerian field obtained from the first operation is diffused with an operator chosen to lead to the final filtered length scale δ_f, which should be much larger than the particle diameter. This methodology allows to use finer meshes while still following the requirements associated with local volume filtering. Each step is detailed below.

Mollification The particle data is first transferred on the Eulerian mesh

using a mollification kernel $g_{\mathcal{M}}$, giving

$$\varepsilon_p \boldsymbol{b}_{\mathcal{M}}(\boldsymbol{x},t) \approx \sum_{i=1}^{N_p} \boldsymbol{b}_i G_{\mathcal{M}}(|\boldsymbol{x}-\boldsymbol{x}_i|)\, V_i, \tag{2.51}$$

where $\boldsymbol{b}_{\mathcal{M}}(\boldsymbol{x},t)$ is the initial particle data mollified onto the Eulerian grid. The mollification kernel is a function that decreases monotonically with the distance from the particle, and is normalized such that it integrates to unity, given by

$$G_{\mathcal{M}}(r) = \frac{1}{\sigma\sqrt{2\pi}} e^{-\frac{r^2}{2\sigma^2}}, \tag{2.52}$$

where σ is the kernel width, taken as $\sigma = \Delta x/2\sqrt{2\ln 2}$ such that the full width at half the height of the kernel, $\delta_{1/2}$, is equal to the grid spacing, and therefore the effect of the particle is typically spread out over the 27 nearest cells. The normalization ensures conservation of the particle data as it is transferred to the Eulerian mesh.

Diffusion To deal with finer grids in a robust manner, a diffusion operation is implemented after the mollification step by solving

$$\frac{\partial \alpha}{\partial \tau} = \mathcal{D}\nabla^2 \alpha, \tag{2.53}$$

where $\mathcal{D}$ is a diffusion coefficient associated with the transfer of particle data to the underlying mesh. The initial condition corresponds to $\alpha(\tau=0) = \boldsymbol{b}_{\mathcal{M}}$ and the solution corresponds to $\alpha(\tau=\tau_f) = \widehat{\boldsymbol{b}}(\boldsymbol{x},t)$, where $\widehat{\boldsymbol{b}}(\boldsymbol{x},t)$ represents the particle data after the convolution of the two filters has been applied. The quantity $\sqrt{\mathcal{D}\tau_f}$ corresponds to a length scale for this diffusion operation. An appropriate choice of value for this quantity should account for the mollification operation already accomplished, such that the application of the two operators produces a result independent of the underlying mesh size. Diffusion of the Gaussian kernel $G_{\mathcal{M}}$ with width Δx should give the full volume filtering kernel G with width δ_f, which

leads to

$$\mathcal{D}\tau_f = \frac{\max\left(\delta_f^2 - \Delta x^2, 0\right)}{16 \ln 2}. \tag{2.54}$$

A value of $\delta_f = 3d_p$ was found to yield appropriate smoothing for a monodisperse system while allowing for detailed capture of mesocale flow features. For polydisperse systems with wide size distributions, we take $\delta_f = \max(d_p)$ instead. Discretization of the diffusion process, Eq. 2.53, can be handled in several ways. For cases with few particles, Eq. 2.53 is solved explicitly using second order central differences. For systems with a large number of particles we solve Eq. 2.53 implicitly in a single step to reduce computational cost. Figure 2.1 shows the initial particle data transferred to the mesh with $\delta_{1/2} = \Delta x$, as well as the diffused kernel with $\delta_{1/2} = \delta_f$.

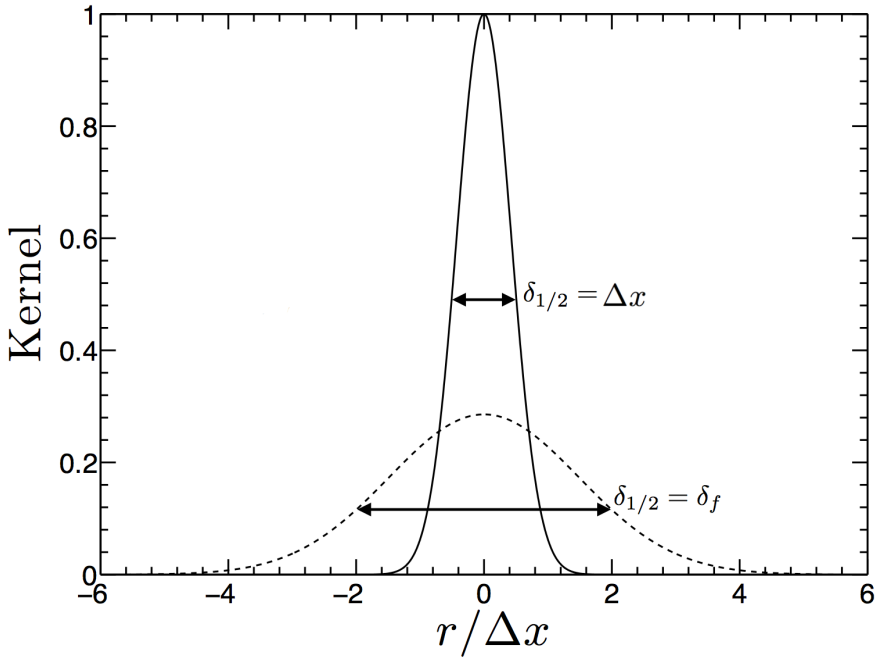

Figure 2.1: Initial filtering kernel $G_{\mathcal{M}}$ with a characteristic width $\delta_{1/2} = \Delta x$ (solid line), full volume filtering kernel G with a characteristic width $\delta_{1/2} = \delta_f$ (dashed line).

Figure 2.2 considers a single particle transferring its data in one dimension.

Figure 2.2(a) shows the mollification kernel $G_{\mathcal{M}}$ as the mesh is refined, Fig. 2.2(b) measures the error associated with the mollification operation compared to the exact solution given by Eq. 2.50 with $\delta_f = 3d_p$. Because this operation is a function of the mesh size, convergence is not achieved during refinement. Instead, the kernel approaches a Dirac distribution, potentially leading to volume fractions greater than unity, illustrating the fact that this operation requires the mesh size to be several times larger than the particle diameter. It is shown that the mollification kernel converges towards the reference solution until $\Delta x < \delta_f$, at which case the kernel width continues to narrow and the solution diverges. The full, two-step filtering operation is considered in Figs. 2.2(c) and 2.2(d). As the mesh is refined, Fig. 2.2(c) shows that the kernel converges towards a Gaussian of characteristic width $\delta_f = 3d_p$. Convergence is shown in Fig. 2.2(d) for a mesh refinement from $\Delta x = 16d_p$ to $\Delta x = d_p/16$. According to Eq. 2.54, for cell sizes larger than δ_f no diffusion is taking place and $G(r) = G_{\mathcal{M}}(r)$. Therefore, convergence for $\Delta x > \delta_f$ is based on the initial mollification. For cell sizes smaller than δ_f, the mollification kernel, $G_{\mathcal{M}}(r)$, continues to narrow and approach a Dirac function (as depicted in Fig. 2.2(a)), the diffusion operation becomes active and allows to obtain second-order convergence.

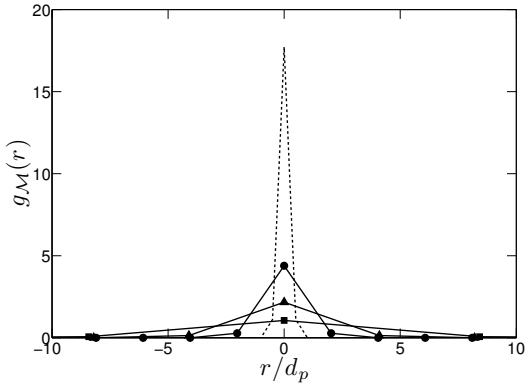

(a) Mollification kernel under mesh refinement, $\Delta x = 8d_p$ (squares), $\Delta x = 4d_p$ (triangles), $\Delta x = 2d_p$ (circles), $\Delta x = d_p/2$ (dashed line)

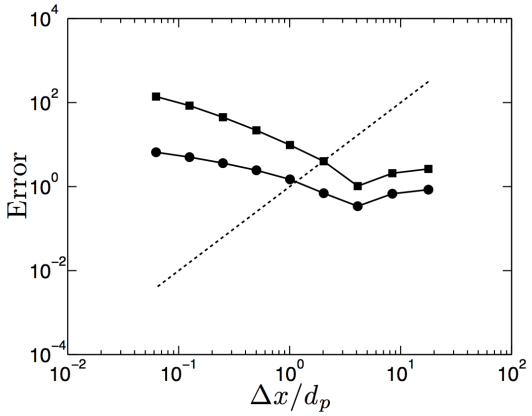

(b) Convergence under mesh refinement from $\Delta x = 16d_p$ to $\Delta x = d_p/16$. L_2 error (circles), L_∞ error (squares), second-order convergence (dashed)

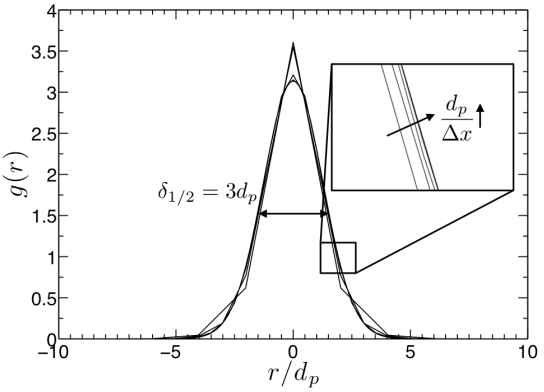

(c) Filtering kernel under mesh refinement from $\Delta x = 2d_p$ to $\Delta x = d_p/8$.

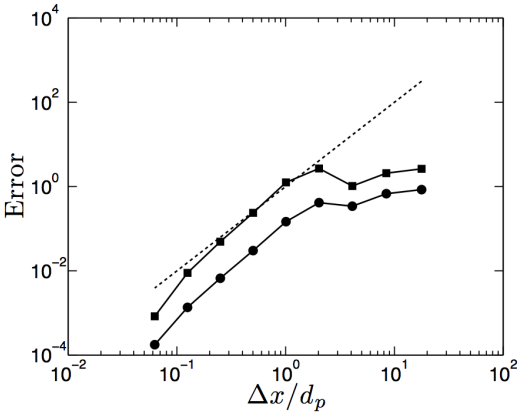

(d) Convergence under mesh refinement from $\Delta x = 16d_p$ to $\Delta x = d_p/16$ for the two-step mollification-diffusion procedure. L_2 error (circles), L_∞ error (squares), second-order convergence (dashed).

Figure 2.2: Mollification and diffusion of a single particle in one-dimension under mesh refinement.

2.4.2 Wall interactions

A conservative immersed-boundary (IB) method is employed to model realistic geometries without requiring a body-fitted grid. The method is based on a cut-cell

formulation that provides discrete conservation of mass and momentum [68, 84]. To compute the area and volume fractions that are at the basis of this approach, it is necessary to fully characterize the location of the immersed geometry surface. This is accomplished through the use of an implicit description in the form of an iso-surface of a smooth function, referred to as a level set function, ψ, chosen such that it corresponds to a standard signed distance function, i.e.,

$$|\psi(\boldsymbol{x}, t)| = |\boldsymbol{x} - \boldsymbol{x}_\Gamma|, \tag{2.55}$$

where $\boldsymbol{x}_\Gamma$ corresponds to the closest point on the solid-fluid interface from $\boldsymbol{x}$, and $\psi(\boldsymbol{x}, t) > 0$ on one side of the interface, and $\psi(\boldsymbol{x}, t) < 0$ on the other side. With this definition, the immersed boundary surface Γ in a domain Ω is defined by $\Gamma(t) = \{\boldsymbol{x} \in \Omega \colon \psi(\boldsymbol{x}, t) = 0\}$.

The coupling of this cut-cell strategy with our particle-laden approach must be handled carefully, such that the particle data being transferred to the underlying mesh is unaffected by the presence of small cut-cells at the walls. In particular, any over-prediction of the fluid volume fraction in near-wall cells is likely to lead to an unphysical behavior with fast fluid layers rising along the walls. During the mollification step, the Neumann boundary condition is enforced by introducing an image particle. Particles close to a wall are mirrored across the boundary and their mollification kernel is superimposed with the original kernel prior to normalization, given by

$$G_{\mathcal{M}}(r) = G_{\mathcal{M}}(r) + G_{\mathcal{M}}(r - 2\psi(\boldsymbol{x}_p, t)), \tag{2.56}$$

where $\psi(\boldsymbol{x}_p, t)$ is the distance from the particle to the closest IB surface. Figure 2.3 shows the analytic mollification kernel as a function of the scaled distance from the particle, along with the image kernel, and the full kernel with Neumann boundary. The solid line represents the wall and the dashed line indicates the particle position.

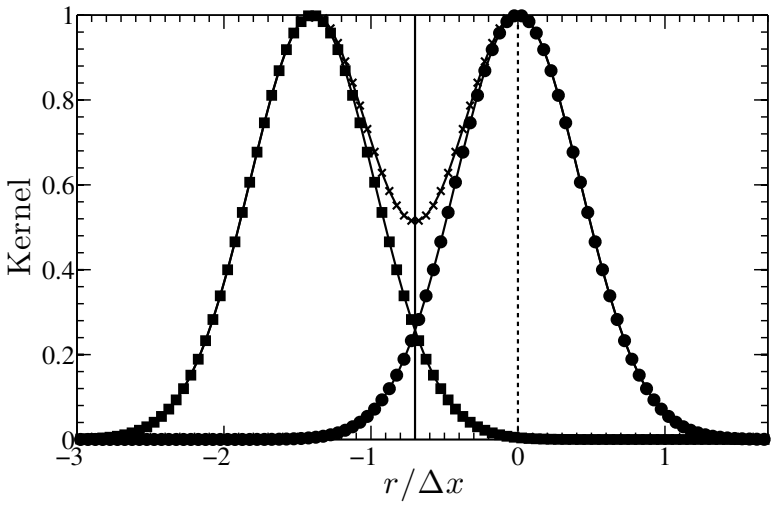

Figure 2.3: Introduction of image particle to impose Neumann condition near walls. Wall (solid line), particle position (dashed line), initial kernel (circles), imaged kernel (squares), superposition (crosses).

Equations 2.50 and 2.51 are implemented in a finite volume formalism. The mollification step requires computing the mollification kernel centered on particle p in cell i as

$$G_{i,p} = \frac{1}{V_i^{\text{cell}}} \int_{V_i^{\text{cell}}} G_{\mathcal{M}} \left(\boldsymbol{x} - \boldsymbol{x}_p \right) d\boldsymbol{x}, \tag{2.57}$$

where V_i^{cell} is the volume of cell i. This integral is approximated by splitting the cell volume into five tetrahedra, such that

$$\int_{V_i^{\text{cell}}} G_{\mathcal{M}} \left(\boldsymbol{x} - \boldsymbol{x}_p \right) d\boldsymbol{x} \approx \sum_{n=1}^{5} G_{\mathcal{M}} \left(\boldsymbol{x}_{i,n}^{\text{tet}} - \boldsymbol{x}_p \right) V_{i,n}^{\text{tet}}, \tag{2.58}$$

where $\boldsymbol{x}_{i,n}^{\text{tet}}$ and $V_{i,n}^{\text{tet}}$ represent respectively the barycenter and the volume of the n^{th} tetrahedron. Figure 2.4 illustrates a flow solver cell divided into five tetrahedra with their corresponding barycenters. Tetrahedra that are cut by the IB surface are split into sub-tetrahedra, using a marching tetrahedra algorithm [85], and the barycenter and volume of the cut tetrahedra are adjusted appropriately. This approach provides an accurate sub-cell integration methodology that accounts fully

for the immersed boundary.

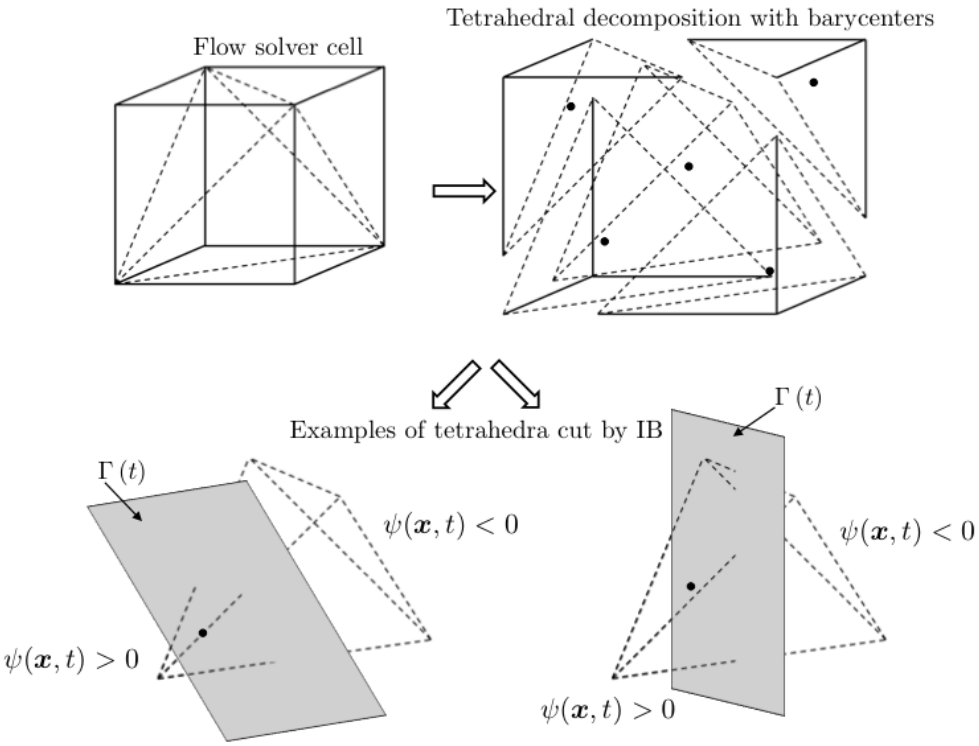

Figure 2.4: Decomposition of a hexahedron cell into 5 tetrahedra and their corresponding barycenters (filled circles) for volume integration. Cells cut by the IB are recomputed via marching tetrahedra algorithm.

2.5 Collision model

2.5.1 Normal collision

Particle-particle and particle-wall collisions are modeled using a soft-sphere approach originally proposed by Cundall and Strack [64]. The particles are represented as a mass-spring-dashpot system, as shown in Fig. 2.5. When two particles

come into contact, a repulsive force $\boldsymbol{f}_n^{\text{col}}$ is created as

$$\boldsymbol{f}_{n,b\to a}^{\text{col}} = \begin{cases} -k\delta_{ab}\boldsymbol{n}_{ab} - \eta\boldsymbol{u}_{ab,n} & \text{if } \; d_{ab} < (r_a + r_b + \lambda)\,, \\ 0 \quad \text{else.} \end{cases} \tag{2.59}$$

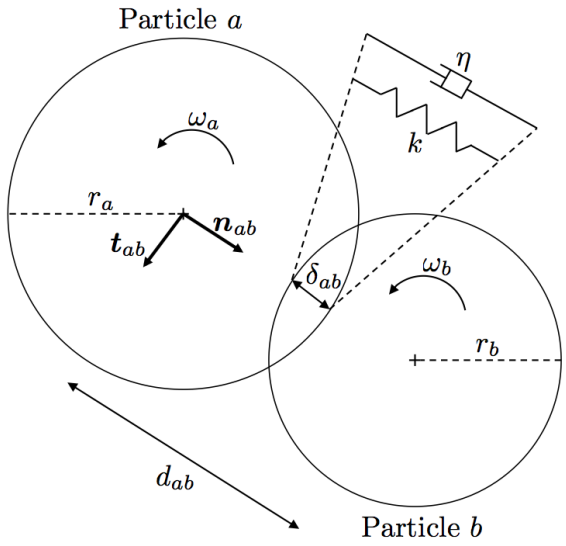

Figure 2.5: Soft-sphere representation of two particles undergoing collision.

For the collision shown in Fig. 2.5, r_a and r_b are the radii of particles a and b, respectively, d_{ab} is the distance between the centers of the particles, δ_{ab} is the overlap between the particles, and $\boldsymbol{n}_{ab}$ is the unit normal vector from particle a to particle b. The normal relative velocity between particles a and b is given by

$$\boldsymbol{u}_{ab,n} = ((\boldsymbol{u}_a - \boldsymbol{u}_b)\cdot\boldsymbol{n}_{ab})\,\boldsymbol{n}_{ab}. \tag{2.60}$$

λ is the force range, which will be discussed in Sec. 2.5.4, and k and η are the spring stiffness and the damping parameter, respectively. A model for the damping parameter uses a coefficient of restitution $0 < e < 1$ and an effective mass $m_{ab} = (1/m_a + 1/m_b)^{-1}$ such that

$$\eta = -2\ln e \frac{\sqrt{m_{ab}k}}{\sqrt{\pi^2 + (\ln e)^2}}. \tag{2.61}$$

Collisions with walls are handled by treating the walls as particles with infinite mass and zero radius.

2.5.2 Inter-particle friction

To account for friction between particles and thus particle rotation, a tangential collision model presented by van der Hoef *et al.* [24] is used. When particle a comes in contact with particle b, the tangential force is described as

$$\boldsymbol{f}^{\text{col}}_{t,b\to a} = \begin{cases} -k_t\boldsymbol{\delta}_t - \eta_t\boldsymbol{u}_{ab,t} & \text{if } \left|\boldsymbol{f}^{\text{col}}_{t,b\to a}\right| \leq \mu_f \left|\boldsymbol{f}^{\text{col}}_{n,b\to a}\right|, \\ -\mu_f \left|\boldsymbol{f}^{\text{col}}_{n,b\to a}\right| \boldsymbol{t}_{ab} & \text{if } \left|\boldsymbol{f}^{\text{col}}_{t,b\to a}\right| > \mu_f \left|\boldsymbol{f}^{\text{col}}_{n,b\to a}\right|, \end{cases} \tag{2.62}$$

where k_t, δ_t, η_t, and μ_f are the tangential spring stiffness, tangential displacement, tangential damping coefficient, and friction coefficient, respectively. The relative tangential velocity, $\boldsymbol{u}_{ab,t}$, is defined as

$$\boldsymbol{u}_{ab,t} = \boldsymbol{u}_{ab} - \boldsymbol{u}_{ab,n}, \tag{2.63}$$

and is used to create a tangential unit vector $\boldsymbol{t}_{ab}$ as

$$\boldsymbol{t}_{ab} = \frac{\boldsymbol{u}_{ab,t}}{|\boldsymbol{u}_{ab,t}|}. \tag{2.64}$$

In two dimensions, the tangential displacement is defined as

$$\boldsymbol{\delta}_t = \boldsymbol{\delta}_{t_0} + \int_{t_0}^{t} \boldsymbol{u}_{ab,t}\, dt, \tag{2.65}$$

where t_0 is the initial time of the collision. Computing Eq. 2.65 can become computationally intensive for particle flows under sustained contact. For instance, in two dimensions with a polydisperse particle system, tens of simultaneous collisions are common, and in three dimensions, hundreds of simultaneous collisions may be possible for a single particle provided the particle size distribution is wide enough.

In order to deal with tangential collisions properly, the tangential displacement, δ_t, needs to be stored for every collision and every particle at each timestep. For systems with tens of thousands of particles or more, this method becomes very computationally expensive. However, the static friction model

$$\boldsymbol{f}^{\text{col}}_{t,b\to a} = -\mu_f \left|\boldsymbol{f}^{\text{col}}_{n,b\to a}\right| \boldsymbol{t}_{ab} \tag{2.66}$$

that simply multiplies the normal component of the collision force by the coefficient of friction does not require storing any additional information. Moreover, this model is valid for sustained contact, which should dominate for dense particle systems. This simplified model was tested against the full linear model, Eq. 2.62, as well as experiments described in Di Renzo and Di Maio's review [86]. The test configuration consists of a single particle colliding with a flat surface, as illustrated in Fig. 2.6. Collision parameters are are given in Table 1, chosen to reflect the simulations performed in Di Renzo and Di Maio [86].

Diameter, d_p	5	mm
Density, ρ_p	4000	kg/m^3
Normal spring constant, k	1.72×10^7	$\text{N}\cdot\text{m}^{-1}$
Tangential spring constant, k	1.48×10^7	$\text{N}\cdot\text{m}^{-1}$
Coefficient of restitution, e	1.0	-
Friction coefficient, μ_f	9.2×10^{-2}	-
Initial velocity, $\boldsymbol{u}_1$	3.9	$\text{m}\cdot\text{s}^{-1}$
Timestep, Δt	1×10^{-8}	s

Table 2.1: Particle collision parameters for rebound test case.

Figure 2.7(a) shows the rebound angle α_2, versus impact angle α_1. The second plot, Fig. 2.7(b), shows the final rotational velocity $\boldsymbol{\omega}_2$, versus α_1. The third plot, Fig. 2.7(c), shows the tangential coefficient of restitution $e_t = |\boldsymbol{u}_{1,t}|/|\boldsymbol{u}_{2,t}|$, versus α_1, where $\boldsymbol{u}_{1,t}$ and $\boldsymbol{u}_{2,t}$ are the tangential velocities before and after the collision, respectively. At smaller contact angles the friction model over-predicts

the tangential force, though overall this approach appears to be a good compromise between accuracy and cost.

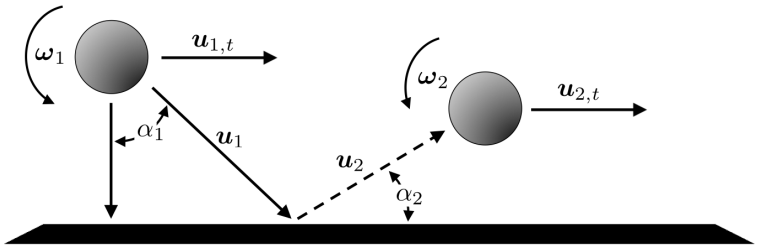

Figure 2.6: Particle collision test. Angular velocity $\boldsymbol{\omega}_p$, impact angle α, impact velocity $\boldsymbol{u}_p$, normal velocity $\boldsymbol{u}_{ab,n}$, tangential velocity $\boldsymbol{u}_{ab,t}$.

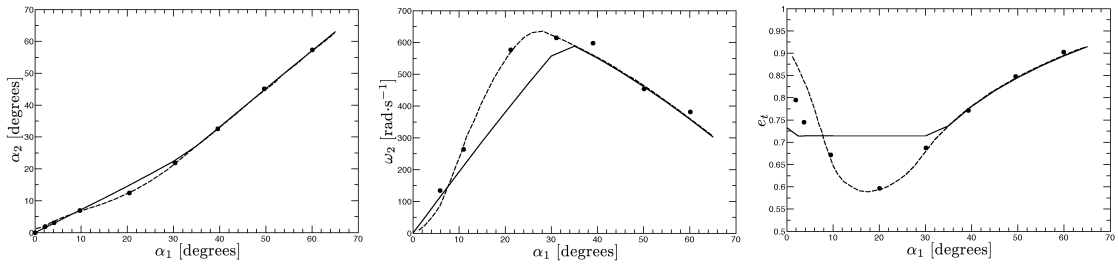

(a) (b) (c)

Figure 2.7: Validation of the simplified tangential collision model (solid line) against full linear model [86] (dashed line) and experimental results [86] (filled circles).

Once each individual collision force is computed, the full collision force that particle p experiences can be expressed as a sum of collisions with all other particles j undergoing collision with p, i.e.,

$$\boldsymbol{F}_p^{\text{col}} = \sum_j \left(\boldsymbol{f}_{n,j\to p}^{\text{col}} + \boldsymbol{f}_{t,j\to p}^{\text{col}} \right). \tag{2.67}$$

2.5.3 Stability criteria

When simulating dense particle-laden flows, particle processes often limit the simulation timestep. The particle Courant-Friedrichs-Lewy (CFL) number, given by

$$\mathrm{CFL}_p = \frac{\Delta t_p |\boldsymbol{u}_p|}{d_p}, \tag{2.68}$$

characterizes the fraction of its diameter the particle moves during the particle timestep, Δt_p. If the particle response time τ_p is less than the simulation timestep Δt, the particle solver iterates with a timestep $\Delta t_p < \tau_p$ for a total time Δt. The timestep for integrating the particle motion is chosen such that $\max_{p=1..N_p} \mathrm{CFL} \leq 0.1$, thereby limiting the inter-particle overlap during collisions.

To avoid excessive overlap which can lead to unphysical solid packing in a bed at rest, the particle stiffness should compensate for the weight of particles above it, leading to the following criterion on the spring constant

$$k \gg H_b \frac{m_p g}{d_p^2}, \tag{2.69}$$

where H_b is the height of the bed. Finally, the spring constant is related to the collision time τ_{col} according to

$$k = m_{ab}/\tau_{col}^2 \left(\pi^2 + \ln(e)^2\right). \tag{2.70}$$

To ensure proper resolution of collisions, Δt is chosen such that $\tau_{col} \geq 15\Delta t$.

2.5.4 Random close-packing limit

As mentioned in Section 2.5.1, a radius of influence λ is introduced to create a collision force when two particles are close, but not yet in contact. The collision model proposed by Patankar (2001) [23] suggests using $\lambda = 0.075 d_p$ when

calculating particle overlap. With a finite, non-zero radius of influence, particles at rest never come in contact, and therefore a settled bed under random close-packed conditions will exhibit an artificially large fluid volume fraction. Theory and experiments have shown that a bed of monodisperse spheres at rest will reach a random close-packed limit of 0.634 [87]. Several three-dimensional simulations were conducted to see the effect of λ on the solid packing for a static bed. The domain is periodic in the span-wise directions and consists of approximately 100,000 monodisperse spheres, shown in Fig. 2.8(a). The particles have a diameter and density of 200 μm and 3300 kg/m^3, respectively. A uniform mesh of $\Delta x = 2d_p$ with 24 cells in the spanwise directions and 50 cells in the height was used for this test. Figure 2.8(b) shows that the random close-packing limit is recovered when λ approaches 0, as expected.

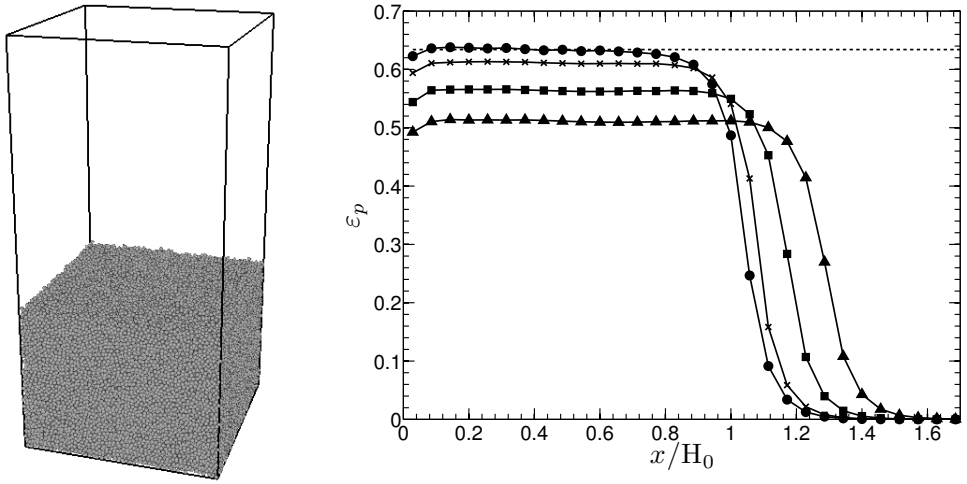

(a) Bed of spheres at rest.

(b) The effect of the radius of influence λ in a settled bed. Random close-packing limit [87] (dashed-line), $\lambda = 0$ (circles), $\lambda = 0.01d_p$ (crosses), $\lambda = 0.0375d_p$ (squares), $\lambda = 0.075d_p$ (triangles).

Figure 2.8: Testing the effective solid packing in a bed at rest.

Following this observation, we modify the expression of the radius of influence,

making it depend on the relative collision velocity. To this end, a particle collision CFL number is introduced as

$$\mathrm{CFL}_{ab}^{\mathrm{col}} = \frac{|\boldsymbol{u}_{ab,n}|\Delta t}{d_{\mathrm{eff}}}, \tag{2.71}$$

where $|\boldsymbol{u}_{ab,n}|$ is the magnitude of the normal relative velocity between particles a and b during a collision, and d_{eff} is the effective particle diameter ($d_{\mathrm{eff}} = d_p$ for wall collisions and $d_{\mathrm{eff}} = r_a + r_b$ for particle-particle collisions). The timestep for integrating the particle motion is chosen such that particles do not move more than 10% of their diameter per timestep, and therefore, the largest value $\mathrm{CFL}_{ab}^{\mathrm{col}}$ will typically be 0.1 for particle-wall collisions, and 0.2 for particle-particle collisions. The radius of influence can then be expressed as

$$\lambda_{wall} = 0.75\,\mathrm{CFL}_{ab}^{\mathrm{col}} d_{\mathrm{eff}}, \tag{2.72}$$

$$\lambda_{particle} = 0.375\,\mathrm{CFL}_{ab}^{\mathrm{col}} d_{\mathrm{eff}}, \tag{2.73}$$

such that it decreases monotonically as the normal collisional velocity decreases, reaching zero when the particles are immobile with respect to one another. This strategy allows to recover the correct random close-packing limit in near motionless regions of the bed, while providing a robust collision model for high-speed collisions.

2.5.5 Numerical implementation

The computation of the collision force requires measuring inter-particle distances, which leads to an $\mathcal{O}(N_p^2)$ problem if implemented using a brute-force strategy. Instead, we make use of the underlying computational mesh in order to speed up the identification of likely collision partners, as illustrated in Fig. 2.9(a). For each particle p, we identify the computational cell (i_p, j_p, k_p) to which particle p belongs.

For this cell and its closest 26 neighbors, we loop over all particles j in that cell, and test whether p and j are undergoing collision. The computational cells are typically large enough to ensure all collisions are captured using this approach. Note that it is also possible to construct a separate grid proportional to the particle diameter for the computation of particle collisions, which might be useful for particles with a wide size distribution, or non-uniform meshes, leading to grid spacing smaller than the particle diameter.

The scheme also relies on ghost particles in order to facilitate the parallel implementation of the collision force calculation. These ghost particles correspond to particles located inside interprocessor ghost cells, and they are communicated between processors like any Eulerian variable, as illustrated in Fig. 2.9(b). Each processor contains its own particles as well as the particles in the nearest layer of cells of the processor immediately neighboring it.

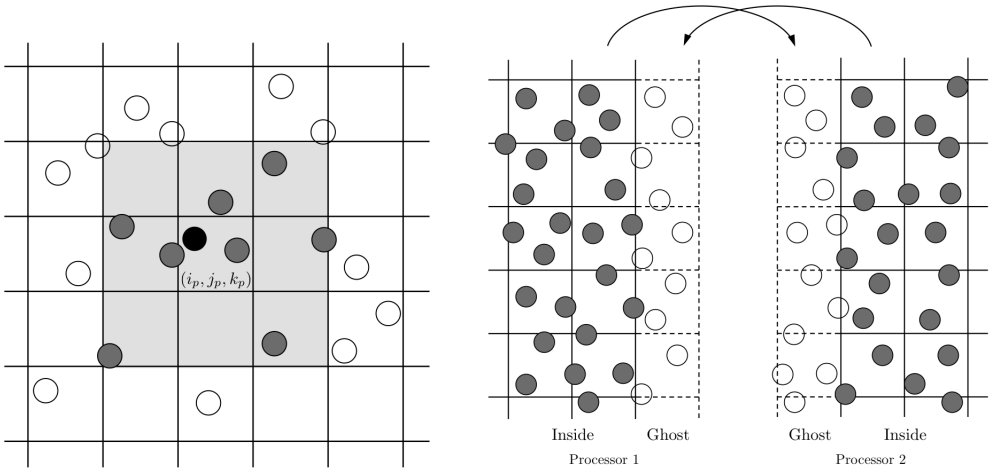

(a) Procedure to detect neighboring particles during collision. Particle p (filled circle), particles j identified during collision (gray circles), particles not identified during collision detection (empty circles).

(b) Procedure to handle interprocessor boundaries. Particles belonging to respective processors (gray circles), ghost particles of that processor (empty circles).

Figure 2.9: Utilization of the Eulerian mesh during computation of particle collisions.

2.6 Numerical implementation and performance

The CFD code NGA [69], a high-order, fully conservative solver tailored for turbulent flow computation, solves the fluid equations on an Eulerian mesh while the particles are tracked individually in a Lagrangian framework. All simulations presented in this paper are performed using second order spatial accuracy for both convective and viscous terms in the Navier-Stokes equations. Time advancement is accomplished using the second order accurate semi-implicit Crank-Nicolson scheme of Pierce and Moin [88]. Based on a fractional step approach [89], this algorithm uses both temporal and spatial staggering between velocity, pressure, and density. The volume fraction ε_f is stored at cell centers, like the density. The details on

the mass, momentum, and energy conserving finite difference scheme are available in [69].

Before each new flow solver timestep, the particle equations are solved using the fluid velocity obtained from an Adams-Bashforth prediction. The initial predictor step is second order accurate, resulting in second order temporal accuracy of the coupling between particles and gas phase [90]. The particle equations consist of a set of nine coupled ordinary differential equations per particle that are solved using a second-order Runge-Kutta scheme. Sub-stepping is used to ensure stability when the particle response time (defined in Eq. 2.45) becomes smaller than the simulation timestep. For low Stokes number cases, this can become computationally expensive as many iterations might be necessary to maintain stability. An implicit solver such as DVODE [91] can be implemented to avoid this issue and reduce computational time.

Particles are distributed among processors based on the underlying domain decomposition of the fluid phase. After each timestep, the particles undergo an interprocessor communication step as they move from one processor sub-domain to another, as illustrated in Fig. 2.10. NGA relies on interprocessor ghost cells in order to facilitate this data exchange. Particles owned by processor 1 that are located within its ghost cells at the end of the timestep are sent to the appropriate neighboring processors before being removed from the memory of processor 1. In this work, the numerical methods have been implemented in parallel using message passing interface (MPI), and detail on the solution procedure as well as parallel performance of the scheme will be provided in the following sections.

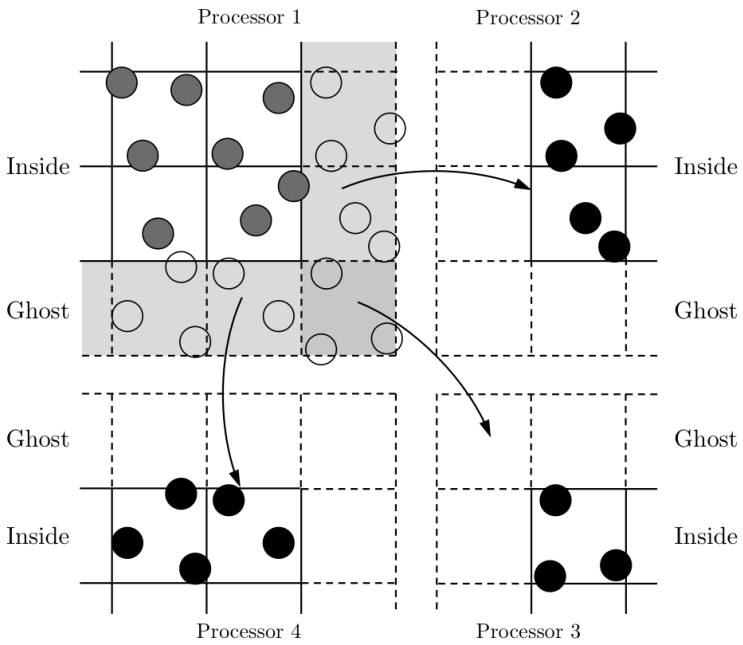

Figure 2.10: Procedure to handle interprocessor particle exchange. Particles belonging to processor 1 (gray circles), particles removed from processor 1 after sending (empty circles), particles received by neighboring processors (filled circles). Dashed lines indicate ghost cell boundaries.

2.6.1 Solution procedure

This section summarizes the solution procedure used in our code, then discusses the relative cost of individual routines.

1. Pre-timestep fluid velocity solver
    - Adam-Bashforth prediction of the fluid velocity at the middle of the particle timestep
2. Localize particles on mesh
    - Find i, j, k of cell in which the center of the particle lies

- Communicate particles with neighboring processors

3. Compute collision force for each particle

   - Loop through the 27 nearest cells and identify neighboring particles
   - Calculate distance d_{ab} between particle a and nearest wall ("b")
   - Calculate distance d_{ab} between particle a and each neighboring particle b
   - If $d_{ab} < 0.075 d_{\text{eff}}$, compute λ (Eqs. 2.72, 2.73)
     - If $d_{ab} < \lambda$
       * Solve normal collision force (Eq. 2.59)
       * Solve tangential collision force (Eq. 2.66)

4. Advance particles

   - Determine particle timestep size such that $\Delta t_p < \tau_p$ (Eq. 2.45)
   - Subiterate for a total time Δt
     - Interpolate the fluid-phase variables ($\nabla \cdot \boldsymbol{\tau}$, ε_f, $\boldsymbol{u}_f$, ρ_f, μ) to the particle position
     - Compute forces acting on the particle (Eq. 2.5)
     - Update position, velocity, and angular velocity with second-order Runge-Kutta

5. Compute interphase exchange term from particles

   - Calculate momentum exchange term (Eqs. 2.42 and 2.44)
   - Exchange source term with fluid phase via mollification (Eqs. 2.51, 2.52)
   - Filter momentum exchange term (Eq. 2.53)

6. Compute volume fraction from particles

- Mollify particle volume to the Eulerian grid (Eqs. 2.51, 2.52)
- Divide by local cell volume
- Filter volume fraction (Eq. 2.53)

7. Communicate particles with neighboring processors
8. Advance fluid velocity
   - Multiply fluid density by volume fraction
   - Compute effective viscosity (Eq. 2.41)
   - Update velocity using Crank-Nicolson scheme
9. Advance the timestep, $t = t + \Delta t$.
10. Repeat if $t < t_{final}$

To assess the timing of each component of the algorithm, a three-dimensional, twice periodic bed of 15.6 million particles was simulated using 20 million grid cells on 720 cores. To avoid any load imbalances, the processors were decomposed in the two span-wise directions only, resulting in approximately 22,000 particles per processor. Timing for the most expensive routines is given in Fig. 2.11, which shows the fraction of time spent in the LPT routine that is outlined in the algorithm above. While each timestep took approximately 6 seconds, it was found that the collision process (step 3) dominates the cost at approximately 72% of the total time. while the particle advancement routine (step 4) and interprocessor communication were found to take approximately 17% and 2% of the total time, respectively. It should be noted that the relative cost of interprocessor communications increases significantly when considering fewer particles per processor.

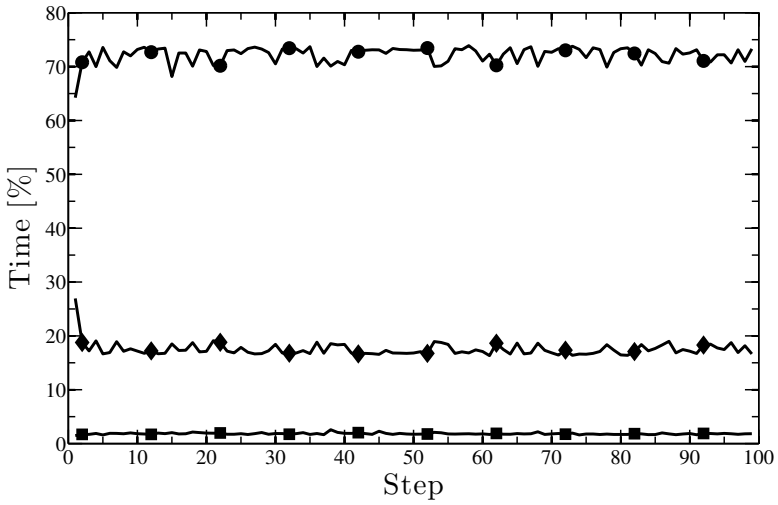

Figure 2.11: Timing of specific particle tracking routines, normalized by the total time per timestep. Simulation contains 15.6 million particles, performed using 720 cores: collision scheme (circles), particle advancement (diamonds), interprocessor communication (squares).

2.6.2 Parallel performance

A scaling analysis was performed on Red Mesa, the National Renewable Energy Laboratory's (NREL) high performance computing system. The system consists of 15,360 cores with a peak performance of 180 TFlops. A series of simulations were run to test the parallel performance of NGA using a reference simulation of 134 million cells and 382 million particles on 4,096 cores. The number of cores is progressively reduced to obtain the speed-up data, while the scale-up data is obtained by proportionally reducing the domain size and number of cores in the vertical direction while keeping the relative bed height constant at half the reactor length. Figure 2.12 shows strong and weak scaling results. Scale-up is computed

as

$$\text{Scale}-\text{up} = N_{\text{core}}^{\text{ref}} \left(\frac{n_x n_y n_z}{t_{\text{step}}} \right) \left(\frac{n_x^{\text{ref}} n_y^{\text{ref}} n_z^{\text{ref}}}{t_{\text{step}}^{\text{ref}}} \right)^{-1}, \tag{2.74}$$

where N_{core} is the number of cores, t_{step} is the time per timestep, n_i represents the number of cells in the i^{th} direction, and the "ref" quantities corresponds to the reference simulation. Similarly, speed-up is defined as

$$\text{Speed}-\text{up} = N_{\text{core}}^{\text{ref}} \frac{t_{\text{step}}}{t_{\text{step}}^{\text{ref}}}. \tag{2.75}$$

The cost of the particle tracking scheme was found to remain roughly constant throughout the simulations. It was found that the particle tracking routines accounted for 83% of the total simulation cost, while the pressure and velocity solver accounted for 14% and 2.4%, respectively. Scaling results are very good up to 4,096 cores, the maximum number used in this test, with increased efficiency for higher loading of cells and particles per processor.

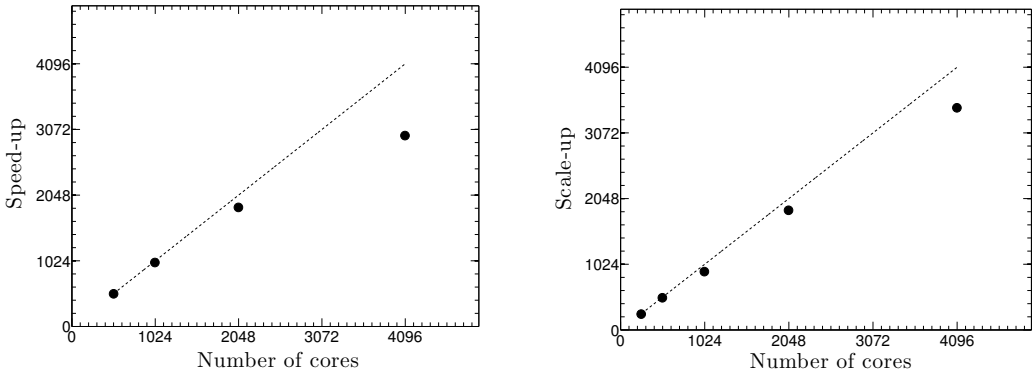

(a) Speed-up (b) Scale-up

Figure 2.12: Scaling analyses of NGA on Red Mesa. Dashed line indicate linear scaling.

2.7 Numerical tests

A range of laboratory scale simulations were conducted in order to validate the methods discussed in this paper. The section begins with an analysis of the force balance at the onset of fluidization. Highly turbulent spout fluidization and bidispersed segregation are then considered in a pseudo two-dimensional reactor, and results are compared against experiments. Finally, a two-inch bubbling fluidized bed is presented, and mean statistics on the flow dynamics and bubble characteristics are discussed.

2.7.1 Onset of fluidization

The phenomenon of fluidization occurs when a fluid passes through a bed of granular material, causing a pressure drop that can support the weight of the bed, allowing the granular material to behave like a fluid. The critical value at which the superficial gas velocity, defined as $\varepsilon_f u_f$ if we assume the x-direction to be vertical, first begins to fluidize the material, is known as the minimum fluidization velocity U_{mf}. Superficial velocities exceeding U_{mf} may lead to rapid particle motion causing bubbling or clustering, allowing for efficient mixing to take place. A study of the onset of fluidization was conducted in order to assess the capability of the proposed strategy to reproduce theory [32]. We consider the periodic bed of particles used in Sec. 2.5.4 and shown in Fig. 2.8(a), and introduce an inlet velocity at the bottom which is increased until fluidization is reached. The simulation parameters for the study can be found in Table 2.

Height	20	mm
Width	9.6	mm
Depth	9.6	mm
Cells in x-direction, n_x	50	-
Cells in y-direction, n_y	24	-
Cells in z-direction, n_z	24	-
Timestep, Δt	5	µs
Filter width, δ_f	700	µm
Number of particles, N_p	101,568	-
Particle diameter, d_p	200	µm
Particle density, ρ_p	2600	kg/m^3
Coefficient of restitution, e	0.8	-
Coefficient of friction, μ_f	0.1	-

Table 2.2: Simulation parameters for the minimum fluidization test.

Prior to fluidization, the pressure drop across the bed balances drag, which can be shown by neglecting friction at the walls and the effect of gravity on the fluid, reducing the momentum balance given by Eq. 2.31 in the vertical direction to

$$-\varepsilon_f \frac{1}{\rho_p}\frac{\partial p}{\partial x} = f^{\text{drag}}. \tag{2.76}$$

The minimum fluidization velocity is reached when the pressure drop can support the weight of the bed [32], given by

$$-\frac{\partial p}{\partial x} = \left(\varepsilon_f \rho_f + \varepsilon_p \rho_p\right) g \approx \varepsilon_p \rho_p g. \tag{2.77}$$

Figure 2.13(a) shows the pressure gradient normalized by the weight of the bed per unit volume acting in the vertical direction plotted against the analytic expressions given by Eqs. 2.76 and 2.77. Equations 2.76 and 2.77 were solved using the volume fraction at minimum fluidization. As the superficial gas velocity increases, the pressure drop across the bed increases near-linearly until minimum fluidization has been reached, at approximately 0.03 m/s.

As the inlet velocity approaches U_{mf}, the forces acting on the particles evolve as well. The relative importance of each component in the particle equation of motion was computed by summing the individual forces acting on each particle over the total number of particles, and is given in Fig. 2.13(b). When the bed is at rest, the collision force exactly balances the weight of the bed. The pressure drop and drag increase with the superficial gas velocity until the particles are no longer in contact and fluidization is reached.

The measured pressure drop in Fig. 2.13(a) verifies the code's ability to reach minimum fluidization for the given drag model as predicted by theory. Figures 2.13(a) and 2.13(b) illustrate the mechanisms that control the multiphase dynamics in fluidized beds, which will be responsible for the phenomenon observed in the subsequent test cases.

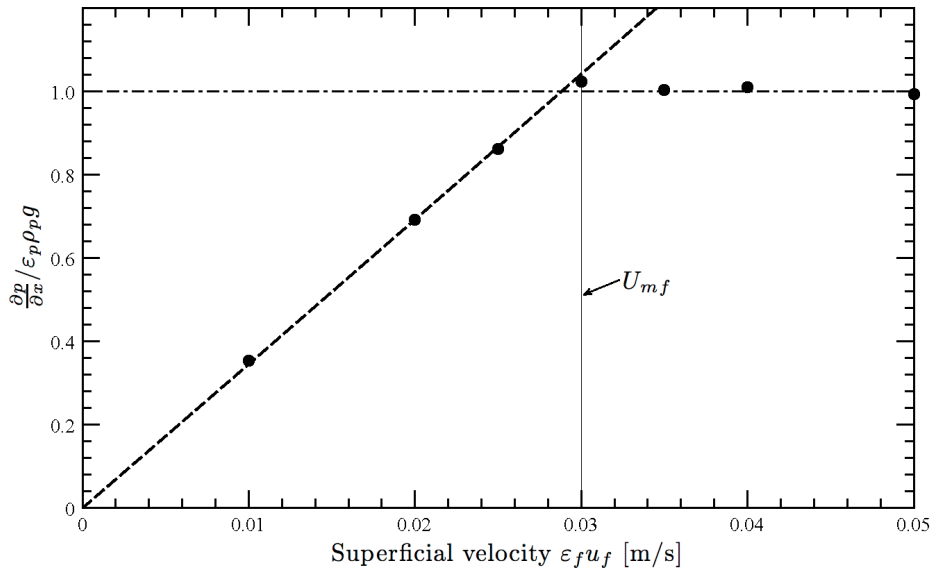

(a) Pressure drop normalized by the weight of the bed per unit volume. Pressure gradient measured in the simulation (circles), drag given by Eq. 2.76 computed using the volume fraction at minimum fluidization (dashed line), weight of the bed given by Eq. 2.77 (broken line).

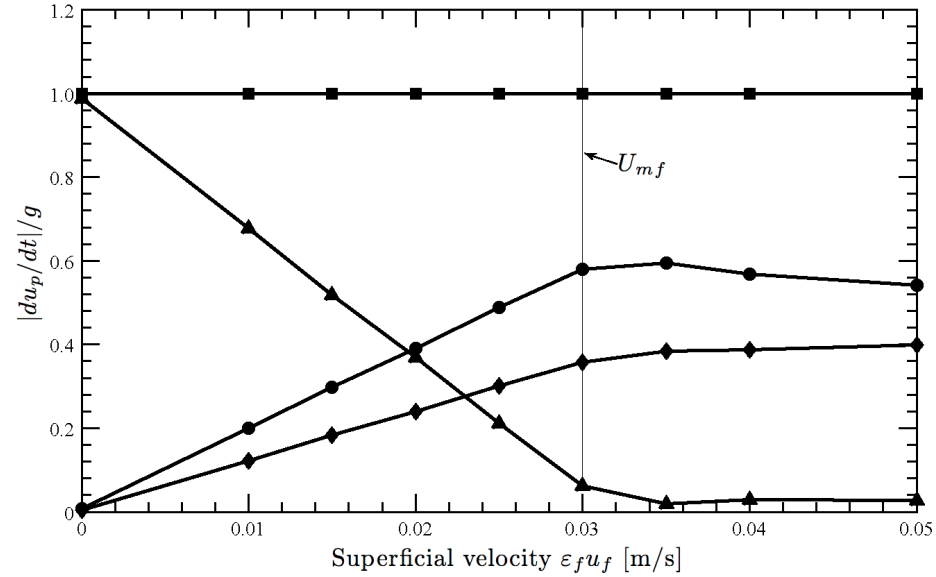

(b) Normalized particle momentum balance. Gravity (squares), pressure drop (circles), drag (diamonds), collisions (triangles).

Figure 2.13: Balance of forces during onset of minimum fluidization.

2.7.2 Pseudo two-dimensional spout fluidization

Numerical simulations of a pseudo two-dimensional spout fluidized bed under two different inflow conditions were conducted and compared to experiments by Link *et al.* [92, 93]. The depth of the bed is large enough to prevent bridge formation between particles, though not too large such that digital-image-analysis is capable of measuring voidage. A schematic of the bed as well as its dimensions can be seen in Fig. 2.14. Except for the height of the reactor, which is reduced to limit the computational expense, all physical parameters used in the simulations match those of the experiments. Simulation parameters for each case can be found in Table 3. A grid size equal to the particle diameter was chosen in order to capture the unsteady nature of the gas phase. Air is injected via three separate sections at the inlet. A high-speed spout velocity is fed through the center orifice while the outside sections feed the background velocity.

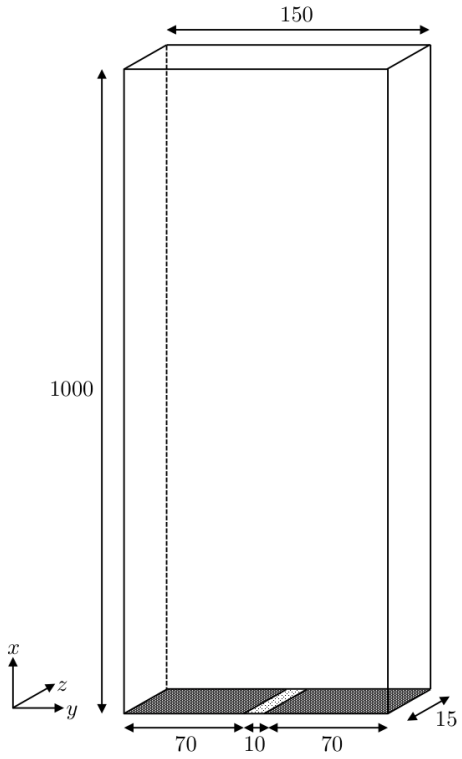

Figure 2.14: Schematic of spout-fluid bed (not to scale), with dimensions in mm [92].

For both cases, relatively high gas velocities are introduced, resulting in particle Reynolds numbers above 300, and gas Reynolds numbers through the spout above 13,000. At such large Reynolds numbers, sub-grid Reynolds stresses are likely to be significant and need to be closed. For both cases A and B, we close $\boldsymbol{\mathcal{R}}_u$ with a dynamic Smagorinsky model [75,76] based on Lagrangian averaging [77]. Note that we do not account for turbulence modulation by the particles, even though it might be important. Two viscosity models are therefore used simultaneously: an eddy viscosity model to account for turbulence, and an effective viscosity model based on experimental correlations to account for the enhancement in viscous stresses in packed regions of the bed. Interactions between these models are unclear. However, Fig. 2.15 reveals a distinct segregation between the models. The effective viscosity

Height	0.75	m		
Width	0.15	m		
Depth	0.015	m		
Cells in x-direction, n_x	300	-		
Cells in y-direction, n_y	30	-		
Cells in z-direction, n_z	3	-		
Timestep, Δt	5	µs		
Filter width, δ_f	7.5	mm		
Number of particles, N_p	24,500	-		
Particle diameter, d_p	2.5	mm		
Particle density, ρ_p	2526	kg/m^3		
Spring constant, k	4,538	kg/s^2		
Coefficient of restitution, e	0.9	-		
Coefficient of friction, μ_f	0.1	-		
Case	A		B	
Background velocity	1.5	m/s	3.0	m/s
Spout velocity	30	m/s	20	m/s

Table 2.3: Simulation parameters for the spout fluidization cases.

dominates in regions with greatest solid packing, while the turbulent viscosity model dominates in the particle-free turbulent regions.

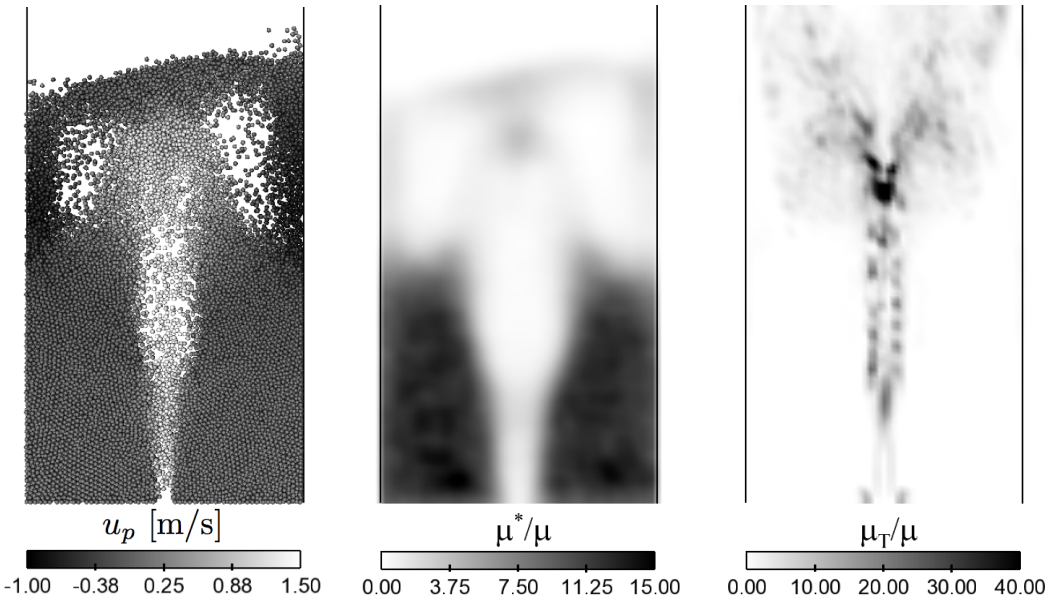

(a) Instantaneous plot of particle position, colored by vertical velocity.

(b) Normalized effective viscosity.

(c) Normalized turbulent viscosity.

Figure 2.15: Instantaneous snapshot of case A of the spout fluidization simulation and corresponding sub-grid viscosity models.

As depicted in Fig. 2.15, the spout velocity in case A leads to a region of fast moving particles in the middle of the bed with a recirculation region at the top. When the background fluidization velocity is increased, the spout has a greater impact on the overall flow pattern. In case B the jet oscillates back and forth due to the production of gas bubbles alongside the spout, as is observed in both experiment and simulation. Figure 2.16 shows qualitative agreement between the experiment and simulation for Case B.

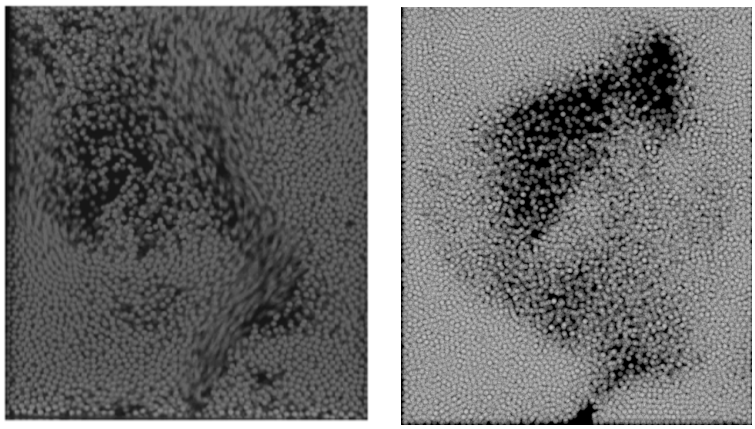

Figure 2.16: Instantaneous particle location showing flapping motion from experiment [92] (left) and simulation (right) for Case B.

Link *et al.* [92, 93] used particle image velocimetry (PIV) to study the particle flow and obtained time-averaged vertical particle flux profiles, $\Phi_{p,x}$, at a height of 0.13 m for each case. A comparison of the particle flux profiles is presented in Fig. 2.17. Although the results fail to match the data at the region near the wall, overall very good agreement is shown in both cases. It should be noted that simulations by Link *et al.* [93] show discrepancies in $\Phi_{p,x}$ at the duct center and regions near the wall. It has already been discussed in Sec. 2.3.5 that several challenges exist when modeling regions near the walls. In particular, key assumptions in the mathematical derivation are violated close to solid boundaries, and a drag model that is aware of walls could alleviate this. Furthermore, a proper prediction of the volume fraction within a particle diameter away from the wall is very difficult to obtain. A Neumann boundary condition on this quantity is used for robustness, though a detailed sub-grid model might be necessary to capture the proper physics.

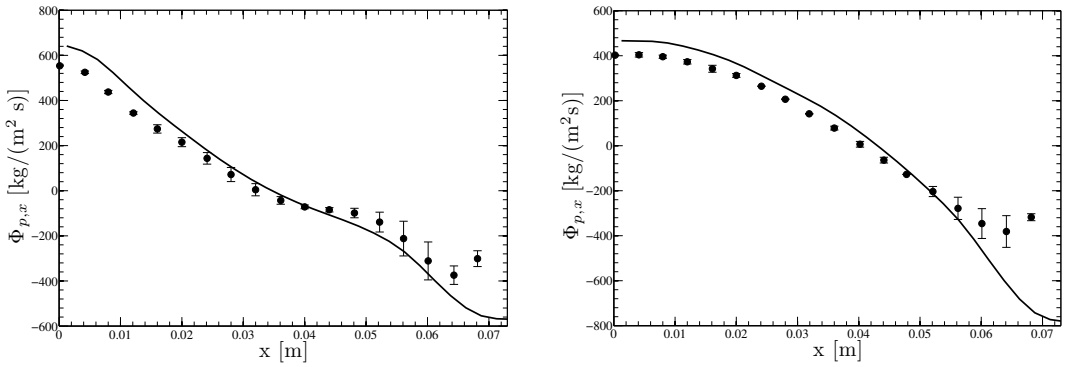

(a) Case A (b) Case B

Figure 2.17: Time-averaged particle flux profiles at a height of 0.13 m for two different cases. Simulations (solid lines), experiment [93] (circles).

2.7.3 Segregation dynamics

Segregation in a bidisperse fluidized bed was studied and compared to experiments performed by Goldschmidt *et al.* [94]. A bed of small and large glass beads was fluidized and the time evolution of both axial and lateral segregation was calculated. In gas-solid fluidized beds, segregation occurs at fluidization velocities close to minimum fluidization. Smaller particles tend to be more dynamic and migrate to the top of the bed. The experiments were conducted in a pseudo two-dimensional duct as shown in Fig. 2.14. Glass particles with diameters of 1.5 and 2.5 mm were fluidized with air at a fluidization velocity of $u_{in} = 1.3$ m/s, corresponding to $0.78U_{mf}$ and $1.25U_{mf}$, respectively. The bed consists of a mass fraction of small particles $\chi_{small} = 0.25$. Simulation parameters are given in Table 4.

The degree of segregation s is defined as

$$s = \frac{S - 1}{S_{max} - 1}, \tag{2.78}$$

where $S = \langle h_{small} \rangle \,/\, \langle h_{large} \rangle$, $S_{max} = (2 - \chi_{small})/(1 - \chi_{small})$. The measure s is

Height	0.45	m		
Width	0.15	m		
Depth	0.015	m		
Cells in x-direction, n_x	90	-		
Cells in y-direction, n_y	30	-		
Cells in z-direction, n_z	3	-		
Timestep, Δt	1e-4	s		
Inlet superficial velocity, u_{in}	1.3	m/s		
Filter width, δ_f	7.5	mm		
Particles	Large		Small	
Number, N_p	17940	-	27720	-
Diameter, d_p	2.5	mm	1.5	mm
Particle density ρ_p	2525	kg/m^3	2525	kg/m^3
Minimum fluidization velocity, U_{mf}	0.78	m/s^2	1.25	m/s^2
Spring constant, k	45.3	kg/s^2	9.8	kg/s^2
Coefficient of restitution, e	0.9	-	0.9	-
Coefficient of friction, μ_f	0.1	-	0.1	-

Table 2.4: Simulation parameters for the bidisperse fluidized bed.

referred to as the percentage of axial segregation, which equals 0 for a perfectly mixed bed, and 1 when the mixture is completely segregated. $\langle h_{small} \rangle$ and $\langle h_{large} \rangle$ refer to the mean height of the small and large particles, respectively. The mean height of the small particles is given by $\langle h_{small} \rangle = \sum_{i=1}^{N_{p,small}} x_{i,small}/N_{p,small}$, where $x_{i,small}$ is the x-position of the i^{th} small particle, and $N_{p,small}$ is the number of small particles. $\langle h_{large} \rangle$ is defined in a similar way for large particles. When calculating lateral segregation, $\langle h_{small} \rangle$ and $\langle h_{large} \rangle$ are taken to be the average y-distances from the center of the bed.

Initially, the bed is at rest and uniformly mixed. At $t = 0$ a uniform inflow is introduced at the bottom of the bed. The simulation runs for 60 seconds, and segregation rates are compared with experimental data. Originally, walls were present in all directions and the bed was found to remain at rest with the given inflow velocity. With three cells across the depth of the bed, a proper boundary

layer could not be established with the imposed no-slip boundary condition, which led to a mismatch in effective U_{mf}, preventing fluidization to occur with the experimental parameters. This was alleviated by removing the walls in the z-direction, allowing the bed to fluidize with the given inflow. Although wall effects may be significant, no significant motion was observed with the particles normal to the z plane. Figure 2.18 shows instantaneous snapshots of particle position during the simulation. The segregation rate is plotted in Fig. 2.19, which shows good agreement with the experiments, although the segregation rate seems to taper off in the simulation while the experiment data shows a continuous rise. The lack of walls in the z-directions might explain this discrepancy. Note that at such low fluidization velocities, the solution becomes very sensitive to the drag model, which does not account for walls appropriately.

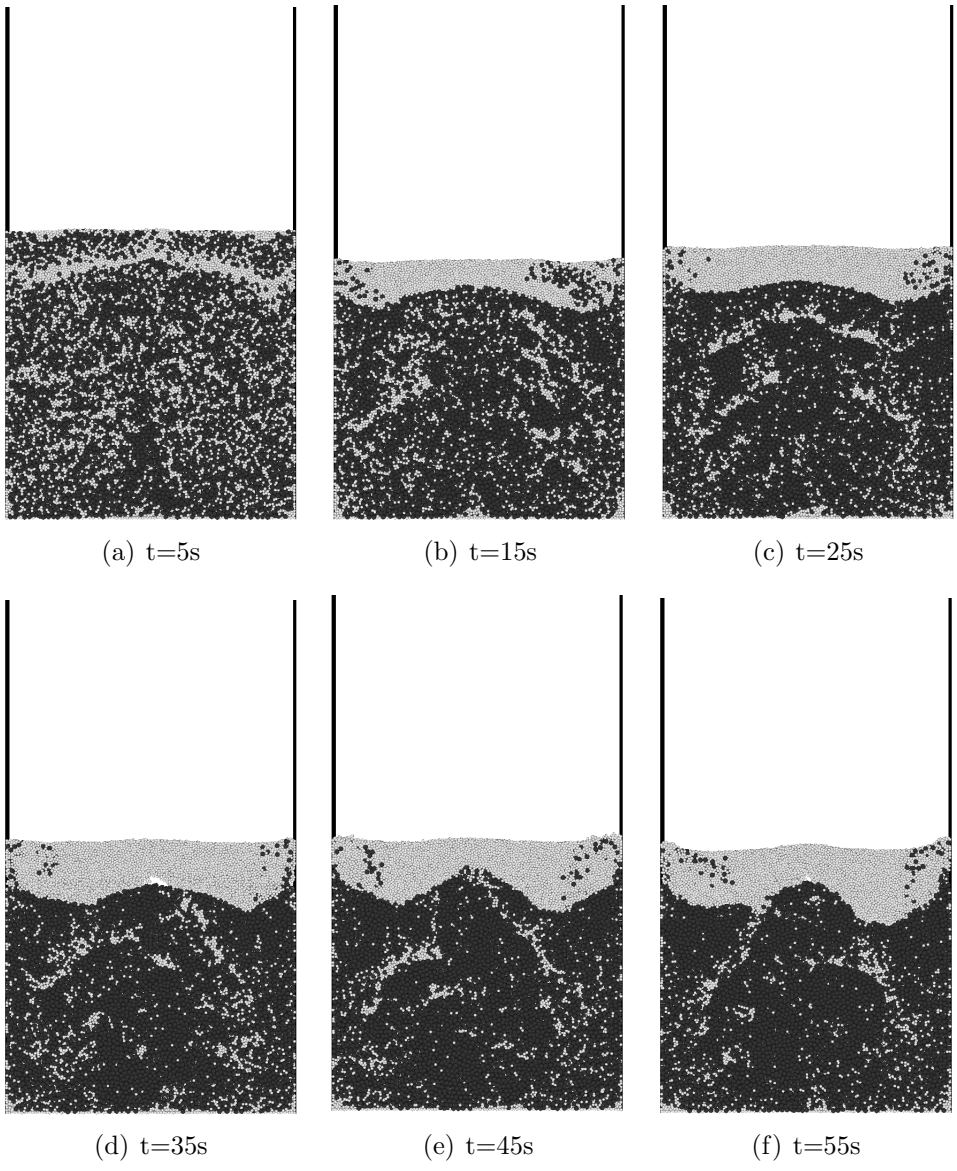

(a) t=5s (b) t=15s (c) t=25s

(d) t=35s (e) t=45s (f) t=55s

Figure 2.18: Segregation of a bidisperse fluidized bed. Large and small particles are shaded dark and light, respectively.

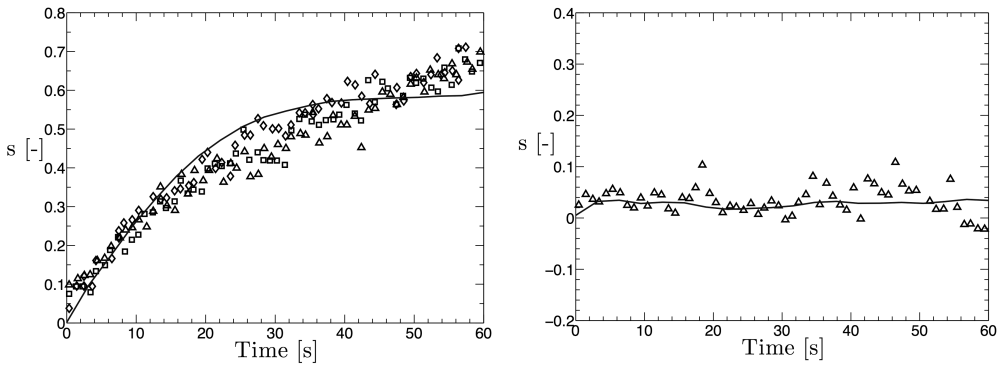

Figure 2.19: Axial segregation rate (left) and lateral segregation rate (right) predicted numerically (solid line) compared to experiments [94] (symbols).

2.7.4 Bubbling fluidized bed reactor

NREL is using a 4-inch fluidized bed reactor to study gasification of biomass [95]. The reactor, shown in Fig. 2.20(a), consists of a freeboard to prevent the particles from escaping the top, a downward-angled feed tube to load the biomass particles, an exit valve to prevent pressure buildup, pressure taps at different intervals along the side of the reactor, and a distributor plate at the bottom. A simulation was conducted as if all the ports were closed off, considering only a cylindrical boundary with a freeboard, as shown in Fig. 2.20(b). The geometry was taken to be half the scale of the physical reactor, including 15.6 million particles and approximately 20 million grid cells. Fluid properties were taken to be those of nitrogen at room temperature. The simulation was performed using 576 cores for three weeks in order to obtain flow statistics. Simulation parameters are given in Table 5.

In order to fluidize the bed material while preventing back flow, gas is forced through a distributor plate pierced with numerous small holes. Franka and Heindel [96] have shown that the superficial gas velocity affects the region directly above

the distributor plate, leading to regions of high gas volume fraction extending from the distributor plate into the bed. Jets are created by a high local gas velocity passing through each hole, potentially leading to non-uniform fluidization. This non-uniform flow pattern affects the bubble characteristics within the bed [96], and has therefore been introduced in the simulation. The gas jets are modeled as Gaussian functions with a characteristic width D_{jet}, distributed along a Cartesian grid, shown in Fig. 2.20(c). The inflow is given by

$$\sum_{j=1}^{n_{jet}} e^{-\left(\frac{(y-y_j)^2}{0.5D_{jet}^2}+\frac{(z-z_j)^2}{0.5D_{jet}^2}\right)}, \tag{2.79}$$

where the j^{th} jet is centered at (x_{in}, y_j, z_j), x_{in} is the location of the inlet, and n_{jet} is the number of jets. The inflow is then rescaled to match the superficial gas velocity.

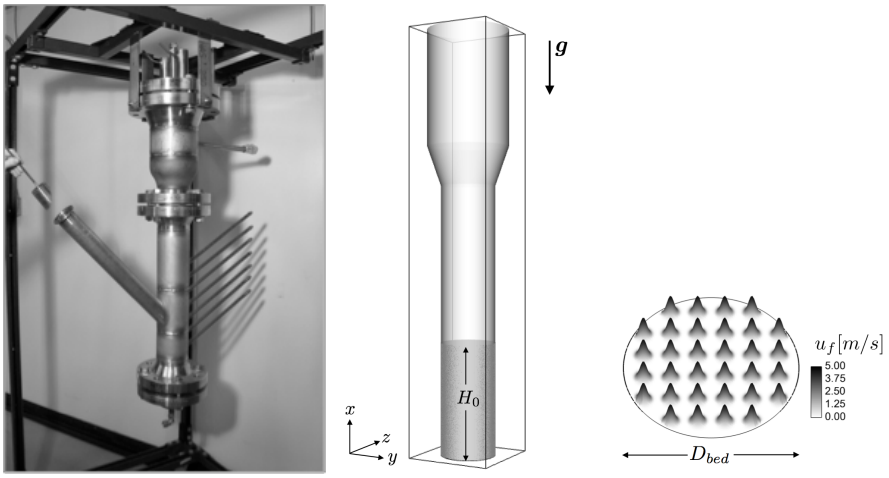

(a) NREL's 4-in fluidized bed reactor [95] (b) Simulation domain (c) Inlet velocity profile

Figure 2.20: Experimental and computational configuration of a lab-scale fluidized bed reactor.

The particle size distribution is created from a random lognormal distribution generator. Given a mean diameter $\langle d_p \rangle$ and a standard deviation σ_d, the standard

Domain length in x	m	0.4
Domain length in y	m	0.079
Domain length in z	m	0.079
Cells in x-direction, n_x	800	-
Cells in y-direction, n_y	158	-
Cells in z-direction, n_z	158	-
Bed diameter, D_{bed}	m	0.051
Initial bed height, H_0	m	0.106
Gas density, ρ_f	kg/m^3	1.13
Gas viscosity, μ	kg/m·s	1.77×10^{-5}
Particle density, ρ_p	kg/m^3	3300
Inlet superficial velocity, u_{in}	m/s	0.494
Orifice diameter, D_{jet}	m	0.002
Number of holes, n_{jet}	-	32
Number of particles, N_p	-	15.6 million
Mean particle diameter, $\langle d_p \rangle$	µm	200
Min particle diameter, d_{min}	µm	102
Max particle diameter, d_{max}	µm	410
Particle standard deviation, σ_d	µm	70
Spring constant, k	3.0	kg/s^2
Coefficient of restitution, e	0.8	-
Coefficient of friction, μ_f	0.092	-
Filter width, δ_f	µm	820 ($2d_{max}$)

Table 2.5: Simulation parameters for lab-scale fluidized bed reactor.

deviation and mean for a lognormal random variable are

$$\sigma_{d,\log} = \sqrt{\ln(1 + (\sigma_d/\langle d_p \rangle)^2)}, \tag{2.80}$$

and

$$\langle d_p \rangle_{\log} = \ln(\langle d_p \rangle) - \sigma^2_{d,\log}/2, \tag{2.81}$$

respectively. Using these parameters for the mean and standard deviation of a random normal distribution then exponentiating this value yields the appropriate particle diameter. A lognormal distribution was created to match the particle size data provided by NREL, as illustrated in Fig 2.21.

Figure 2.22 shows a volumetric rendering of the gas velocity and an iso-surface

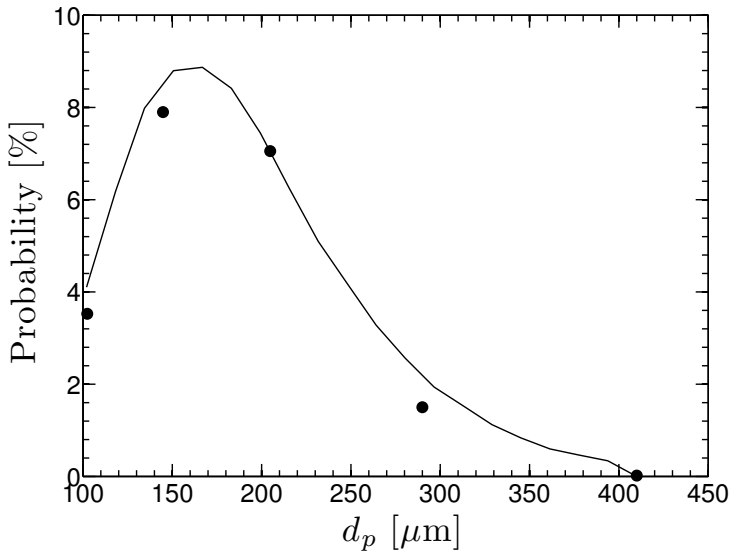

Figure 2.21: Particle size distribution. Data provided by NREL (circles), simulation data (solid line).

of $\varepsilon_f = 0.92$ at a simulation time of 1.5 seconds. The gas jets at the inlet directly lead to the formation of bubbles, which expand and accelerate as they rise until they reach the surface of the bed. The bubbles tend to form in the middle of the bed, leading to a recirculation of particles down the sides of the walls. It is apparent in the figure that the gas velocity is greatest within the bubbles. Instantaneous plots of fluid volume fraction and velocity are presented in Figs. 2.23(a) and 2.23(c), further exemplifying this correlation. Above the bed, the freeboard is seen to induce turbulence in the gas phase, as illustrated in Fig. 2.23(c).

The simulation was run until statistical stationarity was reached. Time-averaged fields of the gas phase volume fraction and velocity are given in Figs. 2.23(b) and 2.23(d), respectively. The highest particle packing is observed at the walls, indicating the tendency for bubbles to form in the middle of the bed. The mean gas velocity is negative in this region as a result of entrainment from the particles. Radial profiles of particle velocities at various heights in the bed

are given in Fig. 2.24, which clearly identifies recirculation at the walls due to rising bubbles. The presence of the bubbles lead to periodic oscillations in the bed height, as depicted in Fig. 2.24(b). The bed height is based on the 90^{th}-percentile of particle height, and indicates convergence in macroscale motions of the bed.

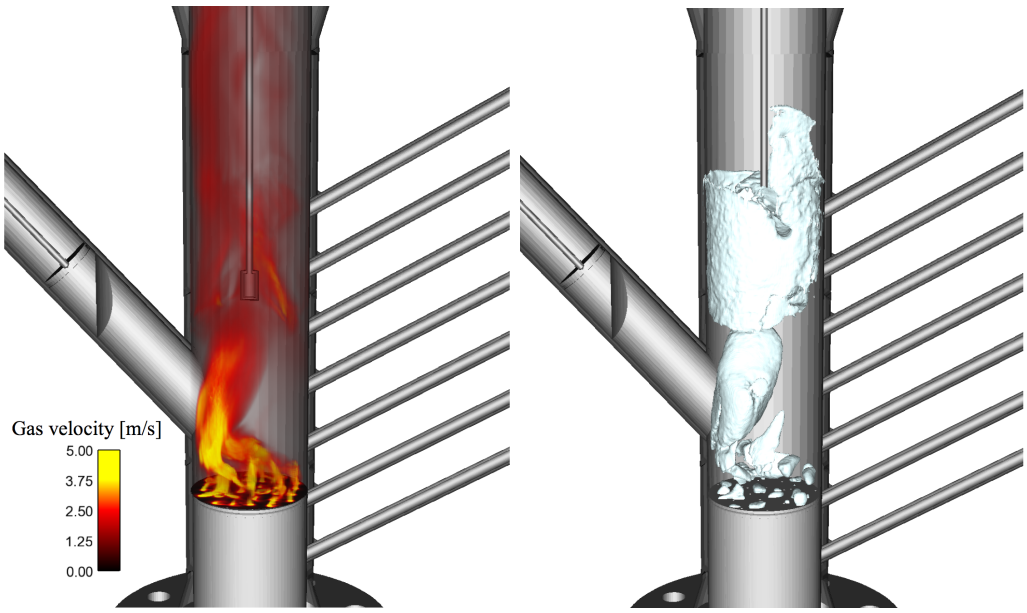

(a) Volume rendering of gas velocity magnitude.

(b) Iso-surface of $\varepsilon_f = 0.92$.

Figure 2.22: Simulation of a two-inch fluidized bed reactor at t=1.5s.

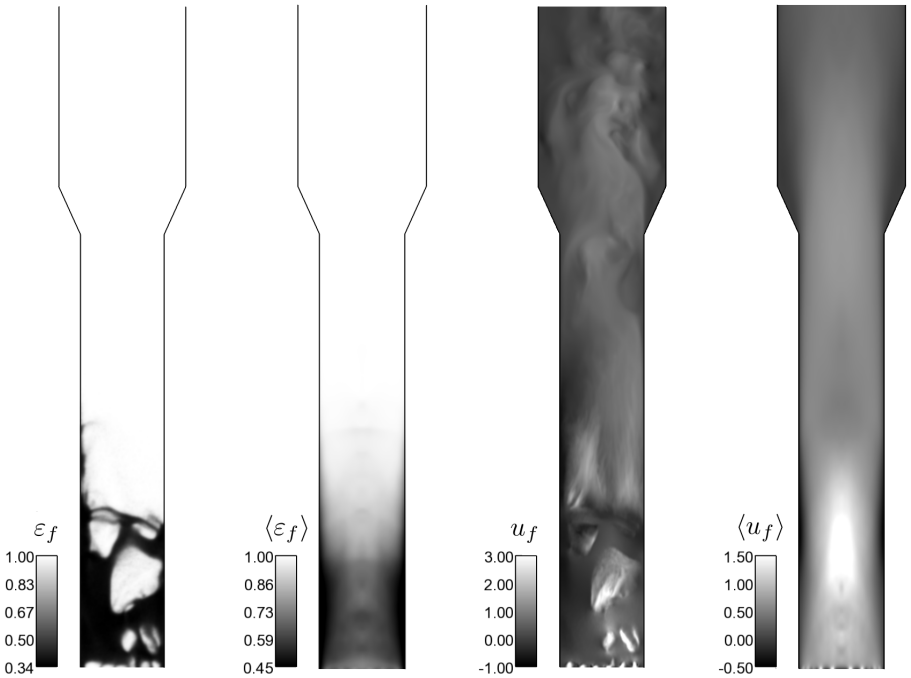

(a) Instantaneous gas volume fraction.

(b) Mean gas volume fraction.

(c) Instantaneous axial fluid velocity (m/s).

(d) Mean axial fluid velocity (m/s).

Figure 2.23: Instantaneous and time-averaged statistics of the two-inch fluidized bed reactor.

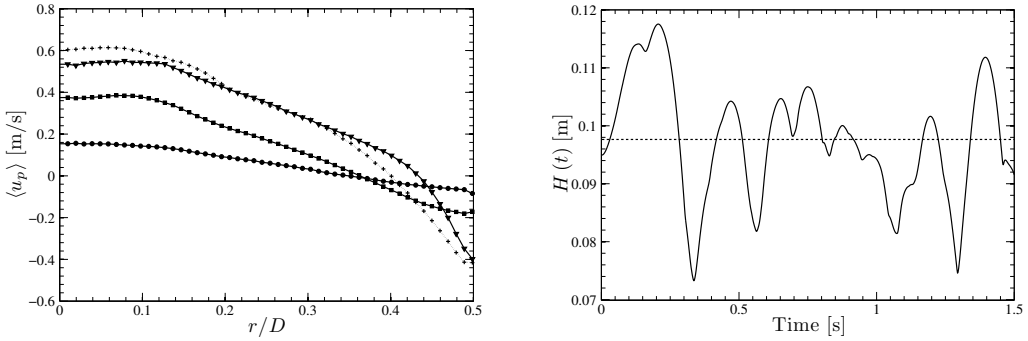

(a) Time-averaged particle velocity. $x/H_0 = 0.25$ (circles), $x/H_0 = 0.5$ (squares), $x/H_0 = 0.75$ (triangles), $x/H_0 = 1$ (crosses).

(b) Bed height based on 90^{th}-percentile particle height (solid line), average bed height (dashed-line).

Figure 2.24: Particle statistics of the two-inch fluidized bed reactor.

Pepiot and Desjardins [63] showed that large variations of residence times are directly related to the local gas volume fraction, and thus bubbling has the potential to affect the chemical processes in reactive beds. In order to develop more insight on the role of bubbles in fluidized bed dynamics, the band growth algorithm of Herrmann *et al.* [97] was implemented to identify and track individual bubbles. For details on the bubble tracking scheme, see Pepiot and Desjardins [63]. With this tool, the volume of each identified structure is calculated and an effective diameter is computed by assuming a perfect sphere. The mean bubble diameter was found to be 18% of the bed diameter, and on average 8 bubbles existed within the bed at any time. Bubbles tend to form at the bottom of the bed and grow in size and velocity as they rise. The bubble height was compared with Darton's correlation [98] in Fig. 2.25, which gives the bubble diameter as a function of height by

$$D_b = 0.54\left(U_{in} - U_{mf}\right)^{0.4}\left(h + 4\sqrt{A_0}\right)^{0.8} g^{-0.2}, \tag{2.82}$$

where A_0 is the catchment area of the distributor plate (area of the plate per orifice). For this case, $A_0 = \pi D_{jet}^2/4$. Due to the non-linearity of the drag, U_{mf} cannot be determined *a priori*, as this would require knowledge of the voidage at fluidization. However, this value of the volume fraction can be postulated, allowing us to compare the correlation with the simulation results. Typically, the voidage at minimum fluidization, ε_{mf}, is taken to be that of a packed bed of uniform spheres in cubic arrangement [32], giving $\varepsilon_{mf} = 1 - \pi/6$. Using this value, u_{in} corresponds to $6U_{mf}$. However, when calculating U_{mf} for experimental runs, NREL uses a value of $\varepsilon_{mf} = 0.405$ to account for polydispersity, corresponding to $11U_{mf}$. It is shown in the figure that the value of U_{mf} does not change the correlation substantially, and it is assumed the simulation fluidization velocity falls between these two values. Due to the highly turbulent nature of the flow, bubble coalescence and breakup lead to

numerous small diameter bubbles throughout the bed. With this large number of small bubbles throughout the bed, smaller bubbles are found to deviate from the correlation, although overall we see good agreement between the simulation data and correlation.

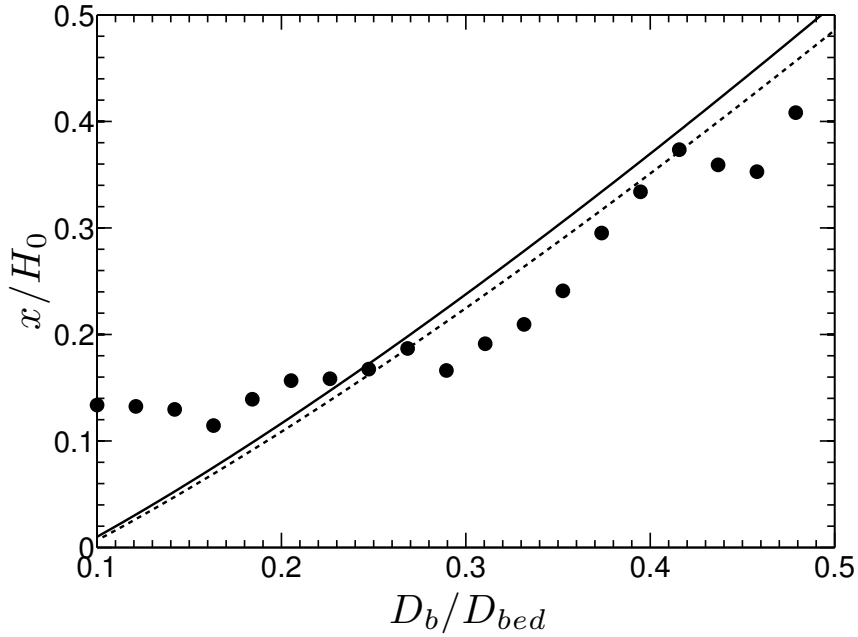

Figure 2.25: Bubble height as a function of diameter compared to Darton's correlation [98]. Correlation corresponding to $u_{in} = 6U_{mf}$ (dashed-line), correlation corresponding to $u_{in} = 11U_{mf}$ (solid line).

2.8 Conclusions

A numerical strategy for simulating gas-solid particle-laden flows in an Eulerian-Lagrangian framework was developed and tested. Starting from the point wise equations of motion that govern each phase, a volume filtered description initially introduced by Anderson and Jackson [70] was presented then extended for chemically reacting flows. All assumptions and models were stated explicitly and

discussed. A two-step filtering process was derived in the context of the volume filtering approach that converges under mesh refinement and allows for cell sizes smaller than the particle diameter if necessary. A conservative immersed boundary method was used for modeling complex geometries. Due to the inherent nature of this approach, detailed information of the particle's distance to the nearest boundary was readily available. Particles near walls were mirrored across the boundary to yield appropriate boundary conditions. A soft-sphere collision model was employed, which was modified for parallel efficiency. Replacing the full linear model for tangential collisions with the static friction model was shown to be a good compromise for cost, as the simpler model does not require storing the collision history. A radius of influence proportional to the relative collisional velocity was used to allow for robust collisions while recovering random close packing for a bed at rest.

Several lab-scale simulations of experiments were conducted for validation purposes. Choosing appropriate values for the simulation timestep that account for both the particle CFL as well as particle stiffness is necessary to prevent excessive overlap leading to unphysical packing while correctly capturing particle collisions. Particle flows close to the minimum fluidization velocity as well as highly turbulent flows were simulated and provided overall good agreement with experiments. For systems with large gas phase Reynolds numbers, a dynamic Smagorinsky eddy viscosity model was used to close the residual stress tensor $\boldsymbol{\mathcal{R}}_u$. Although interactions between the viscosity models are unclear, a distinct segregation was observed where the effective viscosity dominates in regions with greatest solid packing, while the turbulent viscosity model dominates in the particle-free turbulent regions. Finally, a two-inch fluidized bed reactor was simulated, consisting of 15.6 million particles on approximately 20 million grid cells. Mean statistics of the flow were computed

and a band-growth algorithm was used to study bubbling in the bed. Gas jets form at the distributor plate that lead to bubbles that grow in size as they approach the surface of the bed, displaying good agreement with experimental correlations.

It was shown that several challenges exist for properly treating regions near walls. When deriving the volume filtered equations, underlying assumptions are violated when the filter radius is larger than the distance between particles and solid boundaries. Drag models for spherical particles that account for wall interactions are necessary for proper closure. An accurate computation of the volume fraction near walls that accounts for the distribution of distances between particle surfaces is also needed to capture the correct physical behavior. When dealing with high Reynolds number flows, a standard eddy viscosity model does not properly account for turbulence modulation by particles, and significant physical processes might be compromised. Accounting for the exchange of angular momentum from the fluid phase, leading to lift forces that are otherwise neglected, is of interest as well. These shortcomings could be addressed by improved models developed using particle-resolved DNS data. With these considerations, the approaches described in this paper are shown to work well on a range of cases. A filter length scale was chosen such that microscale processes (eg. collisions and drag) were handled with well-accepted models from the literature and mesoscale features were resolved explicitly, allowing to properly capture important multiphase phenomenon including particle segregation and bubbling. However, this segregation in length scales limits the simulation strategy to $\mathcal{O}(10^8)$ Lagrangian particles, and more work is required for scale-up. Furthermore, the efficiency of the proposed methodology, in terms of accuracy versus computational expense, remains to be investigated and compared to that of existing approaches.

CHAPTER 3

EULERIAN-LAGRANGIAN MODELING OF TURBULENT LIQUID-SOLID SLURRIES IN HORIZONTAL PIPES

3.1 Abstract

Computations of liquid-solid slurries in horizontal pipes are performed to investigate the complex multiphase flow dynamics associated with operating conditions above and below the critical deposition velocity. A high-fidelity large-eddy simulation framework is combined with a Lagrangian particle tracking solver to account for polydisperse settling particles in a fully developed turbulent flow. The two phases are fully coupled via volume fraction and momentum exchange terms, and a two-step filtering process is employed to alleviate any dependence of the liquid-phase mesh size on the particle diameter, enabling the capture of a wide range of spatial turbulent scales. A fully conservative immersed boundary method is employed to account for the pipe geometry on a uniform Cartesian mesh. Two cases are simulated, each with a pipe geometry and particle size distribution matching an experimental study from Roco and Balakrishnam [99], which considers a mean volumetric solid concentration of 8.4%, corresponding to just over 16 million particles. The first case considers a Reynolds number based on the bulk flow of the liquid of 85,000, resulting in a heterogeneous suspension of particles throughout the pipe cross section. Statistics on the concentration and velocity of the particle phase for this case show excellent agreement with experimental results. The second case considers a lower Reynolds number of 42,660, leading to the formation of a stationary bed of particles. Three distinct regions are identified in the second case, corresponding to a rigid bed at the bottom of the pipe, a highly-collisional

shear flow just above the bed, and a dilute suspension of particles far from the bed. Computational results indicate segregation in particle size along the vertical direction, with the smallest particles located at the top, increasing monotonically until the bed surface, where the largest particles are located. The covariance of concentration and velocity of each phase is presented, giving further insight on the multiphase dynamics. Statistics on the individual mechanisms that contribute to the motion of each particle, namely forces due to drag, the pressure gradient and viscous stresses of the surrounding fluid, and collisions, are provided for each case. It is observed that for the majority of the pipe cross section, the drag force dominates for each case, which is balanced by inter-particle collisions in the streamwise direction, and by gravity in the vertical direction. Simulation results are also used to investigate closures from Reynolds average modeling of multiphase flows.

3.2 Introduction

Liquid-solid two phase flows, referred to as slurries, are common in many engineering and natural processes, and are often turbulent. Due to the relatively low operation and maintenance costs, slurry pipelines are typically used in chemical and mining industries for long distance transport of bulk materials such as oil sand ore, coal, copper, iron and phosphate concentrates, among others, to processing plants. The slurry consists of settling particles in a turbulent carrier fluid, where the solid material is usually polydisperse with a size distribution that can span several orders of magnitude. At very high flow rates the solid particles are nearly uniformly distributed across the pipe cross section due to the high level of turbulence. Reduction in the flow rate leads to a higher concentration of particles at the bottom of the pipe. As the velocity continues to decrease, the solid material

may form a dense sliding bed and eventually a stationary bed. The bulk slurry velocity associated with the onset of a stationary bed is referred to as the critical deposition velocity. The formation of a bed layer can be very hazardous, leading to wear and possible blockage of the pipeline. The frictional pressure loss is a key parameter in the design of slurry pipelines, as it provides information on the power required to maintain a flow rate above the critical deposition velocity. The solid velocity profile, slip velocity between the phases, solid concentration profile, and particle size distribution all impact the pressure drop in the pipe. However, the wide range of length and time scales associated with disperse multiphase flows makes estimations of these parameters extremely difficult.

Great effort has been made towards the development of predictive and reliable models for the pressure drop and solids concentration distribution in slurry pipelines. Durand and Condolios [100] were some of the first to develop empirical models for computing the hydraulic gradient, suggesting that the Froude number, specific gravity, concentration of particles, and particle drag coefficient are key parameters. Wasp et al. [101] improved their calculation by incorporating the effect of varying-size particles with the assumption that a wide particle size distribution leads to better suspension. Kaushal and Tomita [102] modified the Wasp et al. [101] model by alleviating some of its restrictive assumptions, showing good agreement with laboratory experiments. Wilson [103] used a force balance concept to develop a two-layer model where each layer has a uniform concentration and phase-averaged velocity, which was later improved by a three-layer model proposed by Doron et al. [104] by including a stationary bed at low flow rates. Among these, the Saskatchewan Research Council (SRC) two-layer model of Gillies et al. [105] is most commonly used in the literature for predicting the pressure drop in slurry pipelines. The SRC two-layer model predicts the pressure gradient and deposition

velocity as a function of the particle diameter, pipe diameter, particle concentration, and the mixture velocity based on experimental correlations.

The extensive variety of modeling approaches that exist tends to lead to significantly varying predictions of the critical parameters. Furthermore, the vast majority of these models predict slurry flows without deposition taking place, and are only valid well above the critical deposition velocity. However, it is not always practical to avoid the formation of a bed at the bottom of the pipe, and very limited data is available in the literature for flows in this regime, even though this regime is of great practical importance. Several experiments have shown that the critical deposition velocity remains fairly constant for a wide range of solid loading. Kaushal and Tomita [102] observed that the deposition velocity increases only by a very little amount as solid concentration increases. Schaan et al. [106] saw a similar trend in the flow of various granular material through a 105 mm diameter pipe, reporting that overall the deposition velocity is fairly constant over the range of solid concentrations from 5% to 45% by volume. Further modeling challenges include the lack of data on particle segregation of polydisperse slurries. Kumar et al. [107] show that the pressure drop and deposition velocity is greatly affected by the particle size distribution, though most of the experimental studies used to develop models for pressure drop considered monodisperse or narrow-size distributions. In addition, these models tend to provide information on macroscale features only, while local dynamics can affect pipeline operation significantly. Advancements in the understanding and prediction of detailed processes that contribute to pipeline wear, particle attrition, and agglomeration, is crucial.

With increasing computational resources and advancements in numerical modeling, computational fluid dynamics (CFD) is becoming a valuable tool for inves-

tigating slurry flows. CFD has the capability to generate detailed information of three-dimensional particle-laden flows under a wide range of operating conditions. However, directly solving the flow around each particle remains overly expensive for engineering systems of interest, which has led to the development of a large number of modeling approaches (see e.g. [19, 20, 22–24, 45]). In recent years, liquid-solid slurries have been mostly simulated using Eulerian-based models for the solid phase and Reynolds Averaged Navier-Stokes (RANS) approaches to model the turbulent nature of the carrier fluid. Ling et al. [108] proposed a simplified 3D algebraic slip mixture (ASM) model for the numerical computation of sand-water slurry flows. ASM was coupled with the renormalization group (RNG) $K-\varepsilon$ turbulence model to obtain a solution in fully developed turbulent flows [109]. They concluded that the model was capable of providing good predictions of the mean pressure gradient if the slurry mean velocity is higher than the critical deposition velocity, otherwise a big discrepancy existed between the numerical results and experimental data. Ekambara et al. [110] obtained CFD results of horizontal liquid-solid slurry pipelines using ANSYS-CFX based on the kinetic theory of granular flow. They conducted several simulations with a range of flow parameters and compared local and time-averaged particle concentration profiles, particle and liquid velocity profiles, and frictional pressure loss with experimental data, showing overall good agreement. Concentration profiles compared best with fine-particulate slurries, but simulations were unable to reproduce experimental data when near-wall lift forces took effect. Kaushal et al. [111] simulated pipeline slurry flows of monodisperse fine particles using a Eulerian two-phase model. Simulations were conducted for a range of concentrations and mixture velocities and gave fairly accurate predictions for both the pressure drop and concentration profiles. They presented velocity and slip-velocity distributions that had otherwise not been measured experimentally

at such high particle concentrations. Overall, Eulerian-based methods are capable of producing accurate velocity and particle concentration profiles provided they have been appropriately tuned, and they have the advantage of representing a large number of particles at relatively low computational cost. However, detailed microscale and mesoscale information of the flow is compromised, and an accurate description of the interactions between the interstitial fluid and solid phase is limited. In addition, higher order statistics of the critical flow parameters are out of reach in the context of RANS. In order to gain further insight on local processes and important mesoscale features of the flow, more detailed simulation approaches are required.

In this work, individual particle trajectories are solved in a Lagrangian fashion, while the fully-developed turbulent flow is solved on a background Eulerian mesh in a large-eddy simulation (LES) framework. The two phases are fully coupled via volume fraction and momentum exchange terms. A two-step filtering process is employed during interphase exchange, allowing for Eulerian grid spacing to particle diameter ratios close to unity, enabling the capture of important flow features at the particle scale. This simulation strategy has proven to be very successful for simulating dense gas-solid particulate flows [45], and is employed for liquid-solid flows in this work. In Sec. 3.4, simulations of three-dimensional polydisperse slurries in a horizontal pipe are presented. Two cases are considered, one operated above the critical deposition velocity, leading to a heterogeneous suspension of particles, and another below the critical deposition velocity, leading to a stationary bed. Results for the first case are compared with laboratory data from Roco and Balakrishnam [99]. A detailed investigation of both cases is then presented, providing mean and cross-correlation statistics of particle concentration, velocity, and slip velocity. Lagrangian statistics, including particle segregation and individual

forces acting on each particle, are analyzed and discussed. Finally, in Sec. 3.5 the simulation results are used to study closures from RANS modeling of turbulent multiphase flows.

3.3 Computational approach

Details on the equations used to describe the motion of particle trajectories suspended in a wall-bounded liquid flow and the corresponding numerical implementation can be found in Chapter 2. In addition to fluid drag, other contributions to the interphase exchange that may become relevant in the context of liquid-solid flows include the added mass term, Basset history term, lift, and Faxen forces. Zhang and Prosperetti [33] give an exact expression for the added mass term for an inviscid fluid at low particle concentrations. At higher values of concentration, they include a correction to account for the local volume fraction. They also derive an expression for the lift force for spherical particles in an inviscid fluid. A quite different expression is given by Saffman [80] for viscous flows at low Reynolds numbers. Kaushal and Tomita [112] studied the effect of near-wall lift forces in slurries using a γ-ray densitometer. They observed a decrease in lift with increased flow rate, and concluded that there is an absence of near-wall lift for finer particles while the near-wall lift related to coarser particles is not associated with the Magnus effect, the Saffman force, or other lift-like interaction forces. Although lift effects may have non-negligible contributions to the mean motion of the particles, a broad agreement on an appropriate model for this expression does not exist. Models for the lift coefficient found in the literature are typically valid for a single isolated particle, and become inaccurate for deposition near solid boundaries and high particle Reynolds numbers [113, 114]. As a consequence, such contributions

are not considered in this work. However, since we account for the volume filtered fluid pressure gradient force and viscous stress at the location of each particle explicitly, some of these effects are captured

3.3.1 Momentum forcing

To simulate a fully-developed turbulent flow, periodic boundary conditions are used in the streamwise direction. In order to maintain a constant mass flow rate in this periodic environment, momentum is forced using a uniform source term that is adjusted dynamically in Eq. 2.31. This source term exactly reflects the mean pressure gradient required to maintain the flow rate. At each timestep, momentum is lost via drag on the particles and viscous fluxes at the walls, which must be added back to the momentum equation. Volume integrating Eq. 2.31 and rearranging leads to

$$\boldsymbol{F}^{\mathrm{mfr}} = -\frac{1}{V_f}\int_{V_f}\left[\nabla\cdot(\boldsymbol{\tau}-\boldsymbol{\mathcal{R}}_u)+\varepsilon_f\rho_f\boldsymbol{g}-\boldsymbol{F}^{\mathrm{inter}}\right]dV_f, \tag{3.1}$$

where V_f is the volume occupied by the fluid. Note that the pressure gradient term vanishes due to the periodic boundary condition. The source term is applied to Eq. 2.31, and is added to the pressure gradient in the filtered stress tensor in Eq. 2.42.

3.3.2 Configuration and simulation parameters

The simulations conducted in this work are modeled after the experiments presented by Roco and Balakrishnam [99]. A 5.15 cm diameter pipe with a mean particle volume fraction of 8.4% is considered, illustrated in Fig. 3.1(a). The

slurry consists of sand with a mean diameter of 165 μm ranging from 50 to 307 μm, suspended in water. The particle size distribution in the simulation resembles that of the experiment, shown in the cumulative distribution function (CDF) in Fig. 3.1(b). Periodic boundary conditions are enforced in the x-direction. The pipe length was chosen to be as long as possible while remaining computationally tractable. With this consideration, an aspect ratio of 5 was chosen, corresponding to over 16 million particles and 18.7 million grid cells. A cell size approximately equal to the maximum particle diameter was chosen in order to best capture the range of spatial scales associated with the turbulent flow. The complete set of simulation parameters is given in Table 3.1.

Two cases are considered by keeping all parameters constant and varying only the liquid bulk velocity U_f. Case A has a bulk velocity of 1.6 m/s, resulting in a heterogeneous suspension of particles with a liquid Reynolds number $\mathrm{Re} = \rho_f U_f D/\mu = 85,000$. A slurry with a stationary bed is considered in case B, where the Reynolds number is decreased to 46,660, corresponding to $U_f = 0.83$ m/s, well below the critical deposition velocity of 1.2 m/s predicted by the model of Wasp et al. [101].

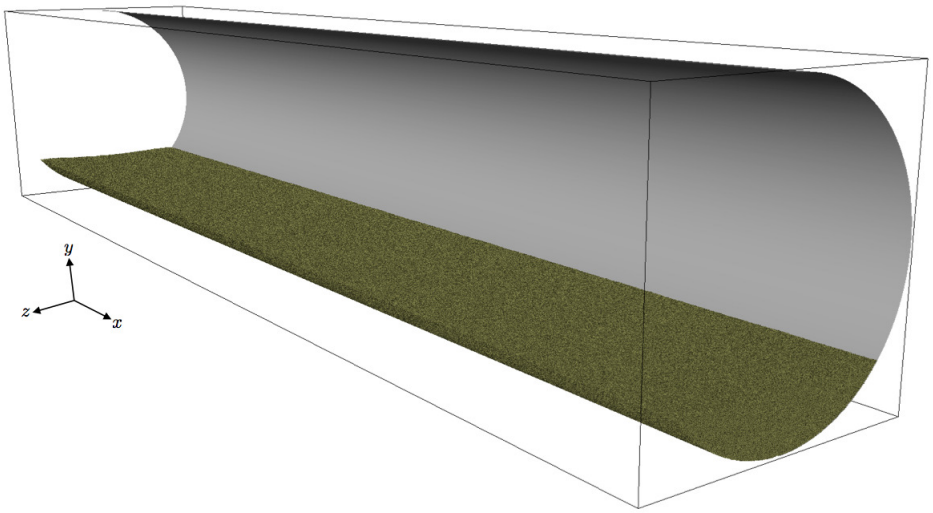

(a) Initial particle distribution and pipe geometry. 8.4% concentration of particles by volume, corresponding to 16 million particles.

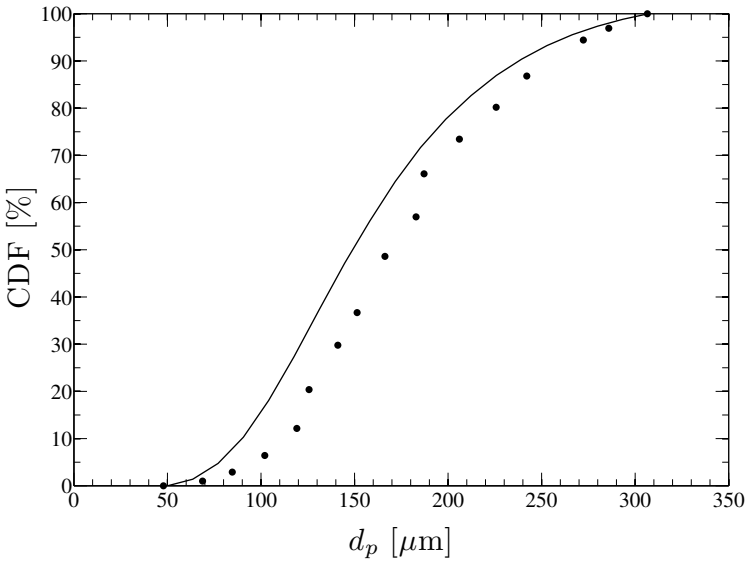

(b) CDF of particle diameter. Experimental data (circles), simulation data (line).

Figure 3.1: Simulation geometry and particle size distribution.

Pipe diameter, D	5.15	cm		
Pipe length	25.75	cm		
Cells in x-direction, nx	768	-		
Cells in y-direction, ny	156	-		
Cells in z-direction, nz	156	-		
Number of particles, N_p	16027332	-		
Mean particle concentration,	0.084	-		
Mean particle diameter	165	μm		
Minimum particle diameter	50	μm		
Maximum particle diameter	307	μm		
Particle standard deviation	70	μm		
Particle density, ρ_p	2650	kg/m^3		
Particle-particle coefficient of restitution	0.9	-		
Particle-wall coefficient of restitution	0.8	-		
Coefficient of friction	0.1	-		
Case	A		B	
Bulk liquid velocity, U_f	1.6	m/s	0.83	m/s
Stokes number, St	23.8	-	7.4	-
Timestep, Δt	4×10^{-6}	s	2×10^{-5}	s

Table 3.1: Simulation parameters for each case. $\mathrm{St} = \tau_p u_\tau^2 \rho_f / \mu$, where the frictional liquid velocity u_τ is computed using Prandtl's friction law for smooth pipes [115].

3.4 Results

3.4.1 Flow characterization

In both simulations, the flow organizes into distinct regions controlled by the dynamics of the flow. To help guide the analysis and discussion of the computational results, these distinct layers are depicted by the thin gray lines in the subsequent figures. Three flow regions are easily identified in case B, denoted throughout as region I, II, and III. Region I corresponds to the rigid bed located at the bottom of the pipe, up to $y/D = -0.405$. The particles in the bed are densely packed and

undergo sustained contact, and as a result do not contribute to the mean motion of the flow. Located just above the bed, region II extends up to ε_p approximately equal to 0.25, which corresponds to $y/D = -0.328$, and consists of highly collisional particles and high liquid turbulence intensity. In this region, particles can be lifted from the bed by strong turbulent eddies or ejected by other particles colliding with the bed. Finally, region III is located far from the bed such that the mean particle concentration is considerably smaller and the particles remain suspended due to liquid velocity fluctuations.

The distinction between the flow regions in case A is less obvious. In this case, there is no formation of a bed at the bottom of the pipe, and instead the flow is divided into regions II and III only. The transition between these regions was chosen to correspond to a concentration similar to the transition between regions II and III in case B. To avoid overly confusing figures, the transition between regions II and III corresponds to the location of the interface separating regions I and II in case B at $y/D = -0.405$.

3.4.2 Comparison with experiments

Experimental results of the local, time-averaged particle concentration, particle velocity distribution, and frictional pressure drop are available for case A only. For each case, simulations were run long enough to reach a statistically stationary state. Results were collected after approximately $\tau = 50$, where $\tau = tU_f/D$ is the non-dimensional time. The mean quantities of interest, denoted by the brackets, were obtained by averaging in the x-direction, in time over approximately 70 non-dimensional time units, and by symmetry about the $z = 0$ plane. Most results are presented as a function of vertical distance for $z = 0$, denoted throughout as the

central vertical axis or vertical centerline, or as a function of z for $y = 0$, denoted as the horizontal centerline. Simulation and experimental results of the particle concentration and velocity profiles along the vertical centerline of the pipe are presented in Fig. 3.2. The distributions are asymmetric, with larger concentrations and lower velocities observed in the bottom half of the central vertical axis due to particle settling. While excellent agreement with the experiment is obtained, a slight over-prediction of particle concentration is observed in region II at the bottom of the pipe. This discrepancy may be attributed to the near-wall modeling challenges discussed in the work by Capecelatro and Desjardins [45], or a result of neglecting lift forces in Eq. 2.42.

Figures 3.3 and 3.4 show contours of particle concentration and velocity in the cross section of the pipe, respectively. Again, excellent agreement is observed with the experiment. From Fig. 3.3, it seen that the concentration in the lower third of the central vertical axis is approximately 10 times the concentration at the top third. In Fig. 3.4, a steeper gradient in particle velocity is observed at the top of the pipe compared to the bottom.

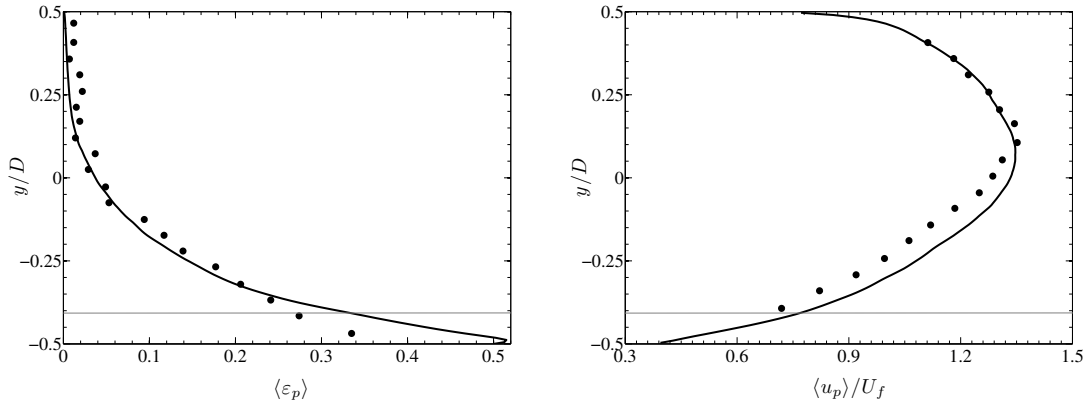

(a) Solid concentration profile.

(b) Solid velocity profile normalized by the bulk fluid velocity.

Figure 3.2: Mean statistics along the central vertical axis of the pipe for case A. Experimental data [99] (circles), simulation results (thick solid line), boundary separating regions II and III (thin solid line).

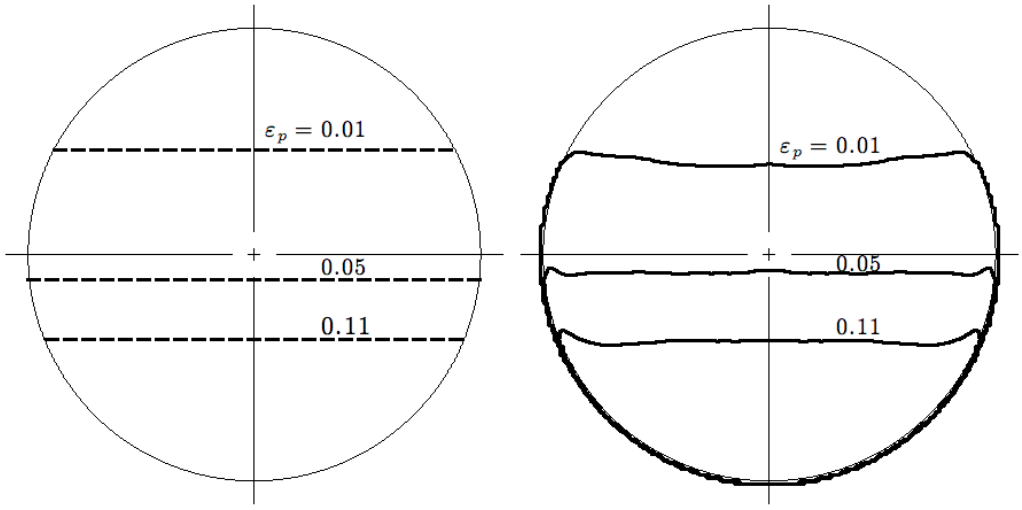

(a) Experimental data [99].

(b) Simulation results.

Figure 3.3: Particle concentration distribution in the pipe cross section for case A.

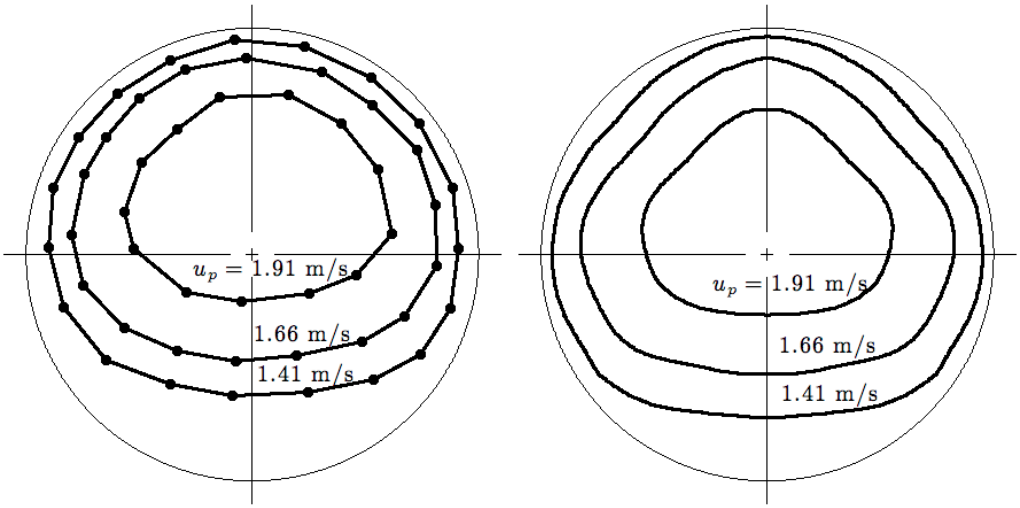

(a) Experimental data [99]. (b) Simulation results.

Figure 3.4: Particle velocity distribution in the pipe cross section for case A.

Finally, the reported experimental pressure drop for this case is -666.3 Pa/m. The pressure drop determined using Eq. 3.1 was found to be -510 Pa/m. This discrepancy is attributed to errors in the calculation of the viscous flux at the IB surface and inaccuracies in the near-wall modeling in the context of LES.

3.4.3 Operating below the critical deposition velocity

Slurry pipelines operated below the critical deposition velocity can severely degrade performance and lead to blockage and equipment failure. At low flow rates, the liquid shear stress cannot overcome the submerged weight of the particles, allowing particles to settle and form a stationary bed. Case B was simulated with a bulk velocity of 0.83 m/s, well below the critical deposition velocity of 1.2 m/s predicted by the model of Wasp et al. [101] for the parameters given in Table 1. Figures 3.5(a) and 3.5(b) show the mean particle concentration and velocity profiles for that case

along the central vertical axis of the pipe. Note that due to polydispersity, the random-close-packing limit for hard spheres, $\varepsilon_{p,\max} = 0.634$, is exceeded. The liquid velocity profiles for both cases are not shown due to the similarities with the particle phase, and instead the relative velocity between the two phases will be provided in Sec. 3.4.5. The solid concentration profile in Fig. 3.5(a) shows that the particles are almost entirely located in the bottom half of the pipe. The solid concentration is nearly constant in region I and decreases rapidly in region II. As seen in Fig. 3.5(b), the particle velocity is very small in region I, and increases rapidly in region II. Above the bed, the solid velocity profile in case B resembles the profile of case A in Fig. 3.2(b).

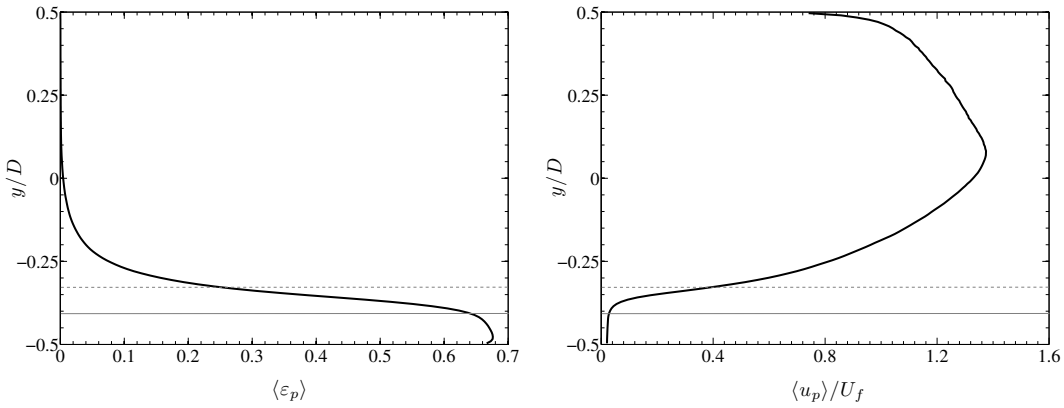

(a) Solid concentration profile.

(b) Solid velocity profile.

Figure 3.5: Mean statistics along the central vertical axis of the pipe for case B. Transition between regions I and II (gray solid line), transition between regions II and III (gray dotted line).

The degree of particle accumulation can be quantified by the probability density function (PDF) of particle number density [116], which is equivalent to the PDF of particle concentration. For a random distribution of particles, in the absence of any processes leading to segregation (e.g., particle settling due to gravitation effects or turbophoresis as a result of turbulence in the carrier phase), a discrete

Poisson distribution is expected, defined as

$$f_p(n_c) = \frac{e^{-\langle n_c \rangle}}{n_c!} \langle n_c \rangle^{n_c}, \tag{3.2}$$

where n_c is the number of particles per computational cell and $\langle n_c \rangle$ is the average number of particles per computational cell. The Poisson distribution is computed by considering particles with a diameter of 165 μm, i.e. the mean diameter of the distribution used in the simulations. The PDF of particle concentration for each case along with the discrete Poisson distribution is given in Fig. 3.6. As can be expected from the large variation in particle concentration observed in Figs. 3.2(a) and 3.5(a), both cases show a higher frequency of regions containing more particles, as well as regions devoid of particles, in comparison to the Poisson distribution. These traits are more pronounced for case B than for case A, and in fact for that case the distribution is bi-modal, reflecting the large number of particles around the close-packing limit that constitute the bed.

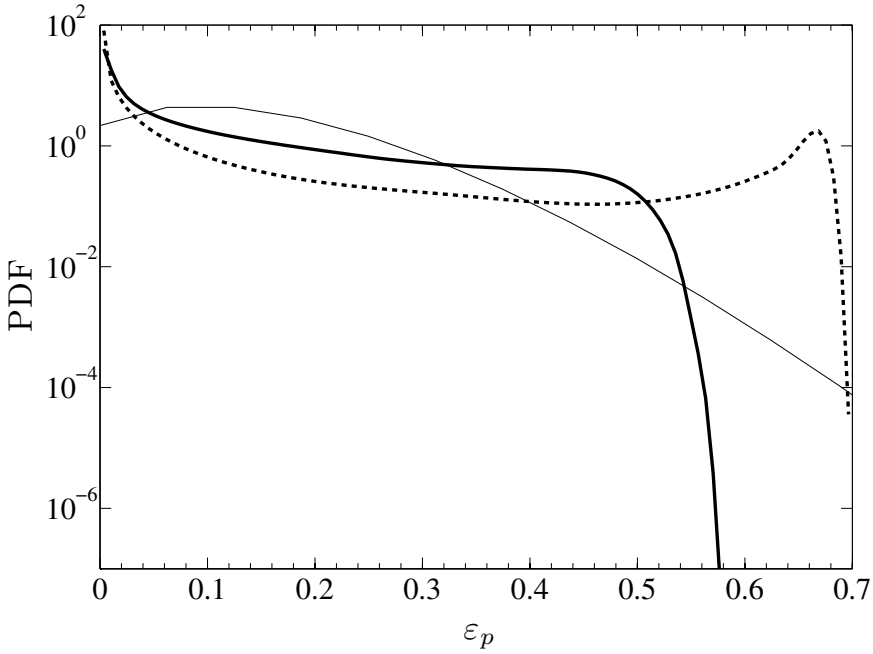

Figure 3.6: PDF of particle concentration. Case A (thick solid line), case B (dashed line), Poisson distribution (thin solid line).

The joint-PDFs of Re_p and ε_p for both cases are displayed in Fig. 3.7. The joint-PDF was computed using the Reynolds number of each particle and the volume fraction interpolated to the position of the respective particle. Several differences can be observed between each case. Due to the presence of the bed, case B shows a very high frequency of low Re_p particles near the close packing limit, while a somewhat wider range of Re_p values is reached for particles in low ε_p regions. In comparison, case A displays much larger values of Re_p that correspond to a wide range of ε_p.

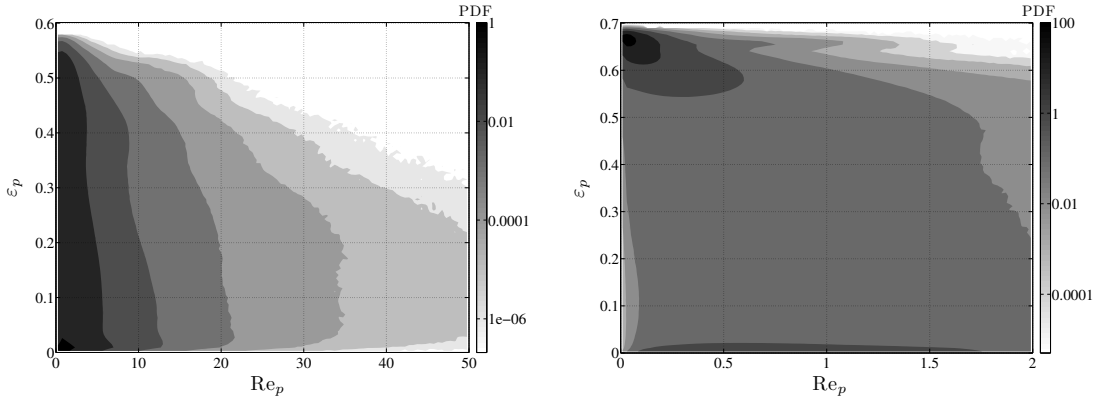

(a) Case A. (b) Case B.

Figure 3.7: Joint-PDF of particle Reynolds number and concentration.

3.4.4 Higher order statistics

Higher order statistics are extracted from both simulations in order to gain further insight on the multiphase dynamics. The particle concentration variance is displayed in Fig. 3.8. For case B, the greatest concentration fluctuations are located at the interface between region II and region III. In region III, the fluctuations decay rapidly to very small values due to the dilute nature of the flow in that layer. The bed region, region I, exhibits no variance in concentration, indicative of

particles remaining in rigid contact. In comparison, concentration fluctuations in case A are non-negligible at the bottom of the pipe, confirming that a stationary bed has not formed. Similarly to case B, the volume fraction variance for case A peaks near the bottom of region III, albeit at a lower value than case B. These fluctuations in case A remain noticeable throughout the majority of the pipe.

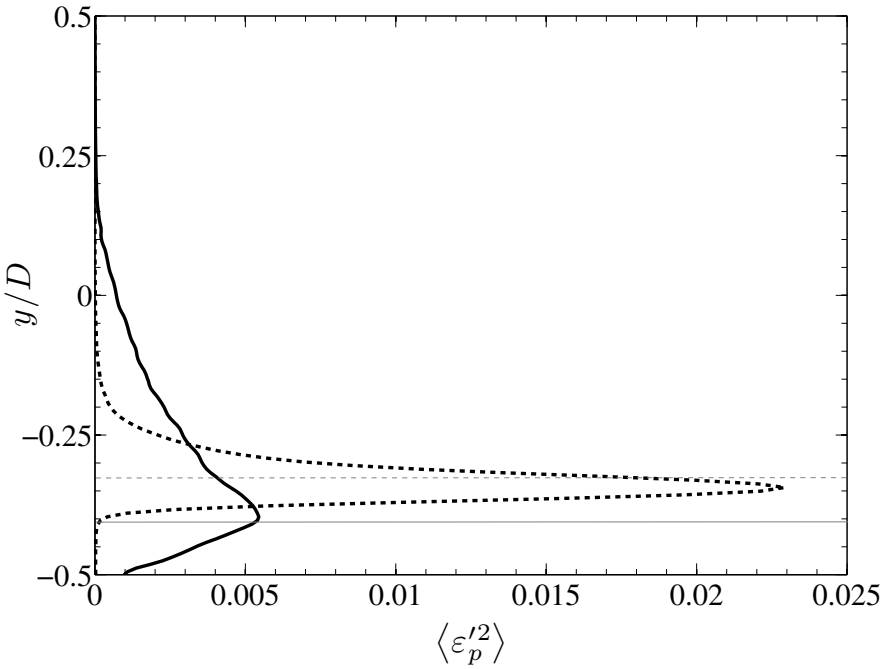

Figure 3.8: Particle concentration variance profile along the central vertical axis of the pipe. Case A (thick solid line), case B (dashed line). The thin gray line separates regions II and III in case A and regions I and II in case B. The gray dotted line separates region II and III in case B.

The components of the Reynolds stress tensor for both phases are displayed in Fig. 3.9. It can be noted that the particles have nearly the same fluctuation intensity as the liquid phase. For both cases, the greatest velocity fluctuations are located near the interface between region II and III, and at the top of the pipe. At the pipe center, turbulence production is minimum since the mean velocity gradient and shear stress are smallest, leading to small velocity fluctuations. In

both simulations, $\langle u'_p v'_p \rangle$ and $\langle u'_f v'_f \rangle$ are negative in the bottom half of the central vertical axis and positive in the upper half, while the other components of the Reynolds stress tensor are positive throughout. The signs of the Reynolds stresses correspond to classical single phase wall-bounded turbulent flows [115]. Figures 3.9(c) and 3.9(d) reveal distinct trends of the velocity covariance profiles within the three regions of case B. In region I, the velocity covariance is negligibly small. In region II, the covariance magnitudes increase due to the nature of the highly collisional shear flow. In region III, the mean shear in the fluid decreases, leading to a decrease in the velocity covariance until contributions in shear from the upper wall in the pipe become significant. The behavior of the velocity covariance profiles along the vertical axis of case A resembles the trends seen in case B above the rigid bed.

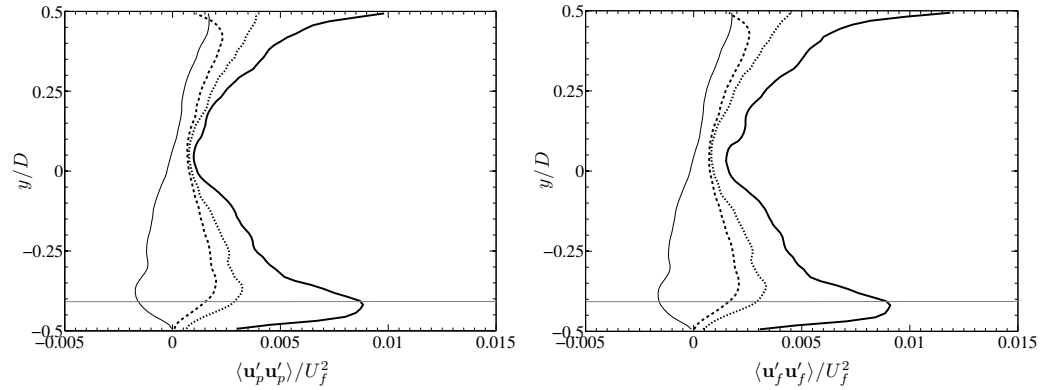

(a) Particle velocity covariance (case A). (b) Fluid velocity covariance (case A).

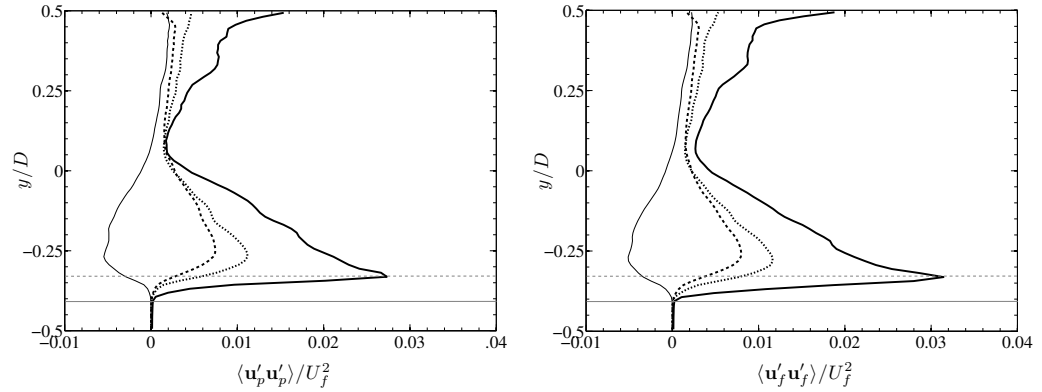

(c) Particle velocity covariance (case B). (d) Fluid velocity covariance (case B).

Figure 3.9: Velocity covariance profiles normalized by the bulk fluid velocity along the central vertical axis of the pipe. $\langle u'u' \rangle$ (thick solid line), $\langle v'v' \rangle$ (dashed line), $\langle w'w' \rangle$ (dotted line), $\langle u'v' \rangle$ (thin solid line). The thin gray line separates regions II and III in case A and regions I and II in case B. The gray dotted line separates region II and III in case B.

Profiles of the covariance between concentration and velocity of each phase along the vertical axis of the pipe are displayed in Fig. 3.10. Again, note the similarities between particle and liquid statistics. From Figs. 3.10(c) and 3.10(d), distinct trends are observed in the three regions in case B. The fluctuation magnitudes are smallest in the bed, increase within region II, and decrease in region III. Due to the small concentration of particles in the upper half of the central vertical axis, $\langle \varepsilon_p' \boldsymbol{u}_p' \rangle$ and $\langle \varepsilon_p' \boldsymbol{u}_f' \rangle$ are negligible in this region compared to the fluctuations

in the lower half, though $\langle \varepsilon'_p w'_p \rangle$ and $\langle \varepsilon'_p w'_f \rangle$ are uncorrelated throughout the entire vertical axis due to the symmetry of the flow. The positive correlation of particle concentration and vertical velocity in region II and the lower half of region III reveals the tendency for local regions of high concentration to move upward, suggesting that groups of particles are drawn up from the bed surface into the more dilute regions. Since they originate from the surface of the stationary bed, these groups tend to move slower than the surrounding mixture in the streamwise direction, leading to a negative $\langle \varepsilon'_p u'_p \rangle$. To be compatible with a positive $\langle \varepsilon'_p v'_p \rangle$, it is expected that particles fall back down to the bed surface in more dilute arrangements. This behavior may be attributed to the presence of Kelvin-Helmholtz-type instabilities in region II, due to the high shear in mixture velocity and steep gradient in concentration. Figure 3.11 confirms that longitudinal waves are visible in the instantaneous particle concentration field.

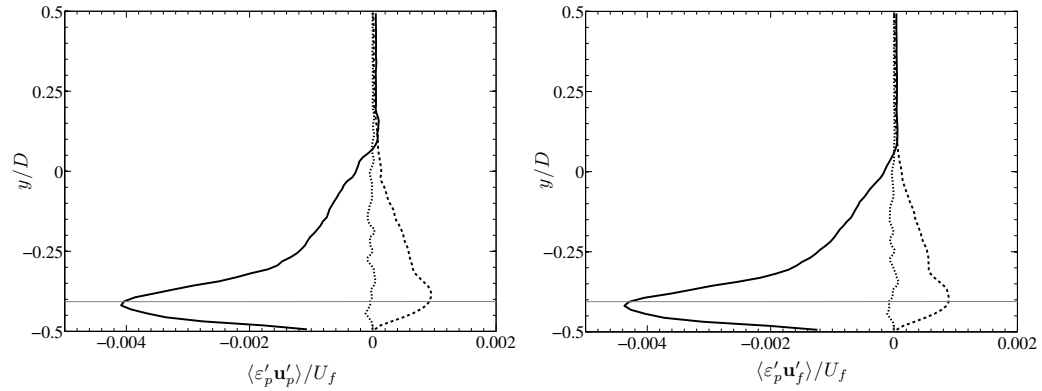

(a) Particle concentration-particle velocity covariance (case A).

(b) Particle concentration-fluid velocity covariance (case A).

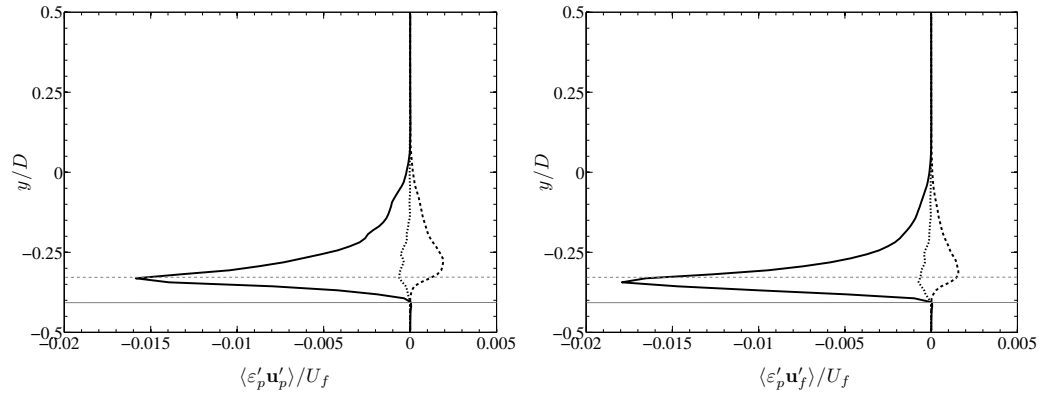

(c) Particle concentration-particle velocity covariance (case B).

(d) Particle concentration-fluid velocity covariance (case B).

Figure 3.10: Particle concentration-velocity covariance profiles normalized by the bulk fluid velocity along the central vertical axis of the pipe. $\langle \varepsilon_p' u' \rangle$ (thick solid line), $\langle \varepsilon_p' v' \rangle$ (dashed line), $\langle \varepsilon_p' w' \rangle$ (dotted line). The thin gray line separates regions II and III in case A and regions I and II in case B. The gray dotted line separates region II and III in case B.

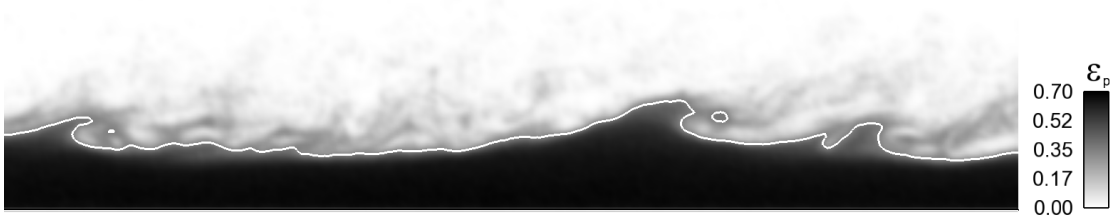

Figure 3.11: Instantaneous snapshot of particle concentration in the $z = 0$ plane of case B. Iso-contour of $\varepsilon_p = 0.35$ given by the white line.

3.4.5 Slip velocity

The slip velocity, $\boldsymbol{u}_s = \boldsymbol{u}_f - \boldsymbol{u}_p$, is a critical parameter for understanding the behavior of slurry flows. For example, drag and lift forces strongly depend on $\boldsymbol{u}_s$, and knowledge of the relative velocities between phases can provide insight on deposition. Vertical and horizontal profiles of the mean and variance of the streamwise slip velocities along the pipe center are given in Fig. 3.12. Except for regions near the wall, the mean slip velocity magnitudes for both cases are relatively small, with maximum values approximately 0.05% of their respective bulk velocities. As seen in Fig. 3.12(c), the mean slip velocity distribution is symmetric along the horizontal centerline, with negative values near the pipe wall. Particles located near the walls maintain their inertia while viscous effects reduce the liquid momentum, which explains these negative slip velocities. Symmetry is also observed in the slip velocity variance given in Fig. 3.12(d), with maximum fluctuations near the pipe wall. However, it is evident from Figs. 3.12(a) and 3.12(b) that the slip velocity

is asymmetric along the vertical centerline. It can be seen that except for the near-wall regions, the particle velocity lags behind the liquid velocity in both cases along the vertical axis. In case B, the slip velocity at the bottom of the pipe is negligible due to the presence of the bed. However, with the absence of a bed in case A, shear induced by the carrier phase leads to non-negligible particle contact forces in the streamwise direction, including normal collisions via Eq. 2.59 and Coloumb friction from Eq. 2.66, reducing the particle motion resulting in a zone of strong positive slip. Profiles of the forces exerted on the particles contributing to this behavior will be given in Sec. 3.4.6. This peak in slip velocity corresponds to the location of maximum solid concentration displayed in Fig. 3.2(a). At the very bottom of the pipe, a negative slip velocity is recovered due to the fact that liquid does not slip while particles do. Fluctuations of the slip velocity along the vertical axis of the pipe are shown in Fig. 3.12(b). In case A, $\langle u_s'^2 \rangle$ is fairly constant in the bottom portion of the pipe, and decreases at the pipe center. In case B, $\langle u_s'^2 \rangle$ is very small within the bed, increases in region II, and decreases in region III until near-wall effects at the top of the pipe become significant. From Fig. 3.9, the smallest slip velocity fluctuations correspond to the smallest velocity fluctuations.

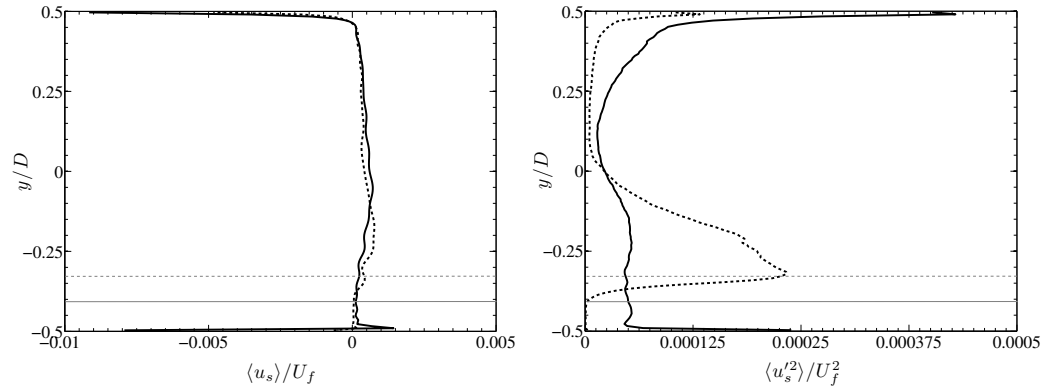

(a) Mean slip velocity along vertical centerline.

(b) Slip velocity variance along vertical centerline.

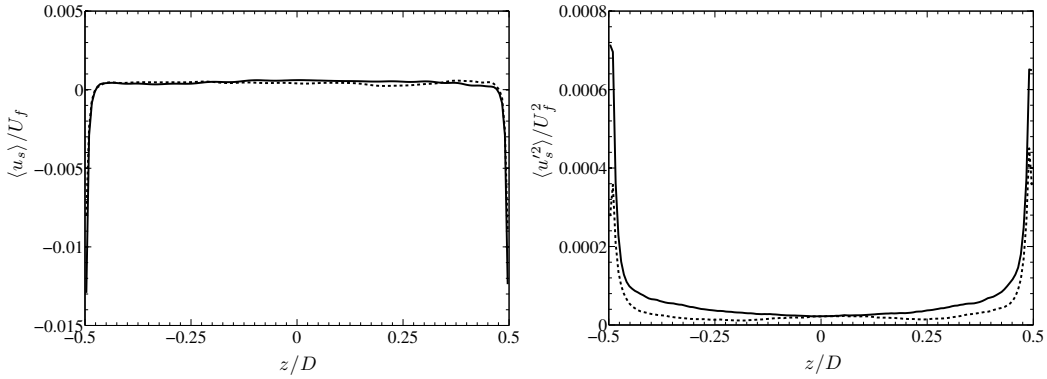

(c) Mean slip velocity along horizontal centerline.

(d) Slip velocity variance along horizontal centerline.

Figure 3.12: Streamwise slip velocity statistics for case A (thick solid line) and case B (dashed line) normalized by the bulk streamwise velocity. The thin gray line separates regions II and III in case A and regions I and II in case B. The gray dotted line separates region II and III in case B.

3.4.6 Force balance

To gain further insight on the phenomenological behavior of both cases, the individual forces exerted on the particles are analyzed. In Figs. 3.13(a) and 3.13(c), components of the streamwise particle acceleration are given along the vertical centerline. This includes the fluid drag given by Eq. 2.44, the volume-filtered pres-

sure gradient, the volume-filtered viscous stress, and the collision force given by Eqs. 2.59 and 2.66. In case B, the competing interactions between these various forces can be distinguished between the three regions of the flow. In region I, drag is balanced by inter-particle collisions, leading to negligible streamwise acceleration. In region III, collisions are negligible and the fluid drag and pressure gradient forces dominate. A complex transition between both regions is observed in region II, with effects from inter-particle collisions, turbulence, and high shear velocities. These trends are not as clear in case A, which might be due in part to the transition from region II to III interacting with near-wall dynamics. In region II, the drag and collision forces dominate in the streamwise direction. In region III, the drag force dominates, although the pressure gradient and collision force remain significant.

The components of the vertical particle acceleration are displayed in Figs. 3.13(b) and 3.13(d). At the bottom of the pipe, the drag force, pressure gradient, and collisions are balanced by gravity. In case B, the vertical drag force is negligible within the bed, and inter-particle collisions and the force due to the pressure gradient are approximately constant. In region II, the drag force increases rapidly and the collision force decreases until drag dominates in region III. Interestingly, the vertical force balance in regions I and II correspond the onset of fluidization observed in dense particle beds [32]. This behavior confirms that the vertical dynamics in region I correspond to a rigid bed, region III is drag dominated and the dynamics approach that of a dilute flow, and region II is a complex transition where all forces contribute to the mean motion of the particles. In case A, the vertical collision force is positive in region II and negative in the lower half of region III. The fluid pressure gradient and gravity have the greatest contributions to the motion of the particles in this region. In region III, the fluid pressure gra-

dient decreases and drag rapidly dominates, as was observed for case B. In both cases, the force due to the filtered viscous stress has minimum effect on the motion of each particle.

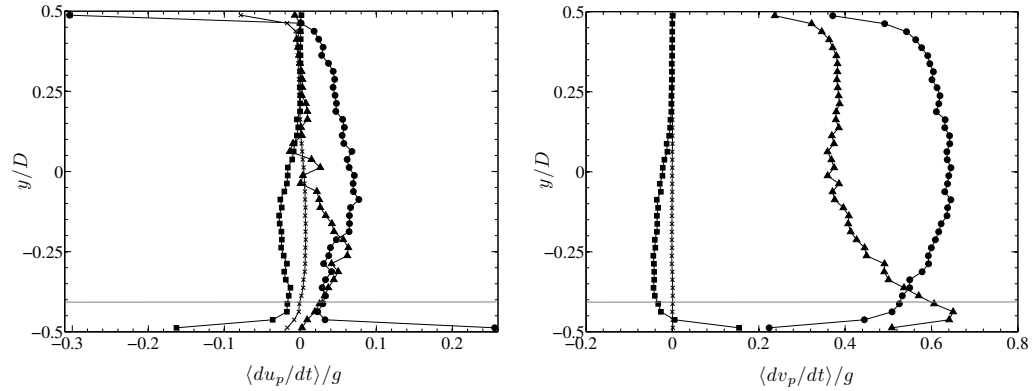

(a) Streamwise particle acceleration for case A.

(b) Vertical particle acceleration for case A.

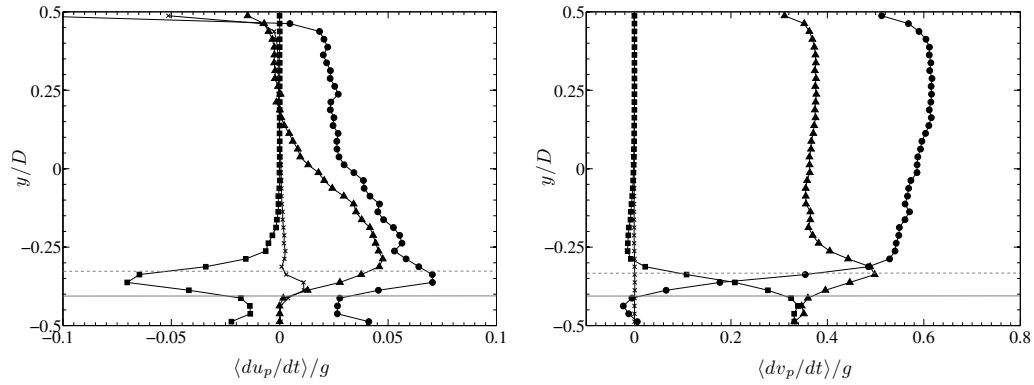

(c) Streamwise particle acceleration for case B.

(d) Vertical particle acceleration for case B.

Figure 3.13: Contributing forces to particle acceleration normalized by gravity. Drag as given by Eq. 2.44 (circles), volume-filtered pressure gradient (triangles), volume-filtered viscous stress (crosses), collisions given by Eqs. 2.59 and 2.66 (squares). The thin gray line separates regions II and III in case A and regions I and II in case B. The gray dotted line separates region II and III in case B.

3.4.7 Particle segregation

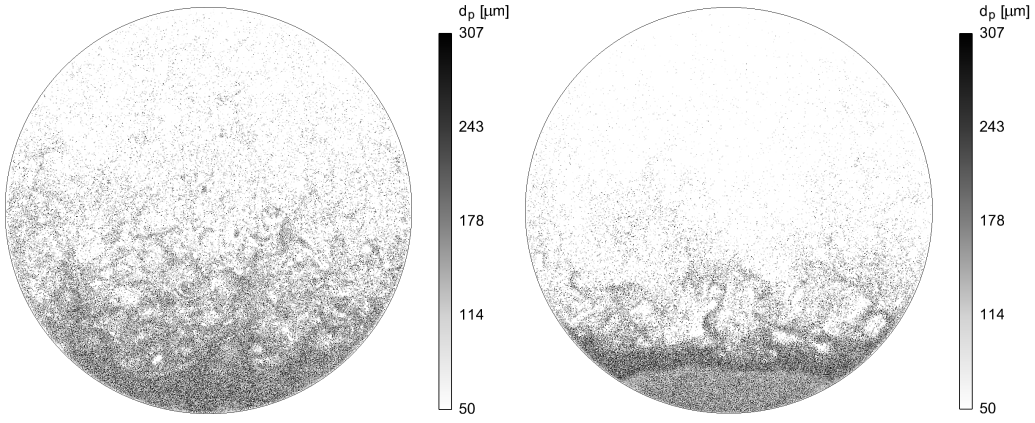

(a) Case A. (b) Case B.

Figure 3.14: Instantaneous snapshot of particle position in an x-plane colored by particle diameter.

The particle size distribution can significantly impact the dynamics of liquid-solid slurries. For example, increasing the particle size will lead to an increase in the Coulomb friction force, resulting in an increase in pressure gradient and slip velocity. Larger particles will also lead to a larger gravitational force, which will enhance the settling rate and steepen the concentration gradient in the vertical direction. Kumar et al. [107] measured the pressure drop and concentration distribution of particles for two materials mixed in different proportions to analyze this effect. It was found that in general, a slurry with a mixture of fine and coarse particles requires less energy for transportation. Interestingly, it was determined that the energy required to transport an optimally distributed mixture of particles is less than that required for a fine slurry. However, due to the strong coupling with the carrier phase turbulence and fluctuations in particle concentration, predictive modeling of particle segregation is particularly challenging.

Instantaneous snapshots of the particle position in a cross-sectional slice of the pipe are given in Fig. 3.14. A vertical gradient in particle diameter is observed in case A, with smaller particles at the top of the pipe and the largest at the bottom. In contrast, a layer of large particles is observed above the dense bed in case B. The mean particle diameter conditioned on the vertical height in the pipe is given in Fig. 3.15(a), providing further detail on the particle segregation. Note that particle size averages are based on number density and not volume. The particle size is seen to decrease monotonically in the vertical direction in case A, except at the very bottom. Interestingly, in case B the slope reverses in region II where the particle size is shown to increase with height. It is postulated that particles are entrained by strong vortical structures directly above the surface of the bed, and the finest particles are ejected while the coarsest particles are too heavy and remain suspended in this region, unable to penetrate the dense bed in region I. To investigate the mechanisms responsible for this behavior, the distribution of vertical forces acting on each particle was computed for a range of particle sizes. The acceleration due to drag and the fluid pressure gradient is given in Fig. 3.16. Note that converging the results for the largest particles at the top of the pipe is challenging due to the small sample size, and are therefore not provided in all figures. As seen in Figs. 3.16(b) and 3.16(d), the motion of each particle due to the fluid pressure gradient is not significantly affected by its diameter. However, from Figs. 3.16(a) and 3.16(c), the vertical component of the acceleration due to drag is shown to be greatly affected by the particle size. In case B, the smallest particles experience the greatest vertical acceleration at the boundary between regions II and III. This behavior suggests that smaller particles are more likely to be ejected vertically than larger particles in this region.

Fluctuations in particle diameter are given in Fig. 3.15(b). The greatest fluc-

tuations are seen to correspond to the largest particles. In both simulations, the maximum fluctuation in particle size is located at the boundary between regions II and III, and the slope reverses below this boundary. In region I of case B, the particle diameter fluctuations are fairly constant. The PDF of particle diameter in each region of case B is given in Fig. 3.17. The PDFs of particle size in regions I and II resemble the PDF along the entire vertical centerline of the pipe, due to the majority of the particles being located in these two regions. Particles located in region III have a narrower PDF, with much fewer large particles and more small particles. Clearly, the width of the PDF is seen to correspond to the magnitude of particle size fluctuations, where the lower regions of the pipe contain a greater variety of particle sizes and thus larger fluctuations compared to the upper region.

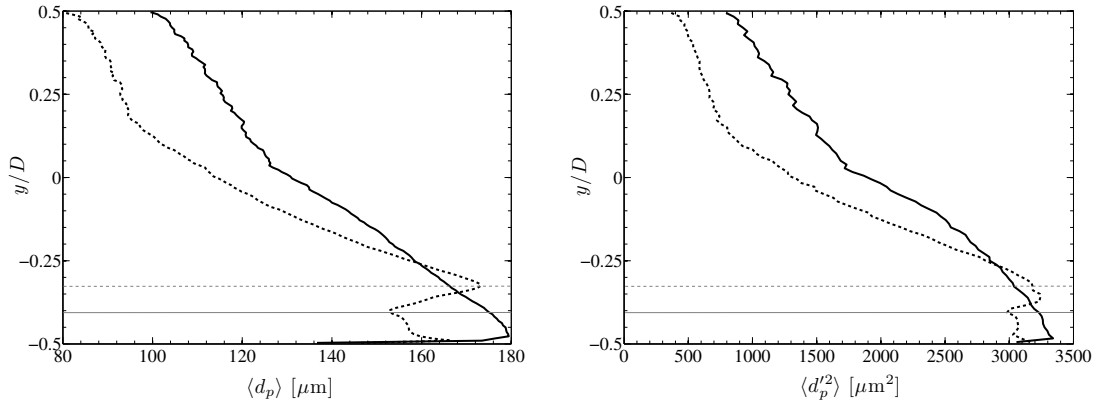

(a) Mean particle size.

(b) Particle size variance.

Figure 3.15: Particle segregation along pipe centerline for case A (solid line) and case B (dashed line). The thin gray line separates regions II and III in case A and regions I and II in case B. The gray dotted line separates region II and III in case B.

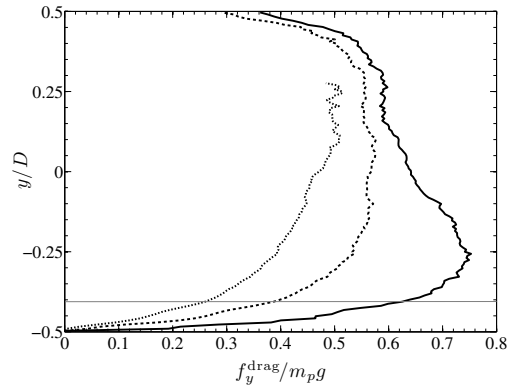

(a) Vertical component of the drag force in case A.

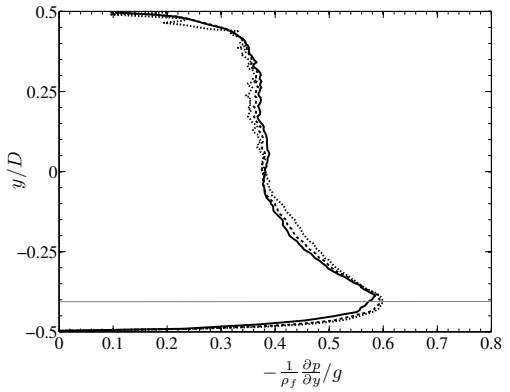

(b) Vertical component of the pressure gradient force in case A.

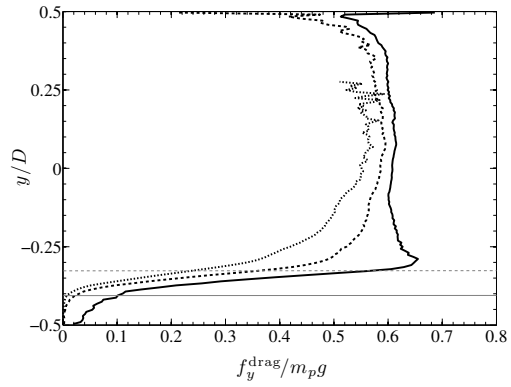

(c) Vertical component of the drag force in case B.

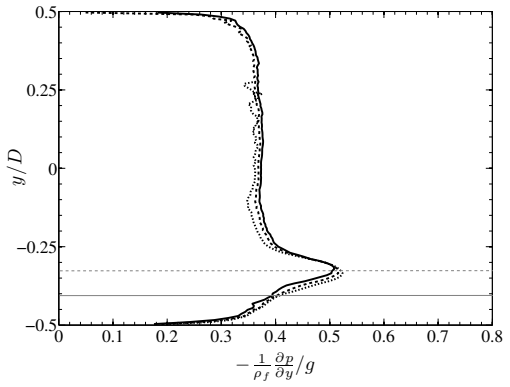

(d) Vertical component of the pressure gradient force in case B.

Figure 3.16: Contributing forces to particle vertical acceleration for different sized particles, normalized by gravity. 50 μm $\leq d_p <$ 136μm (thick solid line), 136 μm $\leq d_p <$ 221 μm (dashed line), 221 μm $\leq d_p <$ 307 μm (dotted line). The thin gray line separates regions II and III in case A and regions I and II in case B. The gray dotted line separates region II and III in case B.

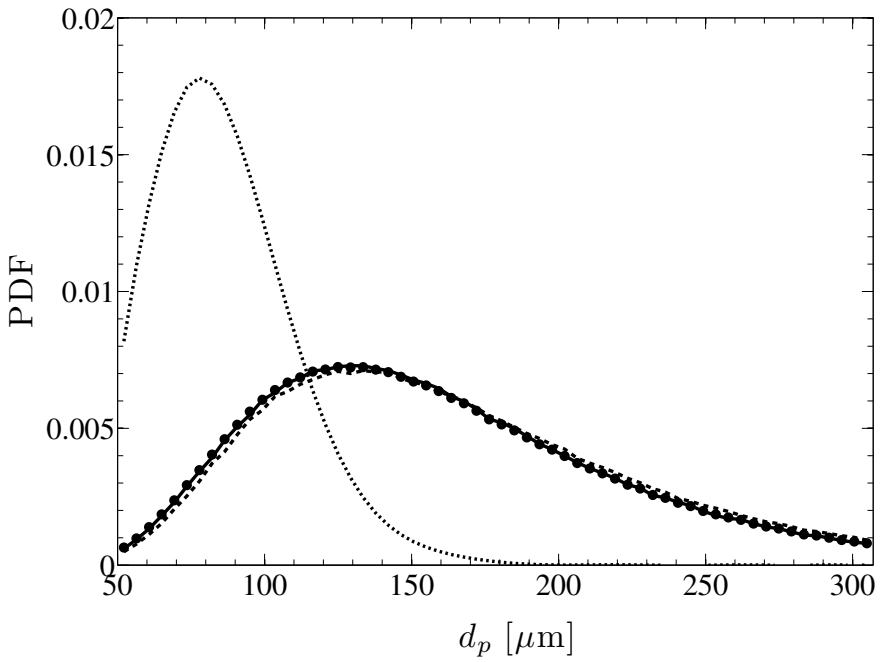

Figure 3.17: PDF of particle diameter along the vertical centerline of the pipe in case B. $-0.5 \leq y_p/D < -0.405$ corresponding to particles within region I (solid line), $-0.405 \leq y_p/D < -0.328$ corresponding to particles within region II (dashed line), $-0.328 \leq y_p/D < 0.5$ corresponding to particles in region III (dotted line), and $-0.5 \leq y_p/D < 0.5$ corresponding to all of the particles along the vertical centerline (circles).

3.5 Investigating turbulence closures

In the literature, Reynolds-averaged modeling of the kinetic theory of granular flows [117] is commonly used for the computation of turbulent slurries (e.g., [108, 110, 111, 118]). A recent study by Fox [47] derived a consistent framework for investigating RANS of particle-laden turbulence. In the study, it is pointed out that closure models for the fluid phase equations can be taken from turbulence models used for variable-density turbulence, and closure models developed for compressible turbulence can be used to close the particle-phase terms. However, the coupling

terms that involve Reynolds-averaging with respect to both the particle and the fluid properties require further investigation. The simulation results in Sec. 3.4.4 can provide useful insight on the relative importance of some of these closures and the validity of existing models.

The covariance of concentration and fluid velocity, referred to as the drift velocity, appears in the Reynolds-averaged fluid-phase transport equations. This term is usually treated as a turbulent flux [119], and simplifies to

$$\langle \varepsilon_p' \boldsymbol{u}_f' \rangle = -\frac{\mu_t}{\rho_f \mathrm{Sc}_t} \nabla \langle \varepsilon_p \rangle, \tag{3.3}$$

where Sc_t is a turbulent Schmidt number that varies with the Stokes number. In a statistically homogeneous flow where the concentration gradient vanishes, this model becomes insufficient, and the following model was proposed for homogeneous directions by Fox [47]:

$$\langle \varepsilon_p' \boldsymbol{u}_f' \rangle = C_g \langle \varepsilon_p \rangle \langle \varepsilon_f \rangle \left(\langle \boldsymbol{u}_p \rangle - \langle \boldsymbol{u}_f \rangle \right), \tag{3.4}$$

where C_g is a model constant that depends on the particle Reynolds number. Equations 3.3 and 3.4 are plotted against simulation results in Figs. 3.18 and 3.19, respectively, where μ_t was computed from the turbulent-viscosity hypothesis [115]

$$\langle u_f v_f \rangle = -\frac{1}{\rho_f} \mu_t \frac{\partial \langle u_f \rangle}{\partial y}. \tag{3.5}$$

The vertical component of the drift velocity is shown in Fig. 3.18. In both cases, $\mathrm{Sc}_t = 1.3$ was determined from the simulations, showing very good agreement between the model and the simulation data. In Fig. 3.19, the model given in Eq. 3.4 is plotted against the simulation results for the streamwise component of the drift velocity. Due to periodicity, the first term on the right-hand side of Eq. 3.4 vanishes, and $\langle \varepsilon_p' v_f' \rangle$ is shown to be a function of the mean concentration and the difference between the mean velocity of each phase. It was found that an

optimal model constant is $C_g = 2.4$ for case A, and $C_g = 1.5$ for case B. With these constants, the model proposed by Fox [47] is shown to give excellent agreement with the results in this work.

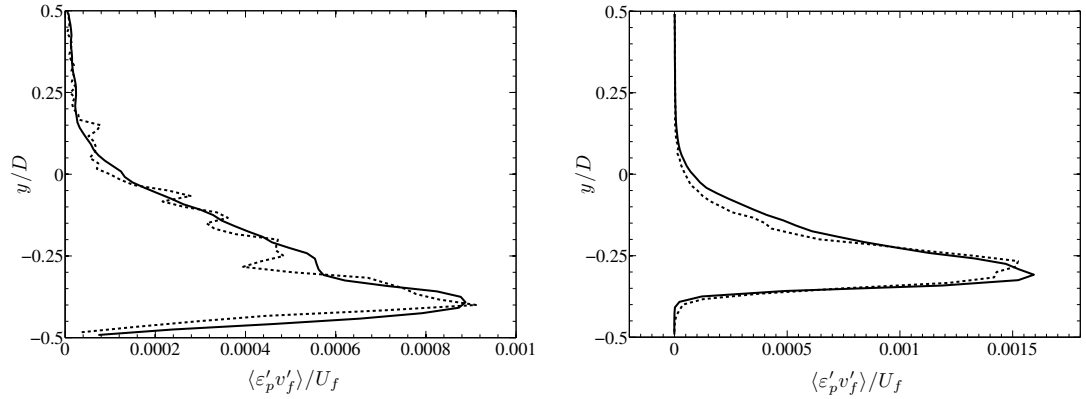

(a) Case A. (b) Case B.

Figure 3.18: Vertical component of the drift velocity normalized by the bulk fluid velocity. Simulation results (solid line), model given by Eq. 3.3 (dashed-line), using $\mathrm{Sc}_t = 1.3$.

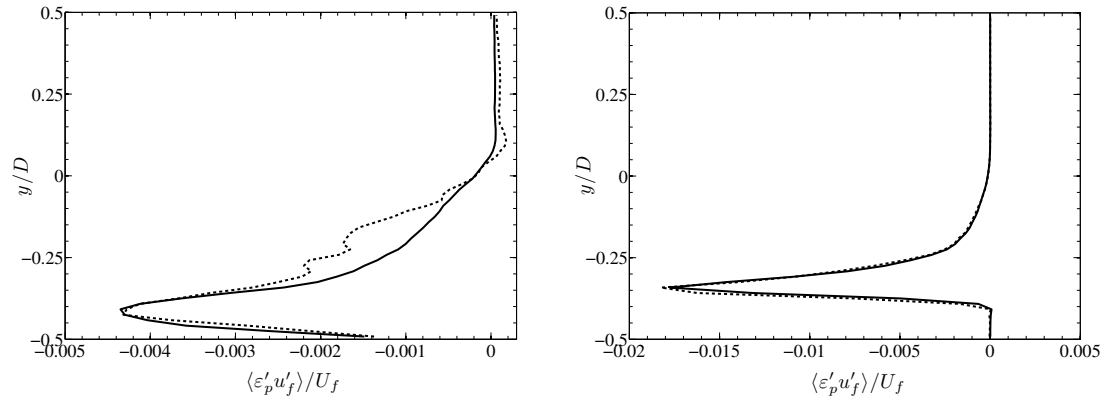

(a) Case A ($C_g = 2.4$). (b) Case B ($C_g = 1.5$).

Figure 3.19: Streamwise component of the drift velocity normalized by the bulk fluid velocity. Simulation results (solid line), model given by Eq. 3.4 (dashed-line).

The covariance of volume fraction and fluid pressure gradient appears in the Reynolds-averaged transport equation for the particle velocity [47], and contributes

to the mean acceleration of particles due to the fluid. This term represents the fluctuations that contribute to the mean buoyancy force and is often assumed to be negligible. Figure 3.20 shows the covariance of volume fraction and fluid pressure gradient normalized by gravity along the vertical axis of the pipe. It is evident that this term contributes little to the particle motion in comparison to the gravitational force, and the assumption to neglect this term in the context of RANS modeling of slurries appears appropriate.

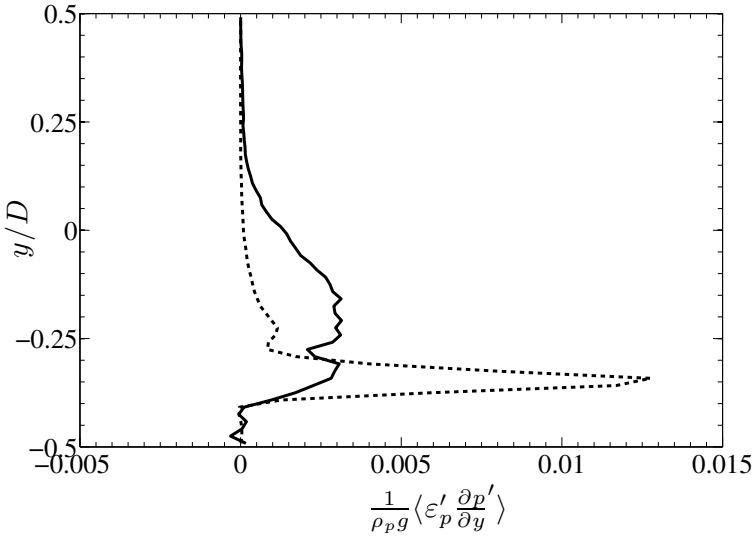

Figure 3.20: Normalized covariance of volume fraction and fluid pressure gradient. Case A (solid line), case B (dashed-line).

3.6 Conclusions

A high-fidelity, large-eddy simulation framework was coupled with a dense Lagrangian particle tracking solver to investigate horizontal slurry pipe flows operated above and below the critical deposition velocity. The background fluid mesh size was approximately equal to the maximum particle diameter in order to best capture the range of relevant length scales associated with the flow.

Mean particle concentration and velocity profiles were computed, showing excellent agreement with laboratory data. Statistics were extracted for both cases, providing correlations between particle concentration and the velocities of each phase that had otherwise not been investigated in the context of slurries. Three distinct regions were identified in the flow operated below the critical deposition velocity, corresponding to a rigid bed, a highly-collisional shear flow, and a freely-suspended particle flow. The maximum fluctuations in concentration, liquid and particle velocities, and particle diameter were located in the region just above the surface of the bed. In this region, a positive correlation between particle concentration and the vertical velocity of each phase was observed, indicating the tendency for particles to be drawn up from the bed with a greater local concentration than when they fall back to the bed. The statistics presented for the case operated above the critical deposition velocity resemble the lower Reynolds number case shifted by the height of the bed.

Profiles of the particle diameter along the vertical centerline of the pipe reveal a strong segregation in particle size, with the smallest particles located at the top of the pipe and the largest towards the bottom. Interestingly, the slurry operated below the critical deposition velocity showed the largest particles to be located just above the surface of the bed. Profiles of the fluid drag and pressure gradient exerted on each particle indicate that the smallest particles in this region experience greater vertical accelerations, leading to a suspension of the largest particles. Throughout the pipe cross section, it was observed that the largest contribution to the motion of each particle comes from the drag force, which is opposed by collisions in the streamwise direction and gravity in the vertical direction.

The level of detail provided by the simulations presents a unique opportunity

to investigate some of the closures that appear in a recent derivation by Fox [47] of the exact Reynolds-averaged kinetic theory equations for multiphase flows. The gradient-diffusion model for the vertical drift velocity compared very well with simulation results when setting the turbulent Schmidt number to $\mathrm{Sc}_t = 1.3$. The Reynolds number-dependent modeling constant used in a recently proposed model for homogeneous gravity-driven flows [47] was determined for each case, showing excellent agreement with the streamwise drift velocity predicted by the simulations. It was also found that the covariance of fluid pressure gradient and vertical fluid velocity can be neglected in both cases and therefore might often be negligible when modeling turbulent slurries.

CHAPTER 4

NUMERICAL CHARACTERIZATION AND MODELING OF PARTICLE CLUSTERING IN WALL-BOUNDED VERTICAL RISERS

4.1 Abstract

This paper aims at investigating the capability of numerical models to accurately capture the physical characteristics of particle clustering in vertical risers. Within the energy sector, particle clustering in vertical risers of circulating fluidized bed reactors are known to play a key role in the multiphase dynamics as well as secondary processes such as catalytic conversion and heat transfer. Recent experiments suggest that particle clustering is most significant in the fully developed flow region of the riser, hence this study focuses on this region. To explore such flows, a high-fidelity large-eddy simulation framework is combined with a Lagrangian particle tracking solver to simulate statistically stationary gravity-driven risers in vertical pipes for a large range of Archimedes numbers. The walls of the reactor are modeled using a conservative immersed boundary scheme integrated with the Lagrangian particle tracking framework. A structure tracking algorithm akin to particle image velocimetry is used to accumulate statistics on individual clusters. Cluster descent velocities display excellent agreement with experimental measurements for the range of flow conditions considered. Predicted volume fraction fluctuations and mean solid concentration within the clusters also match experimental correlations. The probability distribution function of solid concentration and radial distribution function provide insight on the degree of clustering and the characteristic cluster length scale. The degree of particle clustering is found to be

independent of the Archimedes number, and models for the volume fraction distribution are discussed. Statistics on the solid concentration and phase velocities for two- and three-dimensional configurations are compared, and the ramifications of simulating risers in two dimensions are discussed.

4.2 Introduction

Particle-laden flows in vertical pipes play a crucial role in many industrial processes. Within the energy sector, such flows are used in fluidized bed reactors due to their low pressure drops, uniform temperature distribution, and high efficiency in mixing. Since the 1970s, circulating fluidized bed (CFB) reactors have been used in a range of technical processes, including fluid catalytic cracking (FCC) [120, 121], gasification and combustion of coal [122–124], and more recently thermochemical conversion of biomass [125, 126]. CFB reactors were developed to improve the performance of traditional fluidized beds by using higher flow rates to move the bed material resulting in a significant increase in the contact efficiency between the phases. This increased kinetic energy within risers of CFB reactors causes the flow to become unsteady with large particle concentration fluctuations. Local regions of densely packed particles, referred to as clusters, develop in the flow and tend to fall at the walls of the riser, while dilute suspensions of particles rise in the central region. Sustained volume fraction and velocity fluctuations caused by the clusters result in the production of fluid-phase turbulent kinetic energy, which then exists even in the absence of mean shear [47]. Meanwhile, under specific conditions, clusters have been observed to reduce mixing and interaction of particles with the transport gas [127], and therefore may inhibit reaction rates and heat transfer in industrial units, potentially lowering operating efficiencies

significantly. Without the ability to predict and optimize reactor performance, large-scale commercialization of these systems remains severely restricted.

Because the solid phase is opaque and highly unsteady, experimental studies on particle clustering in risers have proven to be an arduous task. Nonetheless, many correlations of cluster characteristics have been derived from experimental data. Noymer and Glicksman [11] compiled numerous measurements of cluster fall velocities from within the literature, observing that although the flow conditions vary significantly, as well as the reactor geometries and particle parameters, the measured velocities were typically close to 1.0 m/s. Previous investigations on risers indicate that clusters tend to fall within 100 μm of the wall [12], placing them within the hydrodynamic boundary layer. Additionally, particles tend to reduce the gas-phase velocity gradients [13], implying that clusters falling near the walls are generally unaffected by the superficial gas velocity. Noymer and Glicksman [11] developed a model to match the observed trends for the measured cluster fall velocities, given by

$$u_{cl} = 0.75\sqrt{\frac{\rho_p}{\rho_f} g d_p}, \tag{4.1}$$

where ρ_p and ρ_f are the particle and fluid densities, respectively, g is the gravitational acceleration, and d_p is the particle diameter. Note that the cluster velocity u_{cl} is independent of the gas-phase viscosity and mass flow rate. Recent studies by Chew *et al.* [14–17] used a fiber optic probe and high-speed video camera to characterize clustering of monodisperse and polydisperse particles in a riser of a pilot-scale CFB. It was found that the riser axial position greatly influences the radial profiles of cluster duration and frequency, but has negligible effect on cluster appearance probability. The particle size distribution and particle properties were shown to have comparatively minor effects on cluster characteristics. Two recent studies [1, 18] used high-speed video and wavelet decomposition analysis of

backscattered optical data to show that clusters were much more prevalent in the fully developed flow region of the riser. It was concluded that a better understanding of particle clustering and their interactions with the gas phase is clearly needed to improve existing models found in the literature.

With increasing computational resources and advancements in numerical methods, many researchers have turned to computational fluid dynamics (CFD) to gain further insight on particle clustering in risers. There exists a spectrum of modeling approaches for simulating coupled fluid-particle flows, each with its own advantages and disadvantages. In recent years, particle-resolved direct numerical simulations (PR-DNS) of three-dimensional gas-solid flows with $\mathcal{O}(10^4)$ particles have become feasible. A recent review article on PR-DNS development can be found in [128]. To the best of the authors' knowledge, state-of-the-art PR-DNS is currently unable to resolve the necessary length scales required in simulating freely-evolving clusters in risers due to excessive computational cost. However, recent efforts have focused on model development for lower cost simulation techniques. For example, Xu and Subramaniam [129] performed PR-DNS of a turbulent flow past uniform and clustered configurations of fixed particle assemblies using a discrete-time, direct-forcing, immersed boundary method. The fluid-phase turbulence was found to be significantly anisotropic due to the fluid-particle interaction, and the level of turbulent kinetic energy in the fluid phase was always found to be greater in the clustered case compared to the uniform particle configuration. Another recent study [130] conducted lattice Boltzmann simulations of a single fixed cluster under a wide range of volume fractions and particle Reynolds numbers. The PR-DNS results revealed that particles arranged in a cluster configuration exhibited considerably lower drag than randomly arranged particles under the same flow conditions, with more significant reduction at lower particle Reynolds numbers.

In order to investigate realistic riser configurations in a tractable manner, Eulerian-Eulerian (EE) and Eulerian-Lagrangian (EL) methods have been used in numerous studies within the literature with various levels of success. EE representations solve the gas phase and solid particles on a common Eulerian grid, greatly reducing the computational cost as individual particles do not need to be tracked. In the limit where the flow is highly collisional and assumed to be nearly at equilibrium, the particle density function is close to Maxwellian and a Chapman-Enskog expansion can be used to derive a two-fluid model (TFM) using ensemble or volume averaging [32–34]. TFM has been used in a large number of studies to simulate two-dimensional (e.g., [53–57, 131, 132]) and three-dimensional (e.g., [6, 133–135]) risers. Most of this work extracts mean profiles of the hydrodynamic variables, typically the solid volume fraction, pressure drop, and velocity of each phase. Chalermsinsuwan et al. [136] compared particle cluster diameter and concentration in risers using two-dimensional TFM. The calculated values were comparable to empirical correlations. Agrawal *et al.* [6] demonstrated that global statistics were strongly dependent on the mesh size but became mesh-independent when mesh size was of the order of a few particle diameters. Furthermore, it was shown that clusters are not properly captured unless sufficient resolution is applied. Ozel *et al.* [133] employed TFM in a recent work at various resolutions to obtain mesh-independent results in periodic CFB risers. It was shown that various sub-grid terms have to be modeled in order to account for the unresolved clusters.

EL strategies provide an alternative framework that typically relies on simpler closures compared to EE, where individual particle trajectories are solved using Newton's laws of motion, and models are required for interphase exchange and particle collisions. Particle clustering in two-dimensional risers using the EL method can be found in a large number of studies from previous years (e.g., [61, 137–141]).

In these studies, large-eddy simulation (LES) is often used to solve the gas-phase turbulence, and particle collisions are typically modeled stochastically by means of the direct simulation Monte Carlo (DSMC) method. Liu and Lu [141] used a DSMC-EL approach to study cluster dynamics in a two-dimensional riser. A cluster identification method was used to obtain the solid concentration and velocities of individual clusters. In order to compare their results with experimental data, the computed two-dimensional voidage used in the drag calculation was modeled as three-dimensional using the correction described in [142]. Mean cluster descent velocities as a function of mean solid concentration showed reasonable agreement with experimental correlations. The mean solid concentration of near wall clusters was shown to increase with the increase of cross-sectional averaged solid concentration. The simulated results, however, consistently under-predicted the experimental findings. In a response to this study by Liu and Lu [141], Berrouk and Wu [143] discussed the severe shortcomings of the phase coupling scheme used in the context of two-dimensional EL methods. It was shown that schemes to correct the two-dimensional void fraction under-predict the momentum source term, which results in a much lower prediction of the pressure drop and erroneous prediction of the minimum fluidization velocity. It was concluded that since the pressure gradient force plays a crucial role in the two-phase dynamics, two-dimensional EL methods may systematically provide an inaccurate analysis of the gas-particle flow behavior in the CFB riser. Due to the computational cost of EL methods, three-dimensional simulations of CFB risers are much less common in the literature. Vreman *et al.* [144] performed LES of two-way and four-way coupled gas-solid flows in a three-dimensional vertical channel. Mean and root-mean-square (RMS) velocity profiles were computed, revealing a strong modulation of the gas-phase turbulence due to the presence of a large number of interacting particles. It was

found that the coupling between the particles and fluid is mainly responsible for the reduction in the thickness of the boundary layer and a strong increase in the skin-friction compared to an unladen channel.

In this work, the EL approach is used to simulate statistically stationary three-dimensional gas-solid flows in vertical pipes. Inelastic particle collisions are accounted for explicitly. Special care is given when exchanging data between the phases to allow for mesh size to particle diameter ratios close to unity, enabling finer meshes for capturing fluid turbulence. A conservative immersed boundary method based on cut-cells is employed in order to model the reactor geometry on a Cartesian mesh [145]. This simulation strategy has been validated against several laboratory-scale experiments of dense particle flows [45,46], and is extended to moderately-dilute particle flows in this work. Section 4.3 presents the simulation parameters and results are discussed in Sec. 4.4. Velocity profiles for each phase and volume fraction statistics are compared for a large range of Archimedes numbers. A numerical algorithm akin to particle image velocimetry [97,146] is used to identify individual clusters and track them in time. Cluster characteristics, including descent velocities and local concentration fluctuations are computed and compared to results from experimental data. The degree of particle clustering is measured by computing the probability distribution function (PDF) of solid concentration and radial distribution function. Models for the PDF are proposed. This paper concludes with a discussion on two-dimensional simulations of CFB risers, describing numerical and physical issues associated with restricting the dimensionality of moderately-dilute four-way coupled flows.

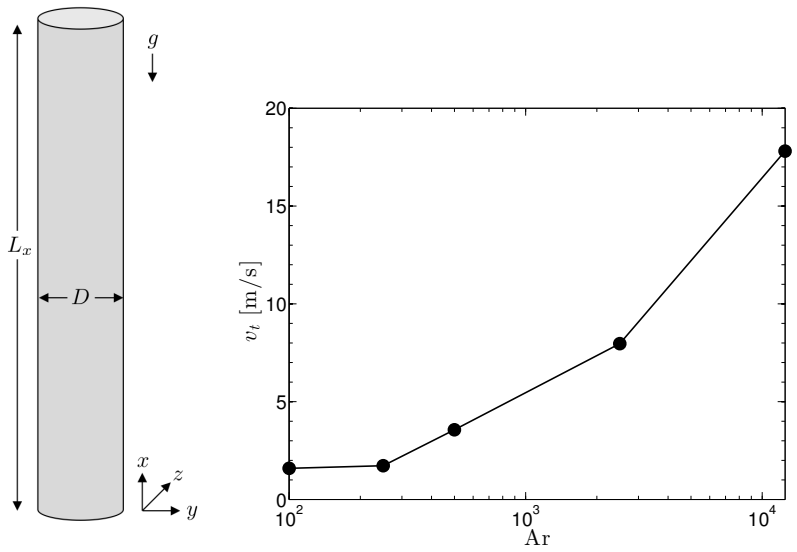

(a) Schematic of the computational domain. (b) Terminal velocity as a function of Ar for the cases provided in Table 2.

Figure 4.1: Simulation configuration.

4.3 Configuration and simulation parameters

Moderately dilute flows of rigid spherical particles in vertical pipes are considered in this work. The particles are inelastic with a coefficient of restitution $e = 0.9$ and coefficient of friction $\mu_f = 0.1$, initially uniformly distributed on a Cartesian lattice with a mean concentration $\langle \varepsilon_p \rangle$. In this work, angled brackets denote an average in space and time. Periodic boundary conditions are enforced in the streamwise direction and the momentum source term $\boldsymbol{F}^{\text{mfr}}$ is adjusted dynamically in Eq. 2.31 to prevent the development of a net mass flow rate in the gas phase that results from momentum coupling with particles settling under gravity. A sketch of the computational domain is given in Fig. 4.1(a). The pipe has an aspect ratio of 10, with a grid size $800 \times 82 \times 82$, corresponding to $\Delta x \approx 1.8 d_p$. The parameters of the computational domain are displayed in Table 1. The analysis presented by Noymer and Glicksman [11] suggests that the terminal velocity of a cluster, when

Parameter	Units	Value
L_x	m	0.5
D	m	0.05
Cells in x-direction	-	800
Cells in y-direction	-	82
Cells in z-direction	-	82
Timestep	µs	10
g	$\mathrm{m{\cdot}s^{-2}}$	9.81

Table 4.1: Parameters used in the numerical simulations.

non-dimensionalized by the minimum fluidization velocity of the particles, depends only on the Archimedes number, defined as

$$\mathrm{Ar} = \frac{(\rho_p - \rho_f)\,\rho_f d_p^3 g}{\mu^2}. \tag{4.2}$$

From Eq. 5.6, the correlation for the cluster fall velocity normalized by the minimum fluidization velocity of the particles is given by

$$\frac{u_{cl}}{u_{mf}} = \frac{1000}{\sqrt{\mathrm{Ar}}}, \tag{4.3}$$

where u_{mf} was derived by Grace [147] as

$$u_{mf} = 0.00075\frac{\rho_p d_p^2 g}{\mu}. \tag{4.4}$$

Other critical dimensionless parameters of the flow include the mean volumetric concentration of particles $\langle\varepsilon_p\rangle$, the pipe diameter to particle diameter ratio D/d_p, and the density ratio ρ_p/ρ_f. A list of parameters for the simulations conducted in this work is shown in Table 2. These parameters represent conditions commonly found in CFB reactors. In each case, Ar is varied by varying the gas-phase viscosity while keeping all other parameters constant. As a consequence of modifying the viscosity, the particle response time τ_p, and thus the terminal velocity $v_t = \tau_p g$, increases with Ar. Figure 4.1(b) shows the dependence of the terminal velocity on Ar for the cases given in Table 2. Note that except for Ar250, each case

Name	Ar	D/d_p	$\langle\varepsilon_p\rangle$	ρ_p/ρ_f	N_p
Ar100	100	150	0.015	2500	728232
Ar250	250	320	0.0015	2500	730275
Ar500	500	150	0.015	2500	728232
Ar2500	2500	150	0.015	2500	728232
Ar12500	12500	150	0.015	2500	728232

Table 4.2: Simulation cases and the corresponding non-dimensional parameters.

has identical properties except for the Archimedes number. Ar250 considers a larger pipe diameter to particle diameter ratio by keeping the number of particle approximately equal and reducing the particle diameter, thus reducing $\langle\varepsilon_p\rangle$.

4.4 Results and discussion

4.4.1 Riser statistics

In order to perform a quantitative analysis on particle clustering, a systematic criterion for identifying clusters must be established. Due to the shallow gradient of volume fraction around individual clusters, isolating coherent structures in the flow can be challenging. Soong et al. [148] proposed three criteria for identifying clusters. (1) The solid fraction in a cluster must be significantly above the time-averaged solid fraction at the given local position. (2) The perturbation in solid fraction caused by the cluster must be greater than the random fluctuations in the background of solid fraction variations. (3) This concentration perturbation should be sampled from a volume with a characteristic length scale greater than one or two orders of particle diameter. With these guidelines in consideration, Sharma *et al.* [149] proposed that the local instantaneous solid volume fraction for a cluster must be greater than the time-mean solid fraction by at least two times

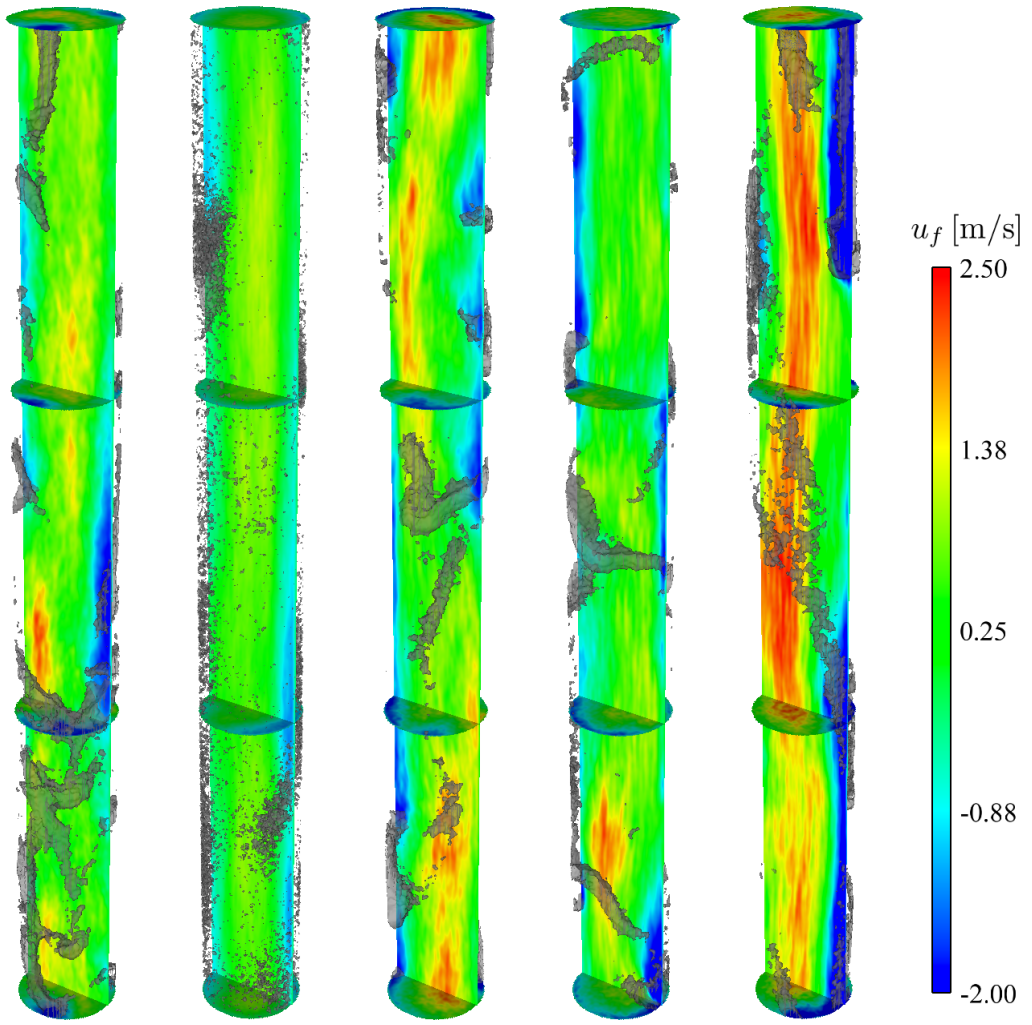

(a) Ar100 (b) Ar250 (c) Ar500 (d) Ar2500 (e) Ar12500

Figure 4.2: Instantaneous snapshots at steady state of the simulations described in Table 4.2. Iso-surface of $\varepsilon_p = \varepsilon_{p,\text{crit}}$ (gray), color represents vertical fluid velocity.

the standard deviation. We adopt this criterion in this work, such that

$$\varepsilon_{p,\text{crit}} = \langle \varepsilon_p \rangle + 2\sqrt{\langle \varepsilon_p'^2 \rangle}, \tag{4.5}$$

where $\varepsilon_p' = \varepsilon_p - \langle \varepsilon_p \rangle$ is the fluctuation in particle volume fraction.

For each case, results are gathered after the initial transient is complete and the flow reaches a statistically stationary state. Instantaneous snapshots of the cases

summarized in Table 2 are shown in Fig. 4.2. Clusters are visualized by iso-surfaces of $\varepsilon_p = \varepsilon_{p,\text{crit}}$, with $\varepsilon_{p,\text{crit}}$ being computed separately for each respective case. It can be seen that clusters entrain the fluid as they fall at the walls, resulting in upward gas jets in the center of the riser. This is consistent with recent experimental observations of a CFB riser with FCC catalyst particles [18]. Besides Ar250, which has a mean volume fraction an order of magnitude smaller than the other cases, the level of clustering in each flow does not appear to be significantly affected by the range of Ar. In order to gain further insight on the flow behavior, statistics are computed along the radial profile of the riser. As shown in Fig. 4.3(a), the average solid concentration in the near-wall region is more than twice as large than in the center of the riser. Fluctuations in solid volume fraction along the radius of the pipe are given in Fig. 4.3(b), showing the greatest variation at the wall. Interestingly, although Ar varies by more than two orders of magnitude in the simulations, the volume fraction statistics are not significantly affected. The mean solid volume fraction decreases with increasing Ar at the wall of the riser, but only slightly. Similarly, larger values of Ar display greater fluctuations at the wall, but the differences are relatively small. As would be expected, the mean fluid velocity and fluctuations in fluid velocity increase monotonically with increasing Ar, as shown in Figs. 4.3(c) and 4.3(d). From the slip velocity profiles in Figs. 4.3(e) and 4.3(f), it is observed that the clusters in the near-wall region entrain the fluid, leading to a reduction in drag between the phases, explaining the strong downward flow of gas closest to the walls.

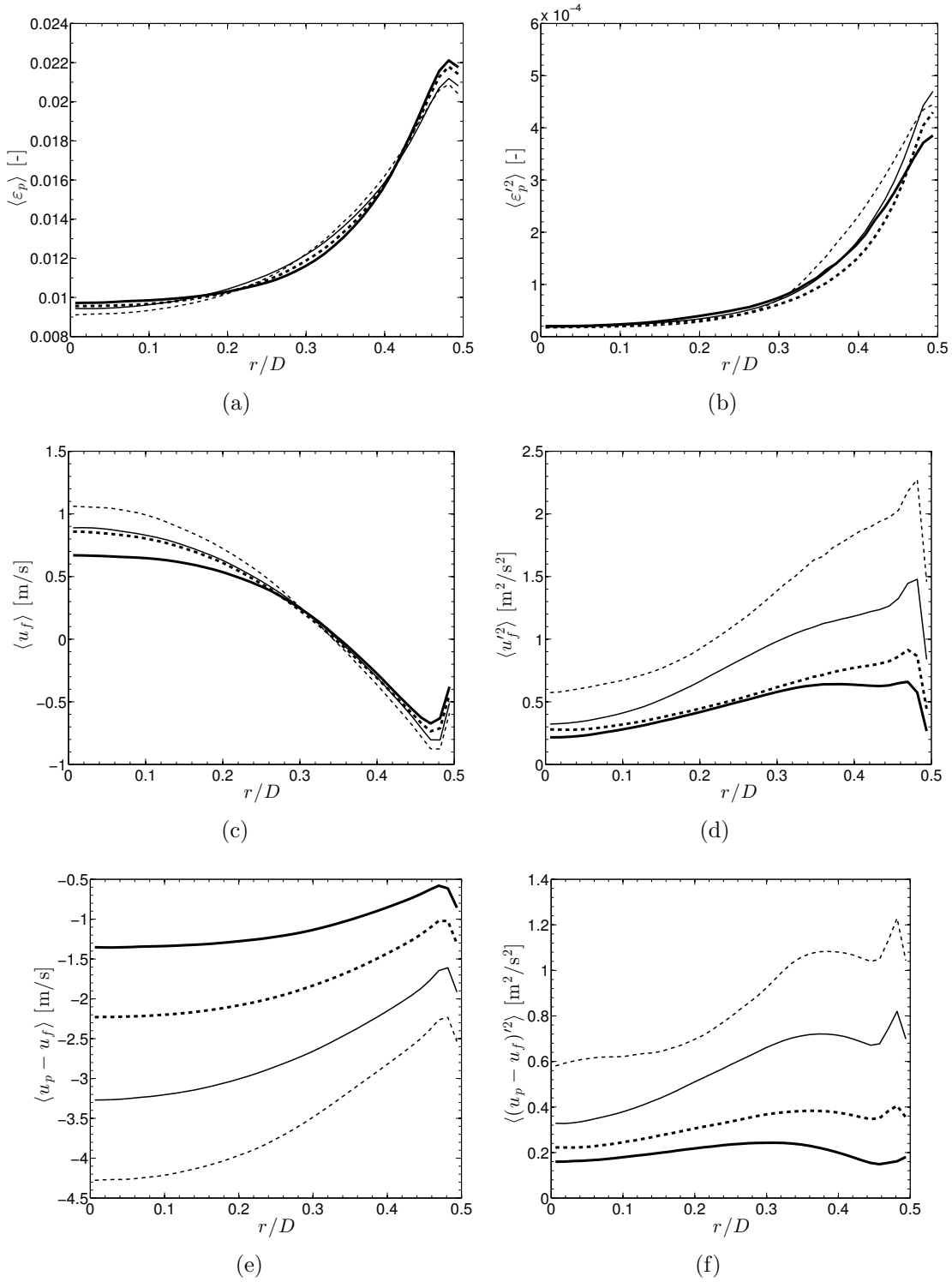

Figure 4.3: Statistics along the radius of the riser. Ar100 (thick solid line), Ar500 (thick dashed line), Ar2500 (thin solid line), Ar12500 (thin dashed line).

4.4.2 Cluster descent velocity

In this work, a band-growth algorithm was used to identify coherent structures in the flow and extract velocity statistics on individual clusters. The displacement of these identified structures can be tracked in time in order to compute cluster velocities, analogous to particle image velocimetry (PIV). The algorithm was originally developed by Hermann [97] for tracking droplets during primary atomization of a turbulent liquid jet, and was later used to track bubbles in dense fluidized beds [146]. At each timestep, the Eulerian solid volume fraction is computed from the Lagrangian particles using the interphase exchange process described in Sec. 2.4. The algorithm identifies grid cells when the condition $\varepsilon_p > \varepsilon_{p,\text{crit}}$ is met, then searches for neighboring cells that also meet this criterion. Once all continuous structures are identified throughout the computation domain, several key quantities are computed by looping over the cells associated with each. This includes the volume of the structure, the mean concentration within the structure, and its center of mass. The principal axes and principal moments of inertia of each structure are obtained from an eigenvalue/eigenvector analysis and are used to construct an equivalent ellipsoid with the same moments of inertia. An example of the structure identification algorithm for Ar2500 is given in Fig. 4.4. An instantaneous snapshot of particle position is shown in Fig. 4.4(a), the corresponding iso-surface of $\varepsilon_p = \varepsilon_{p,\text{crit}}$ is given in Fig. 4.4(b), and Fig. 4.4(c) shows the resulting ellipsoids in two-dimensions. Many small isolated structures can be observed in the flow using the definition 4.5 for identifying clusters. In order to avoid contaminating cluster statistics with these very small structures, a threshold is adopted such that identified clusters with a volume less than 10 times the volume of an individual particle are not considered.

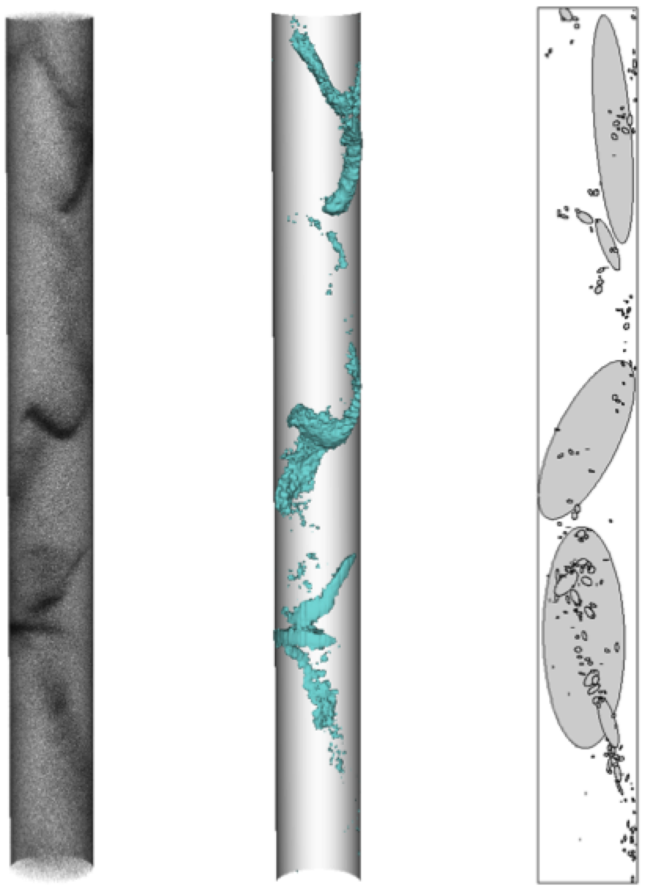

(a) Particle position. (b) Iso-surface of $\varepsilon_p = \varepsilon_{p,\text{crit}}$. (c) Identified clusters.

Figure 4.4: Example of cluster identification for an instantaneous field of Ar2500.

An example of vertical cluster position, x_{cl}, plotted against time is displayed in Fig. 4.5. Two key observations can be made from the figure. First, all clusters tend to fall at similar velocities. Second, the slope of cluster position versus time is linear, indicating that clusters do not accelerate as they fall. For all of the simulations conducted, individual clusters were tracked over time and the velocity of each was computed. As shown in Fig. 4.6, simulated cluster velocities compare very well with Eq. 4.3, as well as the experimental data compiled by Noymer and Glicksman [11]. Note that one explanation for the the correlation of cluster

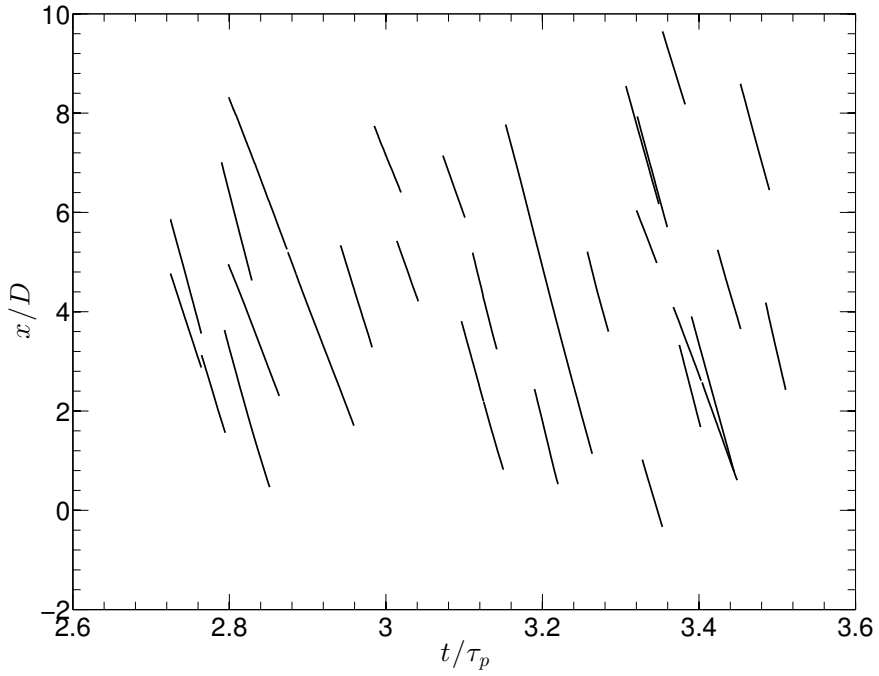

Figure 4.5: Vertical cluster position as a function of time for 27 randomly selected clusters (Ar2500).

fall velocity to be independent of the inflow condition and fluid properties is that clusters tend to fall within the hydrodynamic boundary layer [13]. Much greater resolution would be required to properly capture the fluid boundary layer within the simulations, and thus the clusters are most likely affected by the gas phase, especially at higher Ar. From Fig. 4.6, it can be seen that simulations run at large values of Ar deviate the greatest from the experimental measurements, suggesting that properly resolving the boundary layer in risers might be necessary to most accurately capture cluster fall velocity. Nonetheless, predictions from the LES yield very good agreement with the wide range of experimental measurements.

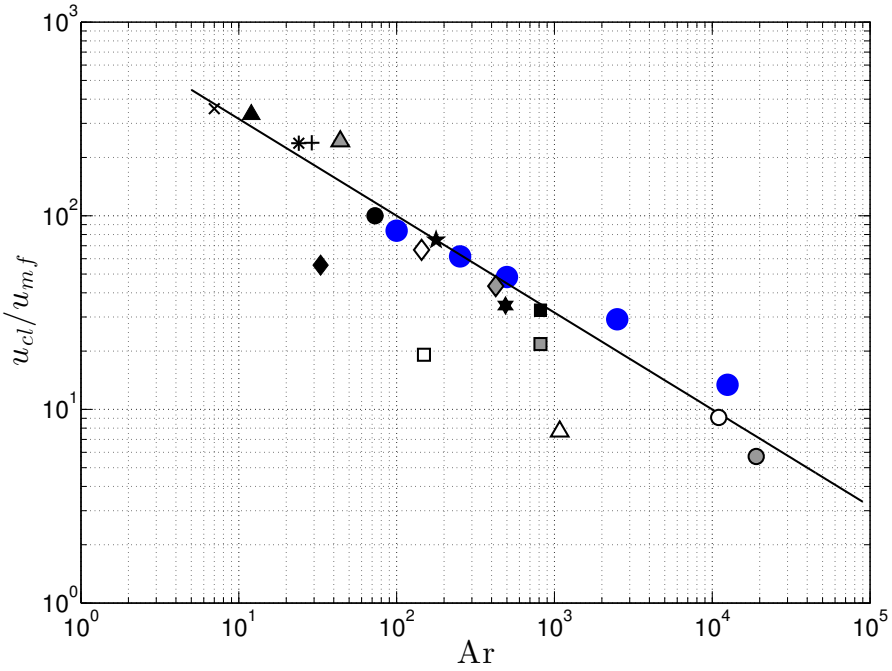

Figure 4.6: Mean cluster velocity normalized by the minimum fluidization velocity. Equation 4.3 (solid line), experimental data points [11] (black, white, and gray symbols), simulation results (blue circles).

4.4.3 Comparisons with experimental correlations on the distribution of solid concentration

Numerous experimental studies on CFB risers exist in the literature, providing insight on the solid concentration distribution for a wide range of operating conditions, riser dimensions, and particle properties. Harris *et al.* [150] presented correlations for predicting the solid concentration within clusters traveling in the near-wall region of the riser. The correlation was developed from experimental data published in the literature on vertical risers ranging from laboratory to industrial scale, and is given by

$$\langle \varepsilon_{cl}|x\rangle = \frac{0.58\langle \varepsilon_p|x\rangle^{1.48}}{0.013 + \langle \varepsilon_p|x\rangle^{1.48}}, \tag{4.6}$$

where $\langle \varepsilon_{cl}|x \rangle$ is the average concentration inside a cluster located at a height x in the near-wall region of the flow, and $\langle \varepsilon_p|x \rangle$ is the average cross-sectional solid concentration at x. Some of these experiments computed mean values of the cluster bulk density defined from peaks in experimental probe data, while others reported time averaged values of the near wall density. However, Harris *et al.* [150] showed these two measures give similar values for the apparent cluster solid concentration at the wall. In this work, $\langle \varepsilon_{cl}|x \rangle$ is computed using the criterion 4.5 based on the average cross-sectional concencentration $\langle \varepsilon_p|x \rangle$. As shown in Fig. 4.7, the simulation results show very good agreement with the experimental data and Eq. 4.6. Although the correlation is only a function of the mean solid concentration, a trend is observed in the results obtained from the simulations, revealing a slope that increases with Ar.

Issangya *et al.* [151] compiled experimental data of solid concentration fluctuations in FCC riser reactors and CFB combustors from numerous studies in the literature. The standard deviation of particle concentration fluctuations was found to be correlated to the time-mean local concentration by

$$\sqrt{\varepsilon_p'^2} = 1.584 \varepsilon_p \left(0.55 - \varepsilon_p\right). \tag{4.7}$$

A comparison between the experimental measurements, Eq. 5.12, and simulation results are given in Fig. 4.8, where $\langle \varepsilon_p'^2|x,r \rangle^{1/2}$ is the average fluctuation about the local mean concentration $\langle \varepsilon_p|x,r \rangle$. It can be seen that the fluctuations in particle concentration increase with the local mean solid concentration up to $\varepsilon_p \approx 0.25$, and then decrease for denser regions of the flow. Due to the vertical periodic boundary condition enforced in the simulations, a dense bed that typically exists at the bottom of CFB risers is unable to develop, and therefore only comparisons with low solid concentrations can be made. Simulation results show excellent agreement against the experimental data for the range of volume fractions considered, indi-

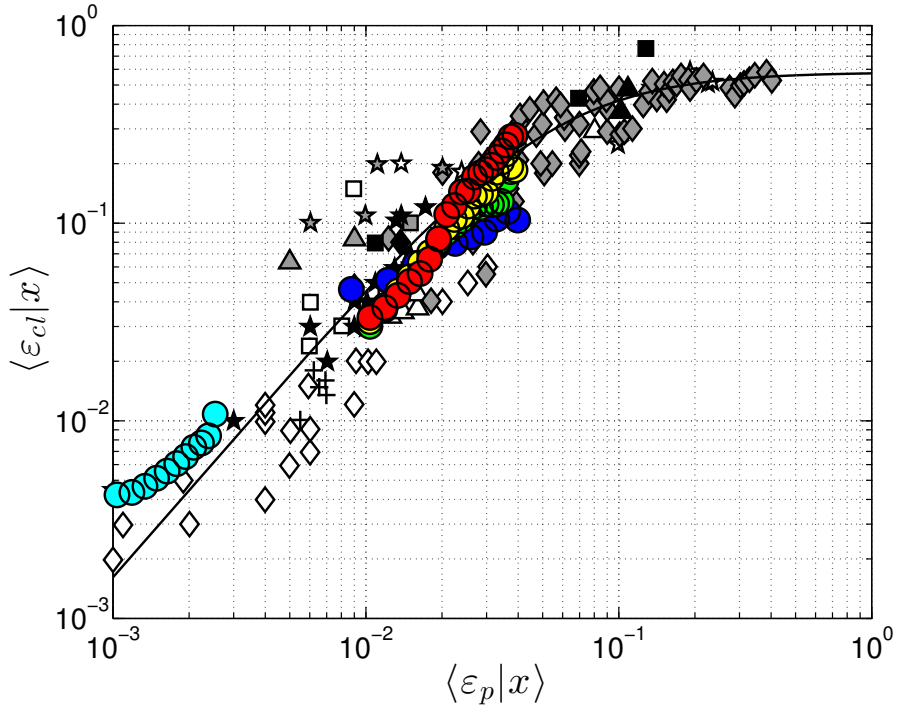

Figure 4.7: Comparison between simulation results and experimental data for the mean solid concentration of near-wall clusters. Black, gray, and white symbols represent independent experimental studies [150]. Ar100 (dark blue circles), Ar250 (light blue circles), Ar500 (green circles), Ar2500 (yellow circles), Ar12500 (red circles), correlation Eq. 4.6 (line).

cating that fluctuations in particle concentration is a function of the local averaged concentration and independent of Ar.

4.4.4 Characterizing the degree of particle segregation

Probability density function of particle concentration

The degree of clustering for each case can be quantified by the probability density function (PDF) of particle number density [116], which is equivalent to the PDF of particle concentration. For a homogeneous distribution of particles, devoid of

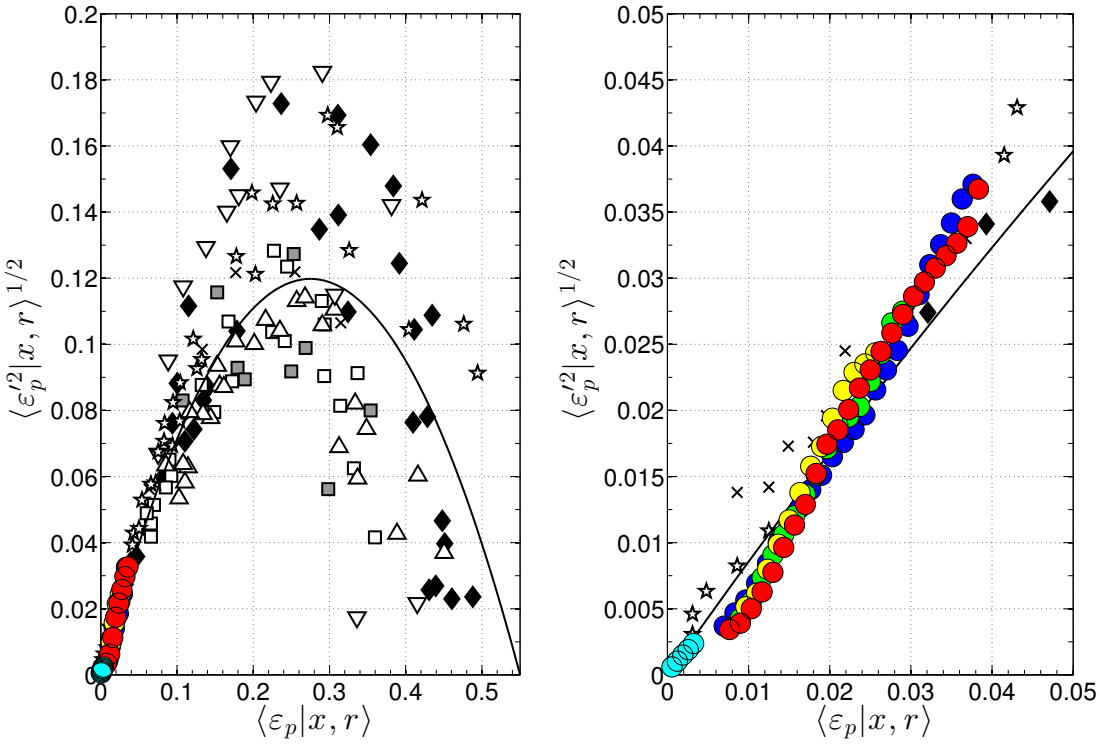

(a) Full range of experimental measurements.

(b) Zoomed in on simulated results.

Figure 4.8: Local time-averaged standard deviation of particle concentration fluctuations with local time-mean particle volume fraction. Black, gray, and white symbols represent independent experimental studies [151]. Ar100 (dark blue circles), Ar250 (light blue circles), Ar500 (green circles), Ar2500 (yellow circles), Ar12500 (red circles), correlation Eq. 5.12 (line).

any clustering, the PDF is given by the discrete Poisson distribution [5,152], which takes the form

$$f_p(N) = \frac{(\overline{N})^N e^{-\overline{N}}}{N!}, \tag{4.8}$$

where N is the observed number of particles in a given sample, and $\overline{N}$ is the average particle number. The PDFs of particle concentration for Ar100, Ar500, Ar2500, and Ar12500 are plotted against 4.8 in Fig. 4.9. Compared to the Poisson distribution, the simulations exhibit a higher probability of local regions empty of particles, as well as local regions of higher solid fraction, as would be expected. Interestingly, the degree of clustering is shown to be unaffected by the Archimedes

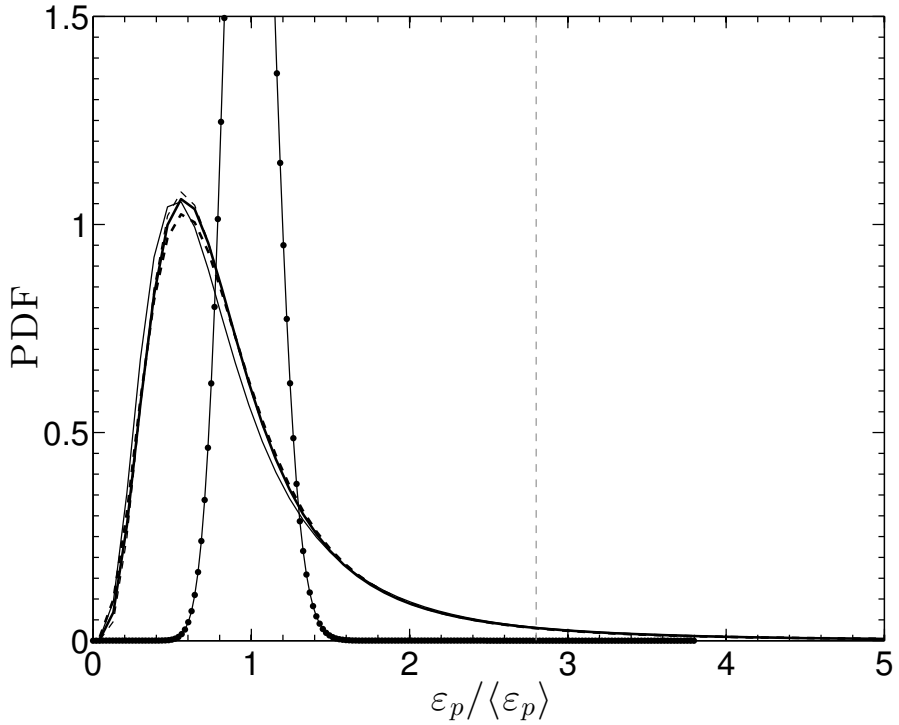

Figure 4.9: PDF of particle concentration. Poisson distribution (dotted line), Ar100 (thick solid line), Ar500 (thick dashed line), Ar2500 (thin solid line), Ar12500 (thin dashed line), $\varepsilon_p = \varepsilon_{p,\text{crit}}$ (thin dashed gray line).

number, suggesting that a model for the PDF can be useful for a wide range of operating conditions in CFB risers.

Wang *et al.* [153] performed an analysis on the fluctuation characteristics of solid concentration in CFB risers to provide a means to define the solid concentration inside clusters. Assuming the volume of a single particle is much smaller than the volume of a typical cluster, and the cluster diameter has minimal affect on the concentration fluctuations, they proposed a model for the standard deviation of volume fraction fluctuations as

$$\sigma_\varepsilon = \langle\varepsilon_p\rangle\sqrt{S(\langle\varepsilon_p\rangle, 0)}, \tag{4.9}$$

where $S(\langle\varepsilon_p\rangle, 0) = (1 - \langle\varepsilon_p\rangle)^4/(1 + 4\langle\varepsilon_p\rangle + 4\langle\varepsilon_p\rangle^2 - 4\langle\varepsilon_p\rangle^3 + \langle\varepsilon_p\rangle^4)$ is the static

Name	$\langle\varepsilon_p\rangle$	$\sqrt{\langle\varepsilon_p'^2\rangle}$	Eq. 5.12	Eq. 4.9
Ar100	0.015	0.0128	0.0127	0.0138
Ar250	0.0015	0.0013	0.0013	0.0014
Ar500	0.015	0.0126	0.0127	0.0138
Ar2500	0.015	0.0137	0.0127	0.0138
Ar12500	0.015	0.0135	0.0127	0.0138

Table 4.3: Comparison between simulation and model predictions of the standard deviation of particle concentration fluctuations.

structure factor in the small wave vector limit [154]. This result indicates that the standard deviation is only a function of its mean value, which agrees with experimental findings [151,155,156]. The study by Wang *et al.* [153] showed Eq. 4.9 to agree well with experimental measurements for dilute and moderately dilute flows, and only qualitative agreement was shown for $\varepsilon_p > 0.2$. A comparison between the simulation predictions, the model given by Eq. 4.9, and the correlation by Issangya *et al.* [151] given by Eq. 5.12 are presented in Table 3. The model of Wang *et al.* [153] slightly over-predicts the experimental correlation provided by Issangya *et al.* [151], though both are within 10% of the simulation results.

As seen in Fig 4.9, the form of the PDF resembles a lognormal distribution. Using the mean and standard deviation of particle concentration extracted from the simulations, a lognormal distribution f_{ε_p} can be constructed, given by

$$f_{\varepsilon_p} = \frac{1}{\varepsilon_p \sigma_{\ln}\sqrt{2\pi}} \exp\left[-\frac{\left(\ln\varepsilon_p - \mu_{\ln}\right)^2}{2\sigma_{\ln}^2}\right], \tag{4.10}$$

where $\mu_{\ln} = \ln\left[\langle\varepsilon_p\rangle^2 / \left(\langle\varepsilon_p'^2\rangle + \langle\varepsilon_p\rangle^2\right)^{1/2}\right]$ and $\sigma_{\ln} = \left[\ln\left(1 + \langle\varepsilon_p'^2\rangle/\langle\varepsilon_p\rangle\right)\right]^{1/2}$. The corresponding lognormal distribution using the average standard deviation from the simulation results is given in Fig. 4.10(a). Good agreement is seen in regions denser than the mean concentration, but a discrepancy occurs in dilute regions. Although lognormal distributions are known to describe the behavior of many nat-

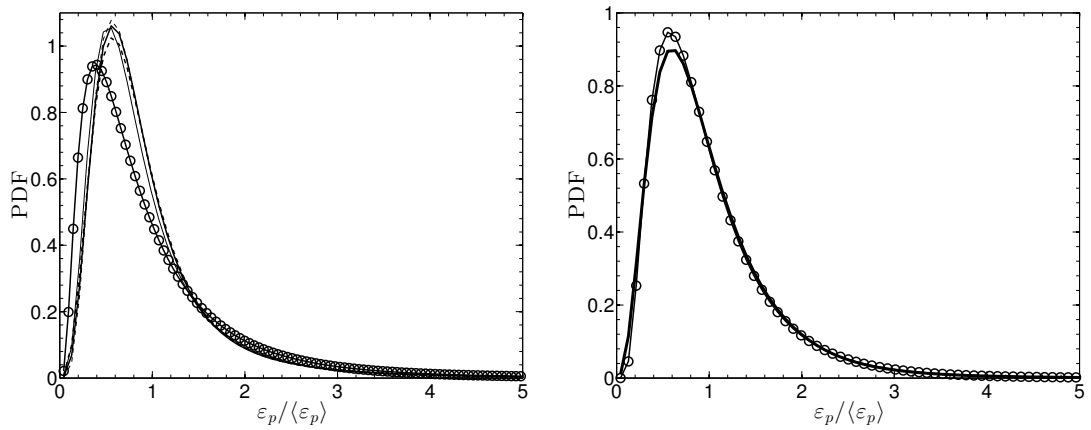

(a) Ar100 (thick solid line), Ar500 (thick dashed line), Ar2500 (thin solid line), Ar12500 (thin dashed line).

(b) Ar2500 without walls (thick line).

Figure 4.10: Comparison between lognormal distribution (circles) and PDF of particle concentration from simulation results.

ural and technical processes, there is no expectation that the particle concentration distribution will take this form. However, it was observed that fully homogeneous risers (CFB risers without walls) do indeed produce concentration distributions that closely resemble a lognormal distribution. Figure 4.10(b) shows the PDF of particle concentration for a simulation with parameters matching that of Ar2500 but without walls, compared to a lognormal distribution using a standard deviation extracted from the simulation. Overall, excellent agreement is observed. Here we see that providing the lognormal distribution function with a mean volume fraction and using Eq. 4.9 to compute the standard deviation is a good model for the PDF of solid concentration, and is valid for a wide range of Ar.

Radial distribution function

An important statistical measure of particle clustering is the radial distribution function (RDF), defined as the number of particle pairs found at a given sepa-

ration normalized by the expected number of pairs found in a homogeneous distribution [157]. The RDF has been used in numerous studies to measure preferential concentration of aerosol particles suspended in isotropic turbulence (see e.g., [158–160]). In this work, we define the RDF as a function of vertical separation x_i between pairs of particles, and radial distance from the riser center r, given by

$$g(x_i, r) = \frac{N_i(r)/\Delta V_i(r)}{N(r)/V(r)}, \tag{4.11}$$

where $N_i(r)$ is the average number of particles found in an elemental volume $\Delta V_i(r)$ at a vertical distance x_i and radial distance r, $V(r)$ is the total volume at a radial distance r, and $N(r)$ is the total number of particle pairs at r. Using this definition, $g(x_i, r) = 1$ represents a homogeneous distribution of particles, and $g(x_i, r) > 1$ implies clustering. As shown in Fig. 4.11, $g(x_i, r)$ increases with r, with the greatest level of clustering in the near-wall region of the riser. It is also seen that $g(x_i, r)$ is reasonably similar for the various Ar, and approaches unity at approximately $150d_p$. This implies a characteristic cluster length scale of approximately the diameter of the reactor D. Several numerical studies on risers in the literature have introduced a characteristic length scale $\tau_p^2 g$ to obtain an *a priori* measure of the cluster size and determine an appropriate domain length such that the results are unaffected by the periodic boundary conditions [6, 133]. The simulations presented in this work have ratios of this characteristic size to particle diameter ranging from $\tau_p^2 g/d_p \approx 770$ to $\tau_p^2 g/d_p \approx 96,000$. Due to the presence of the walls, Fig. 4.11 suggests the cluster size is limited by the characteristic reactor length scale, and thus the simulations in this work are capable of capturing several clusters along the height of the domain.

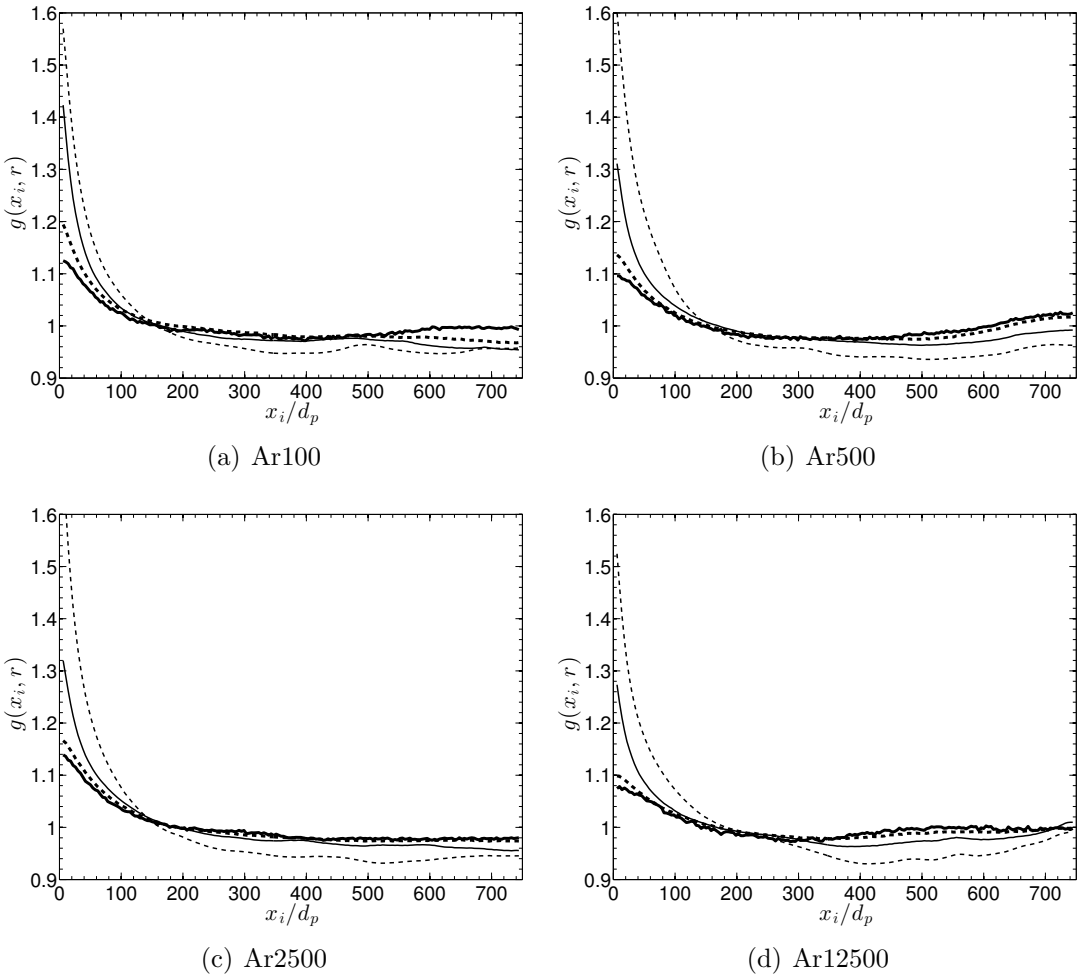

(a) Ar100

(b) Ar500

(c) Ar2500

(d) Ar12500

Figure 4.11: Vertical radial distribution function as a function of radial distance from the wall. $r/D = 0.01$ (thick solid line), $r/D = 0.18$ (thick dashed line), $r/D = 0.34$ (thin solid line), $r/D = 0.50$ (thin dashed line).

4.5 Effects of simulating risers in two-dimensions

Several key issues with simulating two-dimensional risers using the EL approach were already discussed in Sec. 4.2. Namely, as pointed out by Berrouk and Wu [143], corrections to the two-dimensional void fraction will lead to an under-prediction of the momentum source term, and therefore lead to a much lower prediction of the pressure drop and thus an incorrect prediction of the minimum

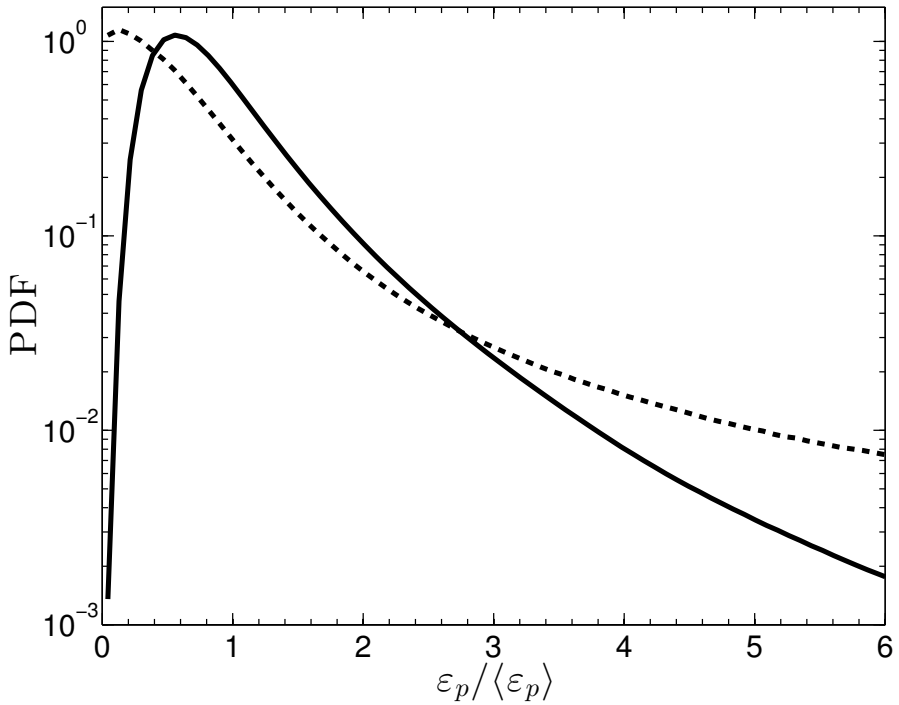

Figure 4.12: PDF of solid concentration for Ar2500. 3D simulation (solid line), 2D simulation (dashed line).

fluidization velocity. However, besides the numerical challenges associated with accurately modeling the flow in two dimensions, it is likely that key physical phenomena are affected by the loss in dimensionality as well. Therefore, before attempting to simulate two-dimensional risers, regardless of the simulation strategy (e.g., PR-DNS, EE, or EL methods), one should be aware of potential ramifications.

A two-dimensional simulation was run with the domain configuration given in Table 1 but with 1 cell in the z-direction, and parameters of Ar2500 from Table 2. Although the simulation is two-dimensional, the particles are represented as spheres and the depth of the domain was set equal to the mean inter-particle spacing, i.e., $\Delta z = [\pi d_p^3/(6\langle\varepsilon_p\rangle)]^{1/3}$. The higher degree of clustering in the two-dimensional case can be observed in the comparison of solid concentration distri-

butions given in Fig. 4.12. There exists very few locations in the three-dimensional flow devoid of particles, while the two-dimensional simulation exhibits a high probability of finding regions with negligible solid concentration. Mean radial profiles of solid concentration and phase velocities are provided in Fig. 4.13, revealing greater fluctuations throughout the radius of the pipe in two dimensions. Due to the higher concentration in two dimensions seen in Fig. 4.13(a), the relative slip velocity between the two phases is smaller, as depicted in Fig. 4.13(e), leading to a greater downward fluid velocity as shown in Fig. 4.13(c). These results clearly show that restricting risers to two dimensions can greatly enhance particle accumulation and fluctuations in volume fraction and phase velocities. In particular, Fig. 4.13 shows a 225% increase in volume fraction fluctuations and a 27% increase in fluid velocity fluctuations in the near-wall region of the riser.

It is postulated that this increase in particle segregation is a result of restricting each particle to a single plane of motion. In particular, particles located in the path of a falling cluster will be much less likely to escape in two dimensions, leading to an unphysical accumulation of solid concentration. As depicted in Fig. 4.14, particles located below the cluster in the near-wall region will be entrained, which would not necessarily be the case in three dimensions. From Fig. 4.14(a), it is observed that in order for particles to avoid the cluster, they must circumvent it laterally in y, leading to the formation of an intense vortex downstream. Figure 4.14(b) shows trajectories of seven particles in the frame of reference of the same cluster over a period of 35 ms. Due to the reduction in drag experienced by particles within the cluster, particles below the cluster are forced to either move radially inward or become entrained. A correlation between inward moving particles and denser regions of the flow is given in Fig. 4.15, where v_p is the particle radial velocity. This result shows that the observation of particles moving towards the reactor center

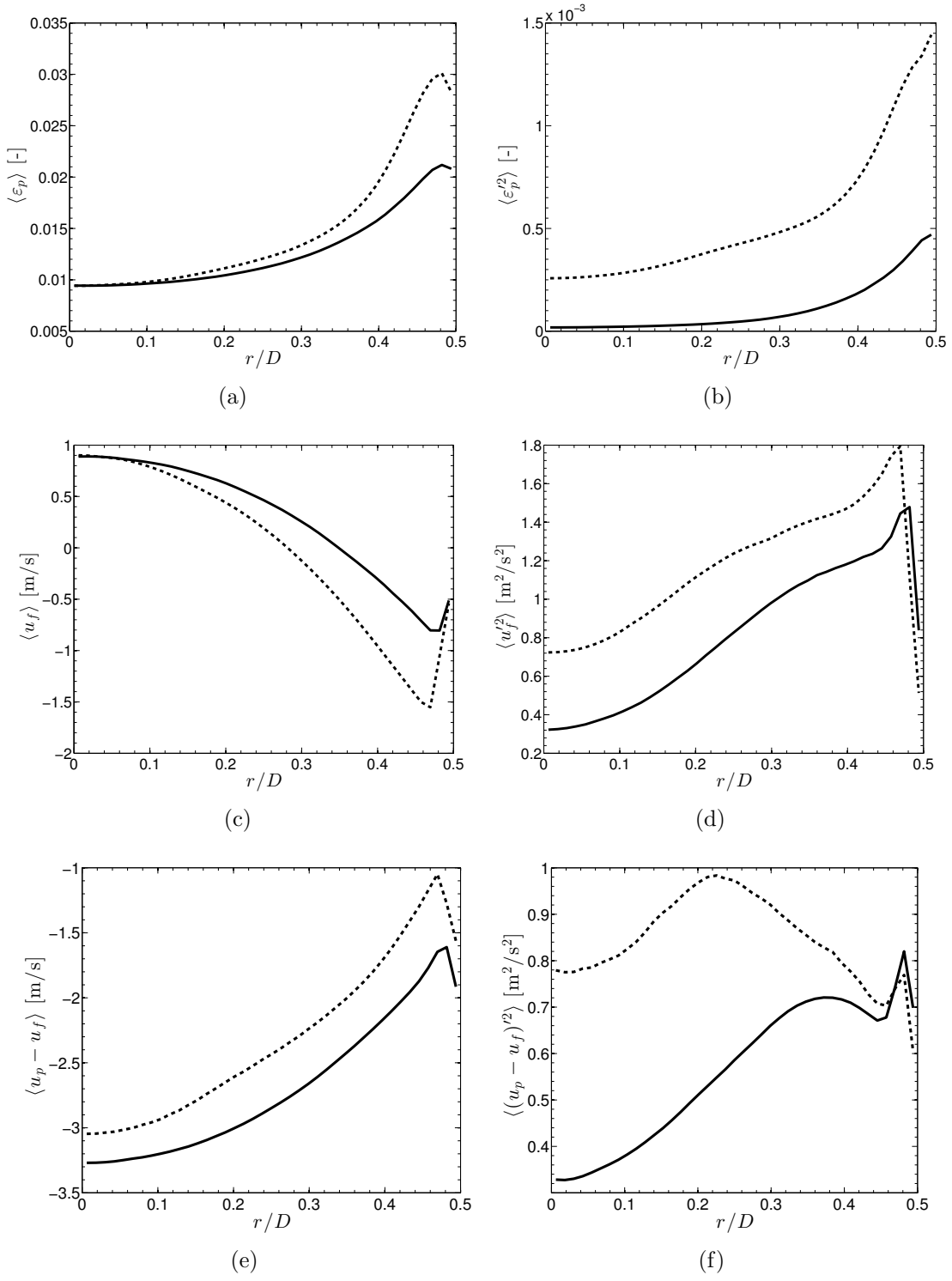

Figure 4.13: Mean statistics along the radius of the riser for Ar2500. 3D (solid line), 2D (dashed line).

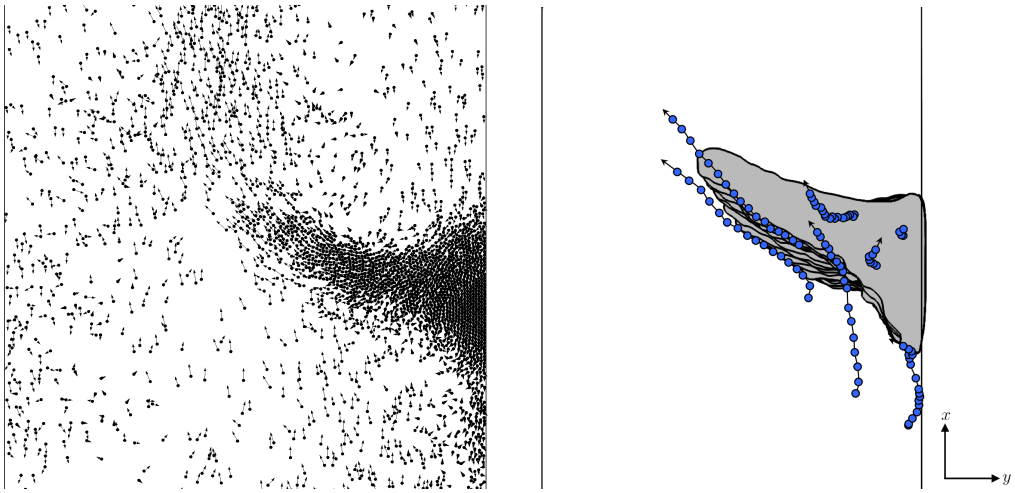

(a) Instantaneous field of particle position. Vector arrows represent fluctuations in particle velocity.

(b) Trajectories of 7 particles in the frame of reference of the cluster.

Figure 4.14: Particles in a section of a two-dimensional riser with Ar = 2500.

depicted in Fig. 4.14(b) is greatly enhanced in two dimensions.

4.6 Conclusions

This work demonstrates the capability of three-dimensional Eulerian-Lagrangian methods to reproduce particle clustering with physical characteristics. A large-eddy simulation framework was coupled with a Euler-Lagrange methodology to simulate fully-developed risers for a range of Archimedes numbers. Normal and tangential particle collisions are handled deterministically via a soft-sphere model. A two-step filtering approach is used during the interphase exchange process, decoupling the mesh size to particle diameter ratio and providing a solution that converges under mesh refinement. The pipe geometry was modeled using a conservative immersed boundary method integrated with the Lagrangian particle solver. Five cases were conducted to investigate the role of the Archimedes number on

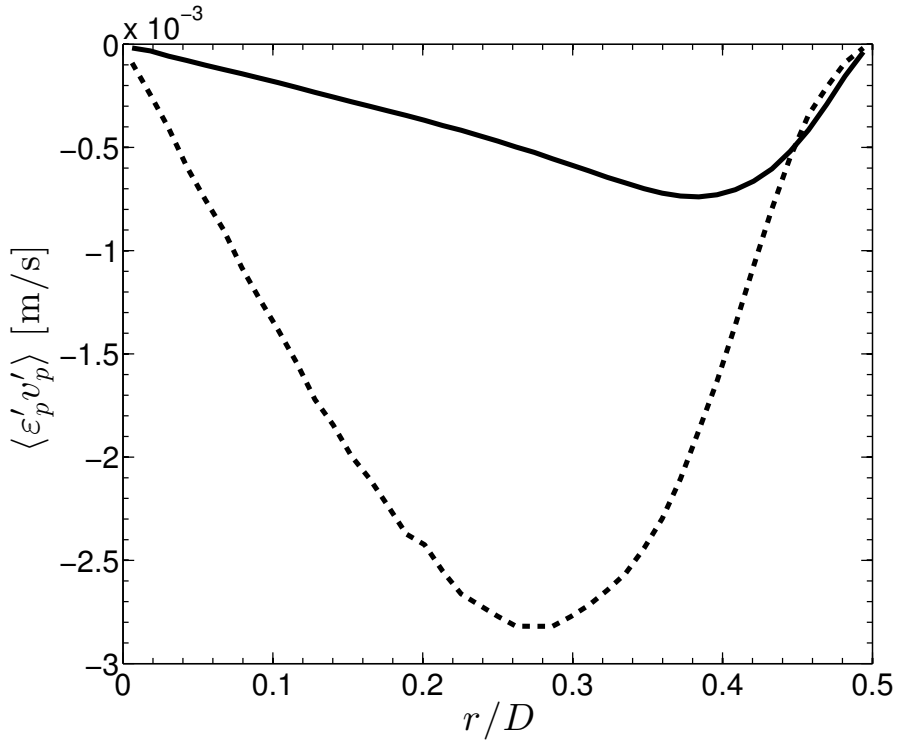

Figure 4.15: Covariance of volume fraction and particle radial velocity along the radius of the riser for Ar2500. 3D (solid line), 2D (dashed line).

the cluster dynamics. An analysis of the numerical results led to the following findings:

- The degree of particle clustering is unaffected by the Archimedes number, and the distributions of solid concentration agree fairly well with a lognormal law, indicating a potential for future modeling efforts;
- The standard deviation of volume fraction fluctuations depend only on the mean concentration, and is predicted within 10% for the range of Archimedes numbers simulated in this study using either the model proposed by Wang *et al.* [153] or the experimental correlation given by Issangya *et al.* [151];
- The radial distribution function suggests that the characteristic cluster length scale is limited by the diameter of the reactor. This prediction is much

smaller than that given by the characteristic length scale for gravity-driven particle-laden flows $\tau_p^2 g$;

- Simulation results show excellent agreement with experimental correlations for the mean concentration within clusters, volume fraction fluctuations, and cluster descent velocities;
- In a CFB riser under statistically stationary conditions, clusters were observed to fall at constant velocities;
- Simulating risers in two dimensions may lead to unphysical accumulation of particles due to the restriction of particle motion in a plane, resulting in gross over-predictions in volume fraction and velocity fluctuations. The radial motion of particles to avoid falling clusters is greatly enhanced in two dimensions.

CHAPTER 5

NUMERICAL INVESTIGATION AND MODELING OF REACTING GAS-SOLID FLOWS IN THE PRESENCE OF CLUSTERS

5.1 Abstract

This work presents a volume-filtered formulation for describing chemically reacting flows in the presence of solid catalytic particles. The equations are discretized in an Eulerian-Lagrangian framework and applied to flows of isothermal, heterogeneously-reacting chemical species in fully-developed three-dimensional risers. The aim of this study is to identify and quantify the influence of particle clusters on heterogenous reactions. The Archimedes number, Ar, is varied from 500 to 12500, and the Damköhler number, Da, from 0.1 to 10. To assess the multiphase dynamic effects on the chemistry, conversion times from the three-dimensional simulations are compared to a zero-dimensional model that solves for the temporal evolution of the species mass fraction and ignores all spatial variations. Due to the presence of clusters, the conversion process associated with the three-dimensional simulations is significantly longer compared to the zero-dimensional solution, with an increasing effect for larger values of Da. To account for the effect of clusters in the reduced-order model, contributions to the covariance between species mass fraction and particle volume fraction are discussed, and a presumed-shape probability distribution function (PDF) approach is investigated. This PDF approach models the fluctuating chemical source term by a product of a beta distribution for the species mass fraction and a lognormal distribution for the particle concentration, and is found to agree very well with the three-dimensional results for the range of Ar and Da considered in this study.

5.2 Introduction

Gas-solid reactions play a major role in many engineering devices, including the combustion of solid fuels, coal gasification, and catalytic upgrading of biomass pyrolysis vapor, to name just a few examples. In all of these applications, the underlying flow field is highly unsteady and often turbulent. Particle-laden flow dynamics affect the conversion of chemical species in several ways. Strong vortical structures and local regions of high shear provide optimal contact between catalysts and fuel species. However, coupling between the two phases (e.g., via drag) can lead to a variety of granular flow regimes that exhibit strong spatial segregation in catalyst concentration, potentially reducing the overall contact efficiency significantly. In riser reactors, solid particles are pneumatically conveyed by a carrier gas phase, characterized by velocities much higher than minimum fluidization. The high flow rates encountered in risers often lead to the spontaneous generation of densely packed catalytic particles, referred to as clusters. Clusters have been observed to reduce mixing and interaction of particles with the transport gas [127], and therefore may inhibit the catalytic conversion process, potentially lowering operating efficiencies significantly. Meanwhile, detailed studies demonstrating the quantitative impact of particle clustering on chemical processes occurring in such flows are severely limited.

A common feature of all reactive gas-solid systems is the complex processes occurring at the surface of each particle, referred heretofore as the microscale. Such processes include heat and mass transfer between the two phases, adsorption on and desorption from the solid surfaces, and the actual chemical reaction between the adsorbed gas and the solid [161]. If the variations in particle concentration becomes significant, the multiphase dynamics will impact the microscale processes

and therefore cannot be ignored. Simultaneously accounting for both the microscale processes and particle dynamics pose significant challenges in developing predictive models.

Simulating heterogeneous reactions in fluidized bed reactors requires a chemical kinetic model to describe the complex chemistry and a framework for solving gas-solid flows. In the context of catalytic cracking in risers, most work found in the literature models the solid phase as a continuous Eulerian field, greatly reducing the computational cost as individual particles do not need to be tracked (see e.g., [85,162–168]). In the limit where the flow is highly collisional and assumed to be nearly at equilibrium, the particle density function is close to Maxwellian and a Chapman-Enskog expansion can be used to derive a two-fluid model (TFM) using ensemble or volume averaging [32–34]. However, due to the strong coupling between the carrier gas and catalytic particles, the solid concentration becomes highly segregated and the velocity distribution deviates far from equilibrium. Agrawal *et al.* [6] demonstrated that global statistics obtained from Eulerian-Eulerian simulations of riser reactors were strongly dependent on the mesh size but became mesh-independent when mesh size is of the order of a few particle diameters. As a result, accurate predictions obtained from TFM are potentially still excessively expensive for such flows. In a recent study, Ozel *et al.* [133] employed TFM at various resolutions to obtain mesh-independent results in periodic circulating fluidized bed (CFB) risers. It was shown that various sub-grid terms have to be modeled in order to account for the unresolved clustering dynamics.

Eulerian-Lagrangian strategies provide an alternative framework that typically relies on simpler closures, where individual particle trajectories are solved using Newton's laws of motion, and models are required for interphase exchange and par-

ticle collisions. Because of the added computational expense of tracking individual particles, Eulerian-Lagrangian methods coupled with a chemistry model have only recently been applied in three dimensions [135, 169], but are typically limited to two-dimensional flows with a relatively small number of particles (e.g., [170–174]). It has been demonstrated in recent work that two-dimensional simulations are only capable of capturing qualitative features of particle clustering, and a fully three-dimensional description is required to accurately capture the quantitative flow behavior [7, 175]. In our previous work, it was shown that three-dimensional Eulerian-Lagrangian simulations are capable of accurately reproducing key cluster characteristics, including fall velocity, mean cluster concentration, and concentration fluctuations in risers [7].

In this study, we focus on characterizing and quantifying the effect of clusters on the chemical conversion process in three-dimensional risers. In Sec. 5.3, we present a volume-filtered formalism for describing chemically reacting flows in the presence of solid particles and provide details on the system under considering. Statistics from the fully-developed, three-dimensional risers are then presented. In Sec. 5.4, results from the three-dimensional simulations are compared to a reduced-order model that solves for the temporal evolution of the average mass fraction and neglects all spatial variations. A transport equation for the fluctuating chemical source term is derived and the various contributions are presented and discussed. Finally, a presumed-shape PDF model is proposed for closure of the fluctuating chemical source term and its validity is evaluated.

5.3 Heterogeneous reactions in a three-dimensional riser

5.3.1 Transport of reactive scalars

Considering a mixture of n chemically reacting species, the pointwise scalar transport equation for the mass fraction Y_i of species i is given by

$$\frac{\partial \rho_f Y_i}{\partial t} + \nabla \cdot (\rho_f Y_i \boldsymbol{u}_f) = \nabla \cdot (\rho_f D_i \nabla Y_i)\,, \tag{5.1}$$

where $i = 1, 2, \ldots, n$, t is time, ρ_f is the fluid-phase density, and D_i is the diffusion coefficient of species i. When computing the species mass fraction, adsorption and desorption that occur during the chemical reaction can be represented as flux boundary conditions at the particle surface. In order to formulate a tractable system of equations that does not require resolving the flow at the particle scale, a separation of length scales must be established. To achieve this, a volume filtering kernel is applied to the pointwise equations of motion. Volume filtering Eq. (5.1) yields

$$\frac{\partial}{\partial t}\left(\varepsilon_f \overline{\rho_f} \widehat{Y_i}\right) + \nabla \cdot \left(\varepsilon_f \overline{\rho_f} \widehat{\boldsymbol{u}_f} \widehat{Y_i}\right) = \varepsilon_f \nabla \cdot \left(\overline{\rho_f} \widehat{D_i \nabla Y_i}\right) - \nabla \cdot \boldsymbol{\mathcal{R}}_{Y_i} + \dot{\omega}_i, \tag{5.2}$$

where ε_f is the fluid-phase volume fraction, and we have introduced the Favre average notation $\widehat{(\cdot)} = \varepsilon_f \overline{\rho_f (\cdot)} / (\varepsilon_f \overline{\rho_f})$, where the bar denotes a volume-filtered quantity. A full description of the mathematical derivation can be found in our previous work [45]. In this work, it is assumed that catalytic coking does not become significant, and therefore particles do not change size and subfilter terms that involve the rate of change of mass are not considered.

In Eq. 5.2, $\boldsymbol{\mathcal{R}}_{Y_i}$ is the subfilter scalar flux expressed as

$$\boldsymbol{\mathcal{R}}_{Y_i} = \varepsilon_f \overline{\rho_f} \widehat{\boldsymbol{u}_f' Y_i'}, \tag{5.3}$$

where the prime notation represents a fluctuation about a Favre-average quantity. In turbulent combustion, closure for $\boldsymbol{\mathcal{R}}_{Y_i}$ is generally obtained by employing a gradient transport assumption and introducing a turbulent diffusivity D_t, i.e.

$$-\widehat{\boldsymbol{u}'_f Y'_i} \sim D_t \nabla \widehat{Y}_i. \tag{5.4}$$

Moin *et al.* [176] introduced a dynamic formulation for D_t that is similar to the dynamic Smagornisky model used in computing the turbulent viscosity in Eq. (2.39). Note that closure for the turbulent diffusivity in Eq. (5.4) is formulated for passive scalars and is not valid for chemically reacting flows in general [177]. In premixed turbulent combustion for example, experiments and DNS have shown that heat release may cause counter-gradient diffusion, and typical gradient transport models are not applicable (see e.g., [178] and references therein). Proper closure for this term requires further investigation and is beyond the scope of this work. Because the chemical species do not feed back to the gas-solid flow in this study, the dynamic model for $\boldsymbol{\mathcal{R}}_{Y_i}$ is employed.

Volume filtering the last term in Eq. (5.1) and assuming that diffusion occurs uniformly over the surface of each particle yields additional subfilter surface contributions that contain fluctuations in the diffusive flux. Studies conducting particle-resolved DNS have observed that scalar spreading increases with decreasing solids volume fraction, and increases with increasing particle Reynolds number [179, 180]. However, modeling multicomponent diffusion aspects in fluidized beds is challenging and often neglected in practical studies [180]. These subfiltered surface contributions also account for the heterogeneous reactions that need to be modeled. In this work, the depletion of mass fraction is taken into account by the chemical source term $\dot{\omega}_i$ in Eq. (5.2), given by

$$\dot{\omega}_i = -\varepsilon_f \overline{\rho_f} k_i \varepsilon_p \widehat{Y}_i / \varepsilon_{p,0}, \tag{5.5}$$

where $\varepsilon_{p,0} = 0.634$ is the random close-packing limit for monodisperse spherical particles [87], and k_i is a coefficient that controls the rate of reaction for species i.

5.3.2 System description

In this study, we consider heterogeneous reactions between a gas phase and a moderately dilute suspension of rigid spherical particles subject to gravity. For simplicity, the notation used for identifying volume filtered and Favre average quantities as defined in Sec. 5.3.1 will be dropped. The flows take place in a vertical (i.e., gravity-aligned) cylindrical pipe with an aspect ratio of 10, on a Cartesian mesh with $800 \times 82 \times 82$ cells and a uniform grid spacing of $\Delta x \approx 1.8 d_p$. Each simulation considers the transport of three chemical species with varied reaction times, k_i. The density ratio and reactor diameter to particle diameter ratio are respectively given by $\rho_p/\rho_f = 2500$ and $D/d_p = 150$. The particles are inelastic with a coefficient of restitution $e = 0.9$ and coefficient of friction $\mu_f = 0.1$, initially uniformly distributed on a Cartesian lattice with a mean concentration $\langle \varepsilon_p \rangle = 0.015$, corresponding to 728,232 particles. In this work, angled brackets denote a spatial average, i.e., $\langle (\cdot) \rangle = \frac{1}{V_f} \int_{V_f} (\cdot) dV_f$. Periodic boundary conditions are enforced in the streamwise direction and the momentum source term $\boldsymbol{F}^{\mathrm{mfr}}$ is adjusted dynamically in Eq. 2.31 to prevent the development of a net mass flow rate in the gas phase due to momentum coupling with the particles.

Once the flow reaches a statistically stationary state, three chemical species are introduced with a mass fraction of unity throughout and a Schmidt number $\mathrm{Sc} = \mu/(\rho_f D_i) = 0.7$. The simulations are then run until 99% of each reactant is depleted. The reaction rate k_i of species i is varied in order to emphasize the relative importance of the two-phase dynamics contributing to the chemical

Name	A_1	A_2	A_3	B_1	B_2	B_3	C_1	C_2	C_3
Ar	500	500	500	2500	2500	2500	12500	12500	12500
Da	0.1	1.0	10.0	0.1	1.0	10.0	0.1	1.0	10.0

Table 5.1: Simulation cases and their corresponding non-dimensional parameters.

conversion process. These effects are quantified by the Damköhler number, Da, which describes the ratio of the flow time scale to reaction time scale. Because the net mass flow rate is forced to zero, an appropriate timescale for the fluid is not obvious. We have shown in a previous numerical study [7] that clusters simulated in vertical risers fall with a constant velocity predicted by the experimental correlation of Noymer & Glicksman [11], given by

$$U_c = 0.75\sqrt{\frac{\rho_p}{\rho_f} g d_p}. \tag{5.6}$$

Using Eq. (5.6) as the characteristic flow velocity and the reactor diameter D as the characteristic length scale for the flow, the Damköhler number of species i can be formulated as

$$\mathrm{Da} = \frac{\langle \varepsilon_p \rangle k_i D}{\varepsilon_{p,0} U_c}, \tag{5.7}$$

where $\varepsilon_{p,0}/(\langle \varepsilon_p \rangle k_i)$ is the characteristic reaction time scale of species i.

A total of 9 simulations are conducted by varying both Da and the Archimedes number Ar, which characterizes the entrainment of the gas phase by the particles [181], defined as

$$\mathrm{Ar} = \frac{(\rho_p - \rho_f)\, \rho_f d_p^3 g}{\mu^2}. \tag{5.8}$$

A list of parameters for the simulations conducted in this work is shown in Table 1. The Archimedes number is varied by varying the gas-phase viscosity while keeping all other parameters constant. As a consequence, the particle response time τ_p, and thus the terminal velocity $v_t = \tau_p g$ increases with Ar. Because the cluster fall velocity is independent of Ar, U_c remains constant for each case. Furthermore, the

Schmidt number is kept constant for each case, and therefore the species diffusivity decreases with increasing Ar.

5.3.3 Multiphase statistics

Simulation results are gathered after the initial transient is complete and the flow reaches a statistically stationary state. Time-averaged radial profiles of the multiphase statistics are shown in Fig. 5.1, where the single-prime notation denotes a fluctuation about the averaged quantity. It can be observed that the volume fraction statistics do not vary significantly with Ar. As seen in Fig. 5.1(a), the average solid concentration in the near-wall region is more than twice as large in comparison with the concentration in the center of the riser. Fluctuations in solid volume fraction along the radius of the pipe are given in Fig. 5.1(b), showing the greatest variation at the wall. The mean fluid velocity and fluctuations in fluid velocity increase monotonically with increasing Ar, as shown in Figs. 5.1(c) and 5.1(d). From the slip velocity profiles in Figs. 5.1(e) and 5.1(f), it is observed that the clusters in the near-wall region entrain the fluid, leading to a reduction in drag between the phases, explaining the strong downward flow of gas closest to the walls. A detailed analysis on the two-phase dynamics can be found in Chapter 4.

5.3.4 Temporal evolution of species mass fraction

After the initial transient is complete, three chemical species are introduced to the flow with a mass fraction $Y_i = 1$. Figure 5.2 shows two-dimensional planes colored by the spatial distribution of species mass fraction as a function of time from case B_2. Due to the strong segregation in particle concentration, the mass fraction

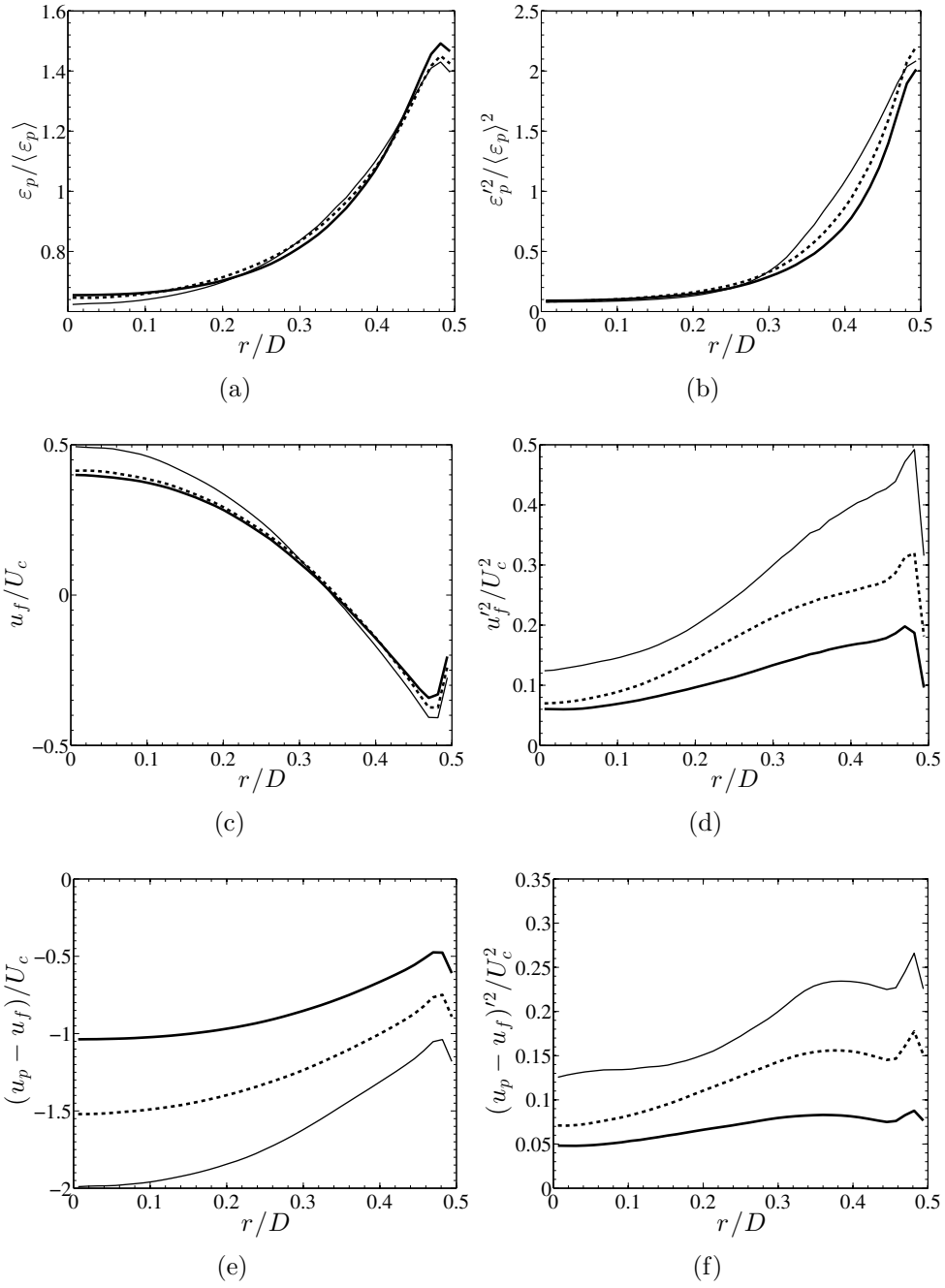

Figure 5.1: Radial profiles extracted from Ar500 (thick solid line), Ar2500 (thick dashed line), and Ar12500 (thin solid line).

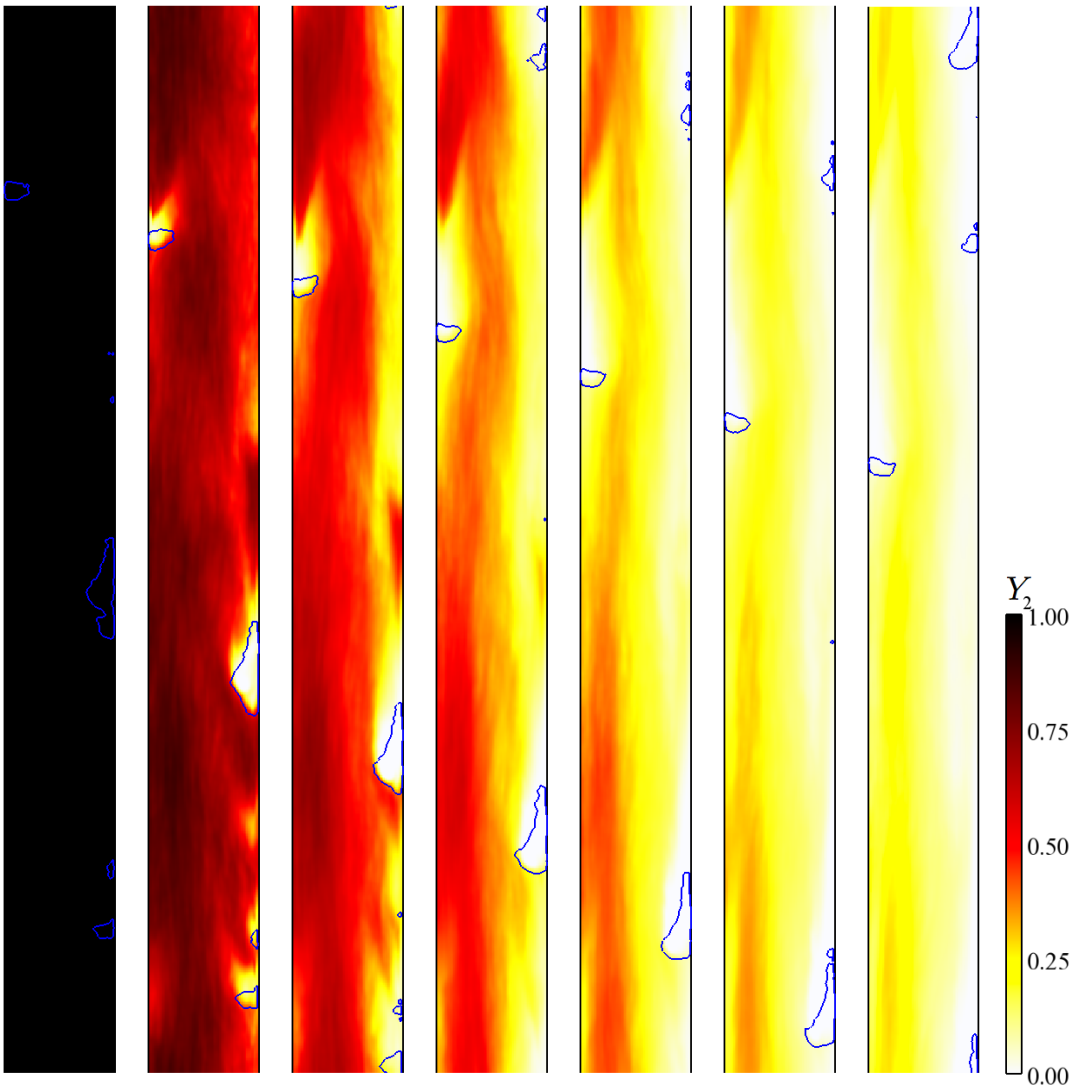

Figure 5.2: Two-dimensional planes showing the spatial distribution of species mass fraction as a function of time for case B_2. Iso-contours of $\varepsilon_p = 3\langle\varepsilon_p\rangle$. (a) $tU_c/D = 0.0$, (b) $tU_c/D = 0.5$, (c) $tU_c/D = 1.0$, (d) $tU_c/D = 1.5$, (e) $tU_c/D = 2.0$, (f) $tU_c/D = 2.5$, and (g) $tU_c/D = 3.0$.

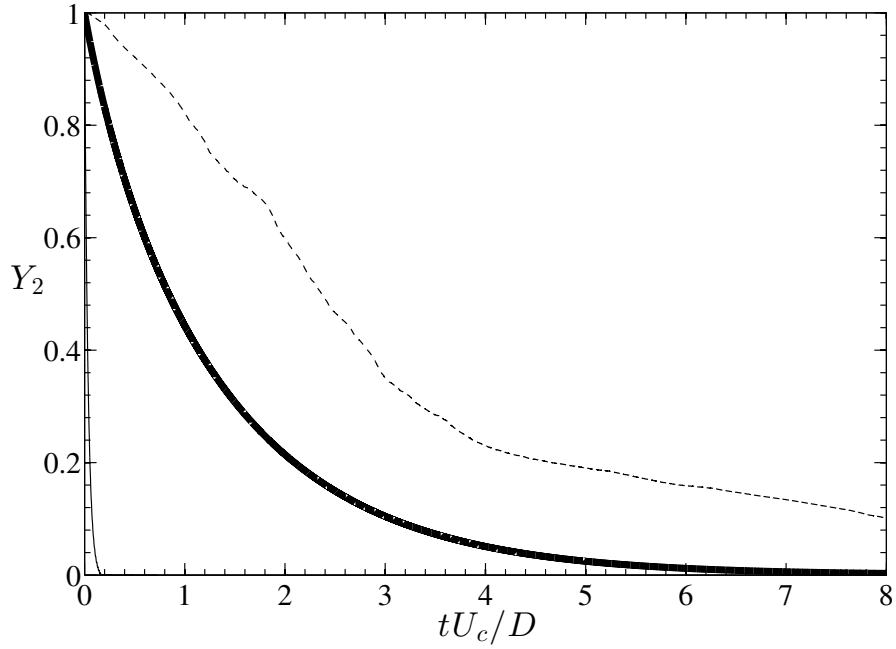

Figure 5.3: Temporal evolution of the species mass fraction for case B_2. Favre average mass fraction (thick solid line), minimum mass fraction (thin solid line), and maximum mass fraction (thin dashed line).

decays rapidly in dense clusters, while maximum values of Y_2 persist upstream of clusters and in the reactor center. The temporal evolution of the corresponding species mass fraction is shown in Fig. 5.3. After $tU_c/D \approx 6$, 99% of the chemical species has been depleted. The instantaneous minimum and maximum values of mass fraction reveal the variation in local depletion times, with 99% conversion of mass fraction after $tU_c/D \approx 0.2$ in some regions of the flow, and 99% conversion of mass fraction after approximately $tU_c/D \approx 100$ in other regions.

5.4 Reduced-order modeling

5.4.1 Zero-dimensional solution

Particle clustering is inherently a three-dimensional process characterized by strong lateral segregation in wall-bounded flows. To assess the effects of clustering on the catalytic conversion process, results from the three-dimensional simulations are compared to a zero-dimensional model that solves for the temporal evolution of the Favre average mass fraction and ignores all spatial variations. Applying the spatial averaging operator $\langle(\cdot)\rangle = \frac{1}{V_f}\int_{V_f}(\cdot)dV_f$ on the three-dimensional scalar transport, Eq. (5.2), yields

$$\frac{\partial \widetilde{Y}_i}{\partial t} + \frac{k_i \widetilde{\varepsilon}_p}{\varepsilon_{p,0}}\widetilde{Y}_i = -\frac{k_i}{\varepsilon_{p,0}}\widetilde{\varepsilon_p'' Y_i''}, \tag{5.9}$$

where we have reintroduced the Favre average notation $\widetilde{(\cdot)} = \langle(\cdot)\varepsilon_f\rho_f\rangle/\langle\varepsilon_f\rho_f\rangle$ in the context of the zero-dimensional averaging operator, with double primes denoting a fluctuation about the Favre average quantity, i.e. $(\cdot)'' = (\cdot) - \widetilde{(\cdot)}$. Because we are considering a constant-density gas phase at steady state, $\langle\varepsilon_f\rho_f\rangle$ is constant and does not appear in Eq. (5.9). The unclosed term $\widetilde{\varepsilon_p'' Y_i''}$ arises from averaging the chemical source term and accounts for fluctuations due to clustering. The homogeneous solution to Eq. (5.9) is given by

$$\widetilde{Y}_i(t) = e^{-t/\tau_i}, \tag{5.10}$$

where $\tau_i = \varepsilon_{p,0}/(k_i\widetilde{\varepsilon}_p)$ is the reaction timescale for species i. The solution provided in Eq. 5.10 yields the temporal evolution of mass fraction given a homogeneous distribution of particles, and thus its deviation from the three-dimensional simulation explicitly accounts for the presence of clusters.

5.4.2 Influence of clusters on the conversion time

The three-dimensional simulations listed in Table 1 are compared to the zero-dimensional solution given by Eq. (5.9) using the corresponding mean reaction timescale τ_i from each case. To assess the performance of the conversion process, the time required to deplete 99% of the reactants predicted by the three-dimensional simulation, t_{99}^{3D}, is compared with the depletion time predicted by the zero-dimensional solution, t_{99}^{0D}. Figure 5.4 shows the effect of Da and Ar on the normalized conversion times for each case. The deviation from the homogeneous solution is observed to increase with increasing Damköhler number, with a maximum of $t_{99}^{3D}/t_{99}^{0D} \approx 1.83$ for Da = 10. At large values of Da, the reaction takes place relatively fast compared to the multiphase flow, too fast for convection and diffusion to aid in the mixing process. Meanwhile, the Archimedes number is observed to have a small impact on the conversion rate.

The discrepancies between the simulation predictions and the homogeneous solutions are accounted for by the fluctuating chemical source term, $\widetilde{\varepsilon_p'' Y_i''}$. In Fig. 5.5, the temporal evolution of the Favre average mass fraction predicted by case A_3 (maximum $t_{\text{res}}^{3D}/t_{\text{res}}^{0D}$) is compared to the corresponding zero-dimensional solutions with and without the fluctuating chemical source term, revealing that an accurate prediction of $\widetilde{\varepsilon_p'' Y_i''}$ is critical when modeling reactive gas-solid flows that exhibit strong spatial segregation in particle concentration. The fluctuating source terms extracted from each simulation are shown in Fig. 5.6. For each case, $\widetilde{\varepsilon_p'' Y_i''}$ peaks at approximately $t/\tau_i \approx 1$, corresponding to the time of maximum decay rate. Due to the non-passive and stochastic nature of the particle-phase volume fraction and its strong coupling with the species mass fraction, modeling $\widetilde{\varepsilon_p'' Y_i''}$ requires careful attention.

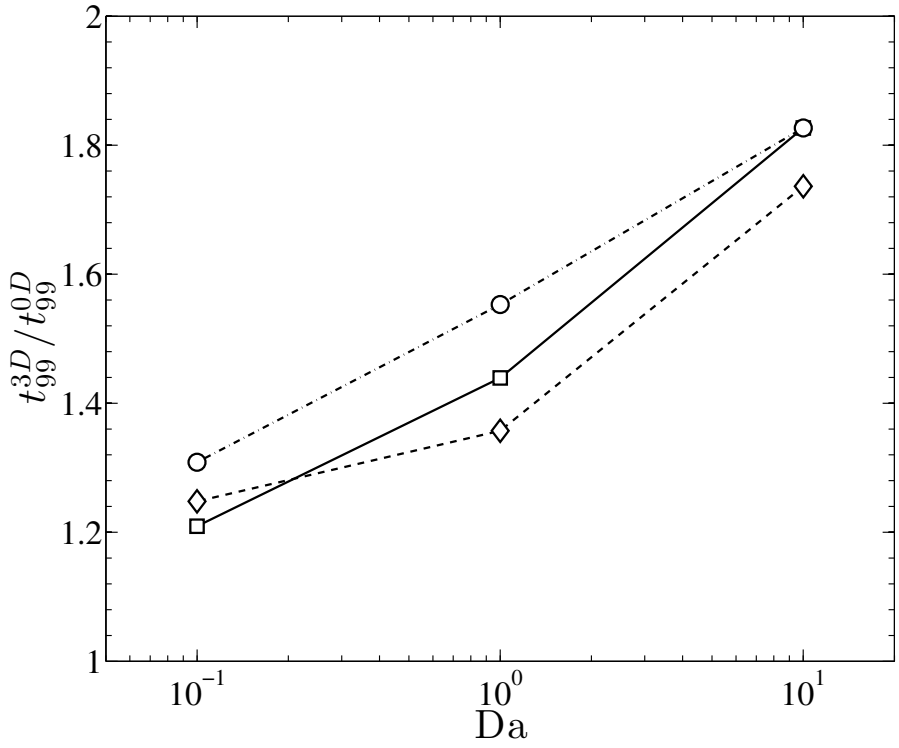

Figure 5.4: Time until 99% of reactants are depleted, normalized by the value predicted by homogeneous solution Eq. (5.10) with Ar = 500 (circles) Ar = 2500 (diamonds), and Ar = 12500 (squares).

5.4.3 Transport of the fluctuating chemical source term

A transport equation for the fluctuating chemical source can be expressed by the following ordinary differential equation

$$\begin{aligned}\frac{\partial}{\partial t}\widetilde{\varepsilon_p'' Y_i''} + \frac{k\widetilde{\varepsilon}_p}{\varepsilon_{p,0}}\widetilde{\varepsilon_p'' Y_i''} = Y_i\widetilde{\boldsymbol{u}_f \cdot \nabla \varepsilon_p''} + D_i\widetilde{\varepsilon_p'' \nabla^2 Y_i''} \\ - \frac{k}{\varepsilon_{p,0}}\left(\widetilde{\varepsilon_p''^2}\widetilde{Y}_i + \widetilde{\varepsilon_p''^2 Y_i''}\right) + \widetilde{Y_i''\frac{\partial \varepsilon_p''}{\partial t}}.\end{aligned} \tag{5.11}$$

The first two terms on the right-hand side of this equation represent sources due to convection and diffusion, respectively. The third and fourth terms account for fluctuations in particle-phase volume fraction. The last term is a correlation between mass fraction fluctuations and the rate of change of volume fraction fluctuations. The relative contributions from each term in Eq. (5.11) are provided in Fig. 5.7. For

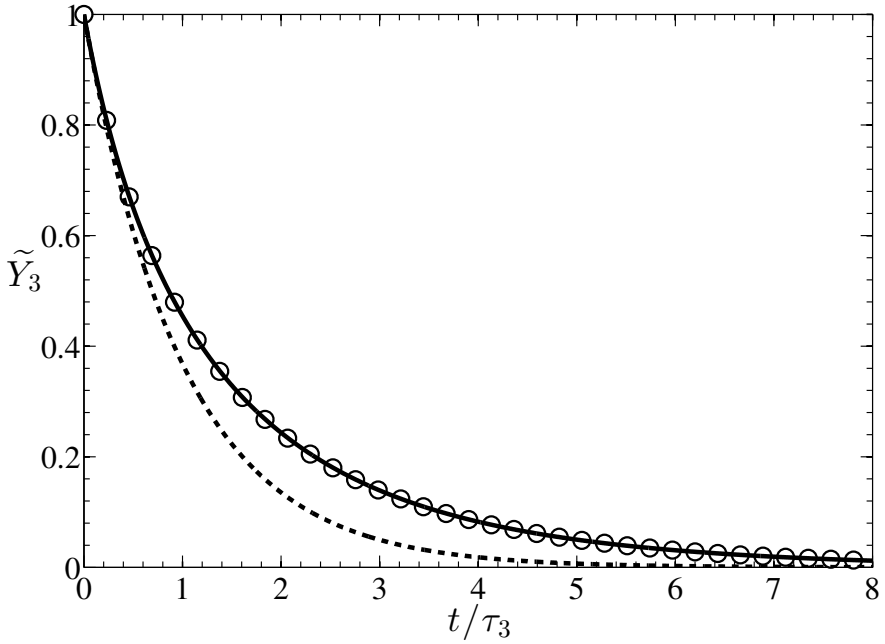

Figure 5.5: Temporal evolution of the species mass fraction for case A_3. Favre average mass fraction (thick solid line), homogeneous solution Eq. (5.10) (thick dashed line), and zero-dimensional model including the fluctuating source term Eq. (5.9) (circles).

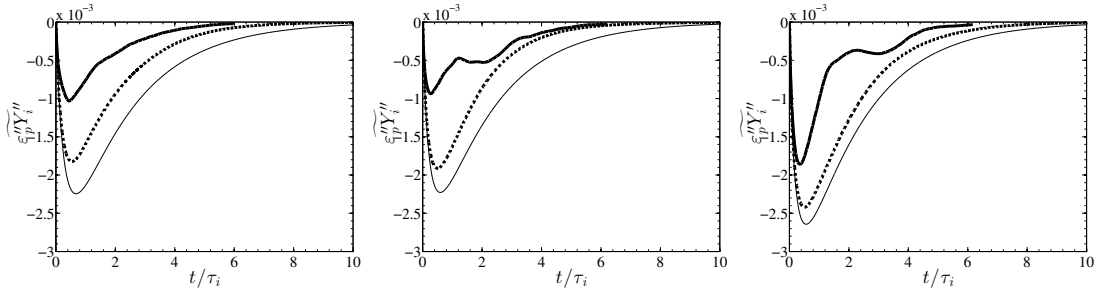

(a) Ar = 500. (b) Ar = 2500. (c) Ar = 12500.

Figure 5.6: Fluctuating chemical source term extracted from the three-dimensional simulations with Da = 0.1 (thick solid line), Da = 1.0 (thick dashed line), and Da = 10 (thin solid line).

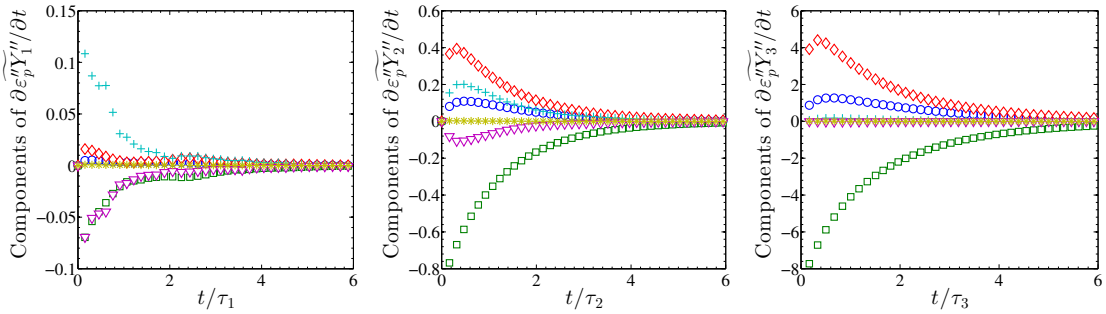

(a) Case B_1. (b) Case B_2. (c) Case B_3.

Figure 5.7: Components of the fluctuating chemical source term Eq. (5.11) for Ar = 2500. $-k_i/\varepsilon_{p,0}\widetilde{\varepsilon}_p\widetilde{\varepsilon_p''Y_i''}$ (blue circles), $Y_i\widetilde{\boldsymbol{u}_f\cdot\nabla\varepsilon_p''}$ (pink triangles), $D_i\widetilde{\varepsilon_p''\nabla^2 Y_i''}$ (yellow stars), $-k_i/\varepsilon_{p,0}\widetilde{Y}_i\widetilde{\varepsilon_p''^2}$ (green squares), $-k_i/\varepsilon_{p,0}\widetilde{\varepsilon_p''^2 Y_i''}$ (red diamonds), and $\widetilde{Y_i''\partial\varepsilon_p''/\partial t}$ (blue crosses).

each case, the diffusive flux is observed to have a negligible contribution, while all other terms contribute to the fluctuating chemical source term in various degrees. When the chemical reaction is sufficiently fast (i.e., Da = 10), convection is seen to have very little influence, but when reactions take place over longer timescales (i.e., smaller Da), the relative importance of convection is higher. Similarly, $\widetilde{Y_i''\partial\varepsilon_p''/\partial t}$ decreases with increasing Da, but with a positive contribution and thus this term inhibits the overall conversion rate. For each case, $-k_i/\varepsilon_{p,0}\widetilde{Y}_i\widetilde{\varepsilon_p''^2}$ has the greatest contribution to the fluctuating chemical source term, and is observed to promote the conversion of species mass fraction, while $-k_i/\varepsilon_{p,0}\widetilde{\varepsilon_p''^2 Y_i''}$ also has a significant impact for each case but reduces the overall conversion rate.

We have demonstrated in our previous work that the empirical model of Issangya *et al.* [151] provides reasonable agreement with the volume fraction variance for a wide range of Ar [7], which can be written in terms of the Favre average concentration as

$$\widetilde{\varepsilon_p''^2} = \left[1.584\widetilde{\varepsilon}_p\left(0.55-\widetilde{\varepsilon}_p\right)\right]^2. \tag{5.12}$$

This expression provides closure for the most significant contribution to the fluctuating chemical source term in Eq. (5.11). Note that a more accurate model for the volume fraction variance based on first-principles, as opposed to an empirical correlation, will be useful in the context of large-eddy simulations, and would require careful analysis of a canonical fluid-particle flow such as the case of fully-developed cluster-induced turbulence recently introduced elsewhere [49]. From Fig. 5.7, it is observed that $\widetilde{\varepsilon_p''^2 Y_i''}$ varies like

$$\widetilde{\varepsilon_p''^2 Y_i''} \approx C \widetilde{\varepsilon_p'' Y_i''} \left(\widetilde{\varepsilon_p''^2} \right)^{1/2}, \tag{5.13}$$

where C is a modeling constant. In Fig. 5.8, the proposed models are compared to results from each simulation case, showing overall good agreement. For smaller Da, contributions from convection and the rate of change in volume fraction fluctuations in the transport of the fluctuating chemical source term become important. Providing models for all of the relevant terms becomes challenging, and alternative modeling approaches should be explored.

5.4.4 Presumed shape PDF approach

The fluctuating chemical source term can be calculated provided the density field is known, i.e.,

$$\widetilde{\varepsilon_p'' Y_i''} = \int \int (\varepsilon_p - \widetilde{\varepsilon}_p)(Y_i - \widetilde{Y}_i) \widetilde{f}\left(\varepsilon_p, Y_i\right) d\varepsilon_p dY_i, \tag{5.14}$$

where $\widetilde{f}(\varepsilon_p, Y_i)$ is the Favre average joint-PDF, given by

$$\widetilde{f}\left(\varepsilon_p, Y_i\right) = \frac{\langle \varepsilon_f \rho_f | \varepsilon_p, Y_i \rangle}{\langle \varepsilon_f \rho_f \rangle} f\left(\varepsilon_p, Y_i\right), \tag{5.15}$$

with $f\left(\varepsilon_p, Y_i\right)$ the joint-PDF of particle volume fraction and species mass fraction. The temporal evolution of the Favre average joint-PDF is given in Fig. 5.9 for case

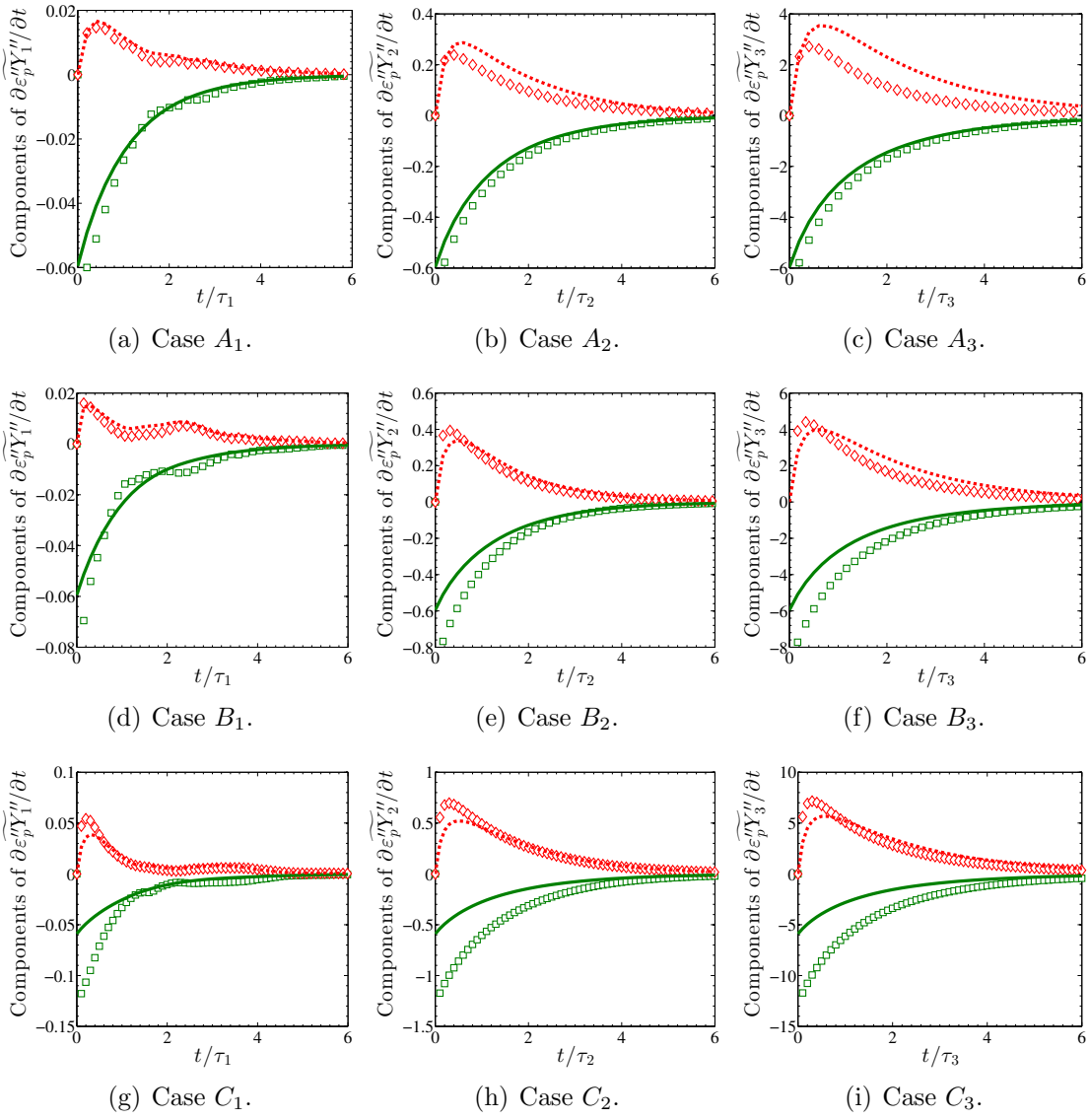

(a) Case A_1. (b) Case A_2. (c) Case A_3.

(d) Case B_1. (e) Case B_2. (f) Case B_3.

(g) Case C_1. (h) Case C_2. (i) Case C_3.

Figure 5.8: Models for selected components of the fluctuating chemical source term (lines) against simulation results (symbols). $-k_i/\varepsilon_{p,0}\widetilde{Y}_i\widetilde{\varepsilon_p''^2}$ (green squares), variance modeled using Eq. (5.12) (green line), $-k_i/\varepsilon_{p,0}\widetilde{\varepsilon_p''^2 Y_i''}$ (red diamonds), Eq. (5.13) with $C = 3$ (red dashed-line).

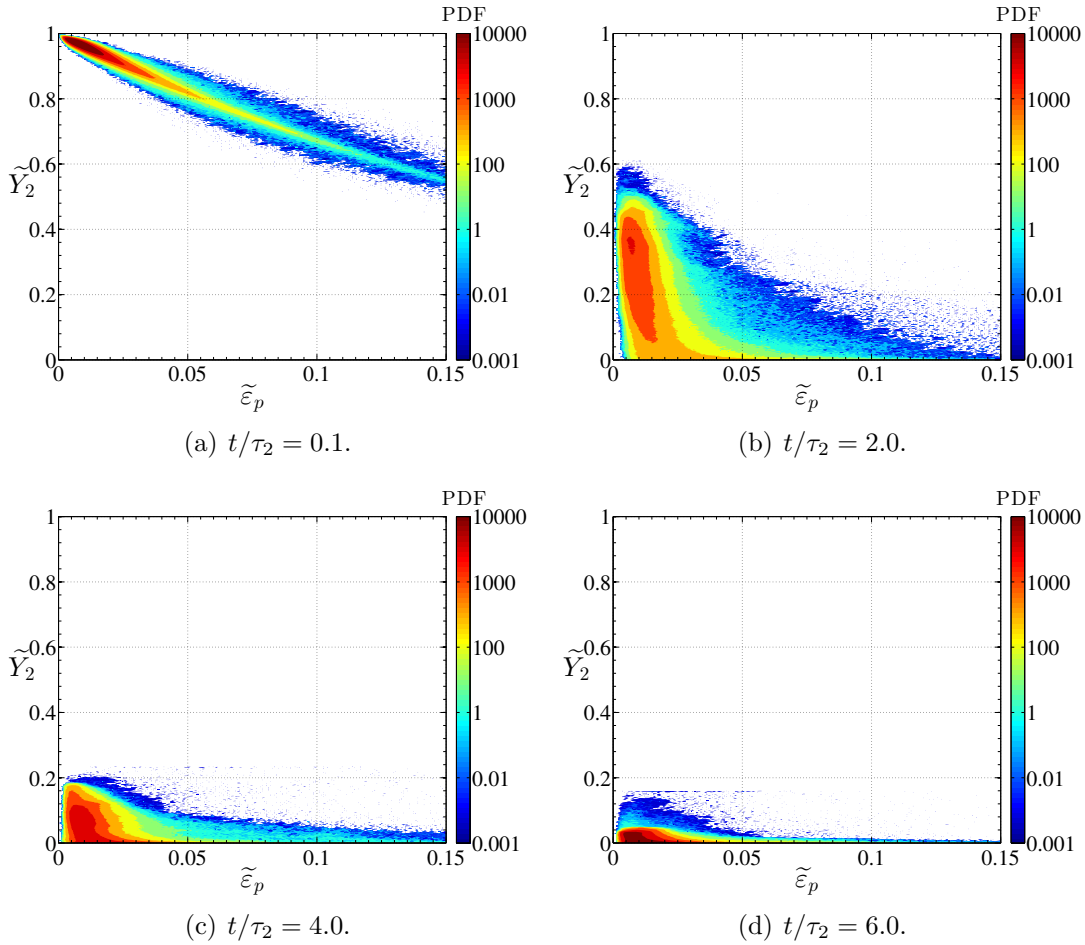

(a) $t/\tau_2 = 0.1$. (b) $t/\tau_2 = 2.0$.

(c) $t/\tau_2 = 4.0$. (d) $t/\tau_2 = 6.0$.

Figure 5.9: Instantaneous Favre average joint-PDFs of particle concentration and species mass fraction for case B_2.

B_2. Because the gas-solid flow is at steady state and there is no feedback from the chemical species, the mean volume fraction remains constant throughout the duration of the simulation. Meanwhile, the Favre average species mass fraction is strongly coupled with both particle concentration and time. Making use of Bayes' theorem, the joint-PDF can be rewritten as

$$\widetilde{f}\left(\varepsilon_p, Y_i\right) = \widetilde{f}\left(Y_i|\varepsilon_p\right)\widetilde{g}\left(\varepsilon_p\right), \tag{5.16}$$

where the conditional PDF $\widetilde{f}(Y_i|\varepsilon_p)$ and volume fraction PDF $\widetilde{g}\left(\varepsilon_p\right)$ may be modeled based on a presumed distribution.

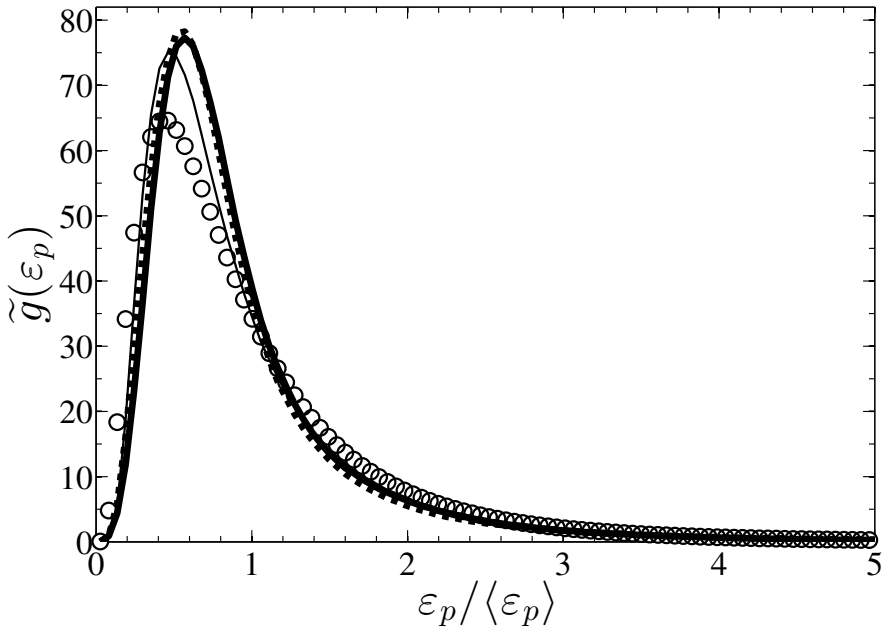

Figure 5.10: Instantaneous Favre average PDF of particle concentration. Ar = 500 (solid line), Ar = 2500 (dashed line), Ar = 12500 (thin solid line), and the corresponding lognormal distribution (Eq. (5.17)) using the correlation provided by Issangya *et al.* [151] for modeling the variance (circles).

Modeling the volume fraction PDF

We have demonstrated in our previous work that the PDF of particle-phase volume fraction in CFB risers closely resembles a lognormal distribution for a wide range of Ar [7]. Using the instantaneous Favre average concentration $\widetilde{\varepsilon}_p$ and making use of Eq. (5.12), the volume fraction PDF can be modeled as

$$\widetilde{g}(\varepsilon_p) = \frac{1}{\varepsilon_p \sigma_{\ln}\sqrt{2\pi}} \exp\left[-\frac{(\ln \varepsilon_p - \mu_{\ln})^2}{2\sigma_{\ln}^2}\right], \tag{5.17}$$

where $\mu_{\ln} = \ln\left[\widetilde{\varepsilon}_p^2 / \left(\widetilde{\varepsilon_p''^2} + \widetilde{\varepsilon}_p^2\right)^{1/2}\right]$ and $\sigma_{\ln} = \left[\ln\left(1 + \widetilde{\varepsilon_p''^2}/\widetilde{\varepsilon}_p\right)\right]^{1/2}$. A comparison between $\widetilde{g}(\varepsilon_p)$ extracted from the simulations with the corresponding lognormal distribution using the model of Issangya *et al.* [151] for the variance is given in Fig. 5.10, showing overall very good agreement.

Modeling the conditional PDF

In non-premixed combustion, the beta PDF has been used in numerous studies to model the mixture fraction distribution of both constant and variable-density flows with much success (see e.g., [182–186]). Recent studies suggest that the beta distribution is also capable of capturing mixing of active scalars in variable-density, buoyancy-driven (or other pressure-gradient-driven) turbulence [187]. However, it remains unclear whether such an approach can be applied to reactive particle-laden flows.

Assuming the species mass fraction is well represented by a beta distribution, the conditional PDF can be written in terms of two parameters a and b as

$$\widetilde{f}\left(Y_i|\varepsilon_p\right) = \frac{(Y_i|\varepsilon_p)^{a-1}(1-Y_i|\varepsilon_p)^{b-1}}{B\left(a,b\right)}, \tag{5.18}$$

which is bounded by $0 \leq Y_i \leq 1$. In Eq. (5.18), $B(a,b)$ is a normalization constant to ensure $\widetilde{f}\left(Y_i|\varepsilon_p\right)$ integrates to unity, given by the beta function

$$B\left(a,b\right) = \int_0^1 y^{a-1}(1-y)^{b-1}dy. \tag{5.19}$$

The two parameters a and b are related to the conditional moments by

$$a = \widetilde{Y}_i|\varepsilon_p \left[\frac{\widetilde{Y}_i|\varepsilon_p(1-\widetilde{Y}_i|\varepsilon_p)}{\widetilde{Y_i''^2}|\varepsilon_p} - 1\right], \tag{5.20}$$

and

$$b = (1-\widetilde{Y}_i|\varepsilon_p)a. \tag{5.21}$$

Using the conditional moments extracted from case B_2, Fig. 5.11 demonstrates the capability of the beta distribution to reproduce the conditional PDF, showing overall excellent agreement. Due to the conditional dependence on the volume fraction, the parameters a and b must be known for every value of ε_p at each time t. In non-premixed combustion problems, conditional moment closure (CMC)

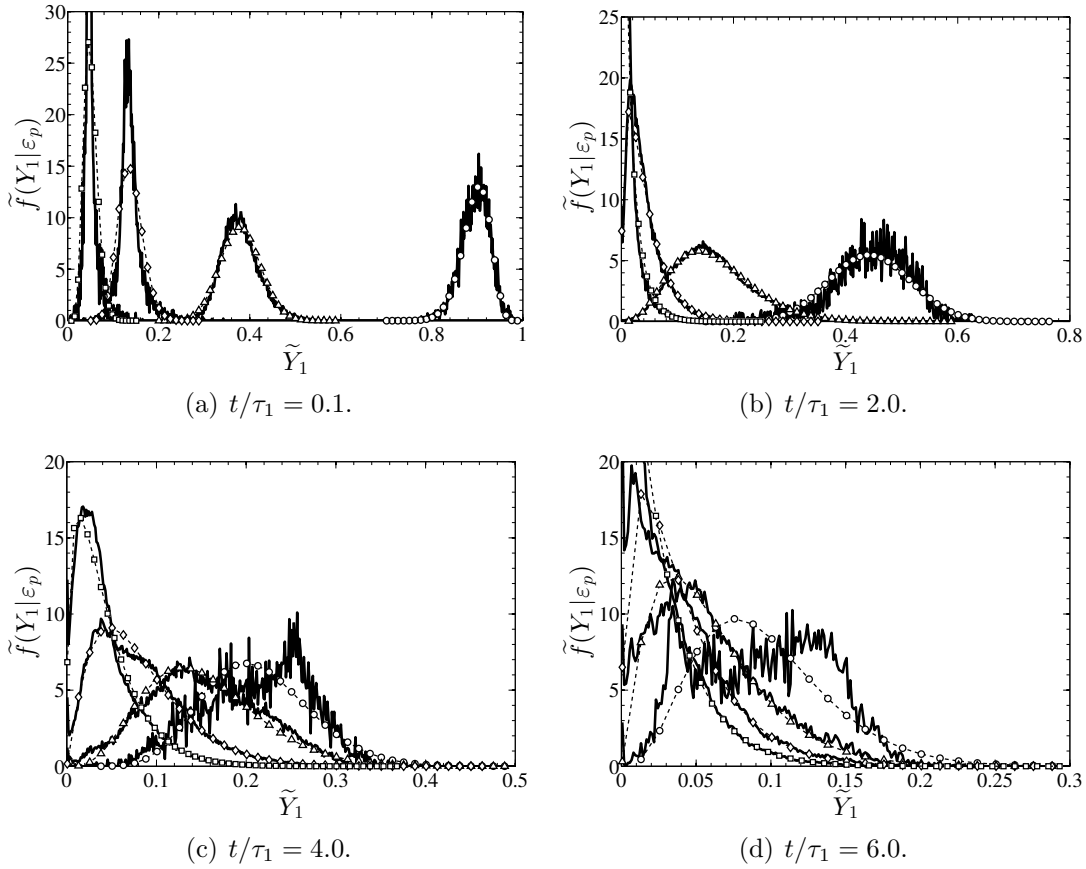

(a) $t/\tau_1 = 0.1$. (b) $t/\tau_1 = 2.0$.

(c) $t/\tau_1 = 4.0$. (d) $t/\tau_1 = 6.0$.

Figure 5.11: Instantaneous conditional PDFs of species mass fraction from case B_1 (solid line) compared to their corresponding beta distributions (symbols) as a function of ε_p. (a) $\varepsilon_p = .001$ (circles), $\varepsilon_p = .025$ (triangles), $\varepsilon_p = .05$ (diamonds), $\varepsilon_p = .075$ (squares). (b) $\varepsilon_p = .001$ (circles), $\varepsilon_p = .01$ (triangles), $\varepsilon_p = .018$ (diamonds), $\varepsilon_p = .025$ (squares). (c) $\varepsilon_p = .001$ (circles), $\varepsilon_p = .003$ (triangles), $\varepsilon_p = .006$ (diamonds), $\varepsilon_p = .01$ (squares). (d) $\varepsilon_p = .001$ (circles), $\varepsilon_p = .003$ (triangles), $\varepsilon_p = .043$ (diamonds), $\varepsilon_p = .006$ (squares).

methods have been used to derive and model equations for the conditional moments of reactive scalars with encouraging success [188]. Modeling $\widetilde{Y}_i|\varepsilon_p$ and $\widetilde{Y_i''^2}|\varepsilon_p$ with CMC methods would require knowledge of the fluid velocity and scalar dissipation conditioned on the particle-phase volume fraction and is beyond the scope of this work.

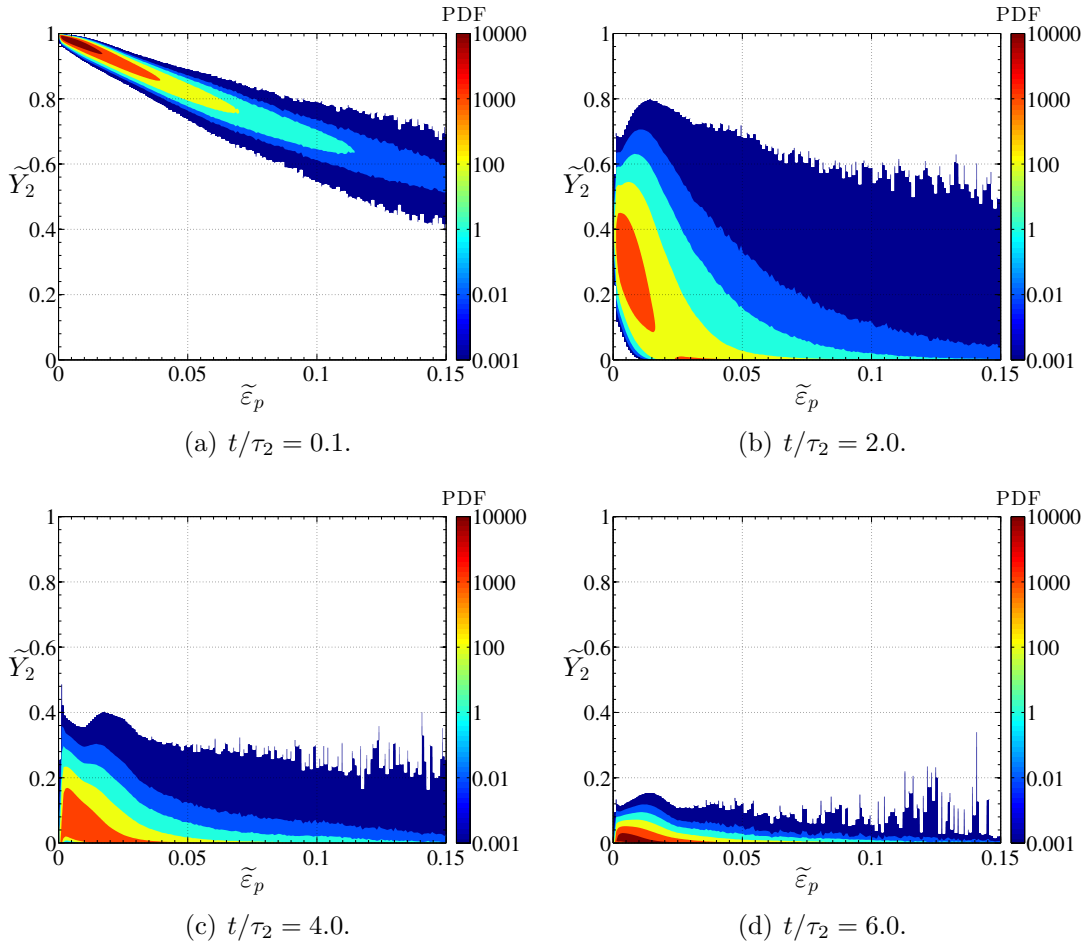

(a) $t/\tau_2 = 0.1$. (b) $t/\tau_2 = 2.0$.

(c) $t/\tau_2 = 4.0$. (d) $t/\tau_2 = 6.0$.

Figure 5.12: Model of the instantaneous Favre average joint-PDFs for case B_2.

Validation of the presumed PDF strategy

The fluctuating chemical source term that appears in the zero-dimensional scalar transport, Eq. (5.9), is closed via Eq. (5.14), where the Favre average joint-PDF is modeled as a product of a beta distribution for the conditional mass fraction and a lognormal distribution for the particle-phase volume fraction. The volume fraction variance is modeled using the correlation by Issangya *et al.* [151], and the conditional moments are obtained from the three-dimensional simulations. Figure 5.12 shows the modeled Favre average joint-PDF as a function of time for case

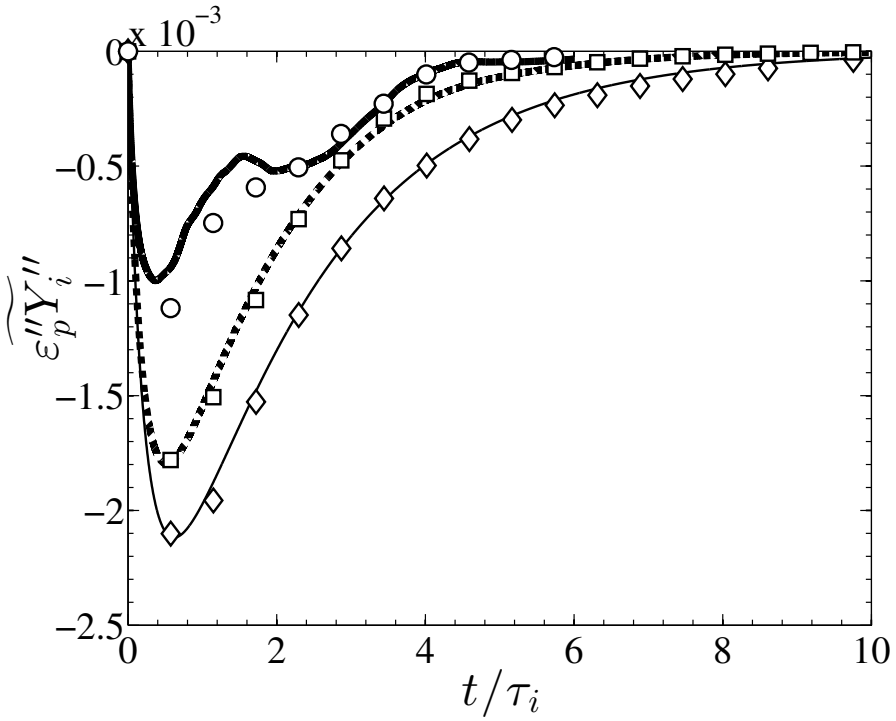

Figure 5.13: Temporal evolution of $\widetilde{\varepsilon_p'' Y_i''}$ for Ar = 2500 extracted from simulations (lines) and presumed-shape PDF model (symbols). Case B_1 (solid line) and corresponding model (circles), case B_2 (dashed line) and corresponding model (squares), and case B_3 (thin solid line) and corresponding model (diamonds).

B_2. The model shows excellent agreement with the joint-PDF predicted by the simulation in Fig. 5.9. Figure 5.13 shows that the PDF model provides an excellent representation of the volume fraction-mass fraction correlation for the range of Da considered in this study.

5.5 Conclusions

The turbulent and multiphase nature of riser reactors will often lead to strong segregation of catalytic particles in the form of dense clusters. It is hypothesized that the non-homogeneity in particle concentration will affect the conversion pro-

cess, rendering optimal operation difficult to achieve since a much higher catalyst loading will be necessary to obtain the desired level of conversion. The aim of this study was to investigate the effect of clusters on the conversion process and develop a reduced-order model that takes these effects into account. In order to formulate a tractable system of equations that accounts for key physical processes of the flow, a volume-filtering operator was applied to the microscale equations of motion. The equations were discretized in an Eulerian-Lagrangian framework and applied to flows of isothermal, linearly-reacting chemical species in fully-developed three-dimensional risers. The Archimedes number, Ar, was varied by a factor of 25, $500 \leq \mathrm{Ar} \leq 12500$, and the Damköhler number, Da, by a factor of 100, $0.1 \leq \mathrm{Da} \leq 10$. Key findings from this work include:

- The PDF of particle-phase volume fraction in fully-developed risers closely resembles a lognormal distribution with a concentration variance modeled using the correlation of Issangya *et al.* [151];
- To assess the impact of clusters on the heterogeneous reaction, a zero-dimensional model that solves for the temporal evolution of the Favre average mass fraction was derived. The correlation between fluctuating mass fraction and volume fraction entirely accounts for the discrepancy between the zero-dimensional model and three-dimensional results;
- Clusters are found to delay the conversion process by up to 85%, with greater impact at higher Da;
- A transport equation for the fluctuating chemical source term was derived, and the correlation of Issangya *et al.* [151] was used to model the two largest contributions, showing overall very good agreement;
- An initial attempt at providing closure for the fluctuating chemical source

term in the zero-dimensional model was obtained by applying a presumed-shape PDF model, where the Favre average joint-PDF is given by a product of a beta distribution for the species mass fraction and a lognormal distribution for the particle concentration. The model yields excellent results for the range of Ar and Da considered in this study.

In practice, riser reactors contain both a population of deactivated catalysts that are trapped in clusters as well as freshly re-injected particles. In future studies, it would be necessary to account for deactivation of catalytic particles that have been exposed to volatiles for a sufficiently long period of time, which is likely to further reduce the conversion efficiency of the reactor, and further amplify the role played by clusters.

CHAPTER 6

COLLISIONAL PARTICLE DYNAMICS IN CLUSTER-INDUCED TURBULENCE

6.1 Abstract

We present a computational study of cluster-induced turbulence (CIT), where the production of fluid-phase kinetic energy results entirely from momentum coupling with finite-size inertial particles. A separation of length scales must be established when evaluating the particle dynamics in order to distinguish between the continuous mesoscopic velocity field and the uncorrelated particle motion. To accomplish this, an adaptive spatial filter is employed on the Lagrangian data with an averaging volume that varies with the local particle-phase volume fraction. This filtering approach ensures sufficient particle sample sizes in order to obtain meaningful statistics while remaining small enough to avoid capturing variations in the mesoscopic particle field. Two-point spatial correlations are computed to assess the validity of the filter in extracting meaningful statistics. The method is used to investigate, for the first time, the properties of a statistically stationary gravity-driven particle-laden flow, where particle-particle and fluid-particle interactions control the multiphase dynamics. Results from fully developed CIT show a strong correlation between the local volume fraction and the granular temperature, with maximum values located at the upstream boundary of clusters (i.e., where maximum compressibility of the particle velocity field exists), while negligible particle agitation is observed within clusters.

6.2 Introduction

The non-trivial interphase coupling encountered in disperse two-phase flows can often lead to a high degree of segregation from an initially homogeneous distribution of particles. For example, when subjected to turbulence, the disperse phase may be ejected from regions of high vorticity and accumulate in regions of high strain (e.g., [20], and references therein), and under the influence of gravity, momentum coupling between the phases may lead to the spontaneous generation of dense clusters (e.g., [6, 7]). In fluidized bed reactors, clusters have been observed to reduce mixing and interaction of particles with the transport gas [127], and may therefore inhibit reaction rates and heat transfer, potentially lowering operating efficiencies significantly. Meanwhile, a fundamental understanding of cluster characteristics and their effect on the carrier phase remains elusive.

In the context of high-inertia particles with response times that are long compared with the characteristic time scale of the turbulence, individual particle trajectories will retain information from previous collisions and interactions with distant turbulent eddies, causing them to deviate from fluid pathlines [2]. The velocities of neighboring particles may therefore be uncorrelated, while ensembles of particles collectively respond to large-scale motions of the flow. Dasgupta et al. [189] first suggested that the fluctuating particle motion can be partitioned into a smooth (continuous) field and a random component at the particle scale referred to as the granular temperature. Later, Février et al. [190] provided an exact definition and a computational methodology for partitioning of the correlated and uncorrelated contributions to the total particle-phase kinetic energy. In a recent study, Fox [47] provided a rigorous derivation of a Reynolds-average turbulence model for collisional fluid-particle flows, demonstrating that the transport equations must contain

separate models for these two contributions. It was shown that new turbulence production terms arise due to correlations between the particle-phase volume fraction and fluid-phase velocity fluctuations. At sufficient mass loadings, the fluid-particle correlations become significant in systems with large variations in particle concentration. In the absence of mean shear, the production of fluid-phase kinetic energy results entirely from momentum coupling between the phases, referred to as cluster-induced turbulence (CIT).

Various mechanisms responsible for the spatial segregation of particles have been studied extensively in the last two decades. In purely granular systems, clustering is enhanced via inelastic dissipation [4, 191] and attenuated via friction [192, 193] during interparticle contact. In the presence of a carrier phase, viscous damping by the fluid results in clustering of non-dissipative particles [194]. In a recent study, Yin et al. [195] compared the relative contributions of these instabilities in dissipative gas-solid systems. One of the most widely investigated mechanisms is preferential concentration of particles by coherent vortical structures, first realized numerically by Eaton and Fessler [5]. Preferential concentration occurs in the absence of a mean velocity difference between the phases and is most obvious for dilute flows with low mass loading. When fluid-particle systems are subjected to a mean body force (e.g., gravity), the relative motion between the phases leads to additional sources of instability as a result of interphase coupling [3], giving rise to CIT. While progress in understanding dissipative instabilities and preferential concentration continues to be made, much less is known about CIT. The production of large-scale fluid turbulence from particle clusters was first observed in simulations of a two-dimensional vertical channel by Tsuji et al. [196]. In our previous work [7], it was demonstrated that the cluster size distribution in wall-bounded flows is constrained by the flow geometry. It was also

shown that the multiphase dynamics in two dimensions differs significantly from three-dimensional flow. Three-dimensional homogeneous flows therefore represent the simplest configuration to study fully-developed CIT.

With the availability of increasing computational resources, detailed simulations are now able to capture such phenomena at moderate Reynolds numbers and particle concentrations. In order to develop an improved understanding of the fundamental nature of such flows, and to exploit these simulations to aid in model development, it is necessary to extract local instantaneous information in a consistent and accurate manner. The objective of the present work is to evaluate the spatial characteristics of finite-size inertial particles in a fully-coupled turbulent flow, where interparticle collisions and momentum coupling between the phases control the flow dynamics. Fully developed gravity-driven CIT is simulated via an Eulerian-Lagrangian framework, where the unsteady fluid motion is sufficiently captured by the mesh and the two phases are coupled through the resolved contributions of the fluid stresses and a drag term. An adaptive spatial filter is introduced which accurately decouples the instantaneous particle-phase turbulent kinetic energy from the granular temperature, providing for the first time access to the local instantaneous spatial distribution of these separate contributions in an Eulerian framework.

6.3 Volume-filtered Euler-Lagrange formalism

In order to resolve the relevant length scales associated with fully-developed CIT while remaining computationally tractable, we employ a mesoscopic formulation based on volume filtering to describe the fluid-particle system. The mesoscale de-

scription of fluid-particle flows refers to a set of equations that explicitly captures the physics associated with length scales larger than the individual particles and models the processes at the particle scale. Unlike in particle-resolved direct numerical simulation (DNS) where the boundary layers are solved around individual particles (see e.g., [25]), in mesoscopic formulations the two phases are coupled via momentum exchange terms (e.g., a drag model) [19]. This level of modeling is similar to large-eddy simulation (LES) of single-phase turbulence, where the large-scale unsteady motions are represented explicitly and the effects of the smaller-scale motions are modeled. However, unlike in LES, these small-scale motions are not universal, and fluid-phase velocity fluctuations may arise from granular agitation at the particle scale, due, for example, to wakes and interparticle collisions. Given an accurate and consistent set of models for the particle-scale dynamics, and assuming that mesoscale structures in the flow (e.g., clusters) are sufficiently resolved and are responsible for generating the majority of fluid-phase velocity fluctuations, this framework has been shown to accurately reproduce the relevant physics in two-way coupled fluid-particle flows [7, 45].

6.3.1 Description of the system

To isolate the effect of turbulence generated by interphase coupling, we consider a flow initially at rest laden with a random distribution of finite-size particles of diameter d_p subject to gravity. The physical parameters are chosen to correspond to typical gas-solid flows encountered in engineering and environmental applications. The dimensionless two-phase parameters that characterize the flow include the particle to fluid density ratio $\rho_p/\rho_f = 1000$, the average particle-phase volume fraction $\langle \varepsilon_p \rangle = 0.01$, and the Reynolds number $\mathrm{Re} = \tau_p g d_p/\nu_f = 1$, where

$\tau_p = \rho_p d_p^2/(18\rho_f \nu_f)$ is the particle response time, ν_f is the fluid-phase kinematic viscosity, and g is the magnitude of the gravity vector $\boldsymbol{g}$. Combination of these non-dimensional numbers yields the mass loading $\phi = \rho_p\langle\varepsilon_p\rangle/(\rho_f\langle\varepsilon_f\rangle) = 10$, where $\langle\varepsilon_f\rangle = 1 - \langle\varepsilon_p\rangle$ is the average fluid-phase volume fraction. To obtain an *a priori* measure of the mesoscale features that arise due to the coupling between the phases, previous studies have introduced a characteristic length scale $\mathcal{L} = \tau_p^2 g$ (see e.g., [6, 133, 197]). This length scale is used in this work to ensure an appropriate domain size such that the effect of the periodic boundary conditions is minimized. The simulation is solved on a triply periodic domain of dimensions $64\mathcal{L}\times16\mathcal{L}\times16\mathcal{L}$, with a mesh size of $2048 \times 512 \times 512$, corresponding to a uniform grid spacing of $\Delta x = 1.75 d_p$ with 55×10^6 particles.

6.3.2 Gas-solid description

The flow of solid spherical particles suspended in an incompressible carrier fluid is solved in an Eulerian-Lagrangian framework, where the displacement of an individual particle i is calculated using Newton's second law of motion,

$$\frac{d\boldsymbol{u}_p^{(i)}}{dt} = \boldsymbol{\mathcal{A}}^{(i)} + \boldsymbol{F}_c^{(i)} + \boldsymbol{g}, \tag{6.1}$$

where $\boldsymbol{u}_p = (u_p, v_p, w_p)$ is the instantaneous particle velocity vector, $\boldsymbol{\mathcal{A}}$ is the interphase exchange term, and $\boldsymbol{F}_c$ is the collision force modeled using a modified soft-sphere approach originally proposed by Cundall and Strack [64]. In this work, we consider inelastic collisions with a coefficient of restitution e = 0.9. The interphase exchange term is given by

$$\boldsymbol{\mathcal{A}}^{(i)} = \frac{1}{\tau_p}\left(\boldsymbol{u}_f[\boldsymbol{x}_p^{(i)}] - \boldsymbol{u}_p^{(i)}\right) - \frac{1}{\rho_p}\nabla p_f^{\star}[\boldsymbol{x}_p^{(i)}] + \frac{1}{\rho_p}\nabla\cdot\boldsymbol{\sigma}_f[\boldsymbol{x}_p^{(i)}], \tag{6.2}$$

where the fluid-phase velocity vector $\boldsymbol{u}_f = (u_f,\, v_f,\, w_f)$, modified pressure gradient $\nabla p_f^\star$ and divergence of the viscous stress tensor $\nabla \cdot \boldsymbol{\sigma}_f$ are taken at $\boldsymbol{x}_p^{(i)}$, the center position of particle i. The term $\nabla p_f^\star$ is a body force that contains the hydrodynamic pressure p_f and is adjusted dynamically in order to maintain statistically stationary CIT. In real systems with moderate Reynolds numbers and particle volume fractions, the particles will experience drag with a non-linear dependence on these terms (e.g., [81]), but for consistency with Fox [47], the higher-order terms are neglected here. To account for the presence of the particle phase in the fluid without requiring resolution of the boundary layers around individual particles, a volume filter is applied to the constant-density Navier-Stokes equations [70], thereby replacing the point variables (fluid velocity, pressure, etc.) by smoother, locally filtered fields. The resulting fluid-phase equations are given by

$$\frac{\partial \varepsilon_f}{\partial t} + \nabla \cdot (\varepsilon_f \boldsymbol{u}_f) = 0, \tag{6.3}$$

and

$$\frac{\partial \varepsilon_f \boldsymbol{u}_f}{\partial t} + \nabla \cdot (\varepsilon_f \boldsymbol{u}_f \otimes \boldsymbol{u}_f) = -\frac{1}{\rho_f}\nabla p_f^\star + \frac{1}{\rho_f}\nabla \cdot \boldsymbol{\sigma}_f - \frac{\rho_p}{\rho_f}\varepsilon_p \widetilde{\boldsymbol{\mathcal{A}}} + \varepsilon_f \boldsymbol{g}. \tag{6.4}$$

The relationship between the interphase exchange term seen by the fluid $\widetilde{\boldsymbol{\mathcal{A}}}$, and that seen by an individual particle i, $\boldsymbol{\mathcal{A}}^{(i)}$, will be made explicit in §6.3.3. Further details on the numerical implementation can be found in [45].

6.3.3 Two-way coupling

To interpolate the fluid variables to the particle location, a second-order trilinear interpolation scheme is used. To extrapolate the particle data back to the Eulerian mesh, we apply the volume filtering approach used in deriving the fluid-phase equations of motion (6.3)–(6.4). We begin by defining a filtering kernel G with a

characteristic length δ_f, such that $G(r) > 0$ decreases monotonically with increasing r, and is normalized such that it integrates to unity. Given a quantity $A^{(i)}(t)$ located at the center of particle i at time t, and assuming that G does not vary significantly over the volume of the particle (i.e., $\delta_f \gg d_p$), its Eulerian projection is given by

$$\varepsilon_p \widetilde{A}(\boldsymbol{x}, t) \approx \sum_{i=1}^{N_p} A^{(i)}(t) G(|\boldsymbol{x} - \boldsymbol{x}_p^{(i)}|) V_p, \tag{6.5}$$

where N_p is the total number of particles in a single realization of the flow and $V_p = \pi d_p^3/6$ is the particle volume. This expression replaces the discontinuous Lagrangian data with an Eulerian field that is a smooth function of the spatial coordinate $\boldsymbol{x}$. Using Eq. (6.5) with $A^{(i)} = 1$, we obtain the particle volume fraction ε_p, and $A^{(i)} = \boldsymbol{\mathcal{A}}^{(i)}$ gives the momentum exchange term $\widetilde{\boldsymbol{\mathcal{A}}}$ seen by the fluid in Eq. (6.4).

It should be noted that Eq. (6.5) will only yield useful information if the spatial variations in the particle field can be decomposed into contributions on a scale comparable with the particle spacing, and a much larger scale corresponding to mesoscopic features in the flow (e.g., clusters), provided that the filter size δ_f is within these scales. For ratios of $\Delta x/d_p \approx 1$, a brute-force implementation of Eq. (6.5) would require looping through a large number of cells for each particle, making this operation prohibitively expensive. Therefore, the filtering procedure is solved in two steps [45]. First, the particle data is transferred to the nearest neighboring neighboring cells via trilinear extrapolation. The data is then diffused such that the final width of the filtering kernel is independent of the mesh size. In this work, G is taken to be Gaussian with a characteristic length scale $\delta_f = 8d_p$, defined as the full width at half the height of the kernel. This value of δ_f will be justified in §6.4.3. To keep the cost low and ensure unconditional stability, the diffusion process is solved in a single implicit step by utilizing the approximate

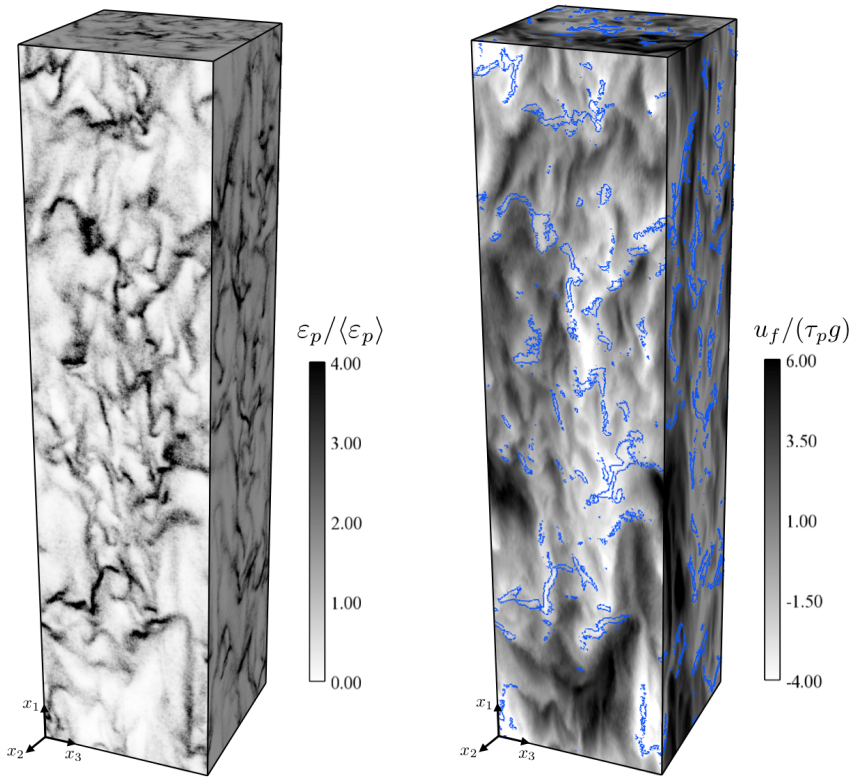

(a) Particle-phase volume fraction.

(b) Vertical component of the fluid velocity with iso-contours of ε_p=3$\langle\varepsilon_p\rangle$ shown in blue.

Figure 6.1: Instantaneous field of fully-developed CIT.

factorization scheme of Briley and McDonald [198].

6.4 Results and discussion

6.4.1 Degree of particle segregation

The simulation is run until the initial transient is complete and the flow reaches a statistically stationary state. Throughout this study, the subscript '1' is used to denote components in the streamwise (gravity-aligned) direction, and the spanwise

directions are denoted by subscripts '2' and '3'. As depicted in Fig. 6.1(a), the resulting particle field is highly unsteady with strong segregation in volume fraction. Figure 6.1(b) suggests that the fluid phase is entrained by the clusters, leading to strong vertical velocities in dilute regions of the flow. This behavior is evident in Fig. 6.2(a), where the vertical slip velocity between the phases is observed to decrease with increasing volume fraction. The degree of particle segregation can be quantified by the probability density function (PDF) of the particle volume fraction [116]. For a homogeneous distribution of particles, the PDF is given by the discrete Poisson distribution [152]. As seen in Fig. 6.2(b), the instantaneous particle field displays a higher frequency of regions containing more particles, as well as regions devoid of particles, in comparison to the Poisson distribution, indicative of a highly clustered field. Moreover, using the mean and variance particle volume fraction extracted from the simulation, the form of the PDF is seen to closely resemble a lognormal distribution, indicating a potential opportunity for future modeling efforts.

6.4.2 Spatial decomposition of the particle velocity field

The averaging operator $\langle(\cdot)\rangle$ is used throughout to denote a particle average when applied to a Lagrangian quantity and a volume average when applied to an Eulerian quantity. Due to the statistical stationarity of the flow, $\langle(\cdot)\rangle$ is neither a function of the spatial coordinate $\boldsymbol{x}$ nor of time t at steady state. For a single realization of the flow, the total particle-phase fluctuating energy is given by

$$\kappa_p = \frac{1}{2}\langle \boldsymbol{u}_p' \cdot \boldsymbol{u}_p' \rangle, \tag{6.6}$$

where $\boldsymbol{u}_p' = \boldsymbol{u}_p - \langle \boldsymbol{u}_p \rangle$ is the total fluctuation in particle velocity with the property $\langle \boldsymbol{u}_p' \rangle = 0$. In order to decompose κ_p into its spatially correlated contribution

and fluctuations at the particle scale, the volume filtering procedure discussed in §6.3.3 is employed. By applying $A^{(i)} = \boldsymbol{u}_p^{(i)}$ in Eq. (6.5), we obtain the local mean particle velocity $\widetilde{\boldsymbol{u}}_p$ in an Eulerian frame of reference. Analogous to Favre averaging in variable-density flows, the phase average (PA) denoted by $\langle(\cdot)\rangle_p = \langle\varepsilon_p(\cdot)\rangle/\langle\varepsilon_p\rangle$ is useful in multiphase modeling. Note that PA Eulerian terms are identical to particle-average Lagrangian terms, e.g. $\langle\widetilde{\boldsymbol{u}}_p\rangle_p = \langle\boldsymbol{u}_p\rangle$. Fluctuations about the PA velocity are expressed as $\widetilde{\boldsymbol{u}}_p''(\boldsymbol{x},t) = \widetilde{\boldsymbol{u}}_p(\boldsymbol{x},t) - \langle\widetilde{\boldsymbol{u}}_p\rangle_p$, with $\langle\widetilde{\boldsymbol{u}}_p''\rangle_p = 0$. It is important to note that $\boldsymbol{u}_p' \neq \widetilde{\boldsymbol{u}}_p''$, and therefore $\langle\widetilde{\boldsymbol{u}}_p''\rangle \neq 0$ in general. Using this definition, the PA particle turbulent kinetic energy is defined as

$$k_p = \frac{1}{2}\langle\widetilde{\boldsymbol{u}}_p'' \cdot \widetilde{\boldsymbol{u}}_p''\rangle_p. \tag{6.7}$$

A quantitative measure of the local uncorrelated particle agitation is given by the granular temperature Θ, which is defined using the residual component of the instantaneous particle velocity,

$$\Theta(\boldsymbol{x},t) = \frac{1}{3}\widetilde{\boldsymbol{\delta u}_p(t) \cdot \boldsymbol{\delta u}_p(t)}, \tag{6.8}$$

where $\boldsymbol{\delta u}_p(t) = \boldsymbol{u}_p(t) - \widetilde{\boldsymbol{u}}_p[\boldsymbol{x}_p(t),t]$. With these definitions, the total particle-phase fluctuating energy κ_p corresponds to the sum of the PA turbulent kinetic energy k_p and the PA granular temperature $\langle\Theta\rangle_p$. The distinction between k_p and $\langle\Theta\rangle_p$ is crucial in turbulence modeling. For instance, in the context of moderately dense particulate flows, $\langle\Theta\rangle_p$ is needed to evaluate the particle-phase viscosity and pressure, which arise due to collisions. Thus, failure to separate these two contributions will lead to a gross over-prediction of the collision rate [47]. Moreover, previous works [190, 199] have shown that the dissipation of k_p enters as a source term for $\langle\Theta\rangle_p$. This is analogous to single-phase flow where dissipation of turbulent kinetic energy leads to viscous heating.

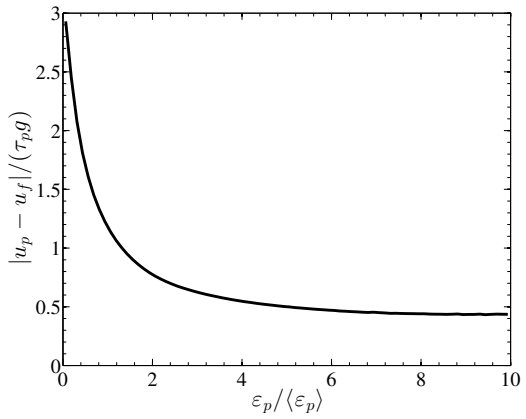

(a) Normalized slip velocity conditioned on ε_p.

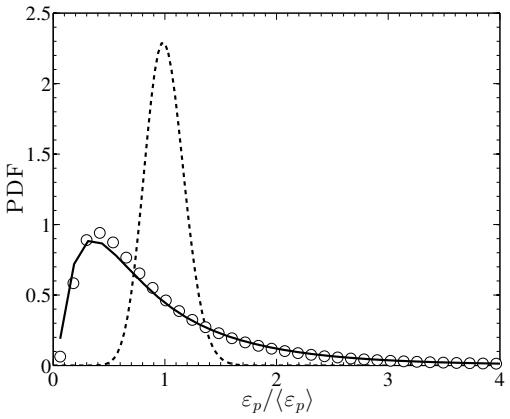

(b) PDF of ε_p (—), corresponding lognormal distribution (◯) and Poisson distribution (−−).

Figure 6.2: Results from a single realization of fully-developed CIT.

6.4.3 The filtering procedure for the extraction of particle statistics

Evaluation of the particle-phase statistics, in particular k_p and $\langle\Theta\rangle_p$, requires the introduction of a separation of length scales into the averaging procedure. To accomplish this, we employ an averaging volume that adapts to the local particle field, allowing for a sufficient number of particles to be sampled in dilute regions of the flow, while remaining optimally compact in dense clusters. Given an ensemble of identical (i.e., monodisperse) particles, and assuming that there are no sharp gradients in the volume fraction, an averaging volume will sample $\mathcal{N}_p$ particles with a filter size

$$\delta_f(\varepsilon_p) = \left(\frac{\mathcal{N}_p d_p^3}{\varepsilon_p}\right)^{1/3}. \tag{6.9}$$

Since δ_f is a function of ε_p, which itself is a filtered quantity and is thus a function of δ_f, Eq. (6.9) cannot be solved directly. Instead, ε_p is initially computed with a constant filter size $\delta_{f,0}$, which is then applied to Eq. (6.9). The resulting volume

fraction field can then be used to recompute Eq. (6.9) in an iterative process. It was found that ε_p converges rapidly to a reference solution regardless of the choice of $\delta_{f,0}$ or $\mathcal{N}_p$. Negligible error was observed after a single iteration, with values of $\delta_{f,0} = 8d_p$ and $\mathcal{N}_p = 10$ yielding the best results.

While the accuracy of the instantaneous multiphase statistics is dependent upon the sample size used when averaging, two-point Lagrangian statistics account for the spatial distribution of particles as a continuous function of particle-pair separation and therefore do not require a specific averaging volume. Thus, they can be used to assess the accuracy of the filtering procedure in extracting Lagrangian data. An important statistical measure of the spatial distribution of particles is the radial distribution function (RDF), defined as the number of particle pairs found at a given separation normalized by the expected number of pairs found in a homogeneous distribution [157]. It can be expressed as

$$g_0(r\boldsymbol{e}_i) = \frac{\left\langle \sum_{m=1}^{N_p} \sum_{n\neq m}^{N_p} \delta(\boldsymbol{x} - \boldsymbol{x}_p^{(m)}) \delta(\boldsymbol{x} + r\boldsymbol{e}_i - \boldsymbol{x}_p^{(n)}) \right\rangle}{\left\langle \sum_{m=1}^{N_p} \delta(\boldsymbol{x} - \boldsymbol{x}_p^{(m)}) \right\rangle \left\langle \sum_{m=1}^{N_p} \delta(\boldsymbol{x} + r\boldsymbol{e}_i - \boldsymbol{x}_p^{(m)}) \right\rangle}, \tag{6.10}$$

where δ is the Dirac delta function, $r \geq d_p$ is the separation between two particles $n \neq m$ and $\boldsymbol{e}_i$ is the unit normal vector in the i-direction. With this definition, $g_0 = 1$ represents a homogeneous distribution of particles and $g_0 > 1$ implies clustering. Similarly, we define the trace of the two-point velocity correlation as

$$R(r\boldsymbol{e}_i) = \frac{1}{2} \frac{\left\langle \sum_{m=1}^{N_p} \sum_{n\neq m}^{N_p} \delta(\boldsymbol{x} - \boldsymbol{x}_p^{(m)}) \delta(\boldsymbol{x} + r\boldsymbol{e}_i - \boldsymbol{x}_p^{(n)}) \boldsymbol{u}_p'^{(m)} \cdot \boldsymbol{u}_p'^{(n)} \right\rangle}{\left\langle \sum_{m=1}^{N_p} \sum_{n\neq m}^{N_p} \delta(\boldsymbol{x} - \boldsymbol{x}_p^{(m)}) \delta(\boldsymbol{x} + r\boldsymbol{e}_i - \boldsymbol{x}_p^{(n)}) \right\rangle}. \tag{6.11}$$

Due to the homogeneity of the flow, Eq. (6.10) and Eq. (6.11) are functions of the pair separation only, but in the presence of gravity, the statistics may exhibit strong anisotropy and therefore depend strongly on the directionality of $r\boldsymbol{e}_i$.

Starting from the one-particle PDF, Février et al. [190] showed that for dilute (non-collisional) suspensions of inertial particles in isotropic turbulence, two-point

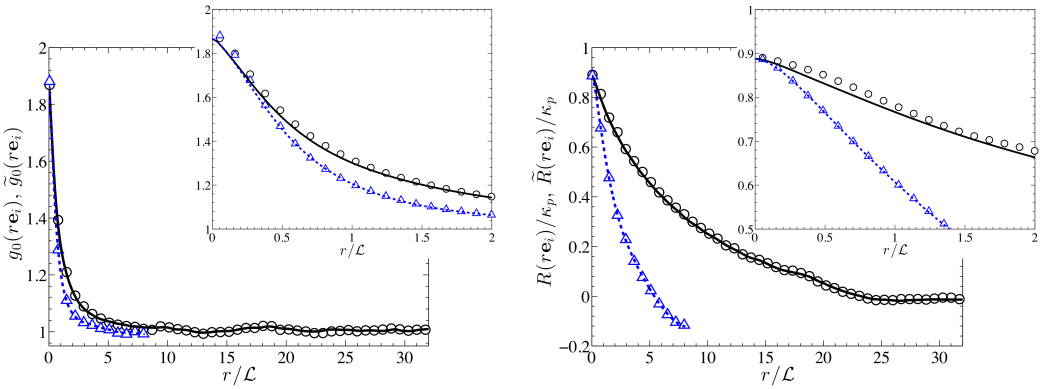

(a) RDF.

(b) Normalized two-point velocity correlations.

Figure 6.3: Comparison of Lagrangian and Eulerian two-point statistics. Lines correspond to Eulerian statistics obtained with the adaptive filter Eq. (6.9) with $\delta_{f,0} = 8d_p$ and $\mathcal{N}_p = 10$, and symbols correspond to two-point Lagrangian statistics. Black lines and circles correspond to a pair separation computed in the streamwise direction ($r\boldsymbol{e}_1$), and blue dashed lines and triangles correspond to a pair separation computed in the spanwise direction ($r\boldsymbol{e}_2$).

Eulerian statistics can be computed by introducing averages conditioned on a given fluid-flow realization, where the Eulerian RDF is given by

$$\widetilde{g}_0(r\boldsymbol{e}_i) = \frac{\langle \varepsilon_p(\boldsymbol{x},t)\varepsilon_p(\boldsymbol{x}+r\boldsymbol{e}_i,t)\rangle}{\langle \varepsilon_p(\boldsymbol{x},t)\rangle\langle \varepsilon_p(\boldsymbol{x}+r\boldsymbol{e}_i,t)\rangle}, \tag{6.12}$$

and the trace of the Eulerian two-point velocity correlation can be written as

$$\widetilde{R}(r\boldsymbol{e}_i) = \frac{1}{2}\frac{\langle \varepsilon_p(\boldsymbol{x},t)\varepsilon_p(\boldsymbol{x}+r\boldsymbol{e}_i,t)\widetilde{\boldsymbol{u}}_p''(\boldsymbol{x},t)\cdot\widetilde{\boldsymbol{u}}_p''(\boldsymbol{x}+r\boldsymbol{e}_i,t)\rangle}{\langle \varepsilon_p(\boldsymbol{x},t)\varepsilon_p(\boldsymbol{x}+r\boldsymbol{e}_i,t)\rangle}. \tag{6.13}$$

A key result found in the work by Février et al. [190] is that the mesoscopic Eulerian contribution to the particle-phase velocity accounts completely for the two-point Lagrangian spatial correlations, such that $g_0(r\boldsymbol{e}_i) = \widetilde{g}_0(r\boldsymbol{e}_i)$ and $R(r\boldsymbol{e}_i) = \widetilde{R}(r\boldsymbol{e}_i)$. Figure 6.3 shows comparisons between the two-point Lagrangian correlations (6.10)–(6.11) and two-point Eulerian statistics (6.12)–(6.13) computed using the adaptive filter in the streamwise ($r\boldsymbol{e}_1$) and spanwise ($r\boldsymbol{e}_2$) directions. In the limit of pair separation $r\to 0$, the two-point velocity correlations remain smaller

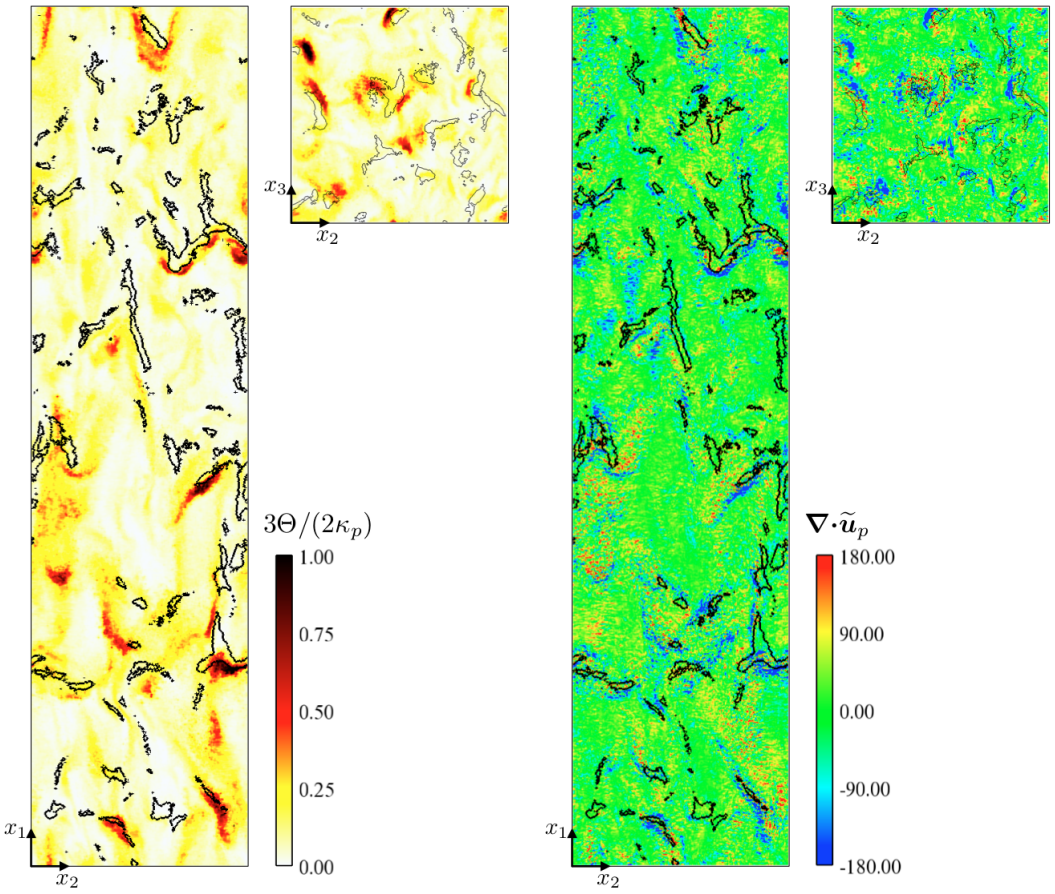

(a) Granular temperature.

(b) Divergence of the filtered particle-phase velocity.

Figure 6.4: Two-dimensional planes from a single realization of fully-developed CIT. Black lines show iso-contours of $\varepsilon_p = 3\langle\varepsilon_p\rangle$.

than κ_p, indicating a finite granular temperature. Overall, the adaptive volume filter yields excellent predictions of the spatial correlation of particle position and velocity, providing confidence that the instantaneous spatial distribution is accurately captured from Lagrangian data. Note that the spanwise velocity correlations in Fig. 6.3(b) do not approach zero at maximum pair separations, suggesting that the domain size might not be large enough. It remains to be known whether or not the cluster size distribution scales with the size of the domain, and thus we present the largest simulation that remains computationally feasible.

6.4.4 Instantaneous results

The adaptive volume filter is applied to an instantaneous field from the simulation using the parameters employed in Fig. 6.3. As shown in Fig. 6.4, negligible granular temperature is observed within clusters, while maximum values exist just upstream of clusters, where the filtered particle velocity field is locally compressive, i.e., $\nabla \cdot \widetilde{\boldsymbol{u}}_p < 0$. This behavior is analogous to a highly compressible gas, where the dilatation of the fluid velocity results in compressive heating [200, 201]. Here, compressive heating will yield local regions of high granular pressure, resulting in increased drag and a reduction in cluster fall velocity. As opposed to the reduction in fluid drag seen in clusters due to entrainment of the surrounding fluid, the change in cluster fall velocity due to enhanced granular pressure should arise even in the absence of a carrier phase. Similar behavior was first observed by Goldhirsch et al. [191] in the context of a gas-solid homogeneous cooling system (HCS). They showed that viscous heating is the dominant effect leading to the development of volume fraction inhomogeneities in dissipative granular flows in the absence of any external forcing (i.e., gravity). In a recent derivation of the Reynolds-average two-equation model for fluid-particle flows, Fox [47] showed that viscous heating acts as a source term in the transport of PA granular temperature. This is consistent with the results shown in Fig. 6.4.

6.5 Conclusions and future outlook

In this work, we present results that are part of a long-term study in which we analyze the turbulence characteristics in fully coupled gravity-driven particle-laden flows. We introduce a canonical flow that isolates the effects of momentum cou-

pling between the two phases on the production of fluid-phase turbulence, which we refer to as cluster-induced turbulence (CIT). The flow is solved in an Eulerian-Lagrangian framework with special care taken during interphase exchange processes to decouple the particle diameter to mesh size ratio. Starting from a random distribution of particles subject to gravity, after an initial transient the flow becomes statistically stationary or fully developed CIT, with a PDF of particle volume fraction that closely resembles a lognormal distribution. The normalized slip velocity $|\boldsymbol{u}_f - \boldsymbol{u}_p|/(\tau_p g)$ is observed to be significantly greater than unity in dense regions of the flow, indicating that clusters have lower drag than individual particles. An adaptive spatial filter is employed to separate the instantaneous particle-phase turbulent kinetic energy and granular temperature, and represent them as Eulerian fields. Excellent agreement with two-point Lagrangian statistics is observed, verifying the capability of the filter to accurately extract local instantaneous data. The instantaneous volume-filtered data suggest that granular temperature appears at the upstream boundary of clusters where the particle velocity field is highly compressible, analogously to shock waves in compressible gas flow. Because the fluid-phase turbulence is generated by momentum coupling with the particles, its properties cannot be predicted *a priori*. It remains to be seen how the local and Reynolds-averaged statistics depend on the key dimensionless parameters, the importance of interparticle collisions in determining the turbulence characteristics, and the mechanisms that determine the cluster size distribution.

CHAPTER 7

CONCLUSIONS

7.1 Summary of achievements

A key contribution from this work involves the development of an Eulerian-Lagrangian framework consistent with an underlying volume filtered formulation. In the limit where the filtering kernel is small, i.e., $\delta_f \ll d_p$ where d_p is the particle diameter, the sub-filter fluctuations can be neglected and the formulation represents a particle-resolved direct numerical simulation (DNS). In the limit where $\delta_f \gg d_p$, fluid stresses and their derivatives can be assumed constant over the particle surface, and the formulation reduces to a point-particle method. This work has focused on exploring the intermediate regime where the majority of fluid-phase velocity fluctuations is generated by mesoscale structures that are sufficiently resolved by the Eulerian mesh. At this level of resolution, the errors associated with exchanging information between the Lagrangian particles and fluid mesh have severely restricted the predictive capabilities of previous work. A major aspect that contributes to the success of the present approach is the use of an efficient implicit solver during the filtering process. The methods are implemented within a conservative finite difference scheme of arbitrary high-order accuracy and applied to various flows relevant to the energy sector. It was ultimately found that particle clustering can significantly reduce the efficiency of the catalytic conversion process in chemical reactors. A model was proposed to account for the effect of clusters on the conversion process via a presumed-shape PDF approach, where the Favre joint-PDF was given by a product of a beta distribution for the species mass fraction and a lognormal distribution for the particle concentration. To better understand

the role of clusters in turbulence, a canonical flow was introduced that isolates the effects of momentum coupling on the production of fluid-phase turbulent kinetic energy. Further details on the contributions made throughout the dissertation are outlined below.

1. In Chapter 2 [45], an Eulerian-Lagrangian strategy for simulating particle-laden flows was developed and validated against a suite of laboratory-scale experiments.

   (a) Volume filtered equations for the carrier phase are derived in detail for variable density flows. The mathematical formulation provides a framework for simulating chemically reacting turbulent flows in the presence of solid particles.

   (b) A two-step filtering process was derived in the context of the volume filtering approach that converges under mesh refinement and allows for cell sizes smaller than the particle diameter if necessary.

   (c) The classical soft-sphere collision model of Cundall and Strack [64] was modified for parallel efficiency. Replacing the full linear model for tangential collisions with the static friction model was shown to be a good compromise for cost, as the simpler model does not require storing the collision history. A radius of influence was introduced that is a function of the particle collision CFL, allowing particles at rest to come in contact while remaining robust during high speed impact.

   (d) The simulation strategy is capable of accurately predicting the bubble size distribution in laboratory-scale fluidized bed reactors.

2. In Chapter 3 [46], computations of high Reynolds number liquid-solid slurries in horizontal pipes were performed at operating conditions above and below

the critical deposition velocity. To the best of our knowledge, this work presents the largest computations of liquid-solid pipe flow, granting access to the detailed particle dynamics that have not been previously explored.

(a) Careful analysis of the results reveal that the flows organize into three distinct layers controlled by the two-phase dynamics. The regimes correspond to a rigid bed at the bottom, a highly-collisional shear flow located just above the bed, and a freely-suspended particle flow in the upper half of the pipe. Maximum fluctuations in particle size distribution, concentration, and phase velocities were located in the region just above the surface of the bed.

(b) Concentration and velocity profiles show excellent agreement with experimental results.

(c) Strong segregation in particle size was observed with non-monotonic behavior along vertical axis. Except for in the layer directly above the bed, particle size decreases with increasing height. Intricate coupling between the particles and turbulence directly above the bed reverses this trend, causing the largest particles to remain suspended.

(d) Model constants from a recent derivation of a Reynolds-average turbulence model for collisional fluid-particle flows [47] were extracted from the simulations. We show that the gradient-diffusion model for the vertical drift velocity compares very well with simulation results when setting the turbulent Schmidt number $\mathrm{Sc}_t = 1.3$. Closure for the drift velocity in the streamwise (homogeneous) direction yields excellent predictions of the streamwise liquid-solid drift velocity. Unclosed terms that appear in the exact Reynolds-average equations involving fluctuations in pressure gradient are negligible in the cases considered in this work.

3. In Chapter 4 [7], simulations of dilute gas-solid flows in vertical risers are presented. We consider flows operated with Archimedes numbers ranging from 100 to 12500. A novel structure tracking algorithm is used to measure the physical characteristics of particle clusters.

   (a) We demonstrate the capability of Eulerian-Lagrangian methods to generate clusters in practical flows that exhibit physical behavior. Simulation results show excellent agreement with experimental correlations for the mean concentration within clusters, volume fraction fluctuations, and cluster descent velocities.

   (b) The standard deviation of volume fraction fluctuations were found to depend only on the mean concentration, and are predicted within 10% for the range of Archimedes numbers simulated in this study using either the model proposed by Wang *et al.* [153] or the experimental correlation given by Issangya *et al.* [151].

   (c) We show that the degree of particle clustering is unaffected by the Archimedes number, and the distributions of solid concentration agree with a lognormal law, indicating a potential for future modeling efforts.

   (d) The radial distribution function was computed for a range of radial positions, indicating that the characteristic cluster length scale is limited by the diameter of the reactor. This prediction is much smaller than that given by the characteristic length scale for homogeneous gravity-driven gas-solid flows $\mathcal{L} = \tau_p^2 g$.

   (e) We demonstrate the limitations of simulating risers in two dimensions. Beyond the numerical challenges in accurately measuring the volume fraction in two-dimensional flows, we show the physical consequences of constraining particle motion within a plane. Namely, such flows will

lead to unphysical accumulation of particles, resulting in gross over-predictions in volume fraction and velocity fluctuations.

4. In Chapter 5, the Eulerian-Lagrangian framework is extended to chemically reacting flows. We characterize and quantify the effects of non-homogeneities caused by the formation of clusters on the chemical conversion of species mass fraction in circulating fluidized bed risers.

   (a) Clusters were found to delay the conversion process by up to 85% compared to a homogenous flow, with greater impact at higher values of the Damköhler number;

   (b) The correlation between fluctuating mass fraction and volume fraction entirely accounts for the discrepancy between the homogeneous solution and three-dimensional results.

   (c) A transport equation for the fluctuating chemical source term was derived, and the correlation of Issangya *et al.* [151] was used to model the two largest contributions, showing overall very good agreement;

   (d) An initial attempt at providing closure for the fluctuating chemical source term in the zero-dimensional model was obtained by applying a presumed-shape PDF model, where the Favre average joint-PDF is given by a product of a beta distribution for the species mass fraction and a lognormal distribution for the particle concentration. The model yields excellent results for the range of Ar and Da considered in this study.

5. In Chapter 6 [49], we explore fully-developed cluster-induced turbulence in a statistically stationary gravity-driven flow. These results are part of a long-term study in which we are interested in analyzing the production of fluid-phase kinetic energy due to momentum coupling with inertial particles.

(a) We introduce a canonical flow that isolates the effects of momentum coupling between the two phases on the production of fluid-phase turbulence, referred to as cluster-induced turbulence (CIT).

(b) We introduce a method for accurately separating particle-phase kinetic energy, which is spatially correlated, from granular temperature, which is spatially uncorrelated, in an accurate and consistent manner. To do this, we employ an adaptive spatial filter that gives results that are parameter-free, which has not yet been achieved in previous work. Excellent agreement with two-point Lagrangian statistics is observed, verifying the capability of the filter to accurately extract local instantaneous data in an Eulerian frame of reference.

(c) Local instantaneous fields of granular temperature for collisional gas-solid flows are shown for the first time.

(d) Instantaneous volume filtered data suggests that granular temperature appears at the upstream boundary of clusters where the particle velocity field is highly compressible, analogous to shock waves in compressible gas flow.

(e) Using the two-point velocity correlation functions, we demonstrate that fully developed CIT requires much larger three-dimensional simulation domains than have been used in previous work.

(f) We demonstrate that the dependence of local volume fraction and Reynolds number on drag is not necessary for clustering to occur.

(g) We show that the corresponding volume fraction distribution closely resembles a lognormal distribution.

7.2 Future perspectives

Volume filtering the point wise equations of motion produces unclosed terms that contribute in various degrees to the non-linear physics. Several of these terms have been addressed within this dissertation, though relative contributions from all sub-filter quantities remain to be explored. In particular, underlying assumptions in the mathematical formulation are violated when the filter radius is larger than the distance between particles and solid boundaries. The hydrodynamic forces acting on finite-size particles in near-wall regions of the flow typically exhibit non-trivial behavior that standard drag and lift correlations fail to predict [202, 203]. The development of sub-filter terms that account for the truncated filter kernel in the form of a wall-aware drag model would be beneficial for future research efforts.

A key assumption in most modeling approaches for disperse multiphase flows is particle sphericity. Meanwhile, the repercussions of neglecting realistic particle shapes might be significant in many systems. Recent studies have shown that friction between particles during contact mitigate cluster formation [192, 193], though at present the effect of particle shape on cluster dynamics remains to be explored. In addition, particle shape would be expected to have a large impact on the onset of fluidization in dense fluidized beds or the initiation of bed formation in liquid-solid slurries. Two main issues arise when dealing with non-spherical particles: contact detection between other particles and walls, and a proper treatment of drag around irregular shapes. A promising technique for handling collisions is referred to in the literature as the multi-sphere method, which represents the particle shape as a cluster of overlapping spheres that move together in rigid body motion. The multi-sphere method has been used for a range of applications in molecular dynamic simulations (e.g., [204–208]), and it has only recently been coupled with

a Navier-Stokes solver (see [209–211]). A key challenge associated with computing the drag around non-spherical particles is in developing a systematic approach for characterizing the complex shape. Because the volume filtered formalism reduces to particle-resolved DNS in the limit where $\delta_f \ll d_p$, *a priori* filtering of such detailed simulations can be useful in developing drag correlations for lower-order modeling approaches.

With exascale computing in the foreseeable future, particle-resolved DNS will become useful in simulating complex fluid-particle systems at larger scales. However, simulations of industrial-scale systems and extreme environmental processes will continue to be out of reach for decades to come. Large-eddy simulation (LES) has been shown to be a powerful technique for the computation of strongly unsteady turbulent flows, yet LES of particle-laden flows is severely limited. The level of detail provided in the Euler-Lagrange strategy presented in this work offers a unique opportunity to investigate multiphase LES based on first principles. In the context of moderately-dilute gas-solid flows, new turbulence production terms arise due to correlations between the particle-phase volume fraction and fluid-phase velocity fluctuations. In the absence of mean shear, the production of fluid-phase turbulent kinetic energy is entirely due to momentum coupling between the phases. In Chapter 6, we introduced a canonical flow that isolates this effect, referred to as cluster-induced turbulence (CIT), and provided tools for evaluating the complex dynamics. Detailed simulations of fully-developed CIT will aid in developing a more quantitative understanding of the mechanisms that control turbulent flows in in the presence of inertial particles.

BIBLIOGRAPHY

[1] J. Xu and J.-X. Zhu, "Visualization of particle aggregation and effects of particle properties on cluster characteristics in a CFB riser," *Chemical Engineering Journal*, vol. 168, no. 1, pp. 376–389, 2011.

[2] M. Maxey, "The gravitational settling of aerosol particles in homogeneous turbulence and random flow fields," *J. Fluid Mech.*, vol. 174, pp. 441–465, 1987.

[3] B. Glasser, S. Sundaresan, and I. Kevrekidis, "From bubbles to clusters in fluidized beds," *Phys. Rev. Lett.*, vol. 81, p. 1849, 1998.

[4] M. Hopkins and M. Louge, "Inelastic microstructure in rapid granular flows of smooth disks," *Physics of Fluids*, vol. 3, no. 1, pp. 47–57, 1991.

[5] J. Eaton and J. Fessler, "Preferential concentration of particles by turbulence," *International Journal of Multiphase Flow*, vol. 20, pp. 169–209, 1994.

[6] K. Agrawal, P. Loezos, M. Syamlal, and S. Sundaresan, "The role of meso-scale structures in rapid gas-solid flows," *Journal of Fluid Mechanics*, vol. 445, pp. 151–186, 2001.

[7] J. Capecelatro, P. Pepiot, and O. Desjardins, "Numerical characterization and modeling of particle clustering in wall-bounded vertical risers," *Chem. Eng. J.*, vol. 245, pp. 295–310, 2014.

[8] T. Tanaka and J. Eaton, "Sub-kolmogorov resolution partical image velocimetry measurements of particle-laden forced turbulence," *Journal of Fluid Mechanics*, vol. 643, pp. 177–206, 2010.

[9] C. Crowe, "On models for turbulence modulation in fluid–particle flows," *International Journal of Multiphase Flow*, vol. 26, no. 5, pp. 719–727, 2000.

[10] J. Kulick, J. Fessler, and J. Eaton, "Particle response and turbulence modification in fully developed channel flow," *Journal of Fluid Mechanics*, vol. 277, no. 1, pp. 109–134, 1994.

[11] P. D. Noymer and L. R. Glicksman, "Descent velocities of particle clusters at the wall of a circulating fluidized bed," *Chemical Engineering Science*, vol. 55, no. 22, pp. 5283–5289, 2000.

[12] M. C. Lints and L. Glicksman, "Parameters governing particle-to-wall heat transfer in a circulating fluidized bed," *Circulating Fluidized Bed Technology IV, AIChE, New York*, pp. 297–304, 1994.

[13] M. Rashidi, G. Hetsroni, and S. Banerjee, "Particle-turbulence interaction in a boundary layer," *International Journal of Multiphase Flow*, vol. 16, no. 6, pp. 935–949, 1990.

[14] J. W. Chew, D. M. Parker, R. A. Cocco, and C. M. Hrenya, "Cluster characteristics of continuous size distributions and binary mixtures of group B particles in dilute riser flow," *Chemical Engineering Journal*, vol. 178, pp. 348–358, 2011.

[15] J. W. Chew, R. Hays, J. G. Findlay, T. M. Knowlton, S. Karri, R. A. Cocco, and C. M. Hrenya, "Impact of material property and operating conditions on mass flux profiles of monodisperse and polydisperse group B particles in a CFB riser," *Powder Technology*, vol. 214, no. 1, pp. 89–98, 2011.

[16] J. W. Chew, R. Hays, J. G. Findlay, T. M. Knowlton, S. Reddy Karri, R. A. Cocco, and C. M. Hrenya, "Cluster characteristics of Geldart group B particles in a pilot-scale CFB riser. I. Monodisperse systems," *Chemical Engineering Science*, vol. 68, no. 1, pp. 72–81, 2012.

[17] J. W. Chew, R. Hays, J. G. Findlay, T. M. Knowlton, S. Karri, R. A. Cocco, and C. M. Hrenya, "Cluster characteristics of Geldart group B particles in a pilot-scale CFB riser. II. Polydisperse systems," *Chemical Engineering Science*, vol. 68, no. 1, pp. 82–93, 2012.

[18] J. McMillan, F. Shaffer, B. Gopalan, J. W. Chew, C. Hrenya, R. Hays, S. Karri, and R. Cocco, "Particle cluster dynamics during fluidization," *Chemical Engineering Science*, 2013.

[19] R. O. Fox, "Large-eddy-simulation tools for multiphase flows," *Annual Review of Fluid Mechanics*, vol. 44, pp. 47–76, 2012.

[20] S. Balachandar and J. Eaton, "Turbulent dispersed multiphase flow," *Annual Review of Fluid Mechanics*, vol. 42, pp. 111–133, 2010.

[21] C. Crowe, J. Schwarzkopf, M. Sommerfeld, and Y. Tsuji, *Multiphase flows with droplets and particles*. CRC press, 2011.

[22] N. Deen, M. Van Sint Annaland, M. Van der Hoef, and J. Kuipers, "Review

of discrete particle modeling of fluidized beds," *Chemical engineering science*, vol. 62, no. 1-2, pp. 28–44, 2007.

[23] N. Patankar and D. Joseph, "Modeling and numerical simulation of particulate flows by the Eulerian-Lagrangian approach," *International journal of multiphase flow*, vol. 27, no. 10, pp. 1659–1684, 2001.

[24] M. Van der Hoef, M. Ye, M. van Sint Annaland, A. Andrews, S. Sundaresan, and J. Kuipers, "Multiscale modeling of gas-fluidized beds," *Advances in Chemical Engineering*, vol. 31, pp. 65–149, 2006.

[25] S. Tenneti and S. Subramaniam, "Particle-resolved direct numerical simulation for gas-solid flow model development," *Annu. Rev. Fluid Mech.*, vol. 46, pp. 199–230, 2014.

[26] R. Fox, "Introduction and fundamentals of modeling approaches for polydisperse multiphase flows," *Multiphase Reacting Flows: Modelling and Simulation*, pp. 1–40, 2007.

[27] S. Subramaniam, "Statistical representation of a spray as a point process," *Physics of Fluids (1994-present)*, vol. 12, no. 10, pp. 2413–2431, 2000.

[28] S. Chapman and T. Cowling, *The mathematical theory of non-uniform gases: an account of the kinetic theory of viscosity, thermal conduction, and diffusion in gases*. Cambridge Univ Pr, 1991.

[29] C. Cercignani, R. Illner, and M. Pulvirenti, *The mathematical theory of dilute gases*, vol. 106. Springer, 1994.

[30] H. Struchtrup, *Macroscopic transport equations for rarefied gas flows: approximation methods in kinetic theory*. Springer Verlag, 2005.

[31] J. Kuipers, K. Van Duin, F. Van Beckum, and W. Van Swaaij, "A numerical model of gas-fluidized beds," *Chemical Engineering Science*, vol. 47, no. 8, pp. 1913–1924, 1992.

[32] D. Gidaspow, *Multiphase flow and fluidization: continuum and kinetic theory descriptions*. Academic Pr, 1994.

[33] D. Zhang and A. Prosperetti, "Averaged equations for inviscid disperse two-phase flow," *Journal of Fluid Mechanics*, vol. 267, pp. 185–220, 1994.

[34] E. Peirano and B. Leckner, "Fundamentals of turbulent gas-solid flows applied to circulating fluidized bed combustion," *Progress in Energy and Combustion Science*, vol. 24, no. 4, pp. 259–296, 1998.

[35] O. Desjardins, R. Fox, and P. Villedieu, "A quadrature-based moment method for dilute fluid-particle flows," *Journal of Computational Physics*, vol. 227, no. 4, pp. 2514–2539, 2008.

[36] O. Simonin, "Prediction of the dispersed phase turbulence in particle-laden jets," in *4th International Symposium On gas-solid flows, Portland*, pp. 23–26, 1991.

[37] A. Passalacqua, R. Fox, R. Garg, and S. Subramaniam, "A fully coupled quadrature-based moment method for dilute to moderately dilute fluid-particle flows," *Chemical Engineering Science*, vol. 65, no. 7, pp. 2267–2283, 2010.

[38] C. Yuan and R. Fox, "Conditional quadrature method of moments for kinetic equations," *Journal of Computational Physics*, 2011.

[39] V. Vikas, Z. Wang, A. Passalacqua, and R. Fox, "Realizable high-order finite-volume schemes for quadrature-based moment methods," *Journal of Computational Physics*, vol. 230, no. 13, pp. 5328–5352, 2011.

[40] G. Bird, "Molecular gas dynamics and the direct simulation of gas flows," *Oxford, United Kingdom: Clarendon Press (Oxford Engineering Science Series,*, vol. 42, 1995.

[41] H. Salman and M. Soteriou, "Lagrangian simulation of evaporating droplet sprays," *Physics of Fluids*, vol. 16, p. 4601, 2004.

[42] R. Garg, C. Narayanan, and S. Subramaniam, "A numerically convergent lagrangian-eulerian simulation method for dispersed two-phase flows," *International Journal of Multiphase Flow*, vol. 35, no. 4, pp. 376–388, 2009.

[43] B. Moses, *Simulation of multiphase fluid flows using a spatial filtering process*. PhD thesis, Stanford University, 2007.

[44] S. Subramaniam, "Lagrangian–Eulerian methods for multiphase flows," *Progress in Energy and Combustion Science*, vol. 39, pp. 215–245, 2012.

[45] J. Capecelatro and O. Desjardins, "An Euler–Lagrange strategy for simulating particle-laden flows," *J. Comp. Phys.*, vol. 238, pp. 1–31, 2013.

[46] J. Capecelatro and O. Desjardins, "Eulerian-Lagrangian modeling of turbulent liquid-solid slurries in horizontal pipes," *Int. J. Multiphase Flow*, vol. 55, pp. 64–79, 2013.

[47] R. Fox, "On multiphase turbulence models for collisional fluid–particle flows," *J. Fluid Mech.*, vol. 742, pp. 368–424, 2014.

[48] J. Capecelatro, O. Desjardins, P. Pepiot, M. Jarvis, and T. Foust, "Numerical investigation of multiphase dynamic effects in catalytic upgrading of biomass pyrolysis vapor," in *AIChE Annual Meeting, Conference Proceedings*, American Institute of Chemical Engineers, 2013.

[49] J. Capecelatro, O. Desjardins, and R. O. Fox, "Numerical study of collisional particle dynamics in cluster-induced turbulence," *J. Fluid Mech.*, vol. 747, pp. R2 1–13, 2014.

[50] M. Pai and S. Subramaniam, "A comprehensive probability density function formalism for multiphase flows," *Journal of Fluid Mechanics*, vol. 628, no. 1, pp. 181–228, 2009.

[51] J. Pritchett, T. Blake, and S. Garg, "A numerical model of gas fluidized beds," in *AIChE Symp. Ser*, vol. 176, pp. 134–148, 1978.

[52] J. Bouillard, R. Lyczkowski, and D. Gidaspow, "Porosity distributions in a fluidized bed with an immersed obstacle," *AIChE Journal*, vol. 35, no. 6, pp. 908–922, 1989.

[53] H. Enwald, E. Peirano, and A. Almstedt, "Eulerian two-phase flow theory applied to fluidization," *International Journal of Multiphase Flow*, vol. 22, pp. 21–66, 1996.

[54] Y. P. Tsuo and D. Gidaspow, "Computation of flow patterns in circulating fluidized beds," *AIChE Journal*, vol. 36, no. 6, pp. 885–896, 1990.

[55] S. Benyahia, H. Arastoopour, T. Knowlton, and H. Massah, "Simulation of particles and gas flow behavior in the riser section of a circulating fluidized bed using the kinetic theory approach for the particulate phase," *Powder Technology*, vol. 112, no. 1, pp. 24–33, 2000.

[56] H. Arastoopour, "Numerical simulation and experimental analysis of gas/solid flow systems: 1999 Fluor-Daniel plenary lecture," *Powder Technology*, vol. 119, no. 2, pp. 59–67, 2001.

[57] D. Gidaspow, J. Jung, and R. Singh, "Hydrodynamics of fluidization using kinetic theory: an emerging paradigm: 2002 Flour-Daniel lecture," *Powder Technology*, vol. 148, no. 2, pp. 123–141, 2004.

[58] H. Grad, "On the kinetic theory of rarefied gases," *Communications on Pure and Applied Mathematics*, vol. 2, no. 4, pp. 331–407, 1949.

[59] D. Marchisio and R. Fox, "Solution of population balance equations using the direct quadrature method of moments," *Journal of Aerosol Science*, vol. 36, no. 1, pp. 43–73, 2005.

[60] A. Kitron, T. Elperin, and A. Tamir, "Monte carlo simulation of gas-solids suspension flows in impinging streams reactors," *International journal of multiphase flow*, vol. 16, no. 1, pp. 1–17, 1990.

[61] T. Tanaka, S. Yonemura, K. Kiribayashi, and Y. Tsuji, "Cluster formation and particle-induced instability in gas-solid flows predicted by the DSMC method," *JSME International Journal-Series B-Fluids and Thermal Engineering*, vol. 39, no. 2, pp. 239–245, 1996.

[62] Y. Tsuji, "Multi-scale modeling of dense phase gas-particle flow," *Chemical engineering science*, vol. 62, no. 13, pp. 3410–3418, 2007.

[63] P. Pepiot and O. Desjardins, "Numerical analysis of the dynamics of two- and three-dimensional fluidized bed reactors using an Euler-Lagrange approach," *Powder Technology*, 2010.

[64] P. Cundall and O. Strack, "A discrete numerical model for granular assemblies," *Geotechnique*, vol. 29, no. 1, pp. 47–65, 1979.

[65] Y. Tsuji, T. Kawaguchi, and T. Tanaka, "Discrete particle simulation of two-dimensional fluidized bed," *Powder technology*, vol. 77, no. 1, pp. 79–87, 1993.

[66] B. Hoomans, J. Kuipers, W. Briels, and W. Van Swaaij, "Discrete particle simulation of bubble and slug formation in a two-dimensional gas-fluidised bed: a hard-sphere approach," *Chemical Engineering Science*, vol. 51, no. 1, pp. 99–118, 1996.

[67] C. Campbell and C. Brennan, "Computer simulation of granular shear flows," *Journal of Fluid Mechanics*, vol. 151, pp. 167–88, 1985.

[68] P. Pepiot and O. Desjardins, "Direct numerical simulation of dense particle-laden flows using a conservative immersed boundary technique," in *Proceedings of the Summer Program*, p. 323, 2010.

[69] O. Desjardins, G. Blanquart, G. Balarac, and H. Pitsch, "High order conservative finite difference scheme for variable density low Mach number turbulent flows," *Journal of Computational Physics*, vol. 227, no. 15, pp. 7125–7159, 2008.

[70] T. Anderson and R. Jackson, "Fluid mechanical description of fluidized beds. Equations of motion," *Industrial & Engineering Chemistry Fundamentals*, vol. 6, no. 4, pp. 527–539, 1967.

[71] D. Zhang and A. Prosperetti, "Momentum and energy equations for disperse two-phase flows and their closure for dilute suspensions," *International journal of multiphase flow*, vol. 23, no. 3, pp. 425–453, 1997.

[72] N. Peters, *Turbulent combustion*. Cambridge university press, 2000.

[73] C. Rogers and J. Eaton, "The effect of small particles on fluid turbulence in a flat-plate, turbulent boundary layer in air," *Physics of Fluids A: Fluid Dynamics*, vol. 3, p. 928, 1991.

[74] Y. He, S. Qin, C. Lim, and J. Grace, "Particle velocity profiles and solid flow patterns in spouted beds," *The Canadian Journal of Chemical Engineering*, vol. 72, no. 4, pp. 561–568, 1994.

[75] M. Germano, U. Piomelli, P. Moin, and W. Cabot, "A dynamic subgrid-scale eddy viscosity model," *Physics of Fluids A: Fluid Dynamics*, vol. 3, p. 1760, 1991.

[76] D. Lilly, "A proposed modification of the germano subgrid-scale closure method," *Physics of Fluids A: Fluid Dynamics*, vol. 4, p. 633, 1992.

[77] C. Meneveau, T. Lund, and W. Cabot, "A lagrangian dynamic subgrid-scale model of turbulence," *Journal of Fluid Mechanics*, vol. 319, no. 1, pp. 353–385, 1996.

[78] A. Di Renzo and F. Di Maio, "Homogeneous and bubbling fluidization

regimes in DEM-CFD simulations: Hydrodynamic stability of gas and liquid fluidized beds," *Chemical engineering science*, vol. 62, no. 1-2, pp. 116–130, 2007.

[79] L. Gibilaro, K. Gallucci, R. Di Felice, and P. Pagliai, "On the apparent viscosity of a fluidized bed," *Chemical engineering science*, vol. 62, no. 1-2, pp. 294–300, 2007.

[80] P. Saffman, "The lift on a small sphere in a slow shear flow," *Journal of Fluid Mechanics*, vol. 22, no. 02, pp. 385–400, 1965.

[81] S. Tenneti, R. Garg, and S. Subramaniam, "Drag law for monodisperse gas-solid systems using particle-resolved direct numerical simulation of flow past fixed assemblies of spheres," *International journal of multiphase flow*, vol. 37, no. 9, pp. 1072–1092, 2011.

[82] D. Snider, P. O'Rourke, and M. Andrews, "Sediment flow in inclined vessels calculated using a multiphase particle-in-cell model for dense particle flows," *International journal of multiphase flow*, vol. 24, no. 8, pp. 1359–1382, 1998.

[83] R. Garg, C. Narayanan, D. Lakehal, and S. Subramaniam, "Accurate numerical estimation of interphase momentum transfer in Lagrangian-Eulerian simulations of dispersed two-phase flows," *International Journal of Multiphase Flow*, vol. 33, no. 12, pp. 1337–1364, 2007.

[84] M. Meyer, A. Devesa, S. Hickel, X. Hu, and N. Adams, "A conservative immersed interface method for Large-Eddy Simulation of incompressible flows," *Journal of Computational Physics*, 2010.

[85] G. Treece, R. Prager, and A. Gee, "Regularised marching tetrahedra: improved iso-surface extraction," *Computers & Graphics*, vol. 23, no. 4, pp. 583–598, 1999.

[86] A. Di Renzo and F. Di Maio, "Comparison of contact-force models for the simulation of collisions in DEM-based granular flow codes," *Chemical engineering science*, vol. 59, no. 3, pp. 525–541, 2004.

[87] G. Scott and D. Kilgour, "The density of random close packing of spheres," *Journal of Physics D: Applied Physics*, vol. 2, p. 863, 1969.

[88] C. Pierce, *Progress-variable approach for large-eddy simulation of turbulent combustion*. PhD thesis, Citeseer, 2001.

[89] J. Kim and P. Moin, "Application of a fractional-step method to incompressible navier-stokes equations," *Journal of Computational Physics*, vol. 59, no. 2, pp. 308–323, 1985.

[90] P. Popov, H. Wang, and S. Pope, "Specific volume coupling and convergence properties in hybrid particle/finite volume algorithms for turbulent reactive flows," *Journal of Computational Physics*, 2012.

[91] P. Brown, G. Byrne, A. Hindmarsh, *et al.*, "Vode: A variable coefficient ode solver," *SIAM J. Sci. Stat. Comput*, vol. 10, no. 5, pp. 1038–1051, 1989.

[92] J. Link, C. Zeilstra, N. Deen, and H. Kuipers, "Validation of a discrete particle model in a 2D spout-fluid bed using non-intrusive optical measuring techniques," *The Canadian Journal of Chemical Engineering*, vol. 82, no. 1, pp. 30–36, 2004.

[93] J. Link, L. Cuypers, N. Deen, and J. Kuipers, "Flow regimes in a spout–fluid bed: A combined experimental and simulation study," *Chemical Engineering Science*, vol. 60, no. 13, pp. 3425–3442, 2005.

[94] M. Goldschmidt, J. Link, S. Mellema, and J. Kuipers, "Digital image analysis measurements of bed expansion and segregation dynamics in dense gas-fluidised beds," *Powder Technology*, vol. 138, no. 2, pp. 135–159, 2003.

[95] K. Gaston, M. Jarvis, P. Pepiot, K. Smith, W. Frederick, and M. Nimlos, "Biomass pyrolysis and gasification of varying particle sizes in a fluidized bed reactor," *Energy & Fuels*, 2011.

[96] N. Franka and T. Heindel, "Local time-averaged gas holdup in a fluidized bed with side air injection using X-ray computed tomography," *Powder Technology*, vol. 193, no. 1, pp. 69–78, 2009.

[97] M. Herrmann, "A parallel Eulerian interface tracking/Lagrangian point particle multi-scale coupling procedure," *Journal of computational physics*, vol. 229, no. 3, pp. 745–759, 2010.

[98] R. Darton, R. LaNauze, J. Davidson, and D. Harrison, "Bubble growth due to coalescence in fluidised beds," *Chemical Engineering Research and Design*, vol. 55, no. a, pp. 274–280, 1977.

[99] M. Roco and N. Balakrishnam, "Multi-dimensional flow analysis of solid-liquid mixtures," *Journal of Rheology*, vol. 29, no. 4, pp. 431–456, 1985.

[100] R. Durand and E. Condolios, "Hydraulic transportation of coal and solid material in pipes," in *London Colloquium of the National Coal Board*, 1952.

[101] E. Wasp, J. Kenny, and R. Gandhi, "Solid-liquid flow: slurry pipeline transportation. [pumps, valves, mechanical equipment, economics]," *Ser. Bulk Mater. Handl.;(United States)*, vol. 1, no. 4, 1977.

[102] D. Kaushal and Y. Tomita, "Solids concentration profiles and pressure drop in pipeline flow of multisized particulate slurries," *International journal of multiphase flow*, vol. 28, no. 10, pp. 1697–1717, 2002.

[103] K. Wilson, "A unified physically-based analysis of solid-liquid pipeline flow," in *Proceedings Hydrotransport*, vol. 4, pp. 1–16, 1976.

[104] P. Doron, D. Granica, and D. Barnea, "Slurry flow in horizontal pipesexperimental and modeling," *International journal of multiphase flow*, vol. 13, no. 4, pp. 535–547, 1987.

[105] R. Gillies, C. Shook, and K. Wilson, "An improved two layer model for horizontal slurry pipeline flow," *The Canadian Journal of Chemical Engineering*, vol. 69, no. 1, pp. 173–178, 1991.

[106] J. Schaan, R. Sumner, R. Gillies, and C. Shook, "The effect of particle shape on pipeline friction for newtonian slurries of fine particles," *The Canadian Journal of Chemical Engineering*, vol. 78, no. 4, pp. 717–725, 2000.

[107] U. Kumar, R. Mishra, S. Singh, and V. Seshadri, "Effect of particle gradation on flow characteristics of ash disposal pipelines," *Powder technology*, vol. 132, no. 1, pp. 39–51, 2003.

[108] J. Ling, P. Skudarnov, C. Lin, and M. Ebadian, "Numerical investigations of liquid–solid slurry flows in a fully developed turbulent flow region," *International journal of heat and fluid flow*, vol. 24, no. 3, pp. 389–398, 2003.

[109] S. A. Orszag, V. Yakhot, W. S. Flannery, F. Boysan, D. Choudhury, J. Maruzewski, and B. Patel, "Renormalization group modeling and turbulence simulations," *Near-wall turbulent flows*, pp. 1031–1046, 1993.

[110] K. Ekambara, R. Sanders, K. Nandakumar, and J. Masliyah, "Hydrodynamic simulation of horizontal slurry pipeline flow using ansys-cfx," *Industrial & Engineering Chemistry Research*, vol. 48, no. 17, pp. 8159–8171, 2009.

[111] D. Kaushal, T. Thinglas, Y. Tomita, S. Kuchii, and H. Tsukamoto, "CFD modeling for pipeline flow of fine particles at high concentration," *International Journal of Multiphase Flow*, 2012.

[112] D. Kaushal and Y. Tomita, "Experimental investigation for near-wall lift of coarser particles in slurry pipeline using γ-ray densitometer," *Powder technology*, vol. 172, no. 3, pp. 177–187, 2007.

[113] Q. Wang, K. Squires, M. Chen, and J. McLaughlin, "On the role of the lift force in turbulence simulations of particle deposition," *International Journal of Multiphase Flow*, vol. 23, no. 4, pp. 749–763, 1997.

[114] R. Kurose and S. Komori, "Drag and lift forces on a rotating sphere in a linear shear flow," *Journal of fluid mechanics*, vol. 384, no. 1, pp. 183–206, 1999.

[115] S. B. Pope, *Turbulent flows*. Cambridge university press, 2000.

[116] J. Pozorski and S. Apte, "Filtered particle tracking in isotropic turbulence and stochastic modeling of subgrid-scale dispersion," *International Journal of Multiphase Flow*, vol. 35, no. 2, pp. 118–128, 2009.

[117] J. Jenkins and S. Savage, "Theory for the rapid flow of identical, smooth, nearly elastic, spherical particles," *Journal of Fluid Mechanics*, vol. 130, no. 1, pp. 187–202, 1983.

[118] A. H. Azimi, D. Z. Zhu, and N. Rajaratnam, "Computational investigation of vertical slurry jets in water," *International Journal of Multiphase Flow*, 2012.

[119] N. Zuber, "Average volumetric concentration in two-phase flow systems," *J. Heat Transfer*, vol. 87, pp. 453–464, 1965.

[120] A. Avidan, M. Edwards, and H. Owen, "Fluid-catalytic cracking-past and future challenges," *Reviews in Chemical Engineering*, vol. 6, no. 1, pp. 1–72, 1990.

[121] A. A. Avidan, "Fluid catalytic cracking," in *Circulating Fluidized Beds*, pp. 466–488, Springer, 1996.

[122] C. Brereton, "Combustion performance," in *Circulating Fluidized Beds*, pp. 369–416, Springer, 1996.

[123] Y. Y. Lee, "Design considerations for CFB boilers," in *Circulating Fluidized Beds*, pp. 417–440, Springer, 1996.

[124] P. Basu, *Combustion and gasification in fluidized beds*. CRC press, 2006.

[125] X. Li, J. Grace, C. Lim, A. Watkinson, H. Chen, and J. Kim, "Biomass gasification in a circulating fluidized bed," *Biomass and Bioenergy*, vol. 26, no. 2, pp. 171–193, 2004.

[126] A. Sanz and J. Corella, "Modeling circulating fluidized bed biomass gasifiers. results from a pseudo-rigorous 1-dimensional model for stationary state," *Fuel Processing Technology*, vol. 87, no. 3, pp. 247–258, 2006.

[127] F. Shaffer, B. Gopalan, R. W. Breault, R. Cocco, S. Karri, R. Hays, and T. Knowlton, "High speed imaging of particle flow fields in CFB risers," *Powder Technology*, 2013.

[128] S. Subramanian and S. Tenneti, "Particle-resolved direct numerical simulation for gas-solid flow model development," *Annual Review of Fluid Mechanics*, vol. 46, no. 1, 2013.

[129] Y. Xu and S. Subramaniam, "Effect of particle clusters on carrier flow turbulence: A direct numerical simulation study," *Flow, Turbulence and Combustion*, vol. 85, no. 3-4, pp. 735–761, 2010.

[130] M. T. Shah, R. P. Utikar, M. O. Tade, G. M. Evans, and V. K. Pareek, "Effect of a cluster on gassolid drag from Lattice Boltzmann simulations," *Chemical Engineering Science*, vol. 102, no. 0, pp. 365 – 372, 2013.

[131] B. Chalermsinsuwan, P. Piumsomboon, and D. Gidaspow, "Kinetic theory based computation of PSRI riser: Part I–Estimate of mass transfer coefficient," *Chemical Engineering Science*, vol. 64, no. 6, pp. 1195–1211, 2009.

[132] B. Chalermsinsuwan, T. Chanchuey, W. Buakhao, D. Gidaspow, and P. Piumsomboon, "Computational fluid dynamics of circulating fluidized bed downer: Study of modeling parameters and system hydrodynamic characteristics," *Chemical Engineering Journal*, vol. 189, pp. 314–335, 2012.

[133] A. Ozel, P. Fede, and O. Simonin, "Development of filtered Euler-Euler two-phase model for circulating fluidised bed: High resolution simulation, formulation and a priori analyses," *International Journal of Multiphase Flow*, 2013.

[134] B. Chalermsinsuwan, Y. Prajongkan, and P. Piumsomboon, "Three-dimensional CFD simulation of the system inlet and outlet boundary condition effects inside a high solid particle flux circulating fluidized bed riser," *Powder Technology*, 2013.

[135] J. Li, Z.-H. Luo, X.-Y. Lan, C.-M. Xu, and J.-S. Gao, "Numerical simulation of the turbulent gas–solid flow and reaction in a polydisperse FCC riser reactor," *Powder Technology*, 2013.

[136] B. Chalermsinsuwan, D. Gidaspow, and P. Piumsomboon, "Comparisons of particle cluster diameter and concentration in circulating fluidized bed riser and downer using computational fluid dynamics simulation," *Korean Journal of Chemical Engineering*, pp. 1–13, 2013.

[137] E. Helland, R. Occelli, and L. Tadrist, "Computational study of fluctuating motions and cluster structures in gas-particle flows," *International Journal of Multiphase Flow*, vol. 28, no. 2, pp. 199–223, 2002.

[138] W. Shuyan, L. Huanpeng, L. Huilin, L. Wentie, J. Ding, and L. Wei, "Flow behavior of clusters in a riser simulated by direct simulation Monte Carlo method," *Chemical Engineering Journal*, vol. 106, no. 3, pp. 197–211, 2005.

[139] Y. He, N. Deen, M. v. S. Annaland, and J. Kuipers, "Gas-solid turbulent flow in a circulating fluidized bed riser: Experimental and numerical study of monodisperse particle systems," *Industrial & Engineering Chemistry Research*, vol. 48, no. 17, pp. 8091–8097, 2009.

[140] X. Liu and X. Xu, "Modelling of dense gas-particle flow in a circulating fluidized bed by distinct cluster method (DCM)," *Powder Technology*, vol. 195, no. 3, pp. 235–244, 2009.

[141] H. Liu and H. Lu, "Numerical study on the cluster flow behavior in the riser of circulating fluidized beds," *Chemical Engineering Journal*, vol. 150, no. 2, pp. 374–384, 2009.

[142] J. Davidson, "Circulating fluidised bed hydrodynamics," *Powder technology*, vol. 113, no. 3, pp. 249–260, 2000.

[143] A. S. Berrouk and C. Wu, "Two-dimensional discrete particle model: Comment on the numerical simulation of cluster flow behavior in the riser of circulating fluidized beds by Liu and Lu," *Chemical Engineering Journal*, vol. 160, no. 2, pp. 810–811, 2010.

[144] B. Vreman, B. J. Geurts, N. Deen, J. Kuipers, and J. Kuerten, "Two- and four-way coupled Euler-Lagrangian large-eddy simulation of turbulent particle-laden channel flow," *Flow, Turbulence and Combustion*, vol. 82, no. 1, pp. 47–71, 2009.

[145] P. Brady and O. Desjardins, "A sharp, robust, discretely conservative cut-cell immersed boundary technique for complex three dimensional geometries," *Journal of Computational Physics*, vol. (Under review), 2014.

[146] P. Pepiot and O. Desjardins, "Numerical analysis of the dynamics of two-and three-dimensional fluidized bed reactors using an Euler-Lagrange approach," *Powder Technology*, vol. 220, pp. 104–121, 2012.

[147] J. Grace, "Fluidized bed hydrodynamics," *Handbook of Multiphase Systems*, vol. 5, 1982.

[148] C. Soong, K. Tuzla, and J. Chen, "Identification of particle clusters in circulating fluidized bed," *Circulating Fluidized Bed Technology IV*, pp. 615–620, 1994.

[149] A. K. Sharma, K. Tuzla, J. Matsen, and J. C. Chen, "Parametric effects of particle size and gas velocity on cluster characteristics in fast fluidized beds," *Powder Technology*, vol. 111, no. 1, pp. 114–122, 2000.

[150] A. Harris, J. Davidson, and R. Thorpe, "The prediction of particle cluster properties in the near wall region of a vertical riser (200157)," *Powder Technology*, vol. 127, no. 2, pp. 128–143, 2002.

[151] A. S. Issangya, J. R. Grace, D. Bai, and J. Zhu, "Further measurements of flow dynamics in a high-density circulating fluidized bed riser," *Powder Technology*, vol. 111, no. 1, pp. 104–113, 2000.

[152] K. D. Squires and J. K. Eaton, "Preferential concentration of particles by turbulence," *Physics of Fluids A: Fluid Dynamics*, vol. 3, p. 1169, 1991.

[153] J. Wang, W. Ge, and J. Li, "Eulerian simulation of heterogeneous gas–solid flows in CFB risers: EMMS-based sub-grid scale model with a revised cluster description," *Chemical Engineering Science*, vol. 63, no. 6, pp. 1553–1571, 2008.

[154] J. Wang and W. Ge, "Collisional particle-phase pressure in particle-fluid flows at high particle inertia," *Physics of Fluids*, vol. 17, p. 128103, 2005.

[155] H. Bi and J. Grace, "Effect of measurement method on the velocities used to demarcate the onset of turbulent fluidization," *The Chemical Engineering Journal and the Biochemical Engineering Journal*, vol. 57, no. 3, pp. 261–271, 1995.

[156] D. Shi, R. Nicolai, and L. Reh, "Wall-to-bed heat transfer in circulating fluidized beds," *Chemical Engineering and Processing: Process Intensification*, vol. 37, no. 4, pp. 287–293, 1998.

[157] D. McQuarrie, *Statistical mechanics*. Harper and Row, 1976.

[158] S. Sundaram and L. R. Collins, "Collision statistics in an isotropic particle-laden turbulent suspension. Part 1. Direct numerical simulations," *Journal of Fluid Mechanics*, vol. 335, no. 75, p. 109, 1997.

[159] W. C. Reade and L. R. Collins, "Effect of preferential concentration on turbulent collision rates," *Physics of Fluids*, vol. 12, p. 2530, 2000.

[160] B. Ray and L. R. Collins, "Preferential concentration and relative velocity statistics of inertial particles in Navier-Stokes turbulence with and without filtering," *Journal of Fluid Mechanics*, vol. 680, no. 1, pp. 488–510, 2011.

[161] J. Szekely, J. W. Evans, and H. Sohn, *Gas-solid reactions*. Academic Press, 1976.

[162] K. Theologos and N. Markatos, "Advanced modeling of fluid catalytic cracking riser-type reactors," *AIChE Journal*, vol. 39, no. 6, pp. 1007–1017, 1993.

[163] C. Derouin, D. Nevicato, M. Forissier, G. Wild, and J. Bernard, "Hydrodynamics of riser units and their impact on FCC operation," *Industrial & engineering chemistry research*, vol. 36, no. 11, pp. 4504–4515, 1997.

[164] A. Gupta and D. Subba Rao, "Model for the performance of a fluid catalytic cracking (FCC) riser reactor: effect of feed atomization," *Chemical Engineering Science*, vol. 56, no. 15, pp. 4489–4503, 2001.

[165] A. Das, E. Baudrez, G. Marin, and G. Heynderickx, "Three-dimensional simulation of a fluid catalytic cracking riser reactor," *Industrial & engineering chemistry research*, vol. 42, no. 12, pp. 2602–2617, 2003.

[166] J. Souza, J. Vargas, O. Von Meien, W. Martignoni, and S. Amico, "A two-

dimensional model for simulation, control, and optimization of FCC risers," *AIChE journal*, vol. 52, no. 5, pp. 1895–1905, 2006.

[167] C. Wu, Y. Cheng, and Y. Jin, "Understanding riser and downer based fluid catalytic cracking processes by a comprehensive two-dimensional reactor model," *Industrial & Engineering Chemistry Research*, vol. 48, no. 1, pp. 12–26, 2008.

[168] S. Prasad Vegendla, G. Heynderickx, and G. Marin, "Probability density function simulation of turbulent reactive gas-solid flow in a FCC riser," *AIChE Journal*, vol. 58, no. 1, pp. 268–284, 2012.

[169] J. Bruchmüller, B. van Wachem, S. Gu, K. Luo, and R. Brown, "Modeling the thermochemical degradation of biomass inside a fast pyrolysis fluidized bed reactor," *AIChE Journal*, vol. 58, no. 10, pp. 3030–3042, 2012.

[170] D. Fletcher, B. Haynes, F. Christo, and S. Joseph, "A CFD based combustion model of an entrained flow biomass gasifier," *Applied mathematical modelling*, vol. 24, no. 3, pp. 165–182, 2000.

[171] K. Papadikis, S. Gu, A. V. Bridgwater, and H. Gerhauser, "Application of CFD to model fast pyrolysis of biomass," *Fuel Processing Technology*, vol. 90, no. 4, pp. 504–512, 2009.

[172] M. Oevermann, S. Gerber, and F. Behrendt, "Euler–Lagrange/DEM simulation of wood gasification in a bubbling fluidized bed reactor," *Particuology*, vol. 7, no. 4, pp. 307–316, 2009.

[173] O. Rabinovich, V. Borodulya, L. Vinogradov, and V. Korban, "Fast pyrolysis of an ensemble of biomass particles in a fluidized bed," *Journal of Engineering Physics and Thermophysics*, vol. 83, no. 4, pp. 742–752, 2010.

[174] C. Wu, Y. Cheng, Y. Ding, and Y. Jin, "CFD–DEM simulation of gas–solid reacting flows in fluid catalytic cracking (FCC) process," *Chemical Engineering Science*, vol. 65, no. 1, pp. 542–549, 2010.

[175] T. Li, S. Pannala, and M. Shahnam, "CFD simulations of circulating fluidized bed risers, part II, evaluation of differences between 2D and 3D simulations," *Powder Technology*, vol. 254, pp. 115–124, 2014.

[176] P. Moin, K. Squires, W. Cabot, and S. Lee, "A dynamic subgrid-scale model

for compressible turbulence and scalar transport," *Physics of Fluids A: Fluid Dynamics*, vol. 3, no. 11, pp. 2746–2757, 1991.

[177] N. Peters, *Turbulent combustion*. Cambridge university press, 2000.

[178] H. Pitsch, "Large-eddy simulation of turbulent combustion," *Annu. Rev. Fluid Mech.*, vol. 38, pp. 453–482, 2006.

[179] J. Derksen, "Scalar mixing by granular particles," *AIChE journal*, vol. 54, no. 7, pp. 1741–1747, 2008.

[180] J. Derksen, "Simulations of scalar dispersion in fluidized solid–liquid suspensions," *AIChE Journal*, 2014.

[181] W. R. Goossens, "Classification of fluidized particles by Archimedes number," *Powder technology*, vol. 98, no. 1, pp. 48–53, 1998.

[182] A. Cook and J. Riley, "A subgrid model for equilibrium chemistry in turbulent flows," *Physics of Fluids (1994-present)*, vol. 6, no. 8, pp. 2868–2870, 1994.

[183] J. Jiménez, A. Liñán, M. M. Rogers, and F. J. Higuera, "A priori testing of subgrid models for chemically reacting non-premixed turbulent shear flows," *Journal of Fluid Mechanics*, vol. 349, pp. 149–171, 1997.

[184] C. Wall, B. Boersma, and P. Moin, "An evaluation of the assumed beta probability density function subgrid-scale model for large eddy simulation of nonpremixed, turbulent combustion with heat release," *Physics of Fluids*, vol. 12, no. 10, pp. 2522–2529, 2000.

[185] C. Tong, "Measurements of conserved scalar filtered density function in a turbulent jet," *Physics of Fluids*, vol. 13, no. 10, pp. 2923–2937, 2001.

[186] C. D. Pierce and P. Moin, "Progress-variable approach for large-eddy simulation of non-premixed turbulent combustion," *Journal of Fluid Mechanics*, vol. 504, pp. 73–97, 2004.

[187] J. Bakosi and R. Ristorcelli, "Probability density function method for variable-density pressure-gradient-driven turbulence and mixing," tech. rep., Los Alamos National Laboratory (LANL), 2010.

[188] A. Klimenko and R. Bilger, "Conditional moment closure for turbulent combustion," *Progress in energy and combustion science*, vol. 25, pp. 595–687, 1999.

[189] S. Dasgupta, R. Jackson, and S. Sundaresan, "Turbulent gas-particle flow in vertical risers," *AIChE J.*, vol. 40, no. 2, pp. 215–228, 1994.

[190] P. Février, O. Simonin, and K. Squires, "Partitioning of particle velocities in gas-solid turbulent flows into a continuous field and a spatially uncorrelated random distribution: theoretical formalism and numerical study," *J. Fluid Mech.*, vol. 533, pp. 1–46, 2005.

[191] I. Goldhirsch and G. Zanetti, "Clustering instability in dissipative gases," *Phys. Rev. Lett.*, vol. 70, no. 11, p. 1619, 1993.

[192] J. Royer, D. Evans, L. Oyarte, Q. Guo, E. Kapit, M. Möbius, S. Waitukaitis, and H. Jaeger, "High-speed tracking of rupture and clustering in freely falling granular streams," *Nature*, vol. 459, no. 7250, pp. 1110–1113, 2009.

[193] P. Mitrano, S. Dahl, A. Hilger, C. Ewasko, and C. Hrenya, "Dual role of friction in granular flows: attenuation versus enhancement of instabilities," *J. Fluid Mech.*, vol. 729, pp. 484–495, 2013.

[194] J. J. Wylie and D. L. Koch, "Particle clustering due to hydrodynamic interactions," *Physics of Fluids*, vol. 12, no. 5, pp. 964–970, 2000.

[195] X. Yin, J. Zenk, P. Mitrano, and C. Hrenya, "Impact of collisional versus viscous dissipation on flow instabilities in gas–solid systems," *J. Fluid Mech.*, vol. 727, p. R2, 2013.

[196] Y. Tsuji, T. Tanaka, and S. Yonemura, "Particle induced turbulence," *Appl. Mech. Rev.*, vol. 47, no. 6, pp. S75–S79, 1994.

[197] Y. Igci, A. Andrews, S. Sundaresan, S. Pannala, and T. O'Brien, "Filtered two-fluid models for fluidized gas-particle suspensions," *AIChE J.*, vol. 54, no. 6, pp. 1431–1448, 2008.

[198] W. Briley and H. McDonald, "Solution of the multidimensional compressible Navier-Stokes equations by a generalized implicit method," *J. Comp. Phys.*, vol. 24, no. 4, pp. 372–397, 1977.

[199] C. Hrenya and J. Sinclair, "Effects of particle-phase turbulence in gas-solid flows," *AIChE J.*, vol. 43, no. 4, pp. 853–869, 1997.

[200] D. Wilcox, *Turbulence modeling for CFD*. 3rd edn. La Canada: DCW industries, 2006.

[201] C. Rumsey, "Compressibility considerations for $\kappa-\omega$ turbulence models in hypersonic boundary layer applications," Tech. Rep. NASA/TM-2009-215705, NASA Center for AeroSpace Information, 2009.

[202] L. Zeng, S. Balachandar, P. Fischer, and F. Najjar, "Interactions of a stationary finite-sized particle with wall turbulence," *Journal of Fluid Mechanics*, vol. 594, pp. 271–305, 2008.

[203] L. Zeng, F. Najjar, S. Balachandar, and P. Fischer, "Forces on a finite-sized particle located close to a wall in a linear shear flow," *Physics of Fluids*, vol. 21, no. 3, p. 033302, 2009.

[204] J. Favier, "Shape representation of axi-symmetrical, non-spherical particles in discrete element simulation using multi-element model particles," *Engineering Computations*, vol. 16, no. 4, pp. 467–480, 1999.

[205] L. Vu-Quoc, X. Zhang, and O. Walton, "A 3-D discrete-element method for dry granular flows of ellipsoidal particles," *Computer Methods in Applied Mechanics and Engineering*, vol. 187, pp. 483–528, July 2000.

[206] A. Dvziugys and B. Peters, "An approach to simulate the motion of spherical and non-spherical fuel particles in combustion chambers," *Granular Matter*, vol. 3, pp. 231–266, Dec. 2001.

[207] P. Langston, M. Al-Awamleh, F. Fraige, and B. Asmar, "Distinct element modelling of non-spherical frictionless particle flow," *Chemical Engineering Science*, vol. 59, pp. 425–435, Jan. 2004.

[208] H. Tao, B. Jin, W. Zhong, X. Wang, B. Ren, Y. Zhang, and R. Xiao, "Discrete element method modeling of non-spherical granular flow in rectangular hopper," *Chemical Engineering and Processing: Process Intensification*, vol. 49, pp. 151–158, Feb. 2010.

[209] W.-Q. Zhong, Y. Zhang, B.-S. Jin, and M.-Y. Zhang, "Discrete Element Method Simulation of Cylinder-Shaped Particle Flow in a Gas-Solid Flu-

idized Bed," *Chemical Engineering & Technology*, vol. 32, no. 3, pp. 386–391, 2009.

[210] J. Hilton, L. Mason, and P. Cleary, "Dynamics of gas-solid fluidized beds with non-spherical particle geometry," *Chemical Engineering Science*, vol. 65, no. 5, pp. 1584–1596, 2010.

[211] B. Ren, W. Zhong, B. Jin, Y. Shao, and Z. Yuan, "Numerical simulation on the mixing behavior of corn-shaped particles in a spouted bed," *Powder Technology*, vol. 234, pp. 58–66, 2013.